CONSTITUTIVE BEHAVIOR AND FRACTURE PROPERTIES OF TEMPERED MARTENSITIC STEELS FOR NUCLEAR APPLICATIONS: Experiments and Modeling

THÈSE N^{O} 3405 (2006)

PRÉSENTÉE LE 6 JANVIER 2006

CRPP Association Euratom

SECTION DE PHYSIQUE

ÉCOLE POLYTECHNIQUE FÉDÉRALE DE LAUSANNE

POUR L'OBTENTION DU GRADE DE DOCTEUR ÈS SCIENCES

PAR

Raul Alejandro BONADÉ

Ingeniero en Materiales, Universidad Nacional de General San Martin, Argentine
et de nationalité argentine

acceptée sur proposition du jury:

Prof. G. Meylan, président du jury
Dr P. Spätig, directeur de thèse
Dr E. Diegele, rapporteur
Prof. J. Giovanola, rapporteur
Prof. P. Gumbsch, rapporteur
Dr R. Schaller, rapporteur

ÉCOLE POLYTECHNIQUE
FÉDÉRALE DE LAUSANNE

Lausanne, EPFL
2006

This work is dedicated to my wife

Guadalupe Falguera

without her support along these years it would have been impossible even to start this PhD.

Abstract

In this study, the tensile and fracture properties and the microstructure of the reduced-activation tempered martensitic steel Eurofer97 have been investigated. This technical alloy is a 9%Cr steel developed within the European fusion material research program. To a lesser extend, the plastic flow properties of a equiaxed ferritic Fe9%Cr model alloy were also studied for comparison with those of the tempered martensitic structure.

The main objectives of this work are described hereafter:

- to correlate the microstructural features with the plastic flow properties measured by the tensile tests for both the Eurofer97 steel and the model alloy. The correlation established should be reflected in a physically-based model of plastic flow.
- to study the fracture properties of the Eurofer97 steel in details in the lower ductile-to-brittle transition region.
- to calculate with finite element modeling the stress fields at the crack tip. This information is further used in conjunction with a local approach model for quasi-cleavage to reconstruct the fracture toughness-temperature curve.

Tensile tests were carried out at different imposed nominal strain rate at several temperatures from 77K up to 473K, on both the Eurofer97 steel and the Fe9%Cr model alloy. The temperature dependence of the yield stress was precisely determined. As expected for body-centered cubic (BCC) materials, a strong increase of the yield stress by decreasing temperature, below 200 K, was observed. At higher temperatures, the temperature dependence of the yield stress was found much weaker, being associated with the temperature dependence of the shear modulus. Efforts were made to analyze in details the post-yield behavior (strain-hardening) as a function of temperature. The post-yield behavior was modeled using the Kocks phenomenological model based on the competition of storage and annihilation of dislocations. While this model was originally developed for face-centered cubic (FCC) metals where the rate-controlling mechanism of dislocation motion is the dislocation-dislocation interaction, we used is model in the high temperature domain (T>200K) of BCC materials, to model the strain-hardening evolution of the Eurofer97 steel and the model alloy. The values obtained for the key parameters of the model, namely the dislocation mean free path and annihilation coefficient, were found consistent with the microstructural features. The parameters temperature-dependence observed was also consistent with the physics of two basic mechanisms of dislocation storage and annihilation (dynamical recovery). For the low temperature domain, the strain-hardening model was modified to account for the strong Peierls lattice friction, based on an original idea of Rauch. Transmission electron microscopy observations were done to characterize the undeformed microstructures and their evolution with strain. A clear correlation was established between the stress-dependence of the strain-hardening and the microstructures.

Fracture toughness tests on the Eurofer97 steel were performed with 0.2T C(T) and 0.4T C(T) specimens in the lower transition. Five temperatures were selected at which many tests were repeated to determine the amplitude of the inherent scatter of quasi-cleavage. The temperature were chosen in such a way that the measure fracture toughness remain below 150 MPa $m^{1/2}$, which correspond for the 0.4T C(T) at a M value larger than 70 at the highest temperature. Such a M value for 0.4T C(T) specimens is known to ensure enough constraint.

An attempt to analyze the experimental data in the framework of the master-curve approach by following the ASTM E-1921 standard was done. It was clearly demonstrated that the assumed shape of the toughness-temperature curve as described in the ASTM E-1921 standard for the reactor pressure vessel steels is not adequate for the tempered martensitic Eurofer97 steel, which present a particularly steep transition. Our Eurofer97 fracture database was then compared to the existing one on another similar steel, the F82H. Differences in the amplitude of the scatter of both steels was found while the lower bound of the toughness-temperature curve, describing the 1% failure probability was shown to be the same. 2D finite element simulations of the compact tension specimens were performed at various temperatures using the constitutive laws determined previously. The stress field around the crack tip were calculated and used to determine a local criterion of quasi-cleavage. The criterion is defined by the attainment of a critical stress encompassing a critical area. The lower bound of the toughness-temperature curve was then successfully reconstructed by using this local criterion. Finally, the relationship between the critical area and the applied stress intensity factor for the C(T) specimen was shown to follow a power law whose coefficients are dependent on the real dimensions of the specimen. Such a relationship allows scaling the C(T) toughness data from one size to another in case of in-plane constraint loss.

Résumé

Dans ce travail, les propriétés mécaniques en traction et de fracture ainsi que la microstructure d'un acier martensitique revenu à activation réduite, Eurofer97, ont été étudiées. Cet acier, de la classe 7-9%Cr, a été développé dans le contexte du programme de recherche européen sur les matériaux de fusion nucléaire. Dans une moindre mesure, les propriétés de l'écoulement plastique d'un alliage modèle ferritique (Fe9%Cr) ont été étudiées afin de les comparer avec celles de la microstructure de l'acier martensitique revenu.

Les objectifs principaux de ce travail sont énumérés ci-dessous :

- corréler les caractéristiques de la microstructure avec les propriétés de l'écoulement plastique mesurées par essais de traction dans l'acier Eurofer97 et l'alliage modèle. La corrélation établie devra être décrite dans le cadre d'un modèle d'écoulement plastique basé sur des mécanismes de dislocations.
- étudier les propriétés en fracture pour l'Eurofer97 en détail dans le niveau bas de la transition fragile-ductile.
- calculer par éléments finis les champs de contraintes en tête de fissure. Cette information sera ensuite utilisée en combinaison avec une approche locale de quasi-clivage pour reconstruire la courbe ténacité-température dans la transition.

Des essais de déformations ont été réalisés à plusieurs vitesses de déformation imposées et différentes températures de 77K à 473K pour l'acier Eurofer97 et l'alliage modèle Fe9%Cr. La dépendance en température de la limite d'élasticité a été déterminée précisément. Comme attendu dans le cas des matériaux cubiques centrés (CC), une forte augmentation de la limite d'élasticité a été observée aux températures inférieures à 200 K. Aux températures plus élevées, la dépendance en température de la limite d'élasticité a été trouvée beaucoup plus faible, étant associée à celle de module de cisaillement. Le durcissement a été analysé en détail en fonction de la température. Il a été modélisé avec la description phénoménologique proposée par Kocks prenant en compte le stockage et l'annihilation des dislocations. Bien que ce modèle ait été originellement développé pour les métaux cubiques à faces centrées (CFC) pour lesquels le mécanisme contrôlant la mobilité des dislocations est l'interaction dislocation-dislocation, nous l'avons utilisé dans le domaine hautes températures (T>200K) pour les matériaux CC afin de modéliser le durcissement de l'acier Eurofer97 et de l'alliage modèle. Les valeurs des paramètres du modèle, à savoir le libre parcours moyen des dislocations et le coefficient d'annihilation, ont été trouvées cohérents avec la microstructure. La dépendance en température observée des paramètres a également été trouvée cohérente avec la nature physique des mécanismes de stockage et d'annihilation. Dans le domaine basse température, le modèle de durcissement a été modifié pour tenir compte de la force de friction du réseau, sur la base d'une idée originale de Rauch. Des observations par microscopie électronique à transmission ont été effectuées pour caractériser la microstructure dans l'état non-déformé et de son évolution avec la déformation. Une corrélation claire a été établie entre la dépendance en contrainte du durcissement et les microstructures.

Des essais de ténacité en fracture ont été réalisés sur l'acier Eurofer97 avec des échantillons de traction compacts 0.2T C(T) et 0.4T C(T) dans la transition basse. Cinq températures ont été sélectionnées auxquelles une série d'essais ont été répétés pour déterminer l'amplitude de

la dispersion des résultats inhérente au quasi-clivage. Les températures ont été choisies de telle manière que les valeurs de la ténacité restent inférieures à 150 MPa $m^{1/2}$, ce qui correspond pour les échantillons 0.4T C(T) à une valeur de M plus grande que 70 à la plus haute température. Une telle valeur de M pour ce type échantillons est suffisante pour assurer un confinement limité des contraintes. Une tentative d'analyse des données expérimentales dans le cadre de l'approche « courbe-maîtresse » décrite dans le récent standard ASTM1921 a été faite. Il a été clairement démontré que la forme supposée de la courbe ténacité-température décrite dans le standard ASTM1921 n'est pas adéquate pour l'acier martensitique revenu Eurofer97, qui présente une transition particulièrement abrupte. L'ensemble de nos données a été comparé à celui existant d'un acier similaire, nommé F82H. Des différences dans l'amplitude de la dispersion des valeurs de ténacité dans la transition entre les deux aciers ont été trouvées alors que la courbe décrivant l% de probabilité de rupture a été montrée être identique pour les deux aciers. Des simulations 2D par éléments finis des échantillons C(T) ont été réalisées à différentes températures en utilisant les lois constitutives établies préalablement. Les champs de contraintes en tête de fissure ont été calculés et utilisés pour déterminer un critère local de quasi-clivage. Le critère est défini par le développement d'une surface critique dans laquelle la contrainte est supérieure à une valeur critique. La courbe de rupture définie à 1% de rupture a été reconstruite avec succès en utilisant ce critère. Finalement, la relation entre la surface critique et le facteur d'intensité de contrainte appliqué pour les échantillons C(T) a été montré suivre une loi puissance dont les coefficients dépendent des dimensions réelles de l'échantillon. Une telle relation permet le transfert des valeurs de ténacité obtenues avec des échantillons d'une certaine dimension à des valeurs obtenues avec des échantillons d'une autre dimension dans le cas où des pertes de confinement des contraintes se produit.

Chapter 1

Introduction

The 9-12%Cr ferritic and martensitic stainless steels have a number of industrial applications in which their corrosion resistance, high thermal conductivity and low thermal expansion, together with their high temperature creep and fatigue properties make them attractive. These steels have also been used in nuclear applications in wrappers and as cladding materials in fast breeder reactors. From the point of view of thermo-nuclear fusion, the foregoing high temperature properties, together with the swelling resistance of these steels in fission nuclear applications led to their selection as the most promising candidate structural materials for a fusion reactor. Despite their attractive mechanical and physical properties, their main drawback resides in the fact that they experience a fracture mode transition, namely from ductile tearing mode with high toughness values at high temperature to cleavage mode with low toughness values at low temperature. Since the materials surrounding a burning plasma in a future fusion reactor will be highly irradiated by energetic neutrons and other type of radiations, a strong degradation of their overall mechanical properties induced by the radiation environment will occur. In particular, a shift of the ductile-brittle transition to the high temperatures results from the irradiation, which limits the use of the ferritic/martensitic steels in fusion applications. The phenomenon is referred as to *embrittlement*. Another effect of irradiation is to decrease the ductile toughness level. Over the years, extensive research have been accomplished on the ferritic/martensitic steels resulting in significant improvement regarding the radiation resistance and low activation chemical composition. However, not enough work has been devoted so far to the characterization and modeling of their fracture behavior in the transition domain from ductile to brittle regime.

The successful design and operation conditions of fusion reactors present important challenges to the material science community. Quantitative prediction methods are required to assess the in-service degradations of the overall mechanical properties. Therefore, assuming for instance that cracks develop during the operation of the thin-wall structure of the first wall, an engineering effective toughness parameter, characterizing the resistance of the material against fast fracture, has to be defined to be used in structural and failure analysis. This parameter will serve to calculate the maximum loads that the structure can sustain. From the engineering point of view, we need to develop reliable methods to characterize the effective toughness of the typical fusion reactor structure in the unirradiated condition but also to be able to predict the effective toughness evolution, over a range of irradiation temperatures covering those of normal operation conditions, throughout the service. Thus, the effect of neutron irradiation on the fracture properties degradations will have to be well understood and monitored in-service.

Evaluating the irradiation effects on fracture will mainly rely on small or even ultra-small specimen test techniques, which do not yield straightforwardly the actual effective toughness of the reactor components. The development of such toughness measurement techniques has been included in fusion material research programs. The ultimate goal of these techniques is to transfer the apparent toughness measured with small specimen to another arbitrary structure configuration. Consequently, both, the understanding of the physical mechanisms

underlying brittle fracture phenomena in tempered martensitic steels and the influence of the structure/loading configuration on the local stress-strain conditions are fundamental.

The 9%Cr reduced-activation tempered martensitic steel Eurofer97 is currently the reference structural material for the first wall and blanket of the next demonstration fusion reactor (DEMO). Up to now, many research activities, scientific papers and international workshops have been devoted to these steels regarding their development, microstructural characterization, and mechanical/physical properties evaluation before and after irradiation. It is clear that the accumulated experience from the operation of fission nuclear power plants has played a central role. Indeed, extensive databases characterizing the ductile to brittle transition behavior of the bainitic reactor pressure (RPV) steels are available. Moreover, the effect of irradiation on the RPV steels is well documented for the typical doses reached at the end-of-live of a fission power station (of the order of 1–2 dpa). However, the applicability of the tempered martensitic steels introduces fusion-related challenges, which are mainly related to:

- the large irradiation dose levels reached shortly after startup of a fusion reactor (50-100 dpa a year in a real fusion machine),
- the build-up of hydrogen and helium in the materials resulting from the specificity of the fusion neutron spectrum.
- and to a lesser extend the specificity of the irradiation response of this type of steel to irradiation with respect the RPV steels.

While the irradiation-induced changes in the mechanical properties between the RPV steel and the martensitic ones are qualitatively similar, differences have bee identified. In the same vein, the irradiation-induced microstructure in both types of steels is known not to be the same. Regarding the effect of irradiation on fracture toughness on the tempered martensitic steels, it has been recently proposed to use a similar approach as that used for the RPV steel to evaluate the embrittlement. The approach consists in indexing a toughness-temperature master-curve on an absolute temperature scale at a reference toughness value as a function of neutron fluence. The extension of the master-curve methodology to the tempered martensitic steel appears indeed as a natural move while many issues have to be addressed to prove the applicability of the method to these types of steels, in particular for the unexplored dose range expected in a fusion environment.

This study was undertaken to characterize fully the constitutive and fracture behavior of the European 9%Cr tempered martensitic steel in the lower transition. In order to determine the constitutive behavior, plain tensile tests were foreseen. Transmission electron microscopy investigations served as the main tool to characterize the microstrutures of the as-received and deformed materials. On the one hand, modeling of the constitutive behavior in relation to the microsctructures and, on the other hand, modeling of the fracture properties by finite elements simulation based upon the established constitutive behavior, were the main goals of this work.

This dissertation is organized as follows. In Chapter 2, a literature survey on the development and irradiation effects in the ferritic-martensitic steels is presented. The investigated materials and their microstructures are described in Chapter 3. They have been studied mainly by optical and electron transmission microscopy. Chapter 4 is devoted to the tensile tests results and the modeling of the post-yield behavior in the framework of simple

dislocation mechanics models. The fracture toughness results are presented, analyzed and modeled with finite element simulations in Chapter 5 where a review on the local approach to cleavage is also provided. Finally in Chapter 6, the conclusions of the work are drawn and perspectives are discussed.

Chapter 2

Literature survey.

2. 1. Introduction

In this chapter we present the general requirements that the fusion materials have to meet to sustain the highly aggressive environment of a burning fusion plasma. Then, we briefly review the development of the high-chromium ferritic-martensitic steel within the framework of the international fusion material programs. In the fourth section, we outline the most challenging issue regarding the application of these steels, which is the existence of the ductile-to-brittle transition in their fracture mode and related embrittlement following neutron irradiation. A survey on the effects of irradiation on the overall properties of these steels is presented in the fifth section with a special emphasis on the degradation of properties under irradiation. A description of the engineering approaches to assess the embrittlement degree for structural materials due to irradiation and the safety operation conditions is given in the sixth section. Finally, the objectives of the thesis are described in the last section.

2. 2. Structural materials requirements for fusion reactor materials.

Thermonuclear fusion power is a source of energy that has the potential to provide a significant contribution to the energy needs of mankind for many millennia [2.1]. The current fusion research programs are oriented towards the utilization of the energy released by the fusion of two hydrogen isotopes, namely the deuterium (D) and the tritium (T). The attractiveness of fusion energy resides in its many inherent advantages, among which we mention: i) the fuels (deuterium – tritium) are plentiful, ii) the product of the nuclear reaction is an inert gas (helium), iii) no uncontrolled chain reaction can occur, iv) the neutron-induced radioactivity of the structural materials can be minimized by a careful selection of low-activation materials and v) the release of tritium in normal operation conditions can be kept to a very low level.
The fusion of these two hydrogen isotopes produces 14 MeV neutrons, which represent 80% of the total energy released by the nuclear reactions, while the remaining 20% of this energy is carried by α particles. About 10% of the 14 MeV neutron energy will be deposited in the first wall and the remaining will be transferred into the blanket of the tokamak [2.2]. These neutrons collide with nuclei of the materials surrounding the plasma, producing displacement cascades with subsequent production and accumulation of irradiation-induced defects. Modifications of the material chemistry through transmutation reaction, production of gaseous impurities (helium and hydrogen) also occurs as well as possible redistribution of elements through radiation-induced segregation and/or phase transformation [2.3]. The successful development of thermonuclear fusion power systems mainly depends on materials maintaining their integrity and their dimensional stability.

There are several critical requirements to be fulfilled by the structural materials to be used for the first wall and the breeding blanket of a fusion reactor. As discussed in details by Ehrlich [2.4], there are three key criteria. First, the material selection for a given component is based upon conventional properties, namely mechanical properties, physical properties, compatibility between different materials, corrosion etc.. The materials foreseen for a given application must have been qualified beforehand and the industrial fabrication processes involved must be well established. In the same vein, welding technology for a given material and experience in real applications need to be available. Second, a precise knowledge of the overall material behavior evolution under a fusion neutron environment is mandatory. The materials integrity under the integrated neutron flux at the service temperatures must be demonstrated. Finally, public acceptance of fusion as a large-scale energy source will be strongly related to the amount of long-term activation of materials produced. Indeed, the structural materials of a fusion reactor will be a source of neutron-induced radioactivity, which will have an important impact on the safety, environmental aspects and public acceptance of power fusion plants. Thus, the development of the so-called *low activation materials* or *reduced activation materials* has been recognized as a key issue in the fusion material community for more than two decades [2.5, 2.6]. The concept of *reduced activation materials* has to be understood as a reduced neutron irradiation-induced long-term activation. In this sense, the induced activity of the reduced-activation steels is expected to decay to acceptable levels in several hundreds years, compared to the thousands of years for non – reduced-activation steels [2.7].

The previously mentioned requirements have led the fusion material community to develop candidate structural materials for first wall and breeding blanket applications that have a chemical composition based on low activation elements (Fe, Cr, V, Ti, W, Ta, Si, C). They

include mainly reduced activation ferritic/martensitic (RAFM) steels, vanadium alloys and SiC/SiC ceramic composites [2.8]. Among them, RAFM steels are presently considered to be the most promising structural materials as they have achieved the greatest technical maturity; i.e., qualified fabrication routes, welding technology and a general industrial experience are already available.

2. 3. The development of the 7-12%Cr tempered martensitic steels for fusion applications.

The 9-12%Cr ferritic-martensitic stainless steels have a number of industrial applications in which their corrosion resistance, low thermal conductivity and expansion, together with their high temperature creep and fatigue properties make them attractive. In the 1980's, the development of "super clean steels" [2.9] led to an additional improvement of creep and fracture properties. These steels are mainly used in large rotors and discs for power generating turbines and have very low P, As and Sb, together with a minimized content of Mn and Si.

The 7-12% Cr tempered martensitic steels have been investigated for applications as fuel cladding in fast fission reactors for which the austenitic steels were initially the undisputed material until the mid-seventies [2.10]. Due to the high propensity of the austenitic steels to volumetric expansion during irradiation (swelling) the applications of these steels for cladding and piping as well as for structural components were challenged by the swelling phenomenon [2.11]. In the early seventies, other steels and alloys were then considered, among which the ferritic and the tempered martensitic steels appear as good alternatives to the austenitic ones. They were introduced into the international fusion material programs in the early eighties. By now, they are one of leading material candidates for fusion structural applications, in particular for the first wall and the blanket.

Initially, the chemical composition and processing of these steels were based on the HT-9 steel, a 12% Cr. 1% Mo. 0.2%C with additions of W and V as well as on the European alloy MANET, another 12% Cr steel containing 0.5% Mo and an addition of Nb as grain-stabilizer [2.12]. A series of investigations were initiated to optimize the overall mechanical properties between low ductile-to-brittle transition temperature, high fracture toughness and high creep resistance. In order to obtain fully martensitic structures in the 12%Cr HT-9 and MANET steels, austenite-stabilizing additions had to be included; Mn and C were considered for that purpose. However, it was found that irradiation induced severe degradation of the Mn-stabilized martensitic alloys [2.13]. Actually, these steels suffer from grain boundary embrittlement as reflected in a drastic degradation of their Charpy impact properties. Modifications of the Cr contents in these steels were then considered and the most promising composition was found in the 7-9%Cr range with 2%W addition [2.14]. Regarding the neutron-induced activity, calculations have shown that some alloying elements like Nb, Mo, Ni, Co, Cu, N generate long-lived radioactive isotopes while other like V, W, Ta presented much better radiological properties [2.15,2.14]. Therefore, in order to develop reduced activation tempered martensitic steels, Ni has been excluded from the steel composition while Nb and Mo had to be replaced by W, V and Ta.

Under the auspices of the International Energy Agency, the working group on Ferritic/Martensitic steel decided to cast a 5000 kg heat called F82H-mod [16]. The F82H-mod steel was produced by NKK Corporation under the sponsorship of Japan Atomic Energy Research Institute. The composition of the F82H-mod steel in wt.% is: 7.87Cr-1.98W-0.19V-0.03Ta-0.1Mn-0.007N.

In Europe, the European Fusion Long Term Program is coordinated under the European Fusion Development Agreement. The first priority of the European Program is to obtain a qualified structural material to be used for the tritium breeding blanket module and first wall of a demonstration fusion reactor (DEMO). The current EU reference material is the so-called Eurofer97. The Eurofer97 plate used in this study, heat E83697, was produced by Böhler AG. The composition of the Eurofer97 steel in wt.% is: 8.90Cr-1.07W-0.20V-0.15Ta-0.46Mn-0.020N.

The major differences between the F82H and Eurofer97 steels lie in the Cr, W and Ta contents. The lower tungsten content was actually intended because the tritium-breeding rate is higher for lower tungsten content. This point was regarded as necessary at the time the alloy was ordered, In addition, lower tungsten levels tend to reduce the amount of Laves phases formed with respect to higher contents.

Note that a great deal of studies has been undertaken on many other steels similar to the F82H-mod and the Eurofer97 ones. We mention the most important developed reduced-activation steels within the fusion programs. In Europe two series of heats, named OPTIFER [2.17, 2.18,] and OPTIMAX [2.19, 2.20, 2.21], were produced to investigate their mechanical properties, microstructure and their stability under irradiation. In the US, the steel with the best properties was ORNL 9Cr-2WVTa [2.22].

2. 4. Ductile to brittle transition of the tempered martensitic steels.

One of the main challenges regarding the engineering applications of the tempered martensitic steels is related to their intrinsic ductile to brittle transition. Indeed, their fracture mode changes from the high-temperature microvoid coalescence to the low-temperature quasi-cleavage one [2.23]. This behavior has been recognized as a serious issue that needs to be addressed in-depth. Further, as a consequence of neutron irradiation, the transition temperature between the ductile and brittle regime is shifted to higher temperatures, possibly limiting the use of these steels in applications to fusion first wall and blanket structures [2.24]. In addition, the effect of gaseous impurities, H and He in particular, generated by transmutation reactions with the 14 MeV fusion neutrons remain to be addressed with a neutron spectrum representative of that of the fusion environment. This will allow to have the correct He/H production rate with respect to the defect production rate [2.25].

It has to be emphasized that, within the framework of the fusion material development program and during the last two decades, the fracture properties have been mainly investigated with Charpy impact tests. However, Charpy impact testing is actually a very simplistic approach to assess the ductile to brittle transition. The technique consists of determining the so-called ductile-to-brittle-transition temperature (DBTT) by measuring the total energy necessary to fracture a V-notched specimen (see for instance [2.26]). Nowadays, Charpy impact testers are instrumented so that the load-time curve can be obtained and evaluated. A typical Charpy curve for a tempered martensitic steel is presented in Figure 2. 1. The effect of irradiation on the Charpy curve is also depicted in Figure 2. 1. In general, irradiation induces a shift of the DBTT to higher temperature and a decrease of the upper shelf energy.

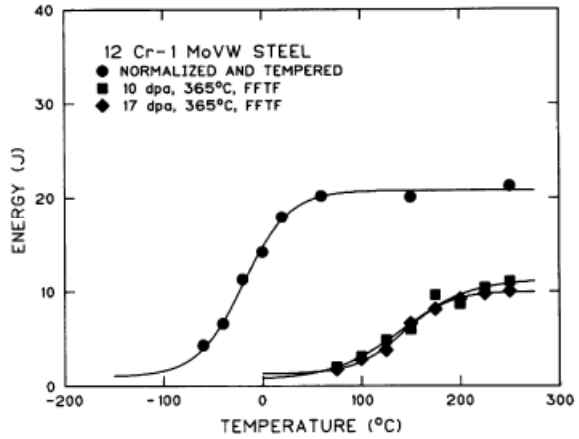

Figure 2. 1: *Charpy curve, HT9 steel before and after irradiation at 10 and 17 dpa at 365 °C [27]***.**

Fracture toughness tests with pre-cracked specimens were also carried out but to a much lesser extend. The material's fracture toughness is determined by the critical level of a certain stress intensity factor. Under specific testing conditions, the measured fracture toughness is a material property independent of the specimen geometry/size used during testing. First, we note that the shape of fracture toughness-temperature curve K(T) curve is quite similar to the Charpy energy-temperature one. It is convenient to divide the overall K(T) into four regions: the lower shelf, the lower transition region, the upper transition region and the upper shelf.

An illustration is shown in Figure 2. 2 where the solid line corresponds to the unirradiated curve of a given steel.

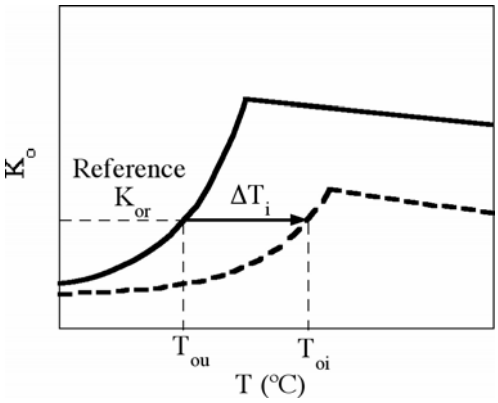

Figure 2. 2: *Effect of irradiation on the K(T) curve in the transition and on the upper shelf, from [28].*

In the lower shelf region no large scatter in the experimental data is observed and cleavage (typically on microstructures composed mostly of equiaxed ferrite) or quasi-cleavage (in bainitic and tempered martensitic structures) are the observed micro-mechanisms of fracture. Beyond a certain temperature, the toughness increases strongly with temperature. This region is referred to as the "ductile –to-brittle transition". In the transition, the toughness data become highly scattered but the fracture mode remains the same (cleavage or quasi-cleavage). At higher temperature, when toughness does not increase any more, it has reached the upper shelf region characterized by a ductile mode of fracture (usually, microvoid coalescence). The effects of irradiation on the K(T) curve are schematically illustrated in Figure 2. 2, where we can see a upper shift of the K(T) curve and a decrease of the upper shelf induced by irradiation. The temperature shift is the so-called "*embrittlement*".

As mentioned above the fracture mode of the lower shelf and in the transition of the tempered martensitic steel is quasi-cleavage. Quasi-cleavage has characteristics different from pure cleavage. In cleavage, fracture occurs on preferred crystallographic plane, typically on the [100] planes for bcc Fe and Fe alloys [2.29] as well as for isotropic tungsten single crystals [2.30]. In ferritic steels for instance, cleavage involves the initiation of a single strain nucleated micro-crack at a carbide or inclusion. Unstable fracture propagation occurs from this site. Typical river patterns develop as the crack propagates from one grain to the adjacent and encounters another crystallographic orientation. An illustration of pure cleavage is given in Figure 2. 3 for an equiaxed ferritic Fe9%Cr model alloy we studied. High loading rates and low temperatures promote cleavage. Quasi-cleavage is characterized by small facets, where cleavage takes place, which are separated by ductile tear ridges formed at the many boundaries present in the tempered martensitic microstructure. The fracture surface units are small and correspond to lath block size or to lath packet size. All the small facets and ridges coalesce into a larger crack making the fracture surface not as clearly defined as in pure cleavage. Quasi-cleavage is not expected to be single event controlled since it involves frequent nucleation and subsequent arrests of micro-cracks at boundaries. Like cleavage, quasi-cleavage is promoted by high loading rates and low temperatures. A typical quasi-cleavage illustration is presented in Figure 2. 4.

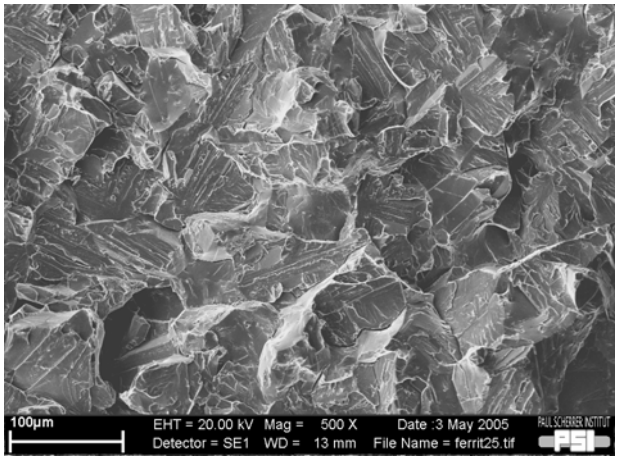

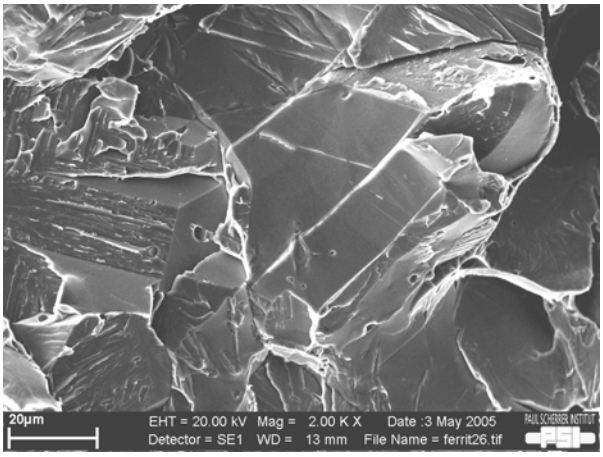

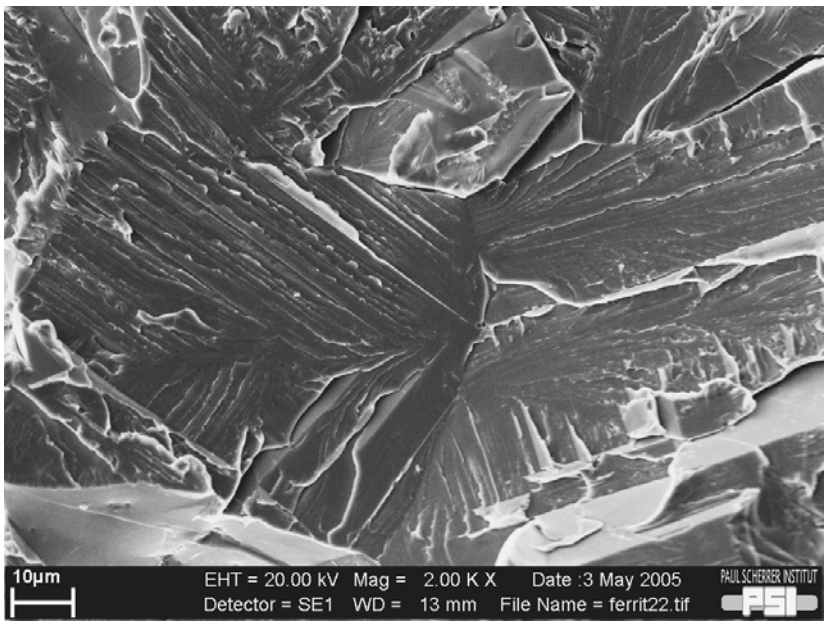

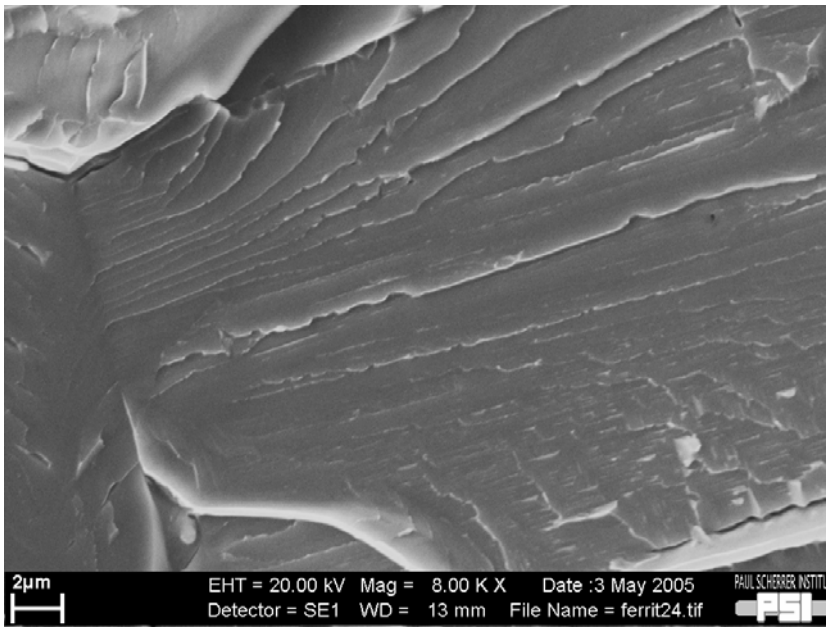

Figure 2. 3: *Typical aspect of a fracture surface formed by transgranular brittle fracture (cleavage). The material is a fully ferritic Fe-9%Cr model alloy (see Chapter 3 for details. Top right: general view of the fracture surface. Top left: Perfectly flat surfaces corresponding to cleavage planes can be easily identified. Note that the dimensions of these regions are consistent with the grain size of the alloy. Left: Example of the so called "river patterns*

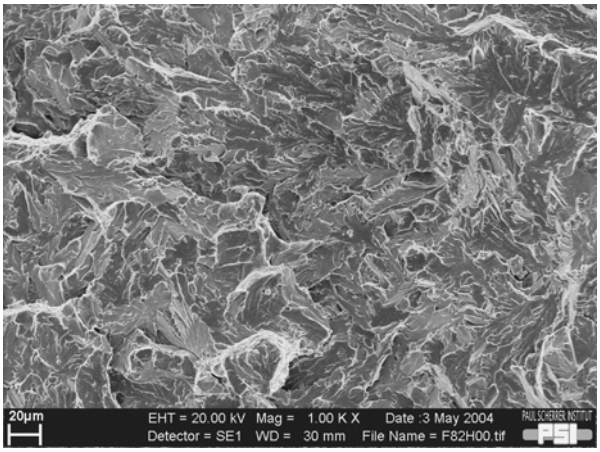

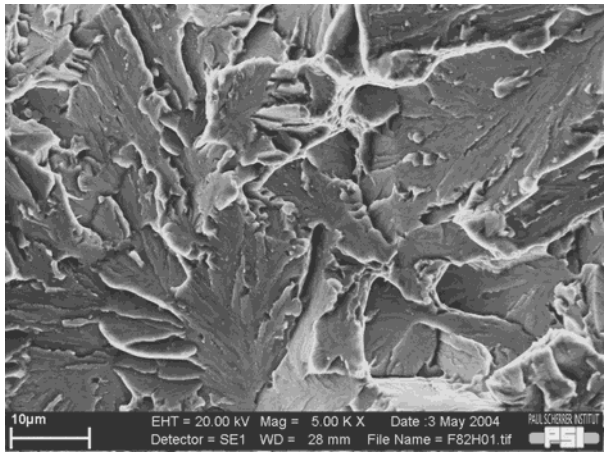

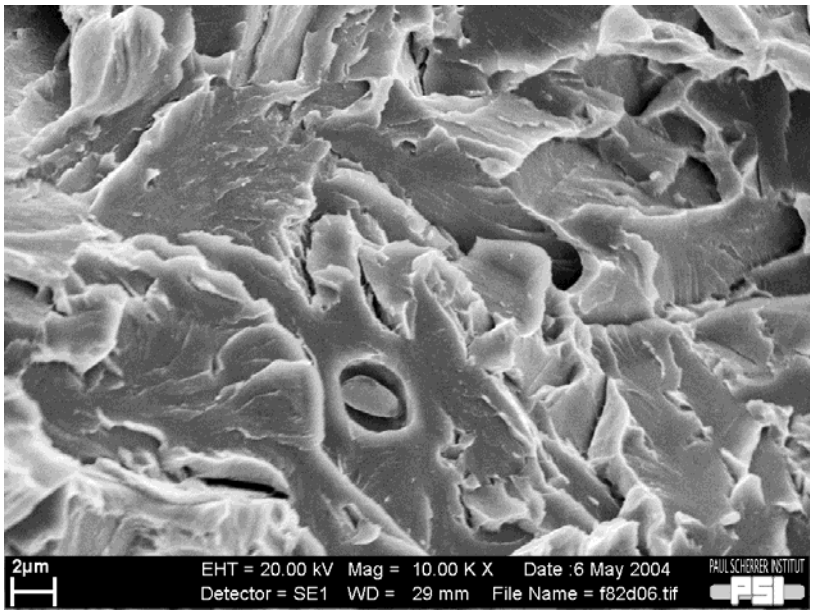

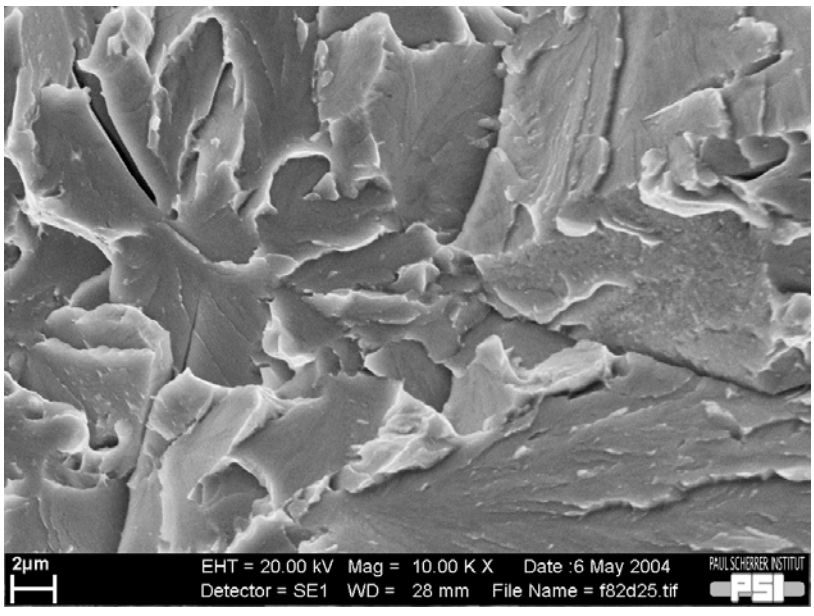

Figure 2. 4: *Aspect of a fracture surface formed by quasi-cleavage, a micromechanism of fracture occurring in martensitic and bainitic steels. In this case the images correspond to F82H, a tempered martensitic stainless steel. Top left: general view. Top right and left: Typical morphology of the quasi-cleavage micromechanism.*

2. 5. Irradiation effects on the properties of tempered martensitic steels.

In the following we briefly review the effect of irradiation on the properties of the tempered martensitic steels with special emphasis on the mechanical properties. Note that most of the papers on this subject have been published in the Proceedings of the series of International Conferences on Fusion Reactor Materials (ICFRM).

Due to the high-energy neutron flux, atoms of the lattice of the materials surrounding a burning plasma will be displaced through displacement cascades from their sites to form interstitials and vacancies. The accumulated dose in the materials is usually quantified in dpa (displacement per atom). The evolution of the mechanical properties results from the accumulation of irradiation-induced defects, namely interstitial and vacancies into voids or dislocation loop. The loop size and loop number density depends on the irradiation temperature and decreases with increasing temperature [2.31]. Gelles [2.32] showed that the reduced-activation tempered martensitic are highly resistance to fast neutron irradiation up to doses as high as 200 dpa. He showed that at such a dose swelling reaches a maximum of 5% at the swelling peak temperature. Besides swelling, it is worth mentioning that the irradiation-induced vacancies accelerate recovery and precipitation processes and induce new phases, altogether modify the initial properties of the steels [2.33].

The 14 MeV neutrons will generate transmutation nuclear reactions with the nuclei leading to the production of gaseous impurities, in particular hydrogen and helium. It is expected that at the temperature of the reactor operation hydrogen will migrate out of the lattice even though there are some ions and proton irradiation studies indicating trapping of hydrogen in martensitic steels [2.34, 2.35]. As far as helium is concerned, there are indications that it may affect swelling [2.36] and that at high concentrations it can play a role in the degradation of the fracture properties [2.37].

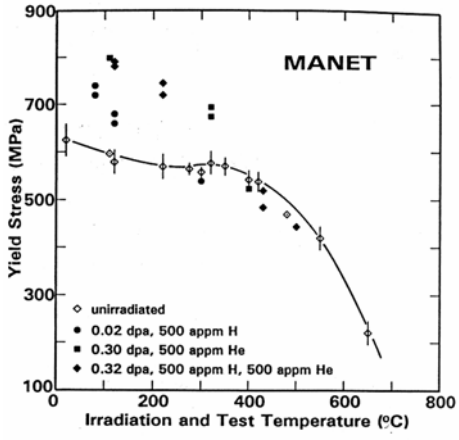

Figure 2. 5: *Temperature dependence of the yield stress before and after irradiation for the 12%Cr steel MANET [2.38]*

The tensile properties are strongly affected by irradiation but the effects depend on the irradiation temperature [2.38, 2.39]. In the hardening regime, namely below 425°C–450°C, the accumulation of irradiation induced loops, precipitates and nano-voids yield a significant increase of the yield stress, the so-called irradiation hardening. When the irradiation temperature is above 425°C–450°C, the tensile properties remain usually unchanged but

softening is sometimes observed depending on the fluence [2.39]. The irradiation hardening as function of temperature is illustrated in Figure 2. 5 where tensile data at three doses are reported for the 12%Cr Manet-1 steel [2.40]. For the F82H steel for example in the hardening regime, the yield stress increases linearly with dose at least up to dose level equal to 10 dpa [2.41].

In the previous section, we have briefly described the effect of irradiation on the Charpy impact and fracture toughness properties. We extend here the survey on this topic; we have separated the papers dealing with Charpy impact tests from those on fracture toughness. We have listed a selection of representative papers to show how the fusion material community has evaluated the fracture properties of steels for the last two decades. Most of the papers have been published in the Proceedings of the International Conferences on Fusion Reactor Materials (ICFRM). We proceed chronologically starting with the ICFRM 1 Proceedings in 1985.

Charpy tests

While far from being exhaustive, this section is intended to show how much efforts have been invested up to now in Charpy testing in the international fusion material programs to assess the fracture properties of the ferritic and martensitic steels.

Standard Charpy V-notched and small ball punch tests, performed on the HT-9 steel, have been reported by T. Misawa et al. [2.42]. With the small ball punch test, they demonstrated that one can determine a clear ductile-brittle fracture energy transition behavior with this type of test, and they correlated small punch test DBTT with the DBTT measured with Charpy-V notched specimens. The effect of proton irradiation on the fracture properties was shown.

Yoshida et al. [2.43] studied with instrumented Charpy test (U-notch half-size) the irradiation response of a Mn austenitic steel, of one 9Cr-1Mo and of one 9Cr-2Mo ferritic steels. The specimens were irradiated at the Japan Materials Testing Reactor (JMTR) to a fast-neutron fluence of 6.5×10^{22} n/m^2 at 573 K. Shifts of the DBTT of 30 to 40 K were measured for the 1Mo and 2Mo ferritic steels respectively

The neutron irradiation embrittlement of different Fe-Cr ferritic steels were studied with instrumented Charpy tests by Kayano et al [2.44], who also carried out tensile tests. General equations were established to correlate strength, ductility, DBTT and fracture toughness (J values).

A study of the effect of long-term aging, from 773 to 873 K during 3600 Ks, on the microstructure and toughness of different Cr-2Mo steel was undertaken by Hosoi et al. [2.45] with V-notched instrumented Charpy testing. A large loss of toughness was observed associated to the precipitation of intermetallic compounds, which include Si and P, in the ferrite.

T. Lechtenberg [2.46] clearly pointed out that the fracture properties of ferritic steels for fusion applications were mainly investigated with measurement of DBTT by Charpy tests. There is however no quantitative method to use the Charpy data in design.

The effects of the trace impurity elements, namely phosphorus, sulfur and silicon, on the impact toughness of a 9Cr-1Mo steel were investigated by Harrelson et al. [2.47] with standard V-notched Charpy tests. Additions of all three elements were found to increase the DBTT and to decrease the upper shelf energy. The effect of sulfur was shown to be more pronounced than that of phosphorus due to the formation of non-metallic inclusions that reduces toughness.

The Charpy impact properties of a 12Cr-1MoVW alloy were determined on sub-sized Charpy specimens by J. M. Vitek et al. [2.48] after irradiation at 300°C in the University of Buffalo Reactor at two different neutron fluences, 0.86×10^{24} and 1×10^{26} n/m^2 respectively. They compared the results with other data in the literature and showed that the largest effect on the impact properties of this alloy occurs for irradiation temperature between 300°C and 400°C. They also assessed the aging effect at 300°C during 2500 h and showed that the DBTT and upper shelf energy were not affected by it.

Microstructural examination, tempering studies, tensile tests and Charpy impact tests with full size V-notch specimens were done on experimental heats of reduced-activation steels by Klueh and Maziasz [2.49]. The major elements of the alloys were: 9Cr-2WV, 9Cr-2WVTA, and 12Cr-2WV. The results show that these Cr-W steels have similar mechanical properties to those of the Cr-Mo while presenting much a better reduced-activation properties. Notably, it was found that the impact behavior of the Cr-W steels was superior to that of the Cr-Mo.

An investigation of the influence of the specimen size on Charpy impact testing was carried out on the HT-9 steel by Louden et al. [2.50]. Pre-cracked and notched specimens were used to develop correlations that predict, on the one hand the DBTT of the full size specimen from the half and third size ones. On the other hand, another correlation between the upper shelf energy for full and sub-sized specimens was proposed. The correlations were based on physical insight such that they were applicable to both pre-cracked and notched specimens.

Kayano et al. [2.51] studied the embrittlement with Charpy tests (1/4 size specimen) after 300°C neutron irradiation in the JMTR to a fast-neutron fluence of 2.2×10^{23} n/m^2 of three classes of steel: i) basic Fe-Cr ferritic steel, ii) low activation steels based on Fe-Cr-W composition, iii) Fe-Cr-Mo, Nb or V ferritic steels. Interestingly, they showed that, for the Fe-Cr and Fe-Cr-Mo, the lower DBTT and irradiation-induced shift of the DBTT were obtained in the composition range 3-9% Cr.

In 1991, Klueh and Alexander [2.52] irradiated capsule of one-half size Charpy specimens in the High Flux Isotope Reactor (HFIR) in Oak Ridge National Laboratory at 300°C and 400°C up to dose as high as 42 dpa. The DBTT shifts and decrease of the upper shelf energy were determined. Both quantities were larger at 400°C than at 300°C. The shifts of the DBTT were of the order of 204°C for a 9Cr-1MoVNb steel and 242°C for a 12Cr-1MoVW steel. These larger shifts were attributed to high helium concentration produced by the irradiation in HFIR.

R. L. Klueh et al. [2.53] reviewed in 1992 the status of ferritic/martensitic steels for fusion application. They outlined that i) the magnitude of shift in the DBTT varies inversely with irradiation temperature, ii) the effect of irradiation is affected by the initial heat-treatment, iii) the shift in DBTT saturates with neutron fluence, iv) tantalum plays a favorable role in

decreasing the irradiation-induced shift of the DBTT by presumably refining the microstructure, v) helium appears to affect the impact behavior after irradiation.

In the framework of the development of small specimen test techniques, Kurishita et al. [2.54] performed an extensive study on the effects of Charpy specimen dimensions and on the effects of the V-notch geometry on the DBTT of a dual phase steel ferritic/martensitic steel developed in Japan. They tested a variety of specimen geometry, among which the smallest had a cross-section as small as 1 mm x 1 mm. They showed that the DBTT is strongly dependent on the V-notch geometry but is uniquely determined by the ratio between the notch depth and notch root radius. Their results led to the conclusion that the DBTT of full-size specimens can be assessed from sub-sized ones. Similarly they developed a specimen size normalization for the upper shelf energy.

Klueh and Alexander [2.55] reported results obtained with one-third-size Charpy specimens on eight different Cr-W steels with Cr contents ranging from 2.25 to 12 wt% irradiated at 365°C to 13-14 dpa in the Fast Flux Test Facility (FFTF) in Hanford. They show that the two 9%Cr steels (9Cr2W0.25V and 9Cr2W0.25V0.07Ta) were least affected by irradiation, having DBTT shift of 29°C and 15°C respectively. The other steels developed shifts of 100°C to 300°C. They also showed that there is a direct proportionality between the DBTT and the irradiation-hardening (increase of the yield stress). This last point was already reported by Odette et al. [2.56].

The irradiation response of the F82H steel irradiated in the Japan Research Reactor-2 and in the Japan Material Test Reactor was analyzed by K. Shiba et al. [2.57]. The irradiation conditions were 0.1-0.5 dpa at irradiation temperatures between 335°C to 460°C. For such low doses and high irradiation temperature, no significant shifts of the DBTT were measured.

M. Rieth et al. [2.58] carried out a series of Charpy tests with small KLST V-notch specimens on different international low activation steels after neutron irradiations in the Petten High Flux Reactor (HFR). They obtained data from the steels: MANET-I, MANET-II, OPTIFER-IA, OPTIFER-II, F82H and ORNL3791. They focused their work on the low doses, namely between 0.2 and 2.4 dpa and for temperature ranging from 250°C to 450°C. The main goal was to compare these steel with one another and to assess the composition effect on the DBTT and embrittlement. Their evaluation clearly indicated that the reduced-activation steels are less prone to embrittlement.

The impact behavior of the F82H steel and another 9Cr-2W-0.2V-Ta steel was characterized after irradiation at 300°C at HFR Petten and three different doses (2.5, 5 and 10 dpa) with KLST specimens. The material as well as TIG welds and EB welds were investigated [2.59]. As the welds were not post-weld heat-treated, their results showed the effect of the pre-irradiation state, in particular the state of tempering, on the post-irradiation impact properties.

The last European reduced-activation steel produced within the fusion program, the Eurofer97, has also been characterized very recently with Charpy impact tests, before and after irradiation at the BR2 reactor in Mol at 300°C at 0.25, 1 and 2.25 dpa [2.60]. The Eurofer97 steel results were compared with the other internationally investigated reduced-activation steel. It was found that the Eurofer97 has the better response to irradiation, i.e., it yields the smallest temperature shift. The dose dependence of the DBTT shift at 300°C for all the advanced steel is shown in Figure 2. 1.

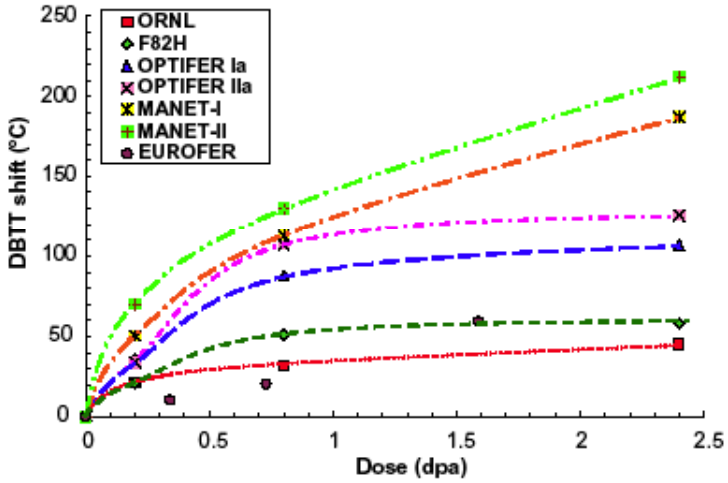

Figure 2. 6: Charpy DBTT shift for different 9.12%Cr steels irradiated at 300°C versus neutron dose [2.60].

Fracture toughness

Fracture tests steel including sub-sized disk-shape compact tension specimens (DCT) were performed on the HT-9 steel by T. Misawa et al. [2.42]. The pre-cracked DCT specimens were tested at room temperature and the crack extension was successfully detected by the electrical potential drop and acoustic emission and the elastic-plastic fracture toughness was determined. However, no fracture toughness tests were carried out over a range of temperature to fully characterize toughness in the transition.

R. E. Clausing et al. [2.61] studied the extend of chemical segregation of Ni, Cr, Si and P, using Auger spectroscopy, following irradiation at 410°C on the commercial HT-9 steel. They tested miniature notched-bar specimens below the DBTT. They suggested that the segregation of these elements is involved in reducing the fracture resistance of the PAG boundaries.

The mechanical properties of the HT-9 steels as a function of the heat-treatment were presented by R. Maiti et al. [2.62]. The lower shelf fracture properties were measured with pre-cracked Charpy V-notched specimens dynamically loaded. For each tempering, the lower shelf fracture toughness was shown to be quite insensitive to the austenitization temperature despite large changes in the prior austenite grain size and lath packet size.

A detailed review of fracture and impact properties on austenitic, bainitic and tempered martensitic steels was presented by G.E. Lucas and D. S. Gelles [2.63]. In particular two martensitic steels are compared, the HT-9 and a modified 9Cr-1Mo. It is outlined that the shift of the DBTT and the reduction of the upper shelf energy of the Charpy curve are alloy composition and irradiation condition dependent. Fracture toughness data, J_{Ic} and K_{Jd} (dynamic fracture toughness) were also reported. The fracture toughness data trends indicate an increase of the transition temperature and a decrease of the upper shelf toughness following irradiation. The Charpy and fracture toughness data were related in a more qualitative than quantitative way. The increase of the transition temperature and the decrease

of the upper shelf toughness and energy were shown to be correlated with the irradiation-induced increase of the yield stress and loss of tensile ductility.

An analysis of cleavage fracture in the HT-9 steel in the framework of a statistical model was presented by G.E. Lucas et al. [2.64]. The model takes into account a critical stress to propagate a carbide-size crack into the surrounding matrix. The critical stress was calculated based on a Griffith approach. Static fracture toughness data were obtained at two temperatures for several heat-treated conditions. A total of 25 heat-treatments (combination of austenitization and tempering treatment) of the HT-9 steel were investigated. These heat-treatments resulted in various prior austenite grain sizes, lath packet sizes, carbide distributions and densities. The predictions of model explained the observed trend of experimental data and it was concluded that cleavage is mediated by microcrack nucleation and propagation from the large boundary carbides.

Odette et al. [2.65] ran a series of finite element simulation of bend specimens to model a data set obtained on the 12 Cr martensitic steel HT-9. They combined the crack tip stress field calculations with a weakest link statistics model of cleavage fracture. The predictions of their model were consistent with the experimental data trends observed for this steel.

The effect of the loading mode at room temperature of the F82H steel was studied by Li et al. [2.66]. The critical J-integrals were measured for the fracture mode I and III, J_{Ic} and J_{IIIc} (see Chapter 5) and for a mixed-mode I/III. A modified compact tension specimen, with crack plane direction off the loading direction by a given angle, was used for the mixed mode characterization. This study was motivated by the fact that many observed real failures include shear components. Interestingly, it was demonstrated that the critical J for the mixed mode, J_{Mc}, is lower than for the other two modes in the ductile regime. The minimum value was obtained for an angle of about 45° between the load line and the normal to the crack plane.

Odette presented a micro-mechanical model for quasi-cleavage in tempered martensitic steel based upon a local approach, involving a critical stress σ^* encompassing a critical area A^* around the crack tip [2.23]. He emphasized that the DBTT is not a measure of toughness due to the influence of many extrinsic factors that may lead to differences in nominal values between 100°C and 300°C for the DBTT. The micro-mechanical model was applied to the HT-9 steel to model the toughness-temperature curve. The underlying mechanism is a stable-to-unstable transition of a process zone formed by the coalescence of many micro-cracks arrested in the tempered martensitic microstructure. The usefulness of the mechanistic approach to safely manage the operation condition of a structure was outlined.

Edsinger et al. [2.67] pursued the same approach as in [2.23]. They modeled the toughness-temperature curve by testing various pre-cracked bend specimens tested of the F82H steel in the transition region. The specimens were loaded statically and dynamically and contained either shallow crack (a/W=0.1) or deep crack (a/W=0.5). 2D finite elements simulations were used to determined the critical stress – critical area of the local criterion for cleavage. They again emphasized the fact that depending on the loading rate, the specimen size or the deepness of the crack, different transition temperatures are measured.

Odette and co-authors continued to work on further development of their model, to account for the influence of the specimen size and geometry on fracture. The main motivation was

naturally driven by the need to obtain reliable data on fracture from small specimens used in irradiation capsules. In 1998, they presented a paper on the assessment of fracture with small specimens where the combined mechanical tests, finite element simulations and confocal microscopy [2.68]. The confocal microscopy was used as a profilometry technique implemented in a technique of fracture reconstruction, ultimately used to follow the growth of the process zone with the crack tip opening displacement. More recently, Odette et al. [2.28] proposed to relate the critical stress σ* of their model to the microarrest toughness of the ferrite matrix.. The underlying idea was to consider that the particle nucleated microcracks arrest unless the local normal stress is higher than the critical stress σ*. Using the Griffith fracture criterion, the model relates the critical stress σ* to both the intrinsic arrest fracture toughness of the matrix and an effective brittle particle size.

Spätig et al. [2.69] reported new data obtained with sub-sized compact specimens of F82H steel. The results were compared with previously published bend bars specimens of the same steel and with compact tension specimens of the T91 steel. The three datasets were plotted together on an adjusted temperature following the indexation of the master curve approach (see next Section).

Within the international research program, several laboratories work on the different heats of F82H to measure fracture toughness [2.24, 2.70, 2.71]. A large variety of specimen sizes, geometries and testing conditions were used resulting in an apparent high scatter in the overall database. However, in 2004, the entire available fracture toughness database was assembled to characterize the fracture toughness-temperature transition by Odette et al. [2.72]. The database is shown in Figure 2. 7. Size effects, reflected in constraint loss and statistical effects associated to the crack front were taken into account. The analysis of the data was done in the philosophy of the ASTM E1921 standard analysis to index the toughness-temperature curve on an absolute temperature scale (see next section). It was concluded that the ASTM E1921 to determine the temperature index T_o could be used for the F82H.

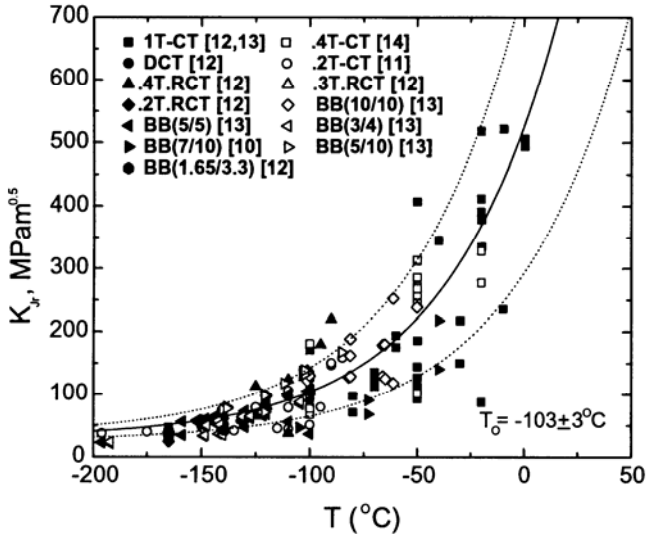

Figure 2. 7: *The F82H database after specimen size correction versus temperature, from [2.72].*

Finally, we mentioned that, as far as the Eurofer97 steel is concerned, the fracture toughness data in the open literature are still scarce. Some have already been published by Rensman et al. [2.73] as well as Lucon et al. [2.60] on both unirradiated and irradiated conditions. Nonetheless, within the European fusion material program, there is a growing fracture database on this steel both in the unirradiated and irradiated conditions. Several European research institutions are currently working on this project.

2. 6. Engineering approaches to assess irradiation embrittlement.

Since neutron irradiation leads to the degradation of the fracture toughness properties of structural components of a nuclear reactor, it is necessary to have reliable failure engineering codes to safely manage this embrittlement. The design of a component against fracture involves three critical variables that are related to each other, namely stress, crack (flaw size) and toughness. In the framework of linear elastic fracture mechanics, the stress intensity factor K scales with the stress and the square root of the crack size (see Chapter 5). Hence, for a crack of characteristic dimension a in a given geometry environment represented by a geometric factor Y under a remote stress σ can be simply expressed by an equation of the type:

Eq. 2. 1 $$K_{(I,II,III)} = Y\sigma\sqrt{\pi a}$$

Note that Y depends on the loading mode (I, II or III). Given for example the stress state acting in a structure and knowing the material's fracture toughness K_{IC}, it is straightforward to determine the critical (maximum) crack size beyond which the crack will propagate in an unstable manner. The approach for evaluating irradiation effects differ from one country to another but most of the European countries approaches are based upon the ASME (American Society of Mechanical Engineers) Boiler and Pressure Vessel Code [2.74]. Hereafter, we briefly describe the ASME approach and the Master Curve method, which appears as a good alternative to the ASME code.

ASME approach

The ASME Boiler and Pressure Vessel Code is based upon linear elastic fracture mechanics. It includes the use of two curves used to characterize toughness of a variety of reactor pressure vessel steels. The first one describes the lower envelope to an extensive dataset of static fracture initiation toughness K_{Ic}. The second one curve corresponds to the lower envelope of a data set containing static, K_{Ic}, dynamic, K_{Id}, and crack arrest, K_{Ia}, fracture toughness. Since the dynamic and crack arrest toughness is usually found lower than static initiation K_{Ic}, the second curve is the more conservative and is consequently called the reference curve K_{IR}. The shape of these curves is considered to be material independent and their respective equations are [2.75]:

Eq. 2. 2 $$K_{IC} = min\begin{cases} 36.5 + 3.084\,exp(\,0.036(\,T - RT_{NDT} + 56\,)) \\ 220 \end{cases}$$

and

Eq. 2. 3 $$K_{IR} = min\begin{cases} 29.5 + 1.344\,exp(\,0.026(\,T - RT_{NDT} + 89\,)) \\ 220 \end{cases}$$

where K_{IC} and K_{IR} are expressed in $MPa\sqrt{m}$ and T in °C.

These curves have been obtained with an "eye ball" lower bound envelope fitting to the data on unirradiated materials. It must be emphasized that the variability in material properties is taken into account by RT_{NDT}. RT_{NDT} is the reference nil-ductility temperature. Within this approach, it is assumed that the irradiation effects on fracture toughness result in an increase of RT_{NDT} while the temperature dependence of fracture toughness is not affected by irradiation. Thus, embrittlement is mainly quantified by a shift of RT_{NDT} towards higher temperatures.

The RT_{NDT} is determined using a combination of the impact Charpy properties and drop weight nil-ductility temperature NDT. The NDT is determined in accordance with the ASTM Method for Conducting Drop-Weight Test to Determine Nil-Ductility Transition Temperature of Ferritic Steels (E208). The RT_{NDT} is finally defined as the higher of the two following temperatures : i) the drop weight NDT and ii) 33°C below the temperature at which three Charpy specimen results are at least 68 J and the lateral expansion at least 0.9 mm.

In the Section XI of the ASME Boiler and Pressure Vessel Code [2.76] two operating mode conditions are distinguished, namely the „normal" and „faulted" ones; the latter being naturally more sever than the former. The K_{IC} curve is intended to determine the critical crack sizes corresponding to the faulted operation condition while the K_{IR} curve is to be used for the normal operation conditions. The critical crack size for the normal and faulted operations is referred to as a_c and a_i respectively. At the end of life of a given component, the crack size is called a_f. If the crack size a_f is such that one of the following conditions is fulfilled:

$$a_f >= 0.1\ a_c \qquad a_f > 0.5\ a_i$$

then the code requires that either the component be replaced or the flaw be repaired. The critical size is then readily obtained by inverting the previous Eq. 2. 1 provided that the appropriate fracture toughness K_{Ic} at the temperature of interest is known as well as the stress and geometry factors.

For irradiated specimens, the determination of NDT with the ASTM standard E 208 is not included in the surveillance programs. Therefore, the irradiation induced shift of the RT_{NDT} reference temperature is defined as the shift in the 41 J impact energy transition temperature T_{41J}. It is assumed that the true static fracture toughness shift and crack arrest shift ΔRT_{NDT} is equal to or less than ΔT_{41J}. However, a significant scatter between the shifts of the toughness–temperature curve and that of T_{41J} has been observed so that special caution has to be exerted. Also an additional margin in the determination of ΔRT_{NDT} can be considered. However, the margin is not directly prescribed in the ASME approach, nor in European approaches equivalent to ASME. Note finally that efforts have been made to determine the shift from the steel chemical composition and the neutron fluence Φ, using a relation of the type:

Eq. 2. 4 $$\Delta RT_{NDT} = F(\%P, \%Cu, \%Ni, \ldots \Phi)$$

MASTER CURVE approach

The recently proposed master-curve temperature-shift (MC-ΔT) method to evaluate fracture toughness of irradiated materials has been gaining acceptance throughout the world to replace the current indirect methods, in which the irradiation-induced shifts of the ductile to brittle transition temperature obtained with Charpy V-notched specimens serves as a measure of embrittlement. Conceptually, the MC-ΔT method is quite similar to the ASME one. It is based on the experimental observation of a universal shape of the mean fracture toughness-temperature curve K(T) for a large body of data on low alloy reactor pressure vessel steels [2.77]. Further, it has also been observed that the shape of the K(T) to be relatively insensitive to irradiation damage effects. The recommended equation of the curve is given by:

Eq. 2. 5
$$K_{J\ median} = 30 + 70 \cdot \exp(\ 0.019\ (T - T_o))$$

The previous equation indicates that the K(T) curve is indexed on a absolute temperature scale by a reference temperature (T_o), at a reference toughness of 100 MPa $m^{1/2}$. The MC approach actually provides an alternative transition temperature index parameter RT_o to that of RT_{NDT}. RT_o is based on a simple addition of 19.4°C to the T_o value. According to the ASTM standard E1921, T_o can be measured with a data set consisting of at least six valid replicate test results determined at one test temperature (for a single temperature T_o determination) Alternatively, T_o can be obtained with at least six valid data distributed over the temperature range $T_o \pm 50$°C. This major benefit of the approach is that RT_o after irradiation can be measured directly on irradiated specimens; it is not obtained from the addition of a temperature shift measured from Charpy specimen results to T_o of the unirradiated material.

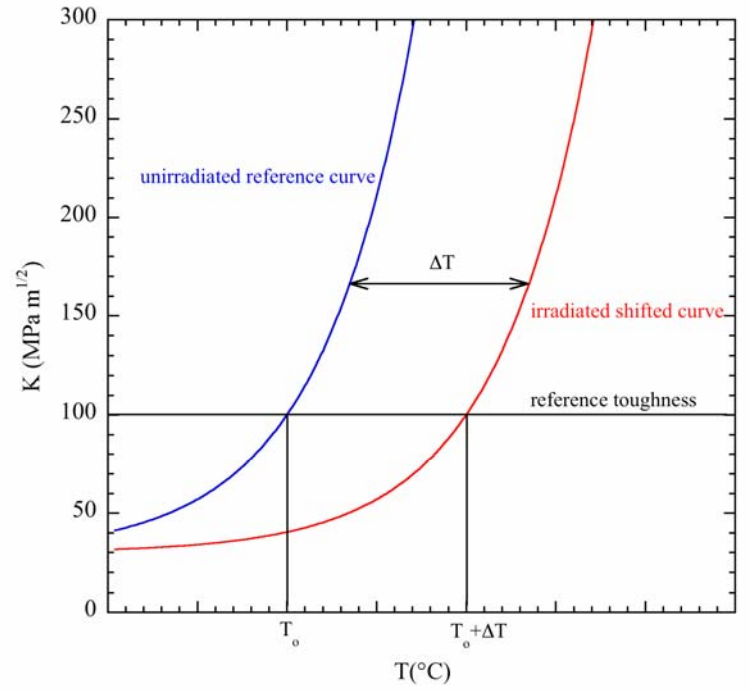

Figure 2. 8: *Schematic illustration indexation of the master on an absolute* T axis.

Furthermore, additional ΔT shifts arising from loading rate and from safety margin consideration for example can be incorporated in the master curve approach. The approach to index the K(T) on an absolute temperature is illustrated in Figure 2. 8.

It is worth to emphasize that the master curve approach has been developed for assessing the embrittlement of reactor pressure vessel steels. While it is quite natural to try to extend the application of such a method to the tempered martensitic steels foreseen for future fusion reactor applications, there are a number of issues that needs to be addressed in details. These include in particular:

- Does the uniqueness of shape of the master curve for a large class of tempered martensitic steels exist?
- What are the effects, if any, of tempering, chemical composition, carbide and other brittle particle distributions on the shape of the K(T) curve?
- What is the effect of irradiation on the K(T) curve shape for the large expected ΔT shifts (several hundreds of degrees) in a real fusion reactor environment?
- How to incorporate properly the realistic crack configurations of the thin-wall structure of the first wall and other shallow crack in the blanket within the framework of the master curve?

Resolving these issues on a sound physical basis constitutes a real scientific challenge. Answering all the issues mentioned above is a real long-term effort that necessitates multi-scale modeling.

2. 7. Objectives of the thesis.

As it has been shown in the foregoing section, a significant amount of studies to assess the mechanical properties of the tempered martensitic steels as well as the effects of irradiation on these properties have been performed for the last two decades. As far as the fracture properties are concerned, they were initially investigated by Charpy impact tests from which the ductile to brittle transition temperature (DBTT) is measured. The effects of neutron irradiations, including irradiation temperature, neutron flux rate, neutron spectrum and fluence, have been mainly quantified by measuring the shift of the DBTT. Fracture toughness measurements have also been performed but to a lesser extend than the impact tests. Systematic studies of fracture toughness on tempered martensitic steels for fusion applications have now become part of the international fusion material development programs only recently.

We have pointed out that the largest fracture toughness database of a tempered martensitic steel has been obtained for the Japanese F82H steel. In the literature survey, we showed that it has been proposed to use the ASTM1921 master curve approach to analyze the fracture toughness data in the transition region. It was found that for the F82H steel the master curve approach describes the data trend satisfactorily. However, it must be emphasized and recognized that most of the studies involving the master-curve approach have been carried out on reactor pressure vessel steels. While attempting to use a master-curve type of approach for the tempered martensitic steels is quite natural, there are a number of issues that need to be assessed. In particular, the shape of the fracture toughness–temperature curve in the transition region must first be shown to have an almost constant shape for all the tempered martensitic steels. Second, to make use of the master curve approach, the effects of irradiation must affect only little the shape of the curve despite the large temperature shifts, due to the very large neutron doses, expected in fusion reactor structural materials.

In this study, we propose to investigate in details the constitutive behavior and fracture properties of the European reference tempered martensitic steel Eurofer97. We will focus our attention in the lower transition region.

The constitutive behavior has been determined with tensile tests carried out at nominal imposed strain rate over a range of temperatures. The strain-hardening calculated from the true stress–true strain relationships has been rationalized within the framework of a phenomenological model of dislocation mechanics. Transmission electron microscopy observations were also be performed on the undeformed an deformed microstructure.

The fracture toughness will be measured with sub-sized pre-cracked compact tension specimens (0.2T C(T) and 0.4T C(T)) in the lower transition to minimize the constraint loss. Owing to the inherent large scatter of fracture toughness data in the transition region, a rather large testing matrix has been foreseen in order to have enough statistics at different temperatures to assess with confidence the shape of the toughness–temperature curve. Having two different sizes of specimen, the size effect will also be investigated. Finite element simulations of the compact tension specimens will be run to analyze the stress-strain fields at the crack tip in order to search for a local criterion for quasi-cleavage based upon a critical stress state.

Therefore, the ultimate goal is to fully characterize the constitutive and fracture properties in the lower transition of the Eurofer97 steel in the perspective of using a well-established reference toughness–temperature curve in the context of the master-curve methodology. Finally, in order to understand the underlying micro-mechanisms of fracture on a sound basis the brittle regime was modeled using a local approach to quasi-cleavage, which was implemented in a finite element code.

References

[2.1] S.Mori, "Prospects and strategy for the development of fusion reactors", *J. Nucl. Mater.*191-194 (1992) pp. 3-6.

[2.2] J.Raeder, *Europhys. News* 29 (1998) pp. 235.

[2.3] M.Victoria, N.Baluc, P.Spätig, "Structural materials for fusion reactors", *Nucl. Fusion*, 41 Nr. 8 (2001) pp. 1047-1053.

[2.4] K.Ehrlich, "The development of structural materials for fusion reactors", *Phil. Trans*. R. Soc. Lond. A 357 (1999) pp. 595-623.

[2.5] G.R.Hopkins, R.J.Price, "Fusion reactor design with ceramics", *Nucl.Engng Design Fusion* 2 (1985) pp. 111-143.

[2.6] G.J.Butterworth, "Low activation structural materials for fusion", *Fusion Engng Design* 11 (1989) p.231.

[2.7] R.L.Klueh, "Reduced activation bainitic and martensitic steels for nuclear fusion applications", *Current Opinion in Solid State and Mat. Sci*. 8 (2004) pp. 239-250.

[2.8] N.Baluc, R.Schäublin, P.Spätig, M.Victoria, "On the Potentiality of Using Ferritic/Martensitic Steels as Structural Materials for Fusion Reactors", *Nuclear Fusion 44* (2004) pp. 56-61.

[2.9] Proceedings of the Conference on Super Clean Steels, The Institute of Metals (GB), London, March (1995).

[2.10] D.S.Gelles, "Development of martensitic steels for high neutron damage applications", *J. Nucl. Mater*.239 (1996) p.99.

[2.11] C.Cawthorne, E.J.Fulton, *Nature* 216 (1967) p.515.

[2.12] D.L.Smith, R.F.Mattas, M.C.Billone, in: *Materials Science and Technology* Vol 10B, 1994, p.263, Eds. R.W.Cahn, P.Haasen, E.J.Kramer.

[2.13] D.S.Gelles, in: *Reduced Activation Materials for Fusion Reactors*, Eds. R. L. Klueh, D.S.Gelles, M.Okada and N.H.Packan (ASTM, Philadelphia, PA) p. 140.

[2.14] K.Ehrlich, *Phil. Trans*. R. Soc. Lond. A 357 (1999) p.595.

[2.15] C.Ponti, *Fusion Technology* 13 (1988) p.157.

[2.16] A.Hishinuma, in: Proceedings of the IEA Working Group Meeting on Ferritic/Martensitic Steels, (1995*) ORNL/M-4230.*

[2.17] K.Ehrlich, S.Kelzenberg, H.D.Röhrig, L.Schäfer, M.Schirra, "The development of ferritic-martensitic steels with reduced long-term activation", *J. Nucl. Mater*.212-215 (1994) pp. 678-683.

[2.18] L.Schäferm, M.Schirra, K.Ehrlich, "Mechanical properties of low activating martensitic 8–10% CrWVTa steels of type OPTIFER"**,** *J. Nucl. Mater*.233-237 Part 1 (1996) pp. 264-269.

[2.19] M.Victoria, D.Gavillet, P.Spätig, F.Rezai-Aria, S.Rossmann, "Microstructure and mechanical properties of newly developed low activation martensitic steels", *J. Nucl Mater.* 233-237 Part 1 (1996) pp. 326-330.

[2.20] N.Baluc, R.Schäublin, C.Bailat, F.Paschoud, M.Victoria, "The mechanical properties and microstructure of the OPTIMAX series of low activation ferritic–martensitic steels", *J. Nucl. Mater.* 283-287 Part 1 (2000) pp. 731-735.

[2.21] N.Baluc, R.Schäublin, P.Spätig, M.Victoria, *Nucl.Fusion* **44** 2004 p.56

[2.22] R.L.Klueh, D.S.Gelles, T.A.Lechtenberg, "Development of ferritic steels for reduced activation: The US program", *J. Nucl. Mater*. 141-143 (1986) pp. 1081-1087.

[2.23] G.R.Odette, "On the ductile to brittle transition in martensitic stainless steels – Mechanisms models and structural applications", J. Nucl. Mater. 212-215 (1994) p.45.

[2.24] J.Rensman, J.van Hoepen, J.B.M.Bakker, R.den Boef, F.P.van den Broek, E.D.L. van Essen, "Tensile properties and transition behaviour of RAFM steel plate and welds irradiated up to 10 dpa at 300 °C", *J. Nucl. Mater*. 307-311 (2002) p.245.

[2.25] A.Möslang, K.Ehrlich, T.E.Shannon, M.J.Rennich, R.A.Jameson, T.Kondo, H. Katsuta, H.Maekawa, M.Martone, V.Teplyakov, *Nucl. Fusion* Vol. 40 No. 3Y (2000) p.619.

[2.26] G.E.Dieter. In: *Mechanical Metallurgy*, SI Metric Edition, McGraw-Hill Book Company, London (1988) p. 475.

[2.27] R.L.Klueh, J.M.Vitek, "Tensile properties of 9Cr-1MoVNb and 12Cr-1MoVW steels irradiated to 23 dpa at 390 to 550 ° C", *J. Nucl. Mater*. 182 (1991) pp. 230-239.

[2.28] G.R.Odette, T.Yamamoto, H.J.Rathbun, M.Y.he, M.L.Hribernik, J. W. Rensman, "Cleavage fracture and irradiation embrittlement of fusion reactor alloys: mechanisms, multiscale models, toughness measurements and implications to structural integrity assessment", *J. Nucl. Mater*. 323 (2003) pp. 313-240.

[2.29] C.R.Barret, W.D.Nix, A.S.Tetelman: "The principle of Engineering Materials" published by Prentice-Hall, Inc. (1973)

[2.30] P.Gumbsch, "Brittle fracture and the brittle-to-ductile transition of tungsten", *J. Nucl. Mater*. 323 (2003) pp. 304-312.

[2.31] R.L.Klueh, D.R.Harris, "High chromium ferritic and martensitic steels for nuclear applications"; West Conshohocken, PA: ASTM 2002.

[2.32] D.S.Gelles, "Microstructural development in reduced activation ferritic alloys irradiated to 200 dpa at 420°C", *J. Nucl. Mater*. 212-215 (1994), pp. 714-719.

[2.33] E.A.Little, L.P.Stoter in: Effects of irradiation on materials: *11th conferences ASTM STP 782*. Eds. H. R. Bragger, J. S. Perrin, (1982) pp. 207-233.

[2.34] J.D.Hunn, M.B.Lewis, E.H.Lee, "Hydrogen retention in iron irradiated steels", in: *Second international topical meeting on nuclear applications of accelerator technology.* La Grange Park, IL; American Nuclear Society, (1998) pp. 375-381.

[2.35] P.Marmy, B.M.Oliver, "High strain fatigue properties of F82H ferritic-martensitic steels under proton irradiation", J. Nucl. Mater. 318 (2003) pp. 132-142.

[2.36] P.J.Maziasz, R.L.Klueh, J.M.Vitek, "Helium effects on void formation in 9Cr-1MoVNb and 12Cr-1MoVW irradiated steels in HFIR", J. Nucl. Mater. 141-143 (1986) pp. 929-937.

[2.37] X.Jia, Y.Dai, "Small punch tests on martensitic/ferritic steels F82H, T91 and Optimax-A irradiated in SINQ Target-3", *J. Nucl. Mater.* 323 (2003) pp. 360-367.

[2.38] R.L.Klueh, J.M.Vitek, "Fluence and helium effects on the tensile properties of ferritic steels at low temperatures.", *J. Nucl. Mater*.161 (1989) pp. 13-23.

[2.39] R.L.Klueh, J.M.Vitek, "Tensile properties of 9Cr-1MoVNb and 12Cr-1MoVW steels irradiated to 23 dap at 390°c to 550°C", *J. Nucl. Mater*. 182 (1991) pp. 230-239.

[2.40] K.K.Bae, K.Ehrlich, A.Möslang, "Tensile behavior and microstructure of the helium and hydrogen implanted 12% Cr-steel MANET", *J. Nucl. Mater*. 191-194 (1992) pp. 905-909.

[2.41] S.Jitsukawa et al. “Development of an extensive database of mechanical and physical properties for reduced-activation martensitic steel F82H”, *J. Nucl. Mater.*, 307-311 (2002) pp. 179-186.

[2.42] T.Misawa, H.Sugawara, R.Miura, Y.Hamaguchi, “Small specimens fracture toughness tests of HT-9 steel irradiated with protons”, *J. Nucl. Mater*. 133-134 (1985) pp. 313-315.

[2.43] H.Yoshida, K.Miyata, Y.Hayashi, M.Narui, H.Kayano, “Instrumented Charpy impact tests of austenitic and ferritic steels”, *J. Nucl. Mater*. 133-134 (1985) pp. 317-320.

[2.44] H.Kayano, M.Narui, S.Ohta, S.Norozumi,“Irradiation embrittlement of neutron-irradiated ferritic steel”, *J. Nucl. Mater*. 133-134 (1985) p. 649-653.

[2.45] Y.Hosoi, N.Wade, T.Urita, M.Tanino, K.Komatsu, “Changes in microstructure and toughness of ferritic-martensitic stainless steels during long-term aging”, *J. Nucl. Mater*.133-134 (1984) pp. 337-342.

[2.46] T.Lechtenberg, “Irradiation effects in ferritic steels”, *J. Nucl. Mater*.133-134 (1984) pp. 149-155.

[2.47] K.J.Harrelson, S.H.Rou, R.C.Wilcox, “Impurity element effects on the toughness of 9Cr-1Mo steel”, *J. Nucl. Mater*. 141-143 (1986) pp. 508-512.

[2.48] J.M.Vitek, W.R.Corwin, R.L.Klueh, J.R.Hawthorne, “On the saturation of the DBTT shift of irradiated 12Cr-1MoVW with increasing fluence”, *J. Nucl. Mater.* 141-413 (1986) pp. 948-953.

[2.49] R.L.Klueh, P.J.Maziasz, “Reduced-activation ferritic steels: A comparison with Cr-Mo steels*”, J. Nucl. Mater.*155-157 (1988) pp. 602-607.

[2.50] B.S.Louden, A.S.Kumar, F.A.Garner, M.L.Hamilton, W.L.Hu. “The influence of specimen size on Charpy impact testing of unirradiated HT-9”, *J. Nucl. Mater*. 155-157 (1988) pp. 662-667.

[2.51] H.Kayano, A.Kimuram M.Narui, Y.Sasaki, Y.Suzuki, S.Ohta, “Irradiation embrittlement of neutron-irradiated low activation ferritic steels”**,** *J. Nucl. Mater.* 155-157 Part 2 (1988) pp. 978-981.

[2.52] R.L.Klueh, D.J.Alexander, “Impact behavior of 9Cr-1MoVNb and 12Cr-1MoVW steels irradiated in HFIR”, *J. Nucl. Mater*. 179-181 (1991) pp.773-776

[2.53] R.L.Klueh, K.Ehrlich, F.Abe, “Ferritic/martensitic steels: promises and problems”, *J. Nucl. Mater*. 191-194 (1992) pp. 116-124.

[2.54] H.Kurishita, H.Kayano, M.Narui, M.Yamazaki, Y.Kano, I.Shibahara, “Effects of V-notvh dimensions on Charpy impact test results for differently sized miniature specimens of ferritic steel”, *Mater. Trans, JIM*, Vol. 34 No. 11 (1993) pp.1042-1052.

[2.55] R.L.Klueh, D.J.Alexander, “Impact toughness of irradiated reduced-activation ferritic steels”, *J. Nucl. Mater.* 212-215 (1994) pp.736-740.

[2.56] G.R.Odette, P.M.Lombrozo, R.A.Wullaert, *Proceedings 12th Int. Symp. on effects of radiation on materials, ASTM-STP 870*, Eds. F. A. Garner, J. S. Perrin (American Society for Testing and Materials, Philadelphia, 1985) p. 840.

[2.57] K.Shiba, M.Suzuki, A.Hishinuma, “Irradiation response on mechanical properties of neutron irradiated F82H”, *J. Nucl. Mater*. 233-237 (1996) pp. 309-312.

[2.58] M.Rieth, B.Dafferner, H.D.Röhrig. “Embrittlement behavior of different international low activation alloys after neutron irradiation”, *J. Nucl. Mater*. 258-263 (1998) pp.1147-1152.

[2.59] J.Rensman, J. van Hoepen, J.B.M.Bakker, R. den Boef, F.P. van den Broek, E.D.L. van Essen, "Tensile properties and transition behaviour of RAFM steel plate and welds irradiated up to 10 dpa at 300°C", *J. Nucl. Mater*. 307-311 (2002) pp. 245-249.

[2.60] E.Lucon, R.Chaouadi, M.Decréton, "Mechanical properties of the European reference RAFM steel (EUROFER97) before and after irradiation at 300°C", *J. Nucl. Mater*.329-33 (2004) pp. 1078-1082.

[2.61] R.E.Clausing, L.Heatherly, R.G.Faulkner, A.F.Rowcliffe, K.Farrell, "Radiation-induced segregation in HT-9 martensitic steel", *J. Nucl. Mat*. 141-143 (1986) pp. 978-981.

[2.62] R.Maiti, G.E.Lucas, G.R.Odette, J.W.Sheckherd, "Mechanical properties of HT-9 as a function of heat-treatment", *J. Nucl. Mater*.141-143 (1986) pp. 527-531.

[2.63] G.E.Lucas and D.S.Gelles, "The influence of irradiation on fracture and impact properties of fusion reactor materials", *J.Nucl.Mater*, 155-157 (1988) pp. 164-177.

[2.64] G.E.Lucas, H.Yih, G.R.Odette, "Analysis of cleavage fracture behavior in HT-9 with a statistical model", *J. Nucl. Mater*. 155-157 (1988) pp. 673-678.

[2.65] G.R.Odette, B.L.Chao, G.E.Lucas, "On the geometry effects on the brittle fracture of ferritic and tempered martensitic steels", *J. Nucl. Mater*. 191-194 (1992) pp.827-830.

[2.66] H.Li, R.H.Jones, J. P.Hirth, D.S.Gelles, "Effect of loading mode on the fracture toughness of a reduced-activation ferritic/martensitic stainless steel", *J. Nucl. Mater*. 212-215 (1994) pp. 741-745.

[2.67] K.Edsinger, G.R.Odette, G.E.Lucas, J.W.Sheckherd, "The effect of size, crack depth and strain rate on fracture toughness-temperature curves of a low activation martensitic stainless steel", *J. Nucl. Mater*. 233-237 (1996) pp. 342-346.

[2.68] G.R.Odette, K.Edsinger, G.E.Lucas, E.Donahue, in *"Small Specimen Test Techniques", ASTM-STP 1329*, Vol 3. American Society for Testing and Materials, 1998, pp.298.

[2.69] P.Spätig, E.Donahue, G.R.Odette, G.E.Lucas, M.Victoria, "Transition regime fracture toughness-temperature properties of two advanced ferritic-martensitic steels", in *Mat. Res. Soc. Symp*. Proc.Vol. 653, Multiscale modeling of Materials (2001) Materials Research Society, Eds. L.P.Kubin, R.L.Selinger, J. L.Bassani, K.Cho. pp. Z7.8.1-Z7.8.6.

[2.70] M.Sokolov, R.Klueh, G.R.Odette, K.Shiba, H.Tanaigawa, in *Effects of Irradiation on Materials 21st International Symposium, ASTM-STP 1447*, American, Society for testing and Materials.

[2.71] K.Wallin, A.Laukkanen, S.Tähtinen, "Examination on fracture resistance of F82H steel and performance of small specimens in transition and ductile regimes", in *Small Specimen test Techniques: 4th volume, ASTM-STP 1418*, Eds. M.Sokolov, J.D.Landes, G.E.Lucas, American Society for Testing and Materials, West Conshohocken, PA, 2002. p. 33.

[2.72] G.R.Odette, T.Yamamoto, H.Kishimoto, M.Sokolov, P.Spätig, W.J.Yang, J.W. Rensman and G.E.Lucas, "A master curve analysis of F82H using statistical and constraint loss size adjustments of small specimen data", *J. Nucl. Mater*. 329-333 (2004) pp. 1243-1247.

[2.73] J. Rensman, H. E. Hofmans, E. W. Schuring, J. van Hoepen, J. B. M. Bakker, R. den Boef, F. P. van den Broek, E. D. L. van Essen, "Characteristics of

unirradiated and 60°C, 2.7 dpa irradiated Eurofer97", *J. Nucl. Mater*. 307-311 (2002) pp. 250-255.

[2.74] Section III, Nuclear Power Plant Component, Division I, ASME Boiler and Pressure Vessel Code, American Society of Mechanical Engineers, New York, (1986).

[2.75] Design and Construction Rules for Mechanical Components of PWR Nuclear Islands, RCC-M Code (1988).

[2.76] Section XI, "Rules for In-service Inspection of Nuclear Power Plant Components", ASME Boiler and Pressure Vessel Code, American Society of Mechanical Engineers, New York, (1986).

[2.77] K.Wallin, "Irradiation damage effects on the fracture toughness transition curve shape for reactor pressure vessel steels", *Int. J. Pres. Ves. & Piping 55* (1993) pp.61-79.

Chapter 3

Materials and microstructures.

3. 1. Introduction.

As discussed in Chapter 1 and Chapter 2, this work is mainly focused on the fracture properties and tensile properties of the Eurofer97 steel in the ductile-to-brittle transition region. Evidently, a detailed study of the mechanical properties cannot be isolated from a in-depth analysis of the main microstructural features of the material. Indeed, one of the big challenges of material science today consists in understanding the relationship between the microstructural features of a given material and its mechanical properties. In the present work, we are interested in the specific case of the tempered martensitic steels, and the microstructural factors mediating the observed fracture toughness. Hence, this chapter is devoted to the study of such features using standard techniques as optical microscopy, transmission electron microscopy (TEM), scanning electron microscopy (SEM) and energy dispersive X-rays analysis (EDX).

We also present results obtained from a fully ferritic Fe-9%Cr model alloy, which has been produced in the framework of an extensive research program related to the development of physically based constitutive equations for these types of materials.

The chapter is organized as follows. Section 2 is devoted to a description of the experimental methods used for the microstructural characterization of the alloys under study. In Section 3, the general features of the as-quenched lath-martensitic microstructures are described. Special attention is also paid to the discussion of the evolution of the as-quenched structure during subsequent tempering of these types of steels. The main microstructural units existing in the typical tempered-lath martensite microstructure is presented in details.

In the fourth section, we discuss the main experimental results obtained for the microstructure of the Eurofer97 steel. Finally, the microstructure of the Fe-9%Cr model alloy is discussed in the fifth section. The thermal treatment developed to obtain a fully ferritic microstructure is described. The problems related to the generation of a high purity Fe-Cr alloy are discussed.

3. 2. Experimental techniques

3. 2. 1. Optical microscopy

3. 2. 1. 1. Basics

Optical microscopy has been used to determine the following microstructural features:

a) % of delta ferrite if any,
b) inclusions content,
c) prior austenitic grain size.

One of the most important features of the martensitic steels is the prior austenitic grain size (PAGS). The chemical/electrochemical attack used to reveal the prior austenitic grains also attacks the boundaries inside the grains. As a result, depending on the material, the determination of the prior austenite grain boundaries can be a difficult task. Thus, the selection of an appropriate method that clearly reveals the PAG boundaries is a fundamental step in the determination of the pre-austenitic grain size.
The PAG size of Eurofer97 steel in the "as-received" condition was measured following the requirements of ASTM E112-96 by the linear intercept method, which is briefly described hereafter (detailed description of the method is outside the scope of this work and can be consulted elsewhere). References [3.1] to [3.3] describe the basic procedure and illustrate its implementation in detail. The linear intercept method consists in superposing a test line of total length L on the micrograph. The test line can adopt different shapes, like concentric circles, square grids, etc.
From the superposition of the test line on the micrograph, several basic measurements (common in quantitative stereology) are calculated. A detailed discussion about quantitative stereology can be found in [3.4].
Two quantities that can be calculated from the superposition of the test lines on the micrographs are the number of grains intercepted by the test line per unit of length, N_L; or the number of intersections between the test line and the grain boundaries per unit of length, P_L, is calculated. For single phase materials P_L and N_L have the same value.
The mean linear intercept length ℓ is calculated in each field from N_L as $\ell = 1/N_L$. The value of G, the ASTM grain size number, is calculated via $\bar{\ell}$, the mean value of ℓ obtained after n independent measurements, by using the equation [3.1]:

Eq. 3. 1 $$G = -6{,}643856 \cdot \log(\bar{\ell}) - 3{,}288$$

where $\bar{\ell}$ is in mm.
A second method, described in ASTM E112-96 to calculate G, is the planimetric (Jeffries) method. In this case, the number of grains inside a known area, N_A has to be determined. This value allows us to calculate the mean grain cross sectional area $\bar{A} = 1/N_A$. Then G can be calculated through the following equation:

Eq. 3. 2 $$G = 3{,}321928 \cdot \log(N_A) - 2{,}954$$

Eq. 3. 1 (linear intercept method) and Eq. 3. 2 (planimetric method) should yield approximately the same value of G.

It is very important to keep in mind that the ASTM grain size number (G) is not a real measure of the 3D grain structure but a characterization of the two dimensional grain structure revealed by planar section through the 3D grain structure. This fact can be illustrated by considering a certain microstructure where the G value has been determined by means of the linear intercept method. The mean grain cross-sectional area $\bar{A}$ can be calculated from Eq. 3. 2.
Finally, a grain "diameter" is estimated as $\bar{d} = \sqrt{\bar{A}}$. Clearly, $\bar{d}$ has no physical significance and of course should not be interpreted as the real volumetric mean diameter of the grains. However, by assuming that the grains have certain determined shape, it's possible to estimate the mean volumetric grain diameter $\bar{D}$ from the measures obtained in the planar section, like $\bar{\ell}$ [3.2]. For instance, by considering that the material microstructure is composed of spheres of uniform size, it is possible to shown that $\bar{D} = 1{,}5\,\bar{\ell}$. It is also interesting to consider a model that involves a space-filling unity. For instance, in the α-tetrakaidecahedron model $\bar{D} = p\,\bar{\ell}$ where $p \approx 1.7$ (see Ref. [3.2] for details). It is also worth mentioning that several three-dimensional parameters developed in the past are statistically exact and are not based on assumptions about grain shape and size. These parameters can be derived from the basic stereological quantities like N_L and P_L [3.4].

3. 2. 1. 2. Experimental procedure.

The samples were initially compression-mounted in epoxy. The grinding process was performed using 320, 500, 1000 and 2400-grit water-cooled silicon carbide papers. Wheel speeds of approximately 300 RPM were used during the process. The polishing process was carried out by using diamond spray of 9, 6 and 3μm on low-nap cloths. Wheel speeds of approximately 200 RPM were used in the polishing process. Finally, the surfaces were polished by using acid alumina-suspension (pH ≈ 4). This suspension is very well suited for final polishing of stainless steels. In this case, napless clothes were used.
The samples were electrochemically etched in an oxalic acid solution in water (10 g oxalic acid in 100 ml of distilled H_2O), at 6 V during 45 to 50 s. The process was carried out at room temperature. This process allows revealing the prior austenitic grain boundaries in the martensitic microstructure.
The prior austenitic grain size was characterized following the ASTM E112-96 standard. Other important magnitudes were also estimated like the area of prior austenitic grain boundaries per unit of volume. An average grain diameter was calculated from this value.

3. 2. 2. Transmission electron microscopy.

TEM specimens were prepared by electro-polishing (Tenupol 5) by using a solution of perchloric acid in ethanol (86% ethanol +14% perchloric acid (in volume)) at 0°C and 20V. Specimens of 1 mm diameter were extracted from thin sheets (thickness ≈ 300 μm) by spark-machining. The specimens were mounted in austenitic stainless steel discs in order to generate the standard 3 mm specimen. This procedure minimizes the problems related to the interaction of the electron beam with ferromagnetic materials.
Second phase particles have been analyzed by using extraction techniques. A very thin layer of carbon was deposited over a previously electropolished surface of a Eurofer97 sample. The carbon layer is extracted by electro-polishing and afterward is mounted on 3 mm copper grids for analysis.
The microscope used was a 200kV JEOL equipped with X-ray energy dispersive spectrometer (EDS).

3. 3. Characterization of the lath martensitic microstructure in steels.

3. 3. 1. Introduction.

Lath martensitic microstructure in steels in the as-quenched condition has been extensively studied in the past [3.10], [3.13]. Lath martensite is the typical microstructure obtained in Fe-C alloys containing less than about 0.6 wt.% C after quenching from the austenitic region. This type of microstructure is also obtained in the case of low-alloy steels, Fe-Ni alloys with less than about 28%wt.% Ni, and even pure Fe provided that the cooling rate is high enough.
In this section, the discussion is focused on the as-quenched lath martensite microstructures in Fe-Cr-C alloys containing between 7-12wt% Cr and 0.1wt%C. The effect of the tempering on the martensitic microstructure will be also discussed.
A martensitic microstructure is obtained after fully austenitization and subsequent quenching down to room temperature. In the case of the Fe-Cr-C alloys, slow cooling rates produce a fully martensitic microstructure. Indeed, a martensite is obtained after air-cooling even in the case of thick sections. This is a consequence of the large content of alloying elements in these steels, which results in an extremely high hardenability.
Lath martensite in steels is a complicated microstructure with a high density of internal boundaries. Figure 3. 1 and Figure 3. 2 show the typical aspect of lath martensite in the optical microscope. Figure 3. 4 presents a TEM image of a typical tempered lath martensite in a Fe-9Cr-0.1C alloy, where the original lath morphology can still be identified.

3. 3. 2. As-quenched lath martensite.

Several studies have been published on the crystallography of the as-quenched lath martensite. Sandvik [3.13] has performed a detailed TEM study of this type of microstructures in the case of Fe-0.2%C and Fe-0.4%Cr alloys. He has experimentally determined the existence of an austenitic-martensitic orientation relationship:

$$(111)_F \,//\, (011)_B$$

$$[\bar{1}01]_F \quad 3.1° \; from \; [\bar{1}\,\bar{1}\,1]_B$$

This orientation relationship is between the Kurdjumov–Sachs orientation relationship ($\{111\}_F \,//\, \{011\}_B$; $<101>_F \,//\, <111>_B$) and the Nishiyama-Wassermann orientation relationship ($\{111\}_F \,//\, \{011\}_B$; $<101>_F$ about $5.3°$ from $<111>_B$ towards the $<111>_B$) (see. Ref. [3.22] for further details).
The lath martensite habit plane has been determined to be close to $(575)_F$ for the particular variant of the orientation relationship presented here [3.13]. Kelly has confirmed this observation using Kikuchi line pattern analysis [3.14]. Sanvik has also studied the crystallography of lath martensite in Fe-20wt% Ni-5wt%Mn alloys. No difference has been found, supporting the conclusion that all the ferrous lath martensites seem to share common crystallographic features.
The smaller microstructural unit in the case of these microstructures is the “lath” (lath shape morphology, one geometrical dimension much larger than the other two). Laths have a typical thickness of about 200 nm. The long direction of these laths is coincident with $\langle 110 \rangle_F$ directions of the parent lattice. Assuming the orientation relationship given

previously, in terms of the martensitic lattice, this is within a few degrees from the $\langle 111 \rangle_B$ directions. Therefore the long direction of the laths is usually considered as parallel to the

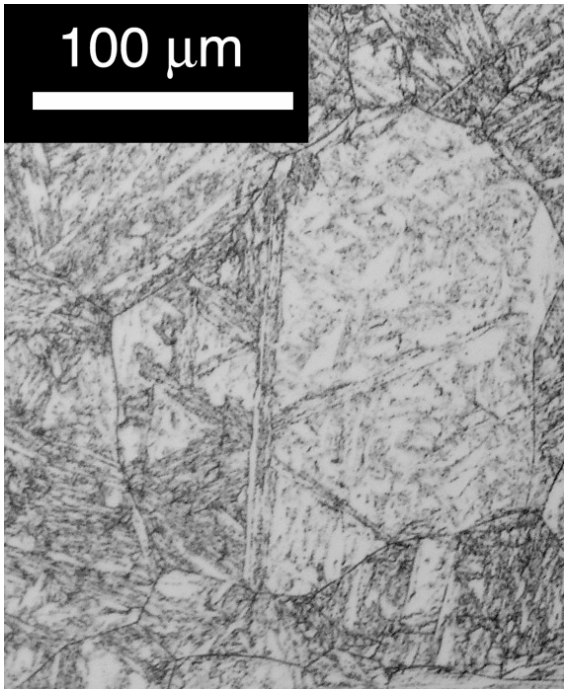

Figure 3. 1: *Typical aspect of the lath martensite microstructure as observed by optical microscopy. Fe-12wt%Cr-0.1wt%C after 230'@980°C, AC + 80'@580°C (electrochemical attack using oxalic acid solution10g/100ml H2O @10V)*

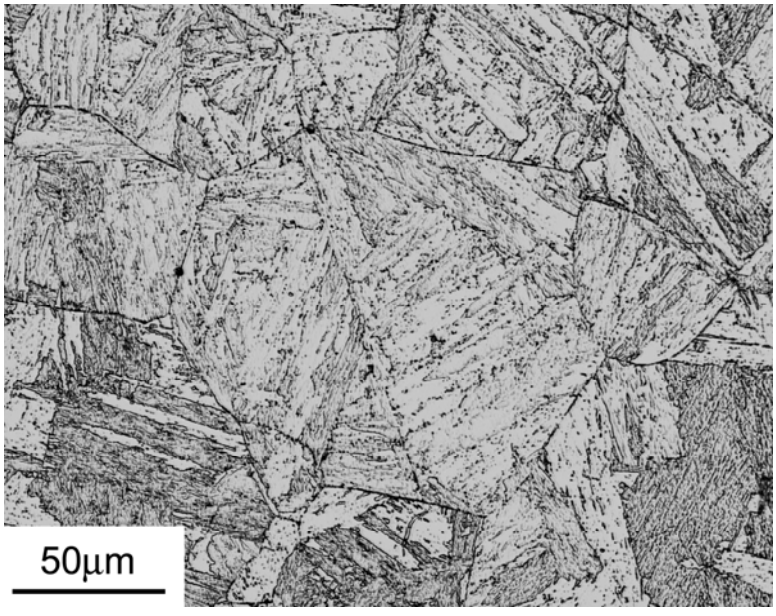

Figure 3. 2: *Prior austenitic grain subdivided into packets. Packets boundaries are clearly visible in the picture. Several parallel blocks can be identified into the packets. Fe-12wt%Cr-0.1wt%C after 230'@980°C, AC + 80'@580°C (electrochemical attack using oxalic acid solution10g/100ml H2O @10V).*

$<111>_B$ ([3.10]). The martensite laths arrange themselves in "bundles" of nearly parallel laths. This is perhaps the first feature being identified in TEM studies of lath martensite. Morito et al. [3.9] named these bundles of parallel laths as *blocks* of laths. In one block, all laths have close-packet planes parallel to each other suggesting a common habit plane, i.e. $(111)_F // (101)_B$. Several blocks of laths can be identified in Figure 3. 1. Detailed TEM studies involving the analysis of Kikuchi diffraction patterns and Electron Back-Scattered Diffraction (EBSD) on SEM allows Morito et al. to determine that in the case of low carbon steels, every block is in fact composed by two subgroups of nearly parallel laths each of which belongs to a particular variant of the orientation relationship. The subgroups actually have a small misorientation angle between them (i.e. case 4 in Table 3. 1). Every subgroup of laths belonging to a certain crystallographic variant is termed a *sub-block*. Therefore, in summary, a block is formed by two sub-blocks, which are in turn composed of individual laths belonging to the same variant.

Several blocks having the same parallel close-packet planes (and therefore, the same habit plane) forms a *packet*. Packets are clearly visible in the optical microscope as shown in Figure 3. 1. Since there exist six different variants for each habit plane, it is then possible to identify at most three crystallographically different types of blocks in a packet, since all the variants are expected to have the same set of close-packed parallel planes.

The possible angles or rotation between adjacent laths in a block are shown in Table 3. 1, assuming Kurdjumov-Sachs orientation relationship with the parent austenitic lattice, and assuming the orientation relationship suggested by Sandvik [3.13].

Case	K-S	Sandvik
1	70.53 (twin relationship)	64.13
2	49.47	55.87
3	60	60
4	10.53	4.13

Table 3. 1: *Possible angles of rotation between two different variants for the* $[011]_B$ *zone. Both variants have been assumed to have* $(011)_B // (111)_F$. *After Sandvik [3.13]). Only the adjacent variants having the lowest misorientation angle among them form a block. The minimum misorientation angle is 4.13°.*

3. 3. 3. Internal structure of the laths in the as-quenched state.

TEM observations show a very dense tangle of dislocations in the laths. Kelly ([3.10]) reports that such dislocations are mostly screw dislocations having all four $(a/2)<111>_B$ Burgers vectors. However, a particular one, $(a/2)[11\bar{1}]$, has been observed to be the most common. It is believed that the dominance of this particular Burgers vector can be associated to the process of lattice invariant shear that produces the martensitic structure. It is accepted that in the case of low-carbon steels, such a process involves only dislocation slip (the existence of twinning relation between adjacent laths has been discarded so far as explained in Ref. [3.10] and [3.13]). As expected, the accommodation of the strain during the martensitic transformation yields a high density of dislocations in the martensitic structure. During the transformation, the strain energy should be kept at a minimum. As a result, the combination of adjacent variants (the sub-block boundaries) is not a random process, but it is

such that the overall strain energy during the transformation is minimized. Concerning the measurement of dislocation densities into the laths as quenched martensite, the data available in the literature are scarce. The as quenched martensite has an extremely high density of dislocations to such an extent that individual dislocations are difficult to identify.

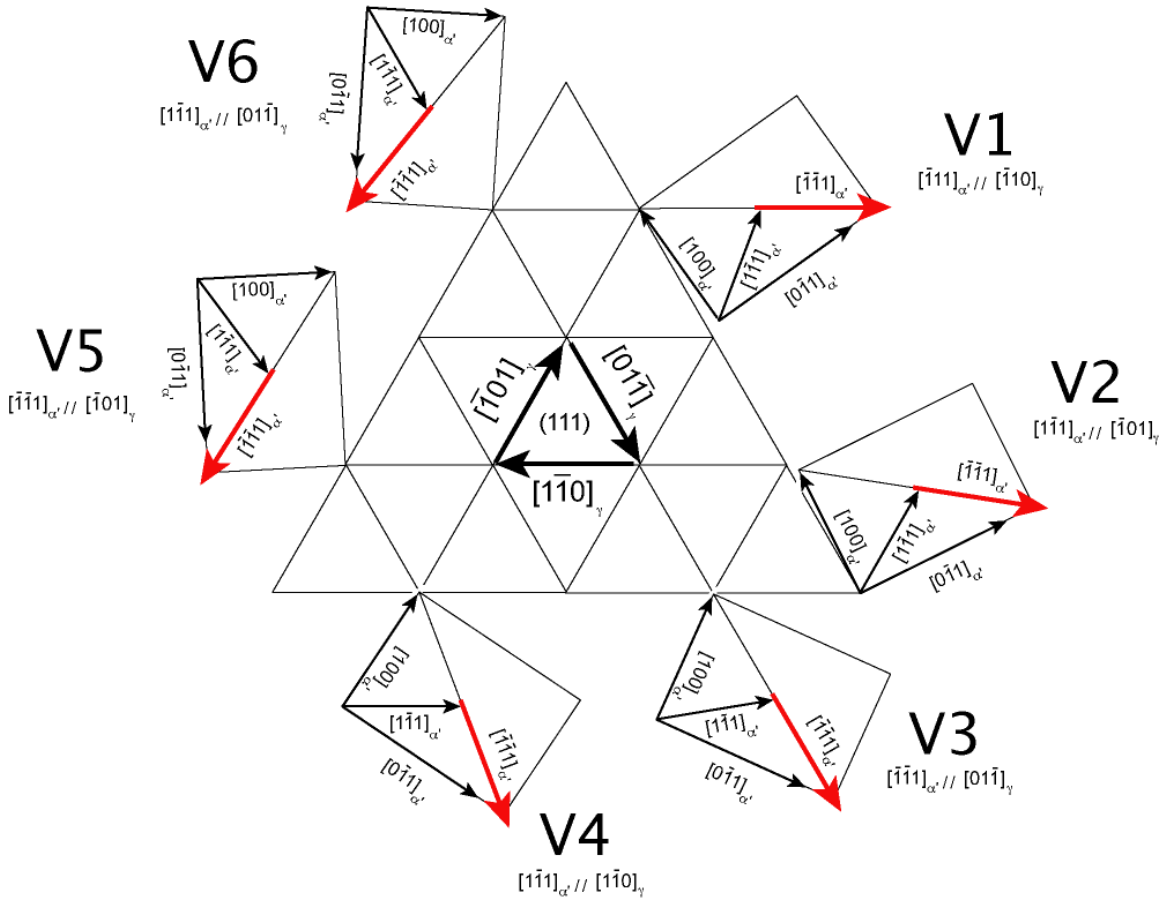

Figure 3. 3: *Example of the Kurdjumov-Sachs orientation relationship. Assuming this orientation relationship as the one dominating in lath martensite, six different variants are then defined for each habit plane, giving rise in this way to 24 possible variants. A block is then composed by two of these variants having small misorientation angle between them: V1-V2; V3-V4; and finally V5-V6.*

At the same time, the high internal stress level makes the Kikuchi lines very diffuse, complicating the procedure to set up the proper diffraction conditions for the analysis. Further complications associated to the ferromagnetic character of the iron-based martensite imply that the astigmatism of the objective lens should be corrected after every movement of the specimen. However, a recent work from Pesicka et al. addresses the topic [3.24]. They have studied the high chromium German grade X20 steel in the as-quenched condition (1h@1050°C+air cooling). The dislocation density in the laths has been measured using TEM pictures (mean intercept length method) and X-ray diffraction techniques (XRD). The values found for the dislocation density were $9.26 \cdot 10^{14}\, m^{-2} \pm 1.95 \cdot 10^{14}\, m^{-2}$ for the TEM measurements and $9.4 \cdot 10^{14}\, m^{-2}$ for the case of the XRD measurements.

3. 3. 4. Effect of tempering on the microstructure.

The effects of tempering on the as-quenched martensite are well known. Even though the microstructural changes depend on the particular conditions of the tempering applied in terms of time and temperature, it is still possible to discuss the topic from a rather general point of view. Among others, the main effect of tempering consists in reducing and eventually eliminating the amount of carbon from the solid solution in the BCT martensitic structure. As a consequence, the hardness of the as-quenched martensite, which mainly depends on the carbon level in solid solution, is highly reduced after tempering. During the tempering process, the BCT structure is transformed into the typical ferritic BCC structure. Precipitation and growth of carbides takes place, mostly at interfaces, which offer also a fast diffusion path for carbon during the carbide grow process. Recovery processes are also another fundamental phenomenon during tempering. As a consequence, the total dislocation density after tempering is highly reduced when compared to the as-quenched dislocation density.
Several works outline the important effect of tempering on the original lath structure of the as-quenched martensite. Before discussing this point, it is worth mentioning that there exists a certain controversy in the materials science community concerning the terminology to use. Strictly speaking, the word “lath” should be used only in the context of the as-quenched martensite. The tempering conditions commonly applied to any technical alloy will produce modifications on the as-quenched lath structure. The formation of sub-cells (polygonal ferritic micrograins) due to the recovery processes acting during tempering is well documented in the literature. Clearly, this type of morphology is far from resembling a lath morphology. However, it is evident that there is not a clear limit from which the first morphology is transformed into the second. Furthermore, in the tempered microstructure, regions where the laths are clearly visible coexist with regions where the sub-grain structure is the dominant feature. In what follows, we refer to all these microstructural features typical for the tempered material as “micrograins”, in an attempt to highlight the intrinsic difference that exist between the as-quenched martensitic microstructure and the type of ferritic microstructures commonly developed after typical tempering conditions (having lath shape or not).
Ennis et al. ([3.15]) performed a detailed study on the P92 steel, a tempered martensitic steel of the 9-11wt.%Cr class. They have studied the size distribution of the micrograins by means of TEM. The mean intercept method was used to determine the size of the micrograins, where the values corresponding to the perpendicular direction to the long axis of the laths were reported. They have found that the mean size of the micrograins is strongly affected by the tempering conditions (see Table 3.2.). It can be observed that the micrograin size increases with increasing the severty of the tempering conditions. They have also reported the evolution of the dislocation density for all the tempering conditions (included in Table 3.2). The mean size of the $M_{23}C_6$ carbides was determined by means of extraction double replica studies and it was investigated as a function of the tempering conditions. They obtained a mean carbide size value around 80 nm.

The microstructural studies presented in [3.15] have been extended in [3.16] to the steels P91 and E911. The mean micrograin sizes and the mean dislocation densities were measured for the tempered material. The results are also presented in Table 3.2. As it can be seen, all the steels studied have about the same dislocation densities, ranging from 6 to $8 \cdot 10^{14}\, m^{-2}$. The mean micrograin size was in all the cases around 400 nm.

Pesicka et al. [3.24] have presented a detailed study of the evolution of the dislocation densities as a function of the tempering conditions for the case of the German grade X20 steel. They have analyzed TEM images by means of the mean intercept method and X-ray diffraction. The TEM results are presented in Table 3. 2. They have pointed out a very important aspect that is probably not recognized enough in the literature, i.e., the distribution of dislocations into the micro grains are highly heterogeneous in the case of the tempered martensite. Indeed, there are important variations in the dislocation density into a same micro grain. This point has been previously stressed by Sandvik and Wayman for as-quenched structures [3.25]. At the same time, relatively clean micro grains coexist with micro grains having a high dislocation density. This is also clearly observed in post mortem analysis of creep specimens. The dislocation density value reported by Pesicka et al. was obtained by averaging five dislocation density values obtained along a single micro grain.

Steel	Thermal treatment	Dislocation density ($10^{14}\,m^{-2}$)	Mean micrograin size (μm)
P91_Ref. [3.16]	1h@1050°C+1h@750°C	7.5±0.8	0.4±0.06
P92_Ref. [3.16]	2h@1070°C+2h@775°C	7.9±0.8	0.4±0.09
E911_Ref. [3.16]	1h@1050°C+1h@750°C	6.5±0.6	0.5±0.05
X20_Ref. [3.24]	1h@1050°C+1h@750°C	0.98±0.27	
F82H_Ref. [3.16]	0.5h@1040°C+2h@740°C	0.86±0.30	

Table 3. 2: *Microstructural features reported for several tempered martensitic steels.*

Dronhofer et al. [3.11] have presented an interesting microstructural study on the German grade X20 CrMoV 12 1 steel. This is a tempered martensitic steel having 12wt.%Cr and 1wt%Mo. They have studied the effect of the austenitization temperature and tempering conditions on the microstructure of the steel. They applied different thermal treatments to generate microstructures having important differences in the prior austenitic grain sizes. The evolution of the PAG sizes with austenitization time was studied at a temperature of 1050 °C. Four austenitization times were considered: 0.25h, 1h, 4h, and 9h. They concluded that the PAG sizes were not affected by the time of austenitization up to 4 h at 1050 °C. However, longer austenitization times produced an important increase in the PAG's. These results were rationalized in term of the time needed for complete dissolution of the stable carbo-nitrides at high temperature (mainly Nb(C,N)). After dissolution of the carbides (t > 4h) the PAG started to growth. In all the cases, the materials were air quenched and the size of the martensitic laths were measured by means of the mean intercept method in the direction perpendicular to the long axis of the laths. It was observed that the lath mean sizes were independent of the austenitization procedure, being in the order of 310 nm for the case of the material studied. Subsequent tempering of the microstructures at 750 °C during 1h only produced a small shift up to larger values in the mean lath size. Dronhofer et al also performed Kikuchi diffraction studies and EBSD analysis in the case of the tempered material to determine potential changes in the relative orientations of the adjacent micrograins with respect to the as-quenched material. Their results support the fact that the main features of the martensitic transformation concerning the orientation between adjacent laths can still be identified in the case of the tempered material.

Schäublin et al. [3.16] have studied the microstructure of the tempered-martesitic F82H steel They have found that the internal dislocation structure in this steel is composed of tangles of dislocations having a dominant screw character with Burgers vectors of the type $a_0 / 2 < 111 >$. They have also measured the dislocation density and obtained a value of $8.6 \cdot 10^{13} m^{-2}$ with a statistical error of 50%. The carbide size distribution of the material was analyzed in detail. The sizes distribution showed a maximum at a size of 50 nm. The largest size observed was 150 nm.

In Figure 3. 4, we show two TEM micrographs that we took on a tempered martensitic model alloys (Fe-12wt%Cr-0.1wt%C). The various boundaries between PAG, packets, blocks and sub-blocks are identified to illustrate the complexity of the tempered martensitic structure.

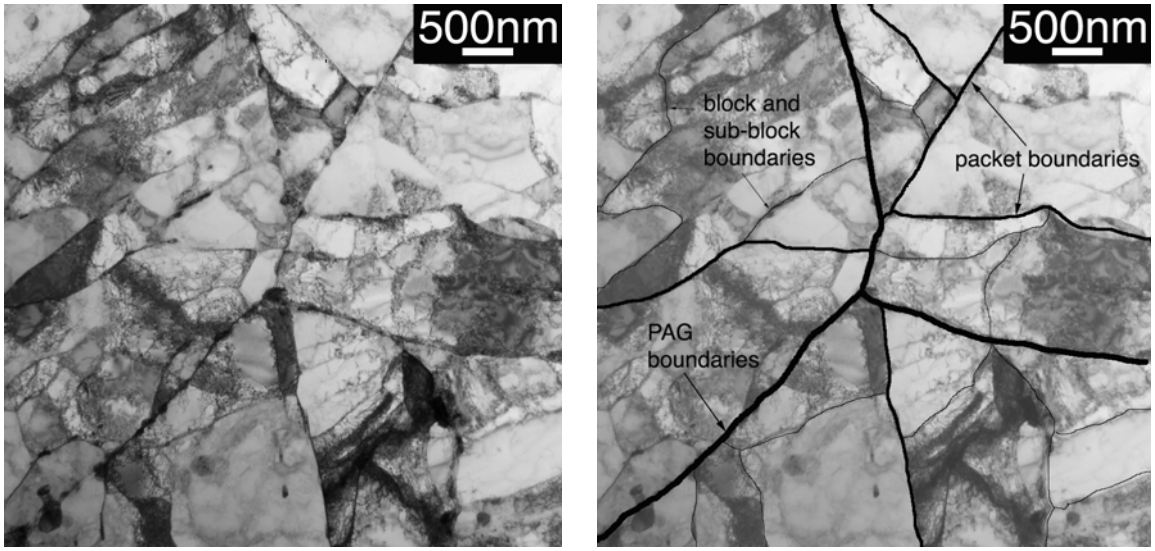

Figure 3. 4: *A TEM picture of a tempered martensitic steel (Fe-12wt%Cr-0.1wt%C after 230'@980°C, AC + 60'@760°C). The main boundaries are indicated in the figure on the right. Note that the original lath structure is clearly visible in the upper corner left of the micrograph.*

3. 4. Microstructural characterization of the reduced-activation tempered-martensitic steel Eurofer97.

3. 4. 1. Introduction.

The reduced activation steel Eurofer97 is a tempered-martensitic stainless steel of the 7-9wt% Cr class, which is one of the reference materials of the European Fusion material program for structural reactor applications. The material has been produced by Bölher AG as rolled plates of 8, 14 and 25 mm. In this work, we have studied only the material coming from the 25 mm plate. The thermal treatment applied to the 25 mm plate was:

i) austenitization during 0.5h@ 980°C followed by air cooling

+

ii) tempering at 1.5h @ 760°C +air cooling.

The chemical composition specified for Eurofer97 is presented in Table 3. 3. In order to obtain the reduced-activation behavior, several alloying elements commonly observed in commercial martensitic stainless steels like Ni, Nb and Mo have been replaced by elements with lower activation. These new alloying elements have similar metallurgical effects than the original ones. In Table 3. 4, the metallurgical effect of these elements is briefly discussed.

3. 4. 2. Microstructure of the Eurofer97.

The microstructural characterization of the steel has been carried out by means of optical microscopy, scanning electron microscopy (SEM) and transmission electron microscopy (TEM). Second phase particles have been characterized by X-rays diffraction and electrons diffraction by TEM. Qualitative energy dispersive analysis (EDX) has also been used to supplement the results.

3. 4. 3. Optical microscopy.

The best etching of prior austenitic grain boundaries was obtained by electrochemical etching with a solution of oxalic acid in water (10 g oxalic acid in 100 ml of distilled water) at room temperature. The potential used was 6V.
Figure 3. 5 shows an image of the microstructure of the Eurofer97 steel. As it can be observed, the steel presents a fully tempered martensitic microstructure. The prior austenitic grains (PAG) are also clearly visible in the micrograph. Several samples with different orientations with respect to the rolling direction were analyzed. The PAGs show no deformation along the rolling direction, being mostly equiaxed.

	Sample				
	Plates			bar	Specification for Eurofer-97
Thickness/Diameter	8 mm	14 mm	25 mm	∅ 100 mm	
Certificate ref (heat, Böhler)	E83698		E83697	E83699	
Chemical composition (avg taken from Heat analyses in appendix I)					
C	0.12		0.12	0.12	0.09-0.12
Si	0.04		0.06	0.07	≤0.05
Mn	0.49		0.46	0.44	0.20-0.60
P	<0.005		<0.005	<0.005	≤0.005
S	0.004		0.004	0.004	≤0.005
Cr	8.93		8.90	8.97	8.50-9.50
Mo	<0.0010		0.0023	<0.001	≤0.005
Ni	0.020		0.022	0.007	≤0.005
V	0.20		0.20	0.19	0.15-0.25
W	1.08		1.07	1.10	1.0-1.2
Cu	0.0019		0.0039	0.0022	≤0.005
Co	0.006		0.006	0.004	≤0.005
Ti	0.006		0.009	0.009	≤0.01
Al	0.009		0.008	0.008	≤0.01
Nb	0.0017		0.0020	<0.001	≤0.001
B	<0.001		<0.001	<0.001	≤0.001
N	0.021		0.020	0.017	0.015-0.045
Pb	<0.0003		<0.0003	<0.0003	
Ta	0.15		0.15	0.14	0.05-0.09
O	0.006		0.0007	0.0012	≤0.01
As	<0.005		<0.005	<0.005	As+Sn+Sb+Zr ≤0.05
Sn	<0.005		<0.005	<0.005	
Zr	<0.005		<0.005	<0.005	
Sb	<0.005		<0.005	<0.005	
Heat treatment					
Normalising Tempering	980°C – 27 min– air-cool		980°C – 30.6 min- air cool	979°C – 1 h 51 min - air	
Tempering	760°C – 90 min air-cool		760°C – 90 min – air-cool	739C – 3h 42 min - air	
Hardness according to appendix I					
Hardness HV30	218-221	208-216	221-222	Edge: 227 D/4: 221 Centre: 220 D/4: 217 Edge: 220 Avg: 221±4	

NOTE: The chemical compositions are homogenous throughout the billets.

Table 3. 3: *Chemical composition of the Eurofer 97.*

Alloying element	Low-activation replacement	Main metallurgical effects
Ni	Mn	Ni and Mn are both austenite-promoter elements. The effect of Ni is much stronger than the one of Mn. They are added to the 12wt%Cr steels mostly to counterbalance the effect of the ferrite formers alloying elements. They mainly decrease the M_s temperature, reducing the autotempering of the martensite, which in turns increases the hardness of the as-quenched structure.
Mo	V/W	One of the most important effects of Mo is to stabilize the M_2X precipitates (Mo dissolves in the $Cr_2(CN)$ producing $(CrMo)_2(CN)$). Mo in solution increases the lattice parameter of the M_2X precipitates and as a consequence, the associated coherency strains, increasing the secondary hardening and the tempering resistance. This stabilization allows the M_2X precipitates to be present in the matrix even after strong tempering conditions. W has exactly the same effect than Mo, i.e., stabilizes the M_2X precipitates, but is not as effective as Mo, in the sense that almost twice the concentration of W is needed to obtain the same effect as Mo. V plays the same role as W. At the same time, both elements are strong carbide formers. In particular V carbides, nitrides and carbonitrides (MX-type particles) precipitate at higher temperatures than the M_2X precipitates. These phases are very stable and increase the tempering resistance.
Nb	Ta	Nb is a strong carbide former, being very stable at high temperatures. It strongly improves the tempering resistance of the alloy by forming MX precipitates in the martensitic lath boundaries (carbides, nitrides and carbonitrides, as in the case of V). The behaviour of Ta is analogous to the behaviour of Nb and Ti.

Table 3. 4: *Main metallurgical effects of typical alloying elements in stainless steels [3.5] [3.18].*

After the electro-chemical attack, the PAG's were visible enough to perform a reliable measurement of the PAG sizes. Ten micrographs were used for the estimation of G. In all the cases, the L-T plane was analyzed, following the procedure described in Section 3.2.1.1. The value found for the EUROFER 97 in the "as received" condition is G=10.2±0.1. The mean linear intercept length $\bar{\ell}$ determined was 9.46 μm. The results are summarized in Table 3. 5. As discussed previously in Section 3.2.1.1, we can use these values to estimate the real three-dimensional size of the PAG's. Assuming a spherical shape for the grains, the volumetric grain diameter is calculated as $D = 1.5\,\bar{\ell} =$ 14.2 μm. Using a more sophisticated model, like the tetrakaidecahedron model, the value obtained is 16.08 μm, slightly larger than in the previous case.

Some small inclusions where occasionally observed. Subsequent analysis in the Scanning Electron Microscope using EDS demonstrated that these particles are mostly FeMnS inclusions, having spherical shape with sizes ranging from 1 to 2 μm.

One of the main motivations for the development of the 9wt%Cr family of steels was to eliminate the presence of δ-ferrite in the microstructure. In practical terms, this means that we must obtain a fully austenitic matrix after the austenitization process. In the case of high chromium tempered-martensitic steels, it is accepted that the presence of δ-ferrite degrades the strength and toughness of the steels [3.5]. In the present study, no δ-ferrite has been observed in the microstructure of the Eurofer97 steel.

Material: EUROFER 97				
number of fields analyzed: 9				
Area of each field:	10 μm			
quantity	**mean value**	**mean std. dev.** $(s/\sqrt{n})$	**95%CI**	**%RA**
P_L (mm^{-1})	105,72	1,23	2,84	2,68
L (μm)	9,46		0,24	
G =	10,16 ±	0,07		

Table 3. 5*: Prior austenitic grain size of the EUROFER 97.*

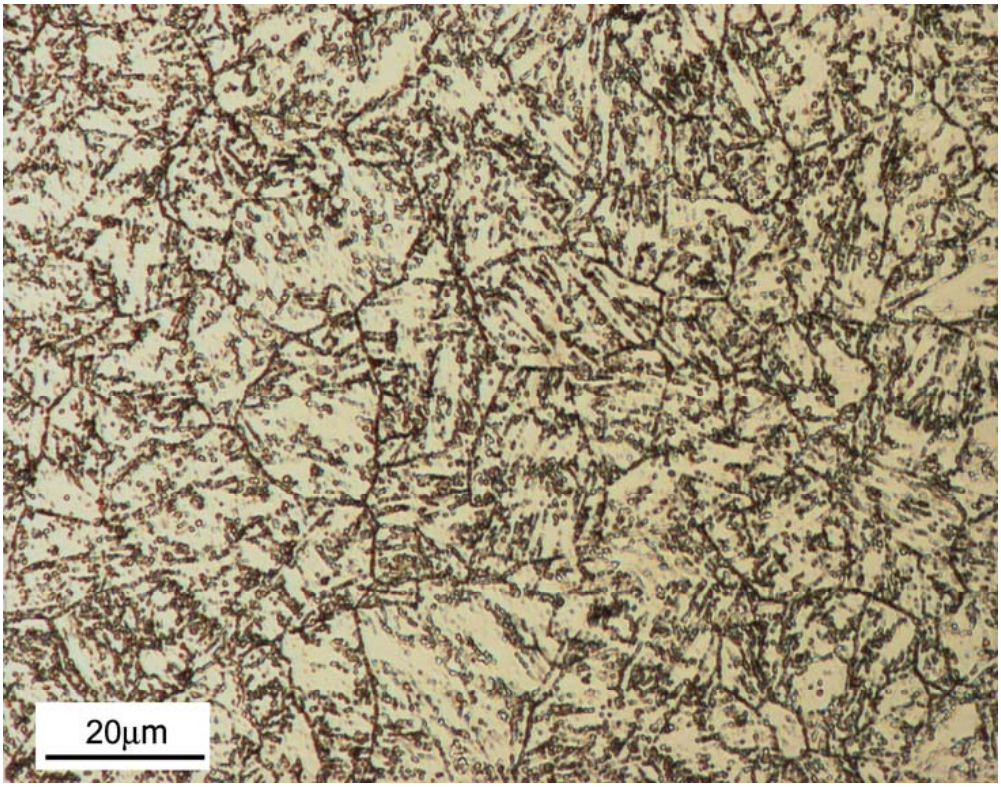

Figure 3. 5: *Micrograph of Eurofer97 (heat 83697) showing the L-T plane of the plate. The prior austenitic grains (PAG) are clearly visible. There is no deformation of the PAG along the rolling direction.*

3. 4. 4. Transmission electron microscopy.

The microstructure of the Eurofer97 steel corresponds to a tempered lath-martensite. The aspect of the microstructure as observed in the TEM is shown in Figure 3. 6. The lath structure typical of the as-quenched martensite can still be recognized on the tempered microstructure. The lath width is in the order of 200 nm. In some regions, the existence of dislocation cell structures has been clearly determined. These regions were formed during the tempering process.

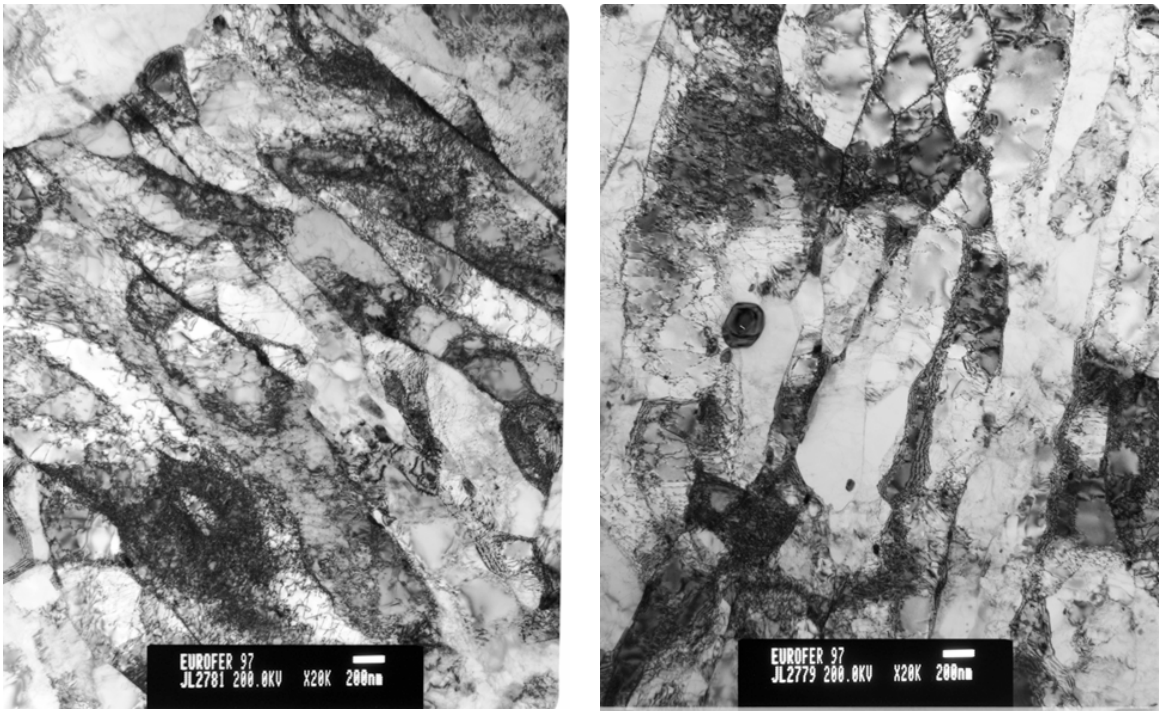

Figure 3. 6: *TEM images of the Eurofer 97 in the as received state.*

Nevertheless the lath structure is the dominant microstructural feature observed in the specimens. As expected, several types of second phase particles decorate the tempered microstructure. The identification of these phases has been carried out by means of electron diffraction and EDS in the TEM. The analysis of the particles indicates that carbides having high Cr content of the type $M_{23}C_6$ are the most important from the point of view of the volume fraction. The $M_{23}C_6$ carbides are shown in Figure 3. 7. The typical size of these carbides ranges between 50 nm and 500 nm. The mean size is approximately 200 nm. $M_{23}C_6$ carbides are the largest particles in the matrix. A qualitative EDS analysis of the $M_{23}C_6$ carried out in extraction replicas, indicates that, besides C, they contain mostly Cr, but Fe, W, V and in some cases small amounts of Mn is also found. Large tantalum rich particles were also detected being the largest size in the order of 400 nm and they can also be included among the largest particles detected in the matrix. The volume fraction of the Ta-rich particles is lower than the correspondent to the $M_{23}C_6$. However, due to the size of the precipitates, they can play an important role in the micromechanism of brittle fracture. The EDS analysis showed that Ta-rich particles also contain W, V, Cr and Mn, see Figure 3.8. Electron diffraction studies of these particles failed due to the thickness of the precipitates. No further efforts were made to fully characterize its nature.

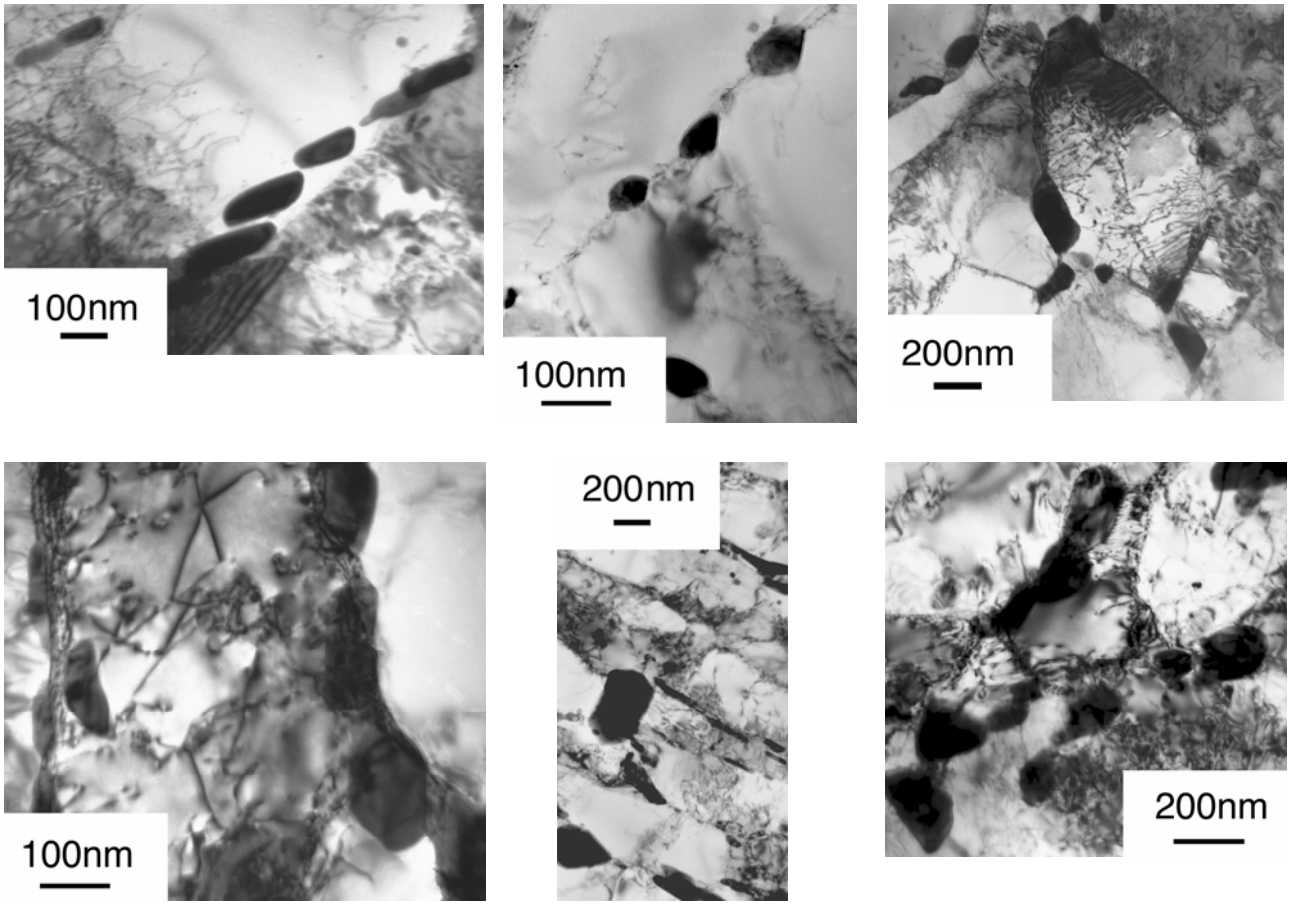

Figure 3. 7: *$M_{23}C_6$ particles in Eurofer97.*

Needle-like M_2X type particles, based on $Cr_2(CN)$ with additions of V and W, precipitates in the martensitic lath boundaries. Due to the stabilizing effect of V and W, a certain fraction of M_2X persists after tempering. The long dimension of the M_2X may reach 50 nm.
Other important particles in these type of steels are the MX (VN, (CrV)N, TaC). As it was pointed out in Table 3. 4, these particles precipitate at higher temperatures than the M_2X particles. Furthermore, after prolonged high temperature aging or creep straining, M_2X particles are replaced by the most stable MX particles which are one of the main factors explaining the good creep properties displayed by the 7-9% chromium tempered martensitic stainless steels. MX particles are observed to precipitate as a fine dispersion in the matrix, having sizes in the order of 15 to 20nm [3.21] [3.15]. MX particles play also a very important role in the determination of the PAG size obtained during the normalization. In the Eurofer97 steel, TaC and V(CN) help to refine the austenitic grains by providing several nucleation sites and impeding the growth of the grains.
Typical dislocation structures observed in the tempered EUROFER 97 are presented in Figure 3. 9 and Figure 3. 10. Our studies indicate that the dislocation density in this material is highly inhomogeneous. Indeed, for the proper diffraction conditions, some laths display a

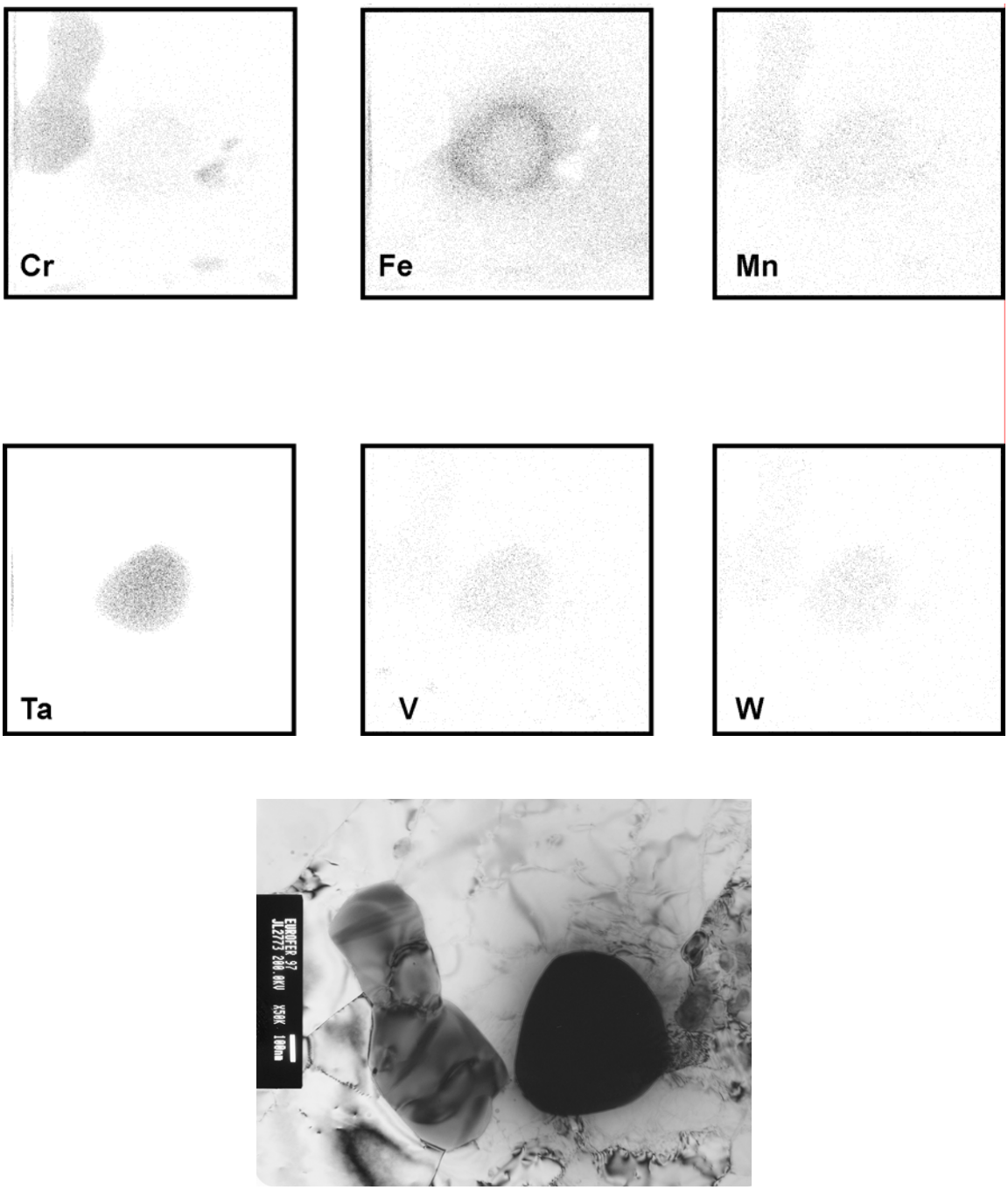

Figure 3. 8: *X-ray mapping of a region containing three large particles. A large Ta-rich particle can be observed.*

very high dislocation density while others are relatively clean. Moreover, the dislocation density is observed to vary strongly along the same lath. Before discussing the main features of Figure 3. 9 and Figure 3. 10, it is worth introducing some concepts on which the interpretation of the images is based.

First, it is important to stress that the characterization of the dislocation structures has been performed assuming a Burgers vector of the type $a/2<111>$. We believe that this assumption is highly justified based on an important amount of previous work in the case of as-quenched and tempered martensitic steels. In BCC materials, slip occurs in the <111>

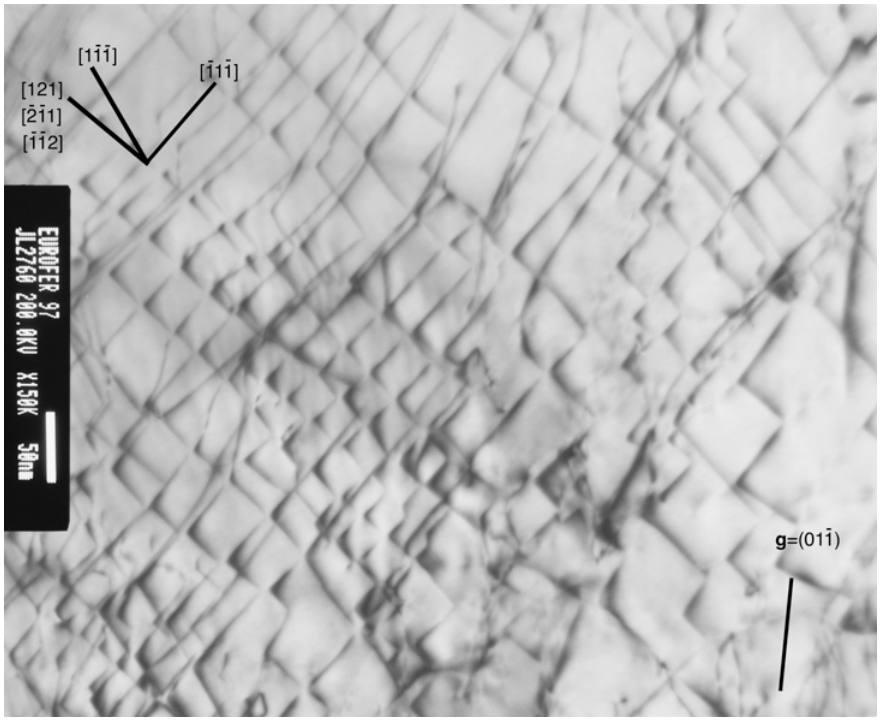

Figure 3. 9: *Dislocations array in a micrograin. The picture has been taken using two beam condition near the (011) zone axis using the* $(01\bar{1})$ *reflection. The relevant crystallographic directions are indicated in the picture. Note that the indexation of the visible dislocations is consistent with the* $\mathbf{g}\cdot\mathbf{b}$ *analysis assuming* $\mathbf{b} = a/2 <111>$.

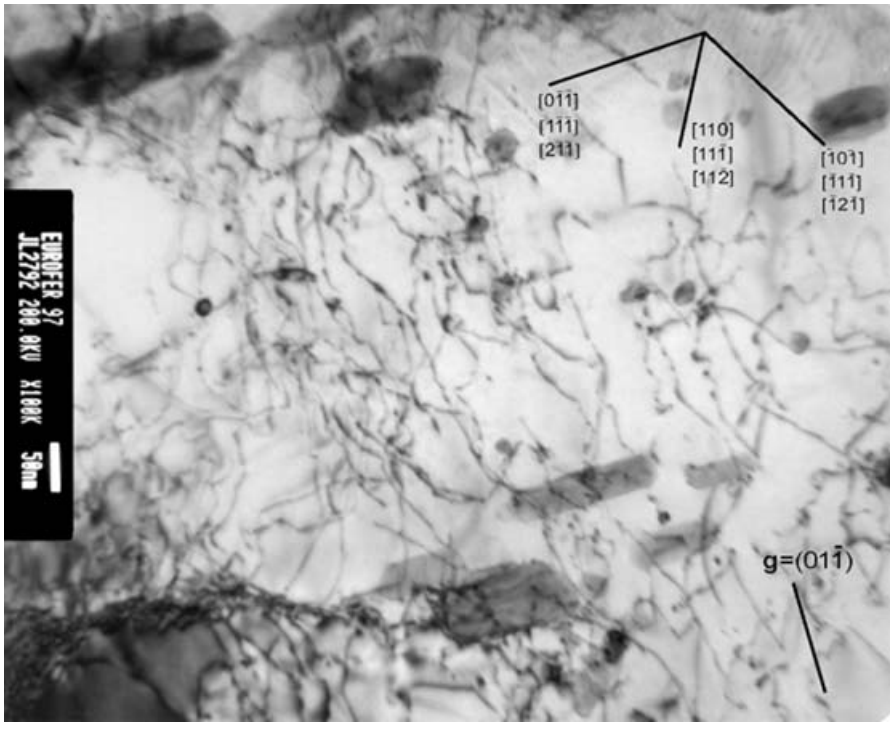

Figure 3. 10*: Dislocations array in a micrograin. The picture has been taken in two beam condition near the (111) zone axis using the* $(01\bar{1})$ *reflection. The relevant crystallographic directions are indicated in the picture. Several* $M_{23}C_6$ *type particles can be seen in the image. Note that the flat interface between the particles and the matrix follows a well defined crystallographic direction, suggesting a coherent interface.*

directions on the {110}, {112} and {123} planes. Since the operative Burgers vectors of tempered martensites are those of the type $a/2<111>$, we may conclude that a dislocation having pure edge character will have a dislocation line ξ on the <112> directions when the slip plane is of the type {110} or {123} and on the <110> directions when the slip plane is of the type {112}. In the case of dislocations having pure screw character, ξ=<111> by definition. Since a TEM image is a projection of a three-dimensional set of features on the plane of the photographic film, dislocations having pure screw character can be distinguish from pure edge dislocations provided that the <111> directions do not overlap with any of the <112> directions in the projection. The analysis of the projections for the (011) and (111) zone axis is presented in Figure 3.11 and Figure 3.12.

We conclude that in the case of the (011) zone axis, it is possible to fully identify the character of the dislocation lines on the TEM micrograph. Indeed, in or near the (011) zone axis, no $<111>$ type direction overlaps any <112> type direction. Therefore there is no uncertainty on the determination of the character of the dislocation lines. However, note that only three <111> directions are accessible since the $[111]$ direction overlaps the $[\bar{1}11]$ direction. The overlapping also happens in the case of the <112> directions. Figure 3.12 shows the analysis for the (111) zone axis. In this case screw dislocations cannot be distinguish from edge dislocations since all the <111> directions overlaps with the <112> directions. However, pure edge dislocations can still be identified with confidence provided that the dislocation lines don't overlap the <111> type directions.

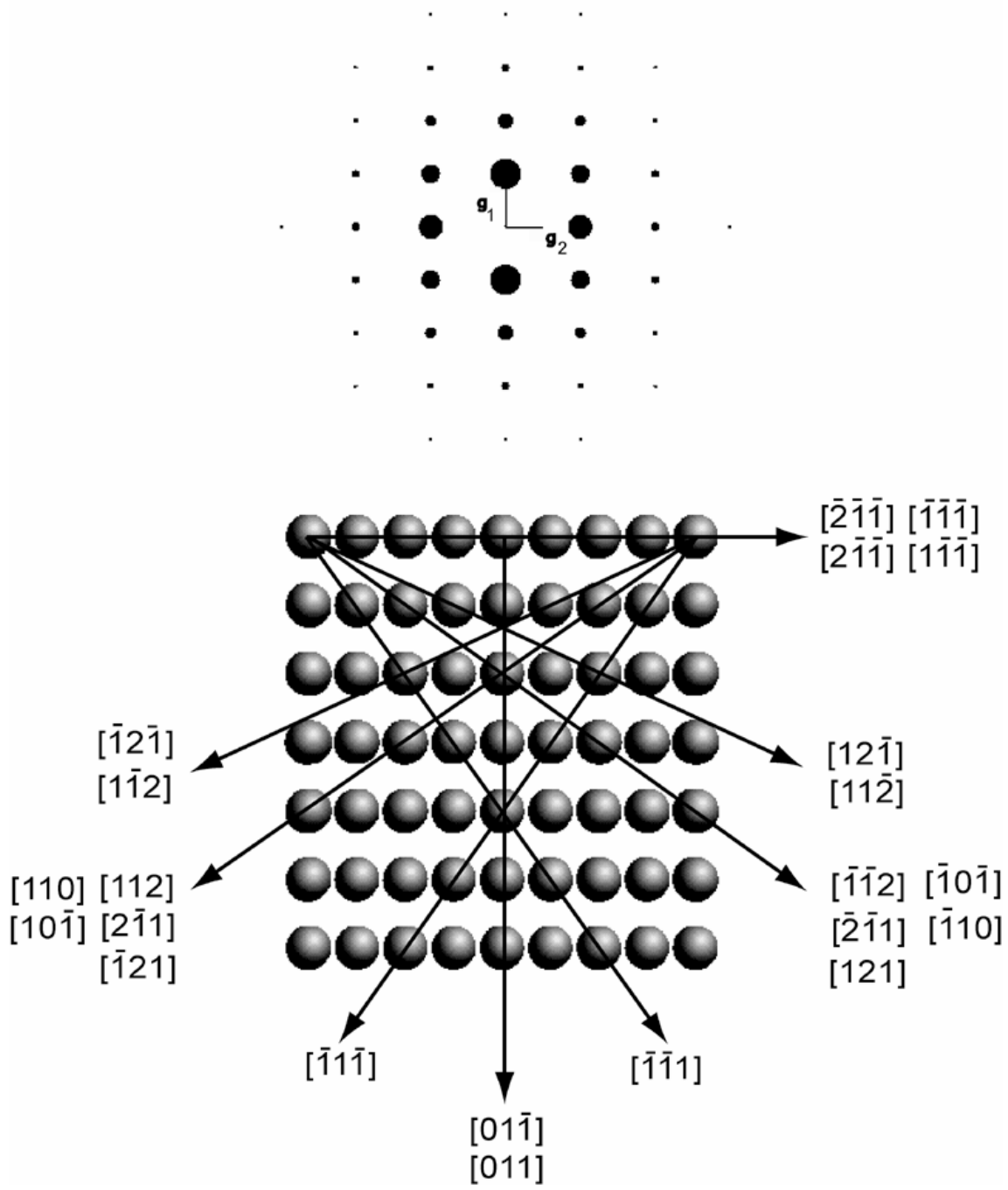

Figure 3. 11: *Diffraction pattern corresponding to the (011) zone axis and projections of the four <111>, the six <110> and the twelve <112> crystallographic directions on the (011) plane. Since the <111> and the <112> directions don't overlap each other, it is possible to identify pure edge and pure screw segments on a micrograph taken near the (011) zone axis (**b**=a/2 <111> assumed on the analysis).* $\boldsymbol{g_1} = (0\,\bar{1}\,1)$*;* $\boldsymbol{g_2} = (\bar{1}00)$*.*

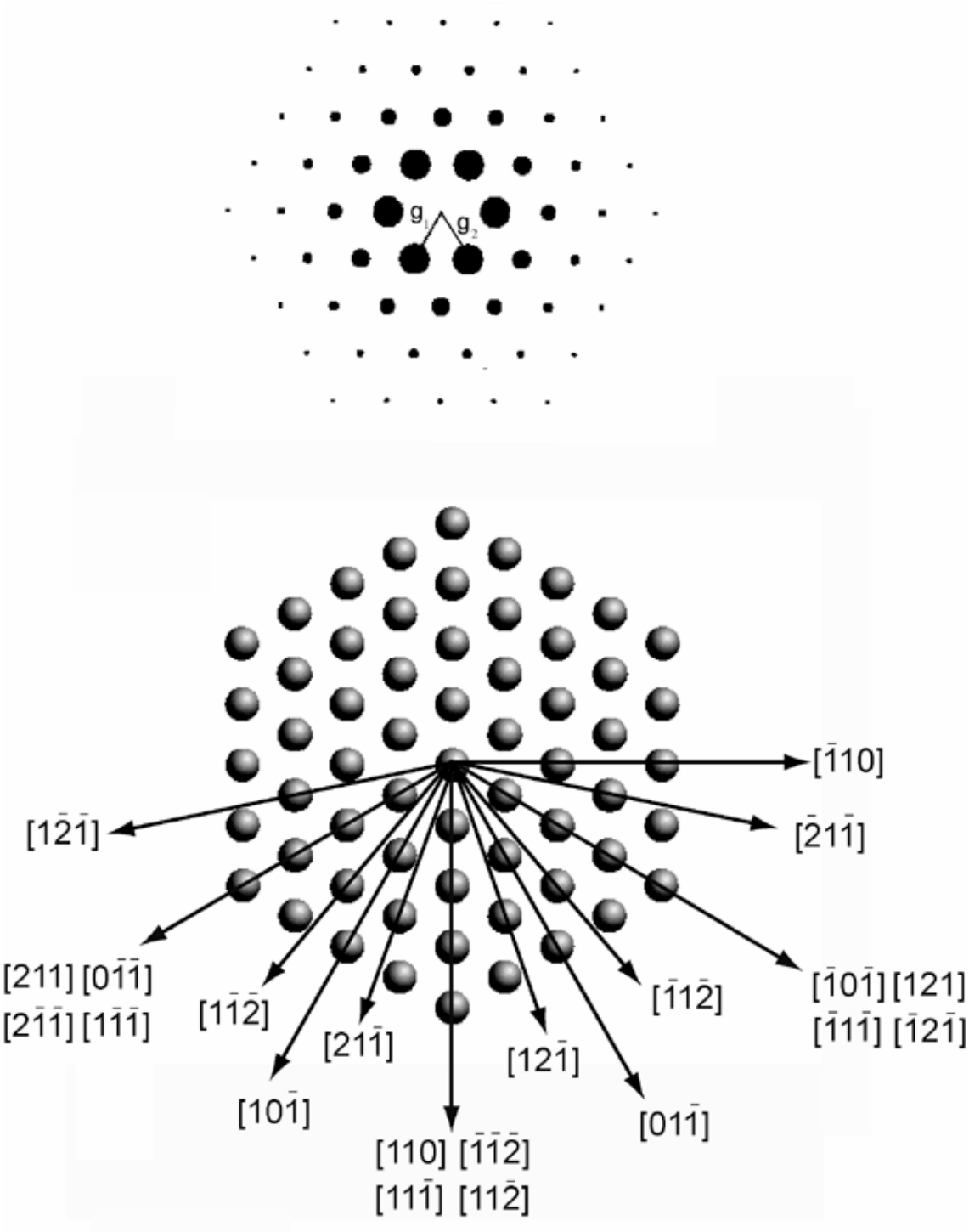

Figure 3. 12: *Diffraction pattern corresponding to the (111) zone axis and projections of the four <111>, the six <110> and the twelve <112> crystallographic directions on the (111) plane. In this case all the <111> projections overlap with the <112> directions. As a consequence, the potential screw character of the dislocation segments cannot be ensured. A second image in other diffraction condition is needed.* $\boldsymbol{g_1} = (10\bar{1})$; $\boldsymbol{g_2} = (01\bar{1})$.

3. 5. Ferritic Model alloy.

3. 5. 1. Introduction.

In order to model the plastic flow properties of tempered martensitic alloys and an equiaxed ferritic one, a Fe-9wt.%Cr alloy was developed by Carpenter, from high purity raw materials using vacuum melting. The ingots were hot forged to obtain small slabs (600x200x40mm). After hot forging, the alloy was re-austenitisized (1h@980°C) and cooled down in air to room temperature. A main concern in the development of high purity Fe-Cr alloys is the final concentration of carbon and nitrogen. The use of high purity materials allows obtaining an acceptable level of carbon (0.002wt%) and nitrogen (0.014wt%). Unfortunately, a further reduction in the interstitial level certainly increases the cost of the model alloy enormously. The overall composition of the alloy is given in Table 3. 6 together with the composition of other commercial low-interstitial alloys for reference.
The presence of oxygen in the melt is an important factor. Due to the overall low level of carbon and other strong deoxidizing elements in the melt, oxygen will react with chromium to form undesired chromium oxide particles. Such particles can be easily detected in the model alloy presented here, being its mean size in the order of 2 to 5 microns (see Figure 3. 13, left). Nitrogen in the melt is also very difficult to remove by classical methods.

Alloy	C	Mn	Si	P	S	Cr	Ni	Mo	Cu	N	O	Fe
Fe-9%Cr	0.002	0.007	0.006	0.005	0.005	9.02	0.008	0.006	-	0.014	0.013	Bal.
AISI 304LN	0.03	2.0	1.0	0.045	0.03	18.0-20.0	8.0-12.0		-	0.10-0.16		Bal.
AISI 316LN	0.03	2.0	1.0	0.045	0.03	16.0-18.0	10.0-14.0	2.0-3.0	-	0.10-0.16		Bal.
Shomac 26-4	0.003					26		4	-	0.005		Bal.

Table 3. 6: *Composition of the Fe-9%Cr model alloy. The composition of other low-interstitial commercial alloys is also presented for reference [3.30].*

3. 5. 2. Microstructures.

3. 5. 2. 1. As received state.

The microstructure of the material in the as received condition observed by optical microscopy is presented in Figure 3. 13. A careful examination shows the existence of several ferritic morphologies.
The $\gamma \rightarrow \alpha$ transformations in Fe, Fe-Cr and Fe-Ni alloys have been studied by several researchers in the past (see Ref. [3.20] [3.26] [3.27] [3.28]). Unfortunately, there is no agreement among them concerning the identification of the transformation products. Wilson [3.26] has reported the existence of five transformation products for the case of pure iron and diluted substitutional alloys: equiaxed ferrite, massive ferrite, bainitic ferrite, lath martensite and twined martensite (for increasing cooling rates). His results are somehow consistent with the work of Bee and Honeycombe [3.20], who reported the existence of equiaxed ferrite, irregular ferrite (Widmanstätten ferrite), bainitic ferrite and lath martensite. A divergence exists concerning the existence of massive ferrite or Widmanstätten ferrite. The comparison of the micrographs corresponding to massive ferrite presented by Wilson and the ones corresponding to “irregular ferrite” presented by Bee and Honeycombe are quite alike, and, in our opinion, the images illustrate exactly the same transformation product. A detailed discussion of these topics is outside the scope of the present work. Further information

concerning massive transformation in pure Fe and its substitutional alloys can be found in [3.29].
The formation of Widmanstätten and bainite usually involve the diffusion of carbon and the formation of carbides. However, in the context of the $\gamma \rightarrow \alpha$ transformation products of pure Fe and dilute Fe-substitutional alloys, the concept "ferritic bainite" must be understood as identifying a certain lath structure where the laths are thicker than in the case of lath martensite and more irregular in shape, having a very high dislocation density. Consistently, the micrograph presented in Figure 3. 13 shows the existence of several transformation products, due to the fact that the material was air cooled from the austenitization temperature. Some large ferritic grains are observed in Figure 3. 13 coexisting with zones of massive ferrite and bainitic ferrite.

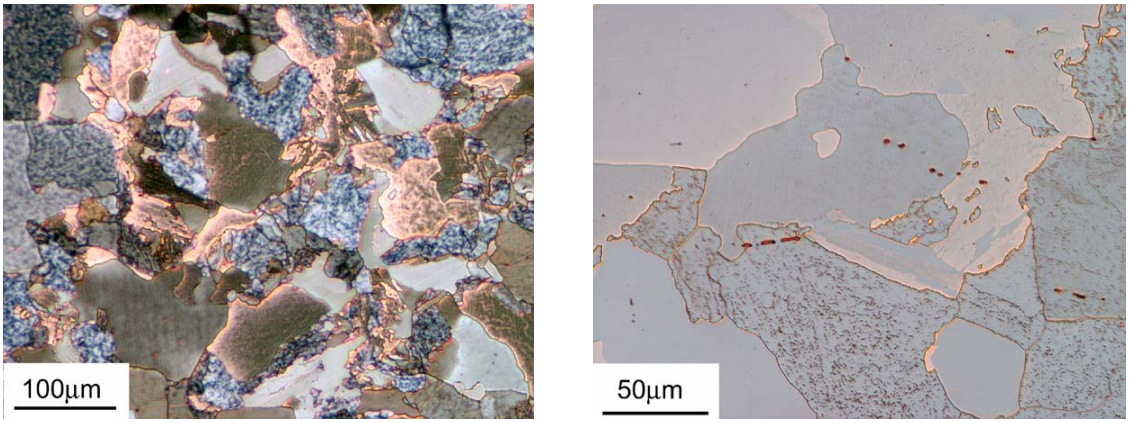

Figure 3. 13*: Typical microstructures of the as-received material (austenitization 1h@980°C + air cooling; Kalling's reagent, 4s at 293 K). Several transformation morphologies can be readily identified. Some chromium oxide particles can be observed in the micrograph of the left.*

3. 5. 2. 2. Thermal treatment.

From the point of view of the study of plastic phenomena on Fe-9wt%Cr model alloy, the microstructures obtained after air-cooling from the austenitization temperature are not appropriate. Indeed, the main idea of producing a Fe-Cr binary alloy consist in obtaining a simple equiaxed ferritic structure where the tensile properties can be related to simple structural parameters like the mean grain size or the dislocation density. Since the as received microstructure is highly complex, composed by ferrite having different morphologies, simple mechanical properties-microstructure relationships may be difficult to develop. Thus, in order to obtain a fully equiaxed ferritic matrix, we selected an isothermal thermal treatment. The TTT diagrams of the Fe-10wt%Cr were available from previous work of Bee and Honeycombe [3.20]. The correspondent TTT diagrams for a Fe-10wt%Cr are presented in Figure 3. 14. The Fe-9wt%Cr model alloy was heat-treated as follows. After full austenitization (0.5h @950 °C) the set point of the PID controller of the furnace was decreased to 790 °C. The temperature of the material was registered with a K-thermocuple attached to it, being consistently kept at 790 °C for periods of 1h, 2hs, 4hs, and 24hs. Following Bee and Honeycombe, in the case of a Fe-10wt.%Cr alloy, a fully equiaxed ferritic microstructure is obtained after approximately 20 minutes of isothermal treatment at 790°C.

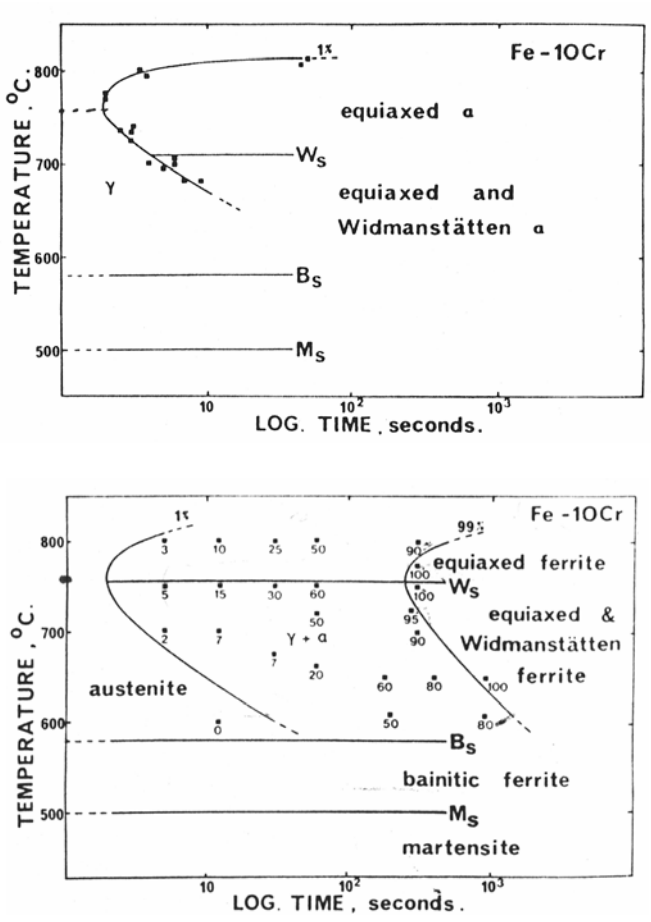

Figure 3. 14: *TTT diagrams of Fe-10wt.%Cr. A) Isothermal dilatometry. B) Optic microscopy. The carbon content of the samples varied between 0.003wt%C to 0.007wt%Cr. The nitrogen content was not reported. After Bee and Honeycombe [3.20].*

As an example, in Figure 3. 15, we show an incomplete transformation after an isothermal treatment of 16'@790°C. In our case, the $\gamma \rightarrow \alpha$ transformation was not completed even after 4hs of isothermal thermal treatment, even though the chromium and specially the carbon content of our model alloy were lower than the one used by Bee and Honeycombe. Both factors are expected to shift the transformation curves to shorter times. A possible argument to explain the apparently contradictory result can be due to the nitrogen content of both alloys. Nitrogen has a very strong effect in the transformation times, comparable to carbon. Our model alloy has a relatively high level of nitrogen (0.014wt%N) and even though Bee and Honeycombe did not report the nitrogen content of their alloys, we may assume that was lower than the one in our model alloy based on the result presented here.
A fully equiaxed ferritic microstructure was obtained after 24h@790°C (see Figure 3. 16) and a TEM micrograph is shown in Figure 3.17. The mean grain size obtained is on the order of 80 microns (mean intercept length). The tensile properties of this material are presented in Chapter 4, together with those of the Eurofer97 steel.

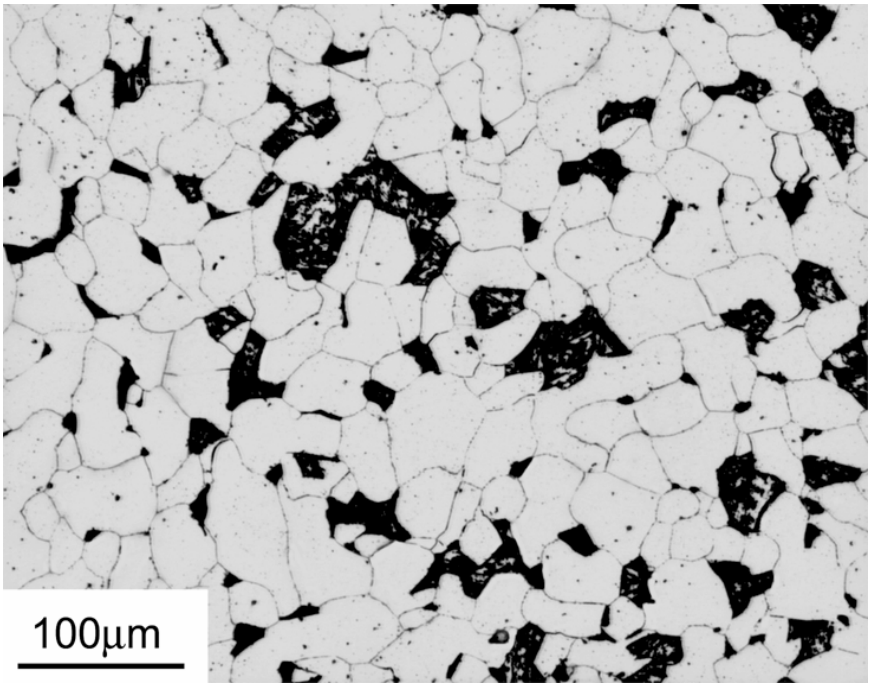

Figure 3. 15: *Fe-9wt%Cr model alloy after 0.5h@950°C+16'@790°C+water quenching. The black areas represent untransformed regions at the end of the isothermal treatment. After water quenching, the remaining austenite in these regions transform to different morphologies (possibly Windmastätten ferrite and "bainitic" ferrite). Electrochemical etching. Solution 60%HNO_3 at 293 K.*

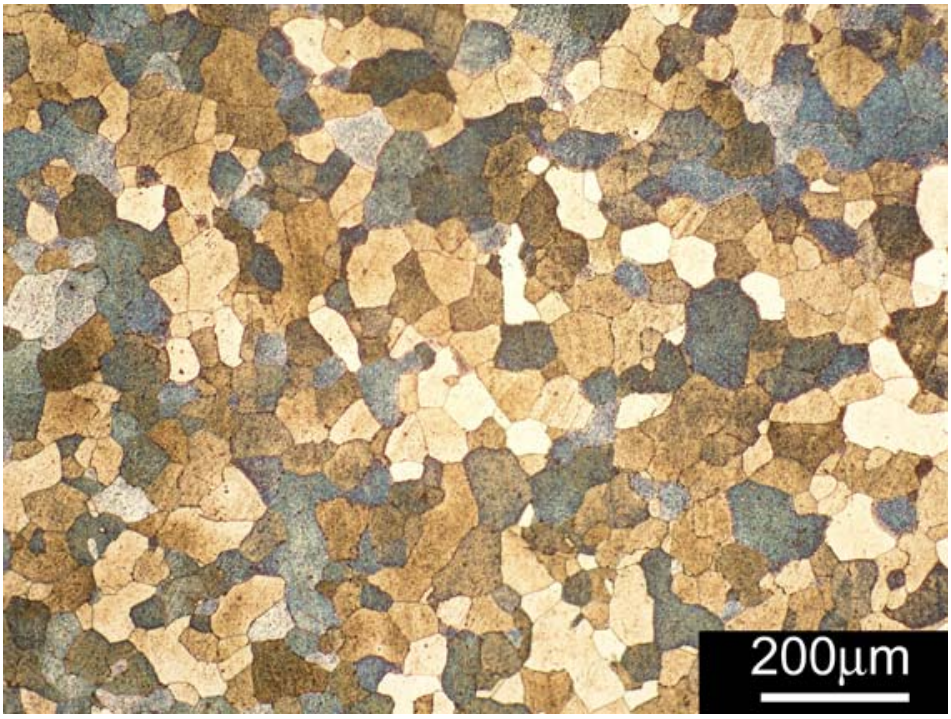

Figure 3. 16: *Final microstructure of the ferritic alloy (0.5h@980°C+24h@790°C). As observed in the micrograph the microstructure consists only of equiaxed ferrite.*

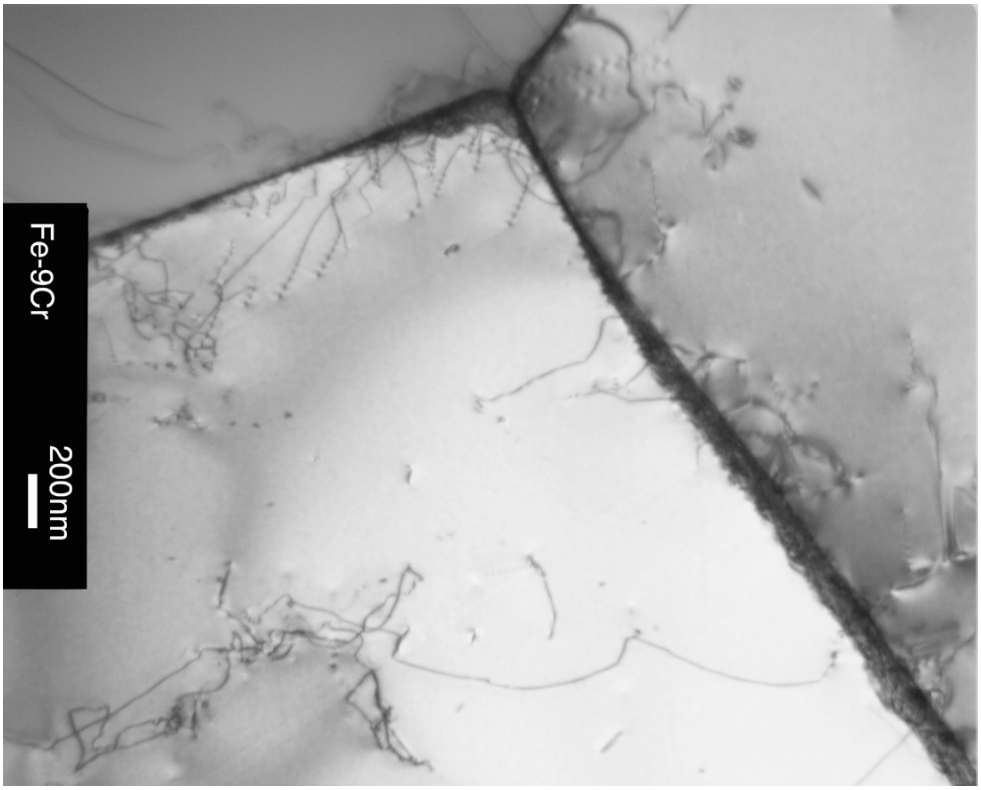

Figure 3. 17: *TEM micrograph of the Fe-9wt%Cr alloy in the final state. As expected, the microstructure has a very low dislocation density.*

References

[3.1] "ASTM Standards methods for Estimating the Average Grain Size of Metals (E112-96) 2002"; Annual Book of ASTM Standards, Volume 03.01, American Society for Testing and Materials, Philadelphia, 2002.

[3.2] Vander Voort, G. F., "Grain Size Measurement", Practical Application of Quantitative Metallography, ASTM STP 839, J.L. McCall and J. H. Steele, Eds. American Society for Testing of Metals, Philadelphia, 1984, pp. 85-131.

[3.3] Hilliard J.E. and Cahn J.W., "An evaluation of Procedures in Quantitative Metallography for Volume-Fraction Analysis", Transactions of the Metallurgical Society of AIME, vol. 221, April 1961, pp. 344-352.

[3.4] E. Underwood, "Quantitative Stereology", Addison-Wesley Inc., 1970.

[3.5] R.L.Klueh and D.R.Harries,"High-Chromium Ferritic and Martensitic Steels for Nuclear Applications ", Monograph 3, D.S.Gelles, R.K. Nanstad, A.S. Kumer, E.A.Little Eds., American Society for Testing and Materials, Philadelphia, 1996.

[3.6] Yaquel, H.L., Acta Crystallogr., Sec. B: Structural Science, 43, 1987, pp. 230.

[3.7] Hilliard J.E. and Cahn J.W., "An evaluation of Procedures in Quantitative Metallography for Volume-Fraction Analysis", Transactions of the Metallurgical Society of AIME, vol. 221, April 1961, pp. 344-352.

[3.8] F. B. Pickering, "Historical Development and Microstructure of High Chromium Ferritic Steels for High Temperature Applications", Microstructural Development and Stability in High Chromium Ferritic Power Plant Steels, A.Strang and D.Gooch Eds., The Institute of Materials, 1997, pp. 1-29.

[3.9] S. Morito, H. Tanaka, R. Konishi, "The Morphology and Cristallography of Lath Martensite in Fe-C Alloys", Acta Materialia 51, (2003), pp.1789-99.

[3.10] P. M. Kelly, "Cristallography of Lath Martensite in Steels", Metallurgical transactions, JIM, Vol. 33, No.3 (1992), pp.235-42.

[3.11] A. Dronhofer, J. Pesicka, A. Dlouhy, G. Eggeler, " On the Nature of Internal Interfaces in Tempered Martensitic Ferritic Steels", Z. Metallkd. 94, (2003),5, pp.511-20.

[3.12] J.P. Naylor, "The influence of the Lath Morphology on the Yield Stress and Transition Temperatures of Martensitic-Bainitic Steels", Metallurgical Transactions A, Vol.10A, July 1979, pp. 861-73.

[3.13] B.P.J. Sandvik, C.M: Wayman, "Cristallography and Substructure of Lath Martensite Formed in Carbon Steels", Metallography 16, 1983, pp.199-227.

[3.14] P.M. Kelly, A. Jostsons and R.G. Blake, "The Orientation Relationship Between Lath Martensite and Austenite in Low Carbon Steels", Acta Metall. Mater., 38, (1990), pp.1075.

[3.15] P.J.Ennis, A.Zielinska-Lipiec, Czyrska-Filemonowicz, "Influence of Heat Treatment on Microstructural Parameters and Mechanical Properties of P92 Steel", Materials Science and Technology, Vol. 16, October 2000, pp.1226-32.

[3.16] R.Schäublin, P. Spätig and M.Victoria: "Microstructure Assessment of the Low Activation Ferritic/Martensitic Steel F82H", J.of Nuclear Materials 258-263, 1998, pp.1178-82.

[3.17] A.Czyrska-Filemonowicz, P.j.Ennis, A.Zielinska-Lipiec, "High Chromium Creep Resistant Steels For Modern Power Plants Applications", in "Metallurgy on the Turn of the 20th Century", K. Swiatkowski Ed., Committee of Metallurgy of the Polish Academy of Sciences, 2002, pp.193-218.

[3.18] K.J.Irvine, F.B.Pickering, "The Physical Metallurgy of 12% Chromium Steels", J. of the Iron and Steel Institute, August 1960, pp.386-405.

[3.19] H.E. Hofmans, “Tensile and Impact Properties of EUROFER 97 Plate and Bar”, 20023/00.38153/P, NGR, Petten, 2000.

[3.20] J.V.Bee and R.W.K. Honeycombe, “The Isothermal Decomposition of Austenite in a High Purity Iron-Chromium Binary Alloy”, Metallurgical Transactions A, Vol.9A, April 1978, pp. 587-593.

[3.21] P. Fernandez, A.M. Lancha, J. Lapena, M. Hernandez-Mayoral,”Metallurgical Characterization of the reduced Activation Ferritic/Martensitic Steel EUROFER 97 on the As-received Condition”, Fusion Engineering and Design, 58-59, (2001), pp. 787-92.

[3.22] H.K.D.H. Bhadeshia, “Worked Examples in the Geometry of Crystals”, 2nd Edition, The Institute of Metals, 2001.

[3.23] A.R.Marder, G.Krauss, “The Effect of the Morphology on the Strength of the Lath Martensite”, in “Proceedings of the Second International Conference on the Strength of Metals and Alloys”, Vol III, 1970, pp.822-23.

[3.24] J.Pesicka, R. Kuzel, A. Dronhofer, G.Eggeler, “The Evolution of Dislocation Density During Heat Treatment and Creep of Tempered Martensite Ferritic Steels”, Acta Materialia 51, 2003, pp.4847-62.

[3.25] B.P.J. Sandvik, C.M: Wayman,”Characteristic of Lath Martensite:Part I. Crystallographic and Substructural Features”, Metallurgical Transactions A, Vol.14A, May 1983, pp.809-34.

[3.26] E.A.Wilson, “$\gamma \rightarrow \alpha$ Transformation in Fe, Fe-Ni and Fe-Cr Alloys”, Metal Science, Vol.18, October 1984, pp.471-84.

[3.27] A. Gilbert, W.S. Owen, Diffusionless transformations in Iron-Nickel, Iron-Chromium and Iron-Silicon Alloys”, Acta Metallurgica, Vol.10, January 1962, pp.45-54.

[3.28] J,S. Pascover and S.V. Radcliffe, “Athermal Transformations in the Iron-Chromium System”, Trans. Met. Soc. Of AIME, Vol. 242, April 1968, pp.675-682.

[3.29] H.K.D:H. Bhadeshia, “Diffusional Formation of Ferrite in Iron and Its Alloys”, Progress in materials Science, Vol.29, 1985, pp.321-86.

[3.30] ASM Specialty Handbook, Stainless Steel, J.Davis, Editor, 1995.

Chapter 4

Tensile properties and constitutive modeling of the Eurofer97 steel.

4. 1. Introduction

In this chapter, we present the results of the study of the tensile properties of the Eurofer97 and of the Fe-9wt%Cr model alloy. The effects of the strain rate and temperature on the mechanical response of both alloys are studied in details. The differences in the observed evolution of the strain hardening are discussed on the basis of the microstructural features of each alloy.

The observed mechanical behavior is rationalized based upon a simple microstructural model characterized by two competitive mechanisms of storage and annihilation of dislocations. This model explains the evolution of the strain hardening in these alloys at temperatures larger than 0.2 T_h (the homologous temperature). Despite its level of simplification, the model accounts for the experimental results in a consistent way.

It is well known that at temperatures smaller than 0.2 T_h, the mechanical behavior of BCC metals and alloys is strongly temperature dependent due to the effect of the Peierls friction of the lattice. Modifications of the high-temperature model are introduced to account for the high lattice friction acting on screw dislocations segments at low temperatures. The modified model successfully describes the observed mechanical response of Eurofer97 at low temperatures.

4. 2. Tensile behavior of the Eurofer97 and Fe-9wt%Cr ferritic model alloy

4. 2. 1. Experimental procedure.

Tensile DIN specimens were machined as 3 mm in diameter and 18 mm in calibrated length. Tensile tests were carried out with an electro-mechanical Schenck testing machine at several temperatures ranging from 473 K down to 77 K. The specimen temperature was controlled with a thermocouple attached to surface of the specimen with a precision of ± 0.5 K. The tests were performed at different constant machine crosshead displacement velocity, ranging from 0.1 mm/min (this corresponds to a nominal strain rate of $9.25 \cdot 10^{-5} s^{-1}$) up to 100 mm/min (nominal strain rate of $9.25 \cdot 10^{-2} s^{-1}$).
At room temperature, the deformation of the specimen was measured with a clip gage attached to it. In all the other cases, the deformation level was assessed indirectly with a LVDT in contact with the crosshead of the testing machine. In this case, the results were compliance–corrected afterwards. This procedure consists in removing from the LVDT signal the elastic component of the displacement arising from the deformation of the load train and testing machine. The validity and accuracy of the compliance correction were checked at room temperature by comparing the data obtained with the clip gage with the compliance corrected data. Excellent agreement was observed among the curves.
The true stress-true strain curves $(\sigma - \varepsilon)$ were calculated from the engineering stress (S) and engineering strain (e) as follows:

Eq. 4. 1 $$\sigma = S \cdot (1 + e)$$

and

Eq. 4. 2 $$\varepsilon = \ln(1 + e)$$

Since Eq. 4. 1 and Eq. 4. 2 are deduced assuming homogeneous plastic deformation, the equations are only valid up to the onset of the plastic instability (necking), defined as the elongation at which the *maximum load* on the specimen is attained.
The plastic component of the true strain (ε_p) has been derived from the $\sigma - \varepsilon$ curves as follows. Assuming that the total strain can be expressed as the addition of a plastic strain component and an elastic component:

Eq. 4. 3 $$\varepsilon = \varepsilon_e + \varepsilon_p$$

The plastic strain ε_p is then defined as:

Eq. 4. 4 $$\varepsilon_p = \varepsilon - \frac{\sigma}{E(T)}$$

where $E(T)$ is the Young modulus at the temperature considered. The plastic strain hardening θ_p is then defined as:

Eq. 4. 5
$$\theta_p = \frac{\theta}{1-\frac{\theta}{E}} = \left.\frac{\partial\sigma}{\partial\varepsilon_p}\right|_{\varepsilon,\dot{T}=cte}$$

4. 2. 2. Eurofer 97. Results.

Figure 4. 1 shows the Eurofer97 tensile curves obtained at different temperatures. As expected, the temperature has a very strong influence in the tensile properties of this material, consistent with the observed behavior of others BCC metals and alloys. The first point to be discussed concerns the dependence of the yield stress $\sigma_{0.2}$ with T. Figure 4. 2 shows $\sigma_{0.2}$ as obtained for two slightly different nominal strain rates, namely $9.25\cdot10^{-5}s^{-1}$and $5\cdot10^{-4}s^{-1}$. Two different stages can be clearly observed in the figure. The first one, at low temperatures (T<200 K) is characterized by a strong dependence of $\sigma_{0.2}$ with T, where $\sigma_{0.2}$ increases sharply when decreasing T. On the contrary, the second stage (T>200 K) features a much weaker dependence of $\sigma_{0.2}$ with T. Such $\sigma_{0.2}$ (T) response, typical of the BCC metals and alloys, is explained with the following arguments. In the low temperature region, the strong dependence of $\sigma_{0.2}$ on temperature is related to the Peierls lattice friction on the screw dislocation segments. A mechanism based on the formation of double kinks plays a fundamental role in the process of overcoming the glide resistance due to lattice friction. This mechanism is thermally activated, resulting in the observed strong temperature and strain rate dependence. The effect of the lattice friction on the flow stress is reduced progressively by increasing the temperature, until finally, above about 200-220 K, $\sigma_{0.2}$ becomes weakly dependent on T, decreasing almost linearly with further increase of the temperature.

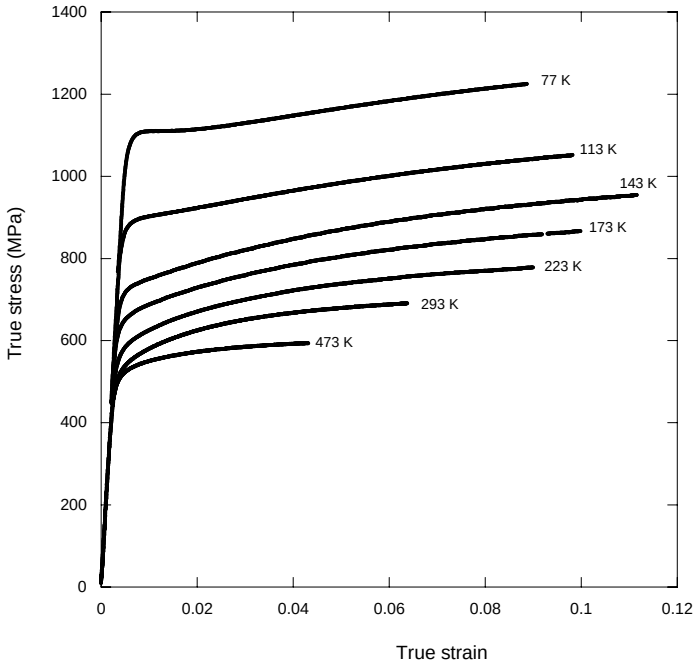

Figure 4. 1: *Effect of the temperature on the tensile properties of the Eurofer97 steel deformed at a nominal strain rate of* $9.25\cdot10^{-5}s^{-1}$.

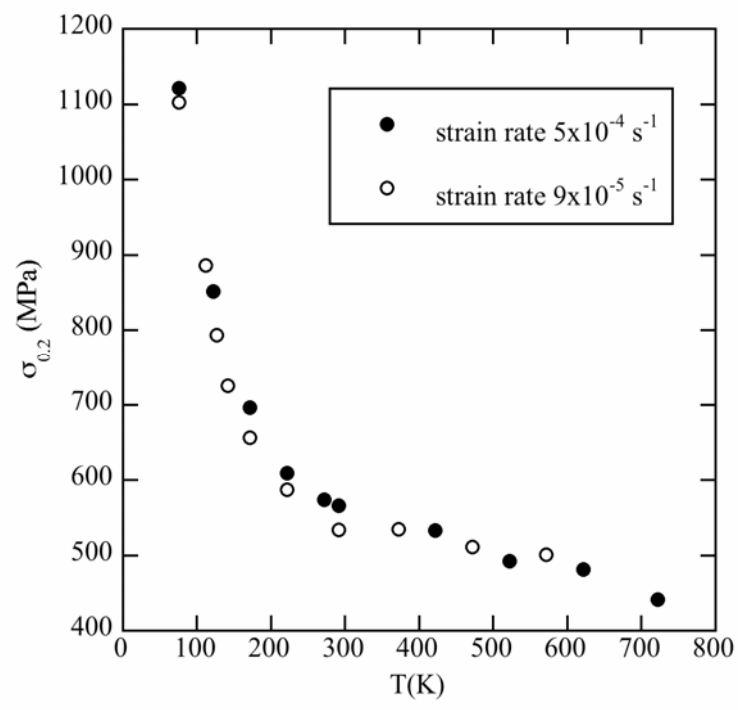

Figure 4. 2: $\sigma_{0.2}$*versus temperature for two different strain rates, Eurofer97.*

In this stage, the temperature dependence observed stems from several factors, mainly the variation of the elastic constants with T as well as from the existence of different weakly thermally-activated mechanisms contributing to the dislocation glide resistance (i.e. dislocation-dislocation intersections).

It is important to stress that at high temperatures (T>600 K), changes in $\sigma_{0.2}$ due to the evolution of the tempered martensitic microstructure, cannot be ruled out as an extra source of $\sigma_{0.2}$ variation with T. This fact introduces new difficulties in the interpretation of the $\sigma_{0.2}(T)$.data. Indeed, microhardness studies on Eurofer 97 showed that after annealing the tempered microstructure during 1h at different temperatures (T> 650 K), the hardness level was clearly reduced when compared to the as-received state [4.20]. This change in the hardness certainly indicates the existence of a microstructural evolution during the annealing process.

Figure 4. 3 shows the evolution of $\sigma_{0.2}$ normalized with the shear modulus $\mu(T)$ plotted as a function of the homologous temperature T_h (the dependence on the temperature of the shear modulus for these types of steels has been taken from [4.9]). As it can be observed, the normalized yield stress starts to increase sharply for $T_h < 0.16$. On the contrary, for $T_h \geq 0.16$, there is almost no variation on the normalized $\sigma_{0.2}$ with further increase of T_h. Based on this observation, it can be concluded that the reduction of $\sigma_{0.2}$ due to increases of T over 220 K is mostly due to the evolution of the shear modulus with $\mu(T)$. Therefore, this region is commonly identified as an *athermal* region, even though, as it was pointed out previously, several weak thermally activated mechanisms are expected to influence the rate of plastic deformation at a given stress level.

The temperature is also expected to strongly influence the post-yield behavior. Figure 4. 4, shows the plastic stress ($\sigma_p = \sigma - \sigma_{0.2}$) plotted as a function of the plastic strain (ε_p) for

different temperatures. Detailed analysis of Figure 4. 4 allows identifying, in all cases, an initial stage at very low plastic strain levels, where the plastic strain hardening θ_p seems to be relatively independent of temperature. This observation is somehow consistent with the main features of Stage II in single crystals (athermal hardening), and it has been suggested that this feature of Stage II exists in the (polycrystal) material plastic behavior at very low plastic strain levels. However, this "athermal" behavior at low plastic strain levels is more likely to be related to the elastic-to-plastic transition phenomenon, taking place at very low levels of "macroscopic" plastic deformation.

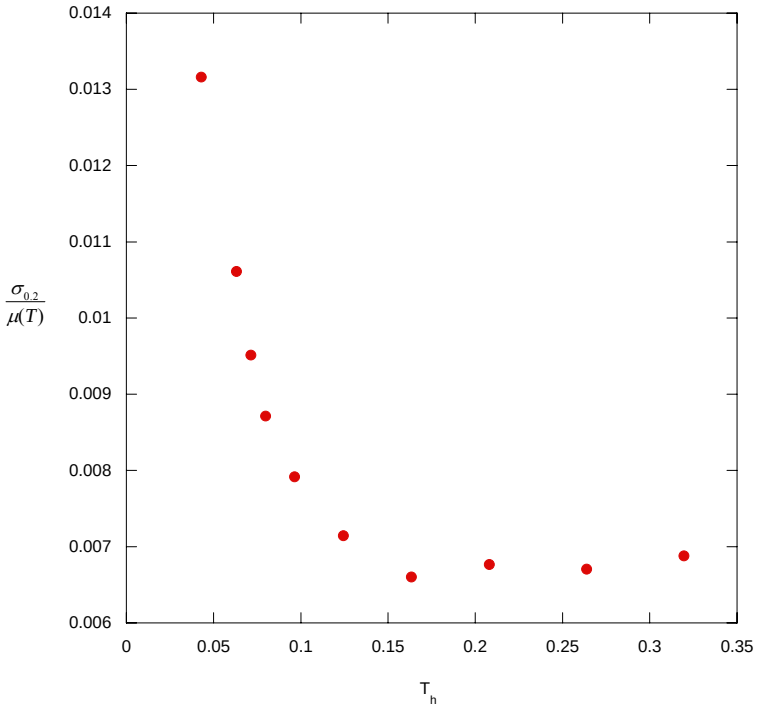

Figure 4. 3: *Plot of $\sigma_{0.2}$ normalized by the shear modulus $\mu(T)$*

The effect of the temperature on the post yield behavior becomes more pronounced at higher plastic strain levels. At high temperatures (approximately $T \geq 223$ K), θ_p decreases quite fast when the plastic deformation level increases. In consequence, the uniform deformation region is very limited, being $\varepsilon_p \approx 0.04$ for 473 K and increases steadily up to $\varepsilon_p \approx 0.09$ for 223 K (note that the limit for the uniform deformation region is approximately given by the Considère criterion, where $\sigma \approx \theta$ at the beginning of the plastic instability). The effect of the friction lattice can be disregarded at these temperatures ($T \geq 223$ K , see Figure 4. 2). Therefore, the effect of the low mobility of the screw segments on plastic strain hardening is not considered to play a fundamental role in the macroscopic response at these temperatures
Comparing the previous high T behavior with the response at lower T, important differences are observed in the evolution of θ_p with plastic deformation when the temperature is decreased down to about 173 K. Indeed, the decreasing rate of θ_p with plastic strain is smaller than in the previous case, which can be associated to the influence of the temperature on the cross slip probability. Cross slip is a thermally activated phenomenon and it plays a fundamental role in the dynamical recovery processes. By decreasing even further the temperature ($T \leq 143$ K), new changes arise in the evolution of θ_p with the plastic strain.

It is interesting to focus our attention on the curve corresponding to 77 K in Figure 4. 4. It is observed that at low plastic strain levels, there exists a region where the deformation proceeds at almost constant stress. The analysis of the curves at higher temperatures indicates that the phenomenon tends to disappear when increasing the temperature; despite the fact that it can be still identified in the tensile curves at 113 K and 143 K. Unfortunately, there are no previous works available reporting or discussing this phenomenon in Fe and Fe-based alloys or in other BCC materials.

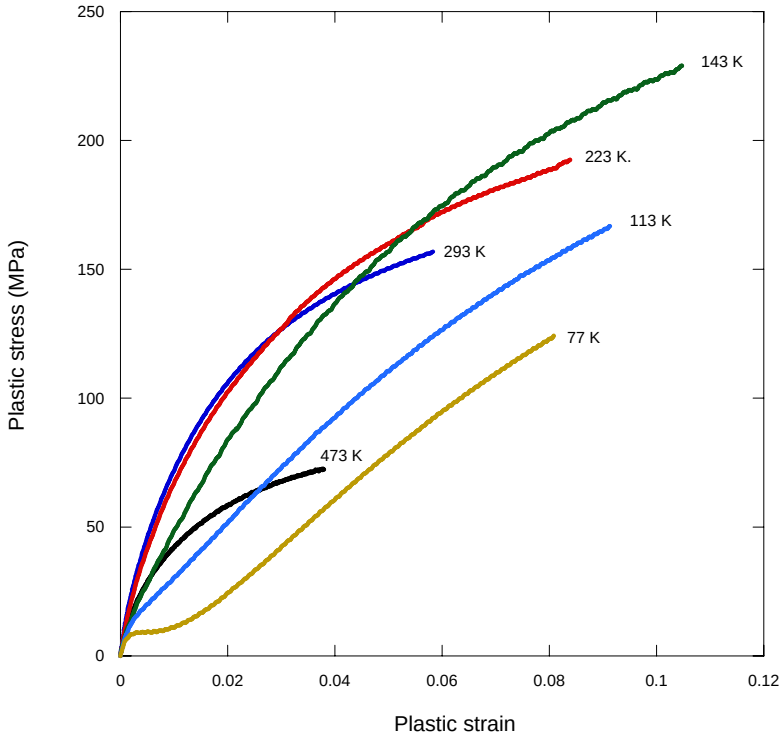

Figure 4. 4: *Plastic stress ($\sigma - \sigma_{0.2}$) as a function of the plastic strain for different temperatures from 77 K up to 473 K.*

However, further experiments carried out with ferritic alloys (discussed next) and different martensitic model alloys, indicated that the phenomenon may be a general feature of iron and its alloys [4.19].

Such behavior may be associated with a mechanism of plastic deformation involving avalanches of dislocations with screw character. This explanation is somehow sustained by the fact that the phenomenon is only observed at very low temperatures where the effect of the friction lattice on the mobility of the screw segments is very strong. By increasing plastic deformation, the $\sigma_p - \varepsilon_p$ curves tend to behave "normally", i.e. they have a positive strain hardening.

The effect of the strain rate ($\dot{\varepsilon}$) on the tensile behavior of Eurofer 97 has also been studied.

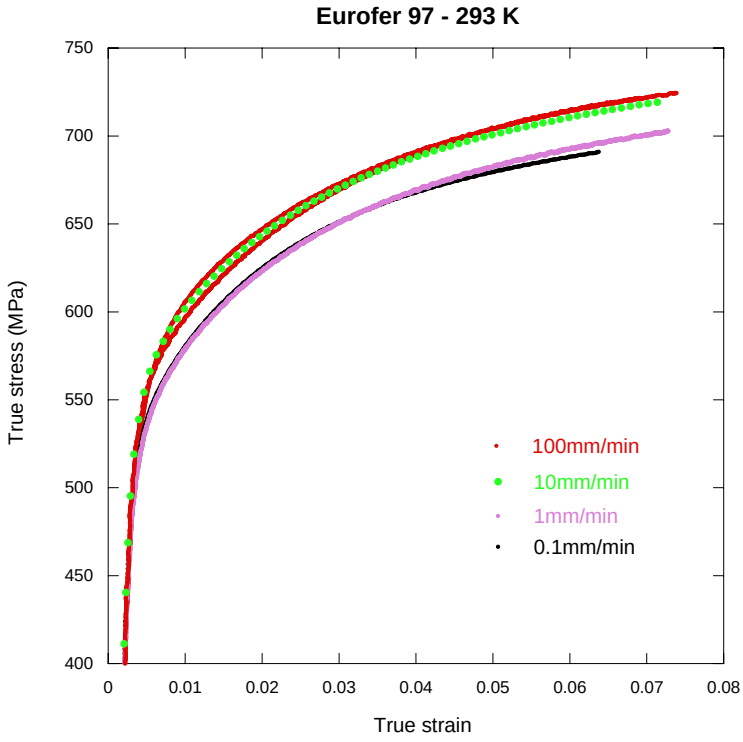

Figure 4. 5: *Effect of the strain rate on the Eurofer97 at 293 K. The machine crosshead velocity is indicated in the figure (0.1mm/min=* $9.25 \cdot 10^{-5} s^{-1}$*).*

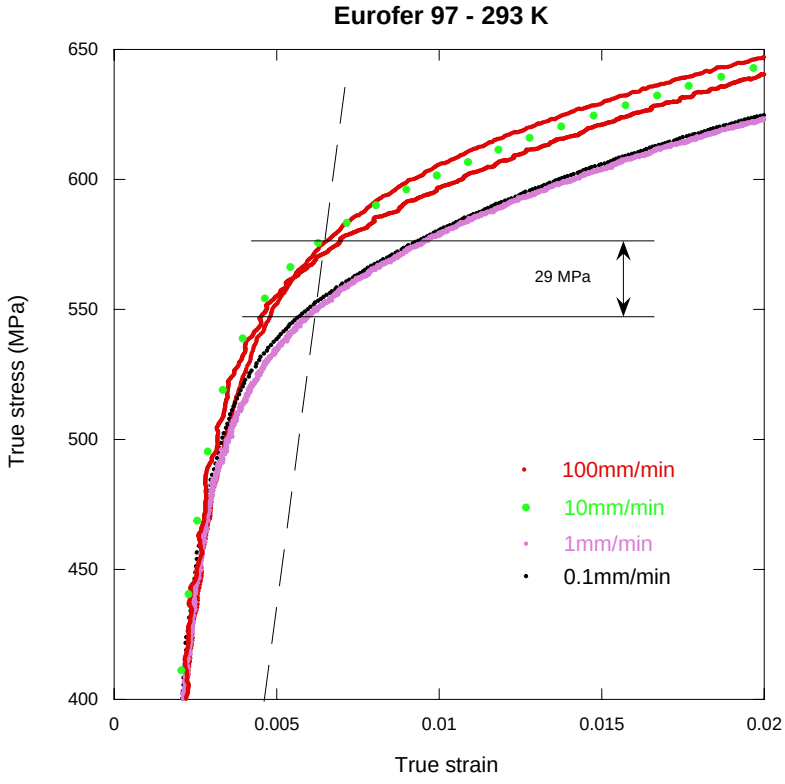

Figure 4. 6: *Effect of the strain rate on the* $\sigma_{0.2}$ *for the Eurofer 97 at 293 K. An increase of three orders of magnitude in the strain rate raises* $\sigma_{0.2}$ *in 29MPa approximately.*

Figure 4. 5 shows different tensile curves obtained at several strain rates at 293 K. As it can be seen in the plot, a change in three orders of magnitude in the strain rate does not produce important changes in the tensile behavior. Overall, the flow curve increases by about 30 MPa for three orders of magnitude change in $\dot{\varepsilon}$. Unfortunately, the effect of $\dot{\varepsilon}$ cannot be studied in detail at temperatures higher than about 220 K for the reason discussed hereafter. The effect of $\dot{\varepsilon}$ on the flow stress is studied under the assumption of "constant structure". Therefore, the effect of $\dot{\varepsilon}$ is typically assessed at very low levels of plastic deformation, i.e. by considering $\sigma_{0.2}(\dot{\varepsilon})$.

However, in the general case of materials having low strain rate sensitivity, the variation in $\sigma_{0.2}$ as a result of a change of one order of magnitude in $\dot{\varepsilon}$ is of the same magnitude as the natural scatter in the measured $\sigma_{0.2}$ values. This observation is generally valid for $T > 223K$ in the case of iron and its alloys.

Plots of the plastic strain hardening as a function of the plastic stress can be very useful in the study of the constitutive behavior of metals and alloys. Despite the intrinsic difficulties associated with the mathematical differentiation of experimental data, θ_p–σ_p plots can reveal features of the plastic phenomena that are not evident on the true stress- true strain curves. At the same time, this type of representation is perfectly suited for studies on the strain hardening behavior.

A θ_p–σ_p plot is presented in Figure 4. 7 for the case of the Eurofer 97 ($\dot{\varepsilon} = 9.25 \cdot 10^{-5} s^{-1}$ at 293 K, 173 K and 77 K).

The effect of the temperature on the plastic strain hardening is clearly revealed on the plot. The high temperature behavior (T >223 K) is represented on the curve corresponding to 293 K, where θ_p decreases smoothly from very high values typical of the elastic to plastic transition, down to low θ_p values near plastic instability. This smooth transition from high to low θ_p values when the stress level is increased can be considered as a typical feature of the evolution of θ_p with the flow stress at high temperatures.

Considering the curve at 173 K, the θ_p - σ_p plot is now composed of two different regions. The first one is characterized by a fast initial decrease of θ_p when increasing σ_p, similar to what has been observed in the high temperature case at low stresses. Next, a second region is identified, where the rate of change of θ_p with the plastic stress is strongly reduced in comparison to the first region. There exists a clear transition between these two regions, located at a stress level $\sigma_p \approx 25MPa$. In the second region, the changing rate of θ_p with σ_p is also lower than that observed on the curve illustrating the high temperature case (293 K), revealing an important effect of the temperature on θ_p. In Section 4.3, this dependence on T will be explained based on an effect of the temperature on the dynamic recovery processes.

The evolution of the θ_p - σ_p curves suggests that a saturation value for θ_p will be finally attained at high deformation levels. However, based on the analysis of the data, it is certainly impossible to predict whether this value will be a finite quantity (as expected for the case of Stage IV hardening) or it will tend to zero, consistent with the attainment of a saturation stress in the stress-strain plot.

The last case presented in Figure 4. 7 corresponds to 77 K. This curve reveals new features in the evolution of θ_p. Initially, θ_p decreases sharply when increasing σ_p, as observed in the two previous cases, with the difference that this stage ends at $\theta_p \approx 0$. Note that this is

consistent with the "plateau" in the 77 K tensile curve, Figure 4. 4. The plateau in the stress-strain plot is represented by a single point in the θ_p-σ_p curve. Once this stage ends, θ_p increases when increasing the σ_p level until eventually, a maximum in the curve is reached. Beyond this point, θ_p decreases almost linearly with σ_p. The rate of change of θ_p with σ_p in this region is smaller than in all the previous cases.

In summary, at low temperatures, the θ_p-σ_p curves for the Eurofer97 steel display two different regions. The first one is associated with the elastic-to-plastic transition and is completely athermal. However, the particular characteristics of the transition between the first and the second region are strongly temperature-dependent. It has been pointed out previously that the behavior observed in the curve corresponding to 77 K at low stresses (low plastic strain levels) could be associated with avalanches of screw dislocations. The problem has not been investigated in detail and as a consequence, this part of the hardening curves will not be further discussed. Finally, during the second region of the hardening curves, θ_p decreases monotonously with increasing σ_p for all the temperatures. The relation between these two parameters tends to be linear when decreasing the temperature. The rate of change of θ_p with σ_p strongly depends on the temperature, decreasing when decreasing T.

In Section 4.3, we introduce a model for the plastic behavior at high and low temperatures. The features presented previously will be discussed, and rationalized in terms of two competitive processes of storage and annihilation of dislocations. In the case of low temperatures, we will only focus our attention on the modeling of the second stage of the θ_p-σ_p curve.

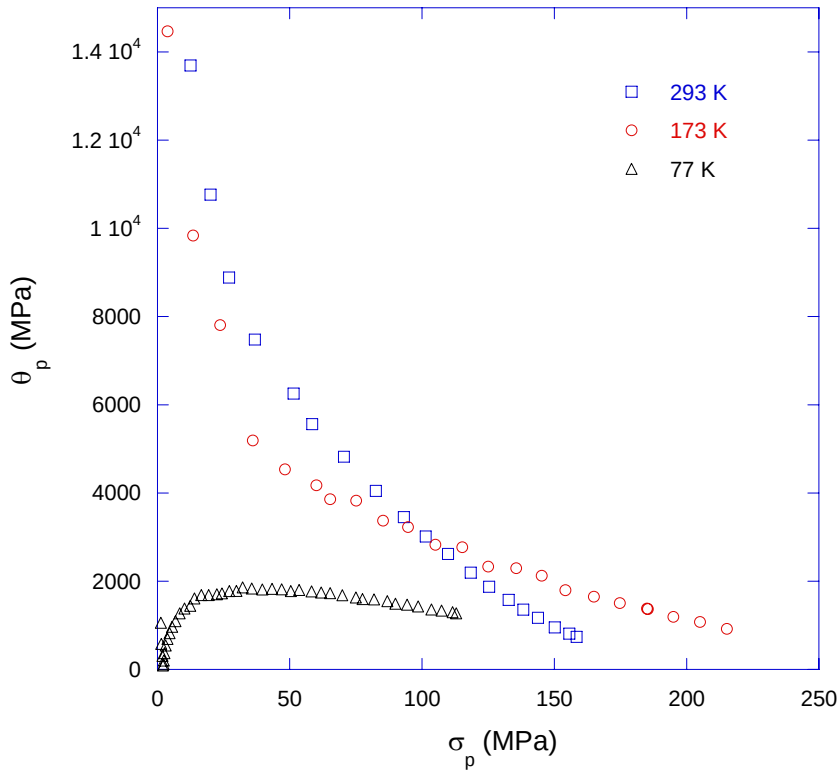

Figure 4. 7: *Evolution of the plastic strain hardening as a function of the plastic stress for the case of three different temperatures. Eurofer97 steel.*

4. 2. 3. Fe-9wt% Cr model alloy. Experimental results

In this section, we present the results related to the tensile behavior of the ferritic Fe-9wt%Cr model alloy. The main results are shown in Figure 4. 8 for temperatures ranging from 473 K down to 103 K. The evolution of the $\sigma_{0.2}$ with T is consistent with what has been observed previously for Eurofer97 steel, i.e. by decreasing the temperature below 220 K, a fast increase in $\sigma_{0.2}$ is observed. As discussed, this is due to the effect of the high lattice friction on the screw segments. The overall dependence of $\sigma_{0.2}$ with T is presented in Figure 4. 9, where $\sigma_{0.2}$ has been normalized with the shear modulus. Consistent with the behavior presented in Figure 4. 3 for the Eurofer97 steel, the beginning of the regime dominated by the lattice friction phenomenon starts approximately at $T_h = 0.16$. Above this temperature, the dependence of $\sigma_{0.2}$ with T is almost completely due to the shear modulus dependence on T .

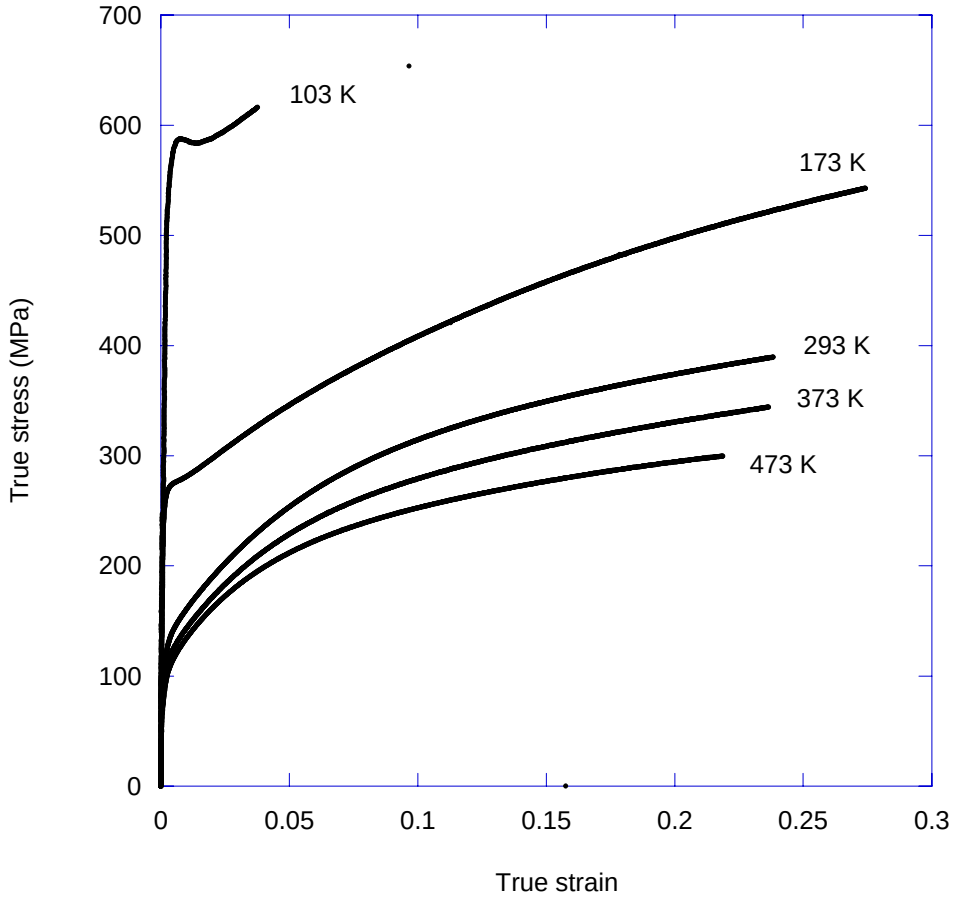

Figure 4. 8:*True stress vs. true strain curves for the Fe-9wt%Cr ferritic alloy at several temperatures.*

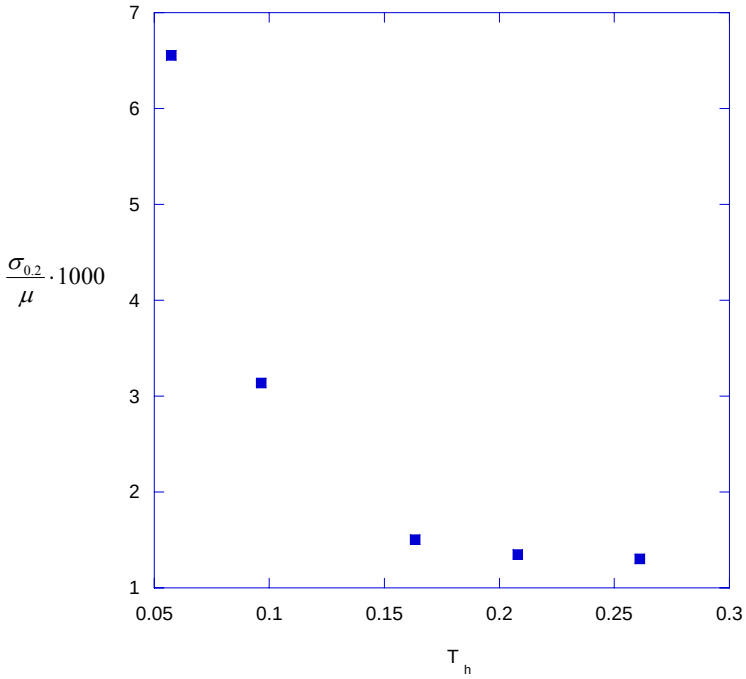

Figure 4. 9: *Evolution of the yield stress as a function of the temperature. curves for the case of the Fe-9wt%Cr ferritic alloy.(strain rate* $= 9.25\cdot 10^{-5} s^{-1}$*).*

The main features of the post-yield behavior of this model alloy can be derived from Figure 4. 8 in combination with Figure 4. 10 and Figure 4. 11. We focus the discussion only on the high temperature results (T >220 K) since the occurrence of brittle fracture at very low levels of plastic deformation impedes the attainment of large deformations at low temperatures (Figure 4. 8). This phenomenon is likely to be related to the existence of relatively big chromium oxide particles in the ferritic matrix (see Chapter 3). As it will be discussed in Chapter 5, the fracture of these particles can initiate microcracks that may become unstable under the influence of remote stresses.

The effect of the temperature on the strain hardening can be assessed from Figure 4. 10 and Figure 4. 11. In this case, three different regions can be identified in the θ_p vs. σ plots. The first region, characterized by a fast decrease of θ_p with σ, is related to the elastic-to-plastic transition. Once the fully plastic conditions have been established, we can identify a second region characterized by a linear relation between θ_p and σ. However, the extension of this second region is strongly temperature dependent, being reduced when increasing T. Finally a third region is identified, where the linearity between θ_p and σ disappears, and the changing rate of change of θ_p with σ strongly decreases. This suggests the attainment of a "saturation" θ_p value, which would be consistent with the existence of a stage IV of strain-hardening at large plastic strains.

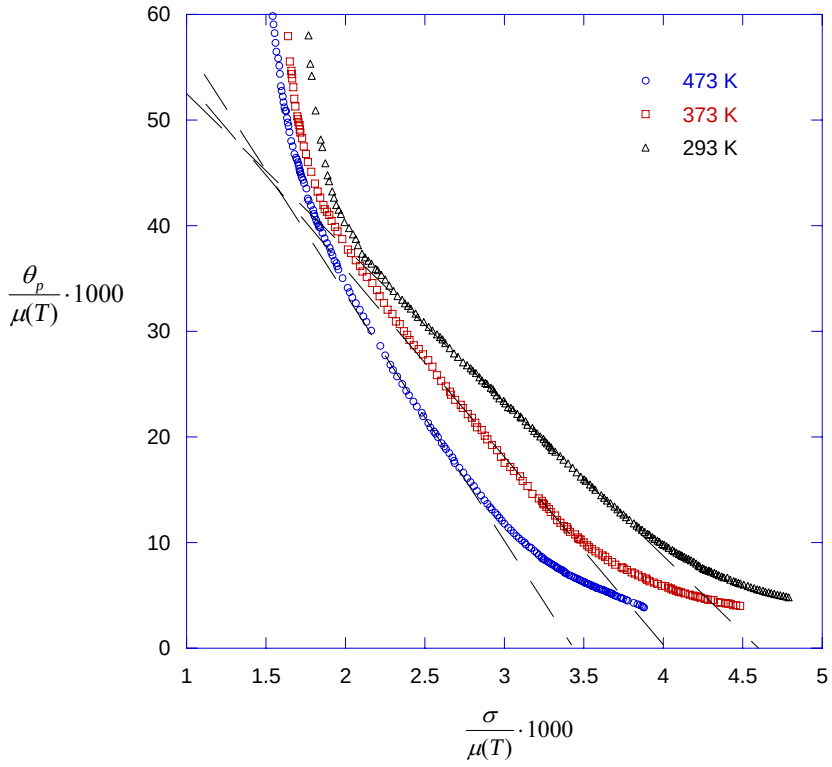

Figure 4. 10: *High temperature behavior of the plastic strain hardening with the stress. The data has been normalized with the shear modulus at each temperature.*

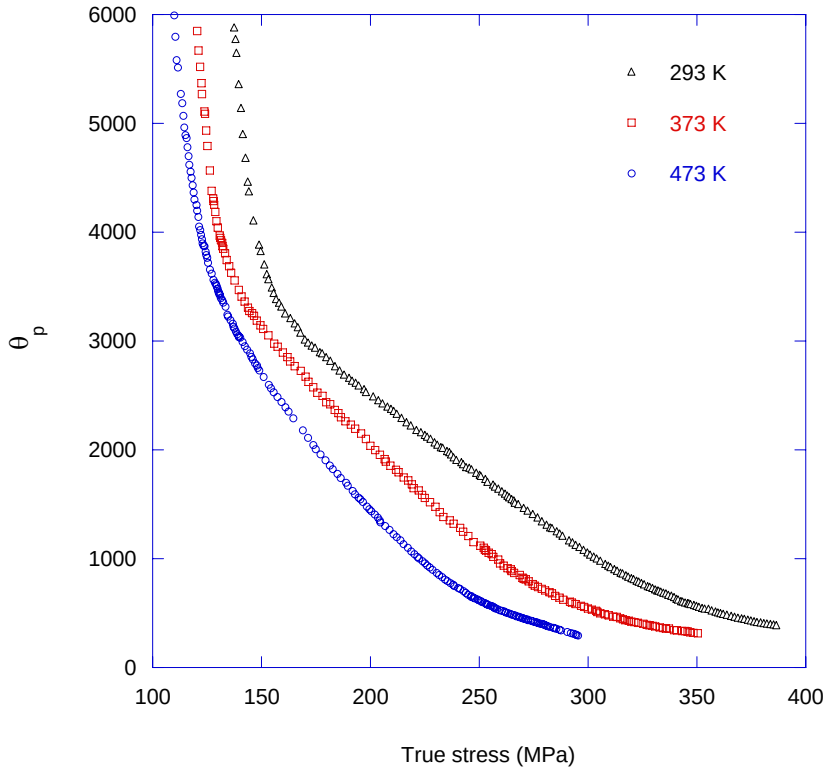

Figure 4. 11: *Plastic strain hardening versus true stress.*

Since this model alloy has a relatively simple microstructure, it may be possible in principle to correlate the different regions of the θ_p vs. σ curves with the main microstructural features responsible for the observed behavior. In this sense, owing to the simplifications introduced by the use of a model alloy, the main microstructural factors expected to play a significant role are the total dislocation density and its correspondening collective behavior. In order to gain insight into this issue, deformed structures were studied by TEM after tensile tests performed up to different strain levels (nominal strain rate of $9.25 \cdot 10^{-5} s^{-1}$) at 293 K. Some of the TEM micrographs images are presented in Figure 4. 12. Recalling Figure 3.17 (Chapter 3), the undeformed microstructure is characterized by equiaxed ferritic grains (80 microns of mean intercept length) having a very low dislocation density. This is somehow reflected in the low $\sigma_{0.2}$ values of the model alloy.

After a relatively small amount of plastic strain of 0.03, the dislocation density strongly increases as compared to the undeformed state. The observed dislocation distribution after a small amount of plastic deformation is not homogeneous. Indeed, some grains have the structures observed in Figure 4. 12 (upper left). The micrograph shows the microstructure corresponding to a flow stress of $\sigma \approx 200MPa$ ($\varepsilon \approx 0.03$). As expected, some dislocation cells in the initial stage of formations can be identified, indicating a strong tendency to the formation of dislocation structures. This fact yields inhomogeneous distribution of dislocations, even at very low levels of plastic strain. However, it is worth noting that other grains display much lower dislocation densities, which suggests that during the early stages of plastic deformation, different grains undergo different levels of plastic strain. This is certainly related to the relative orientation of the grains and the tensile axis.
The main features of the dislocation structure have also been studied in detail at the end of the second strain-hardening region. Two micrographs representing the typical microstructure associated with this region are presented in Figure 4. 12 (upper right and lower left). In this case, the microstructure corresponds to a flow stress of $\sigma \approx 300MPa$ ($\varepsilon \approx 0.07$). Due to the larger level of plastic deformation, all the grains seem to have similar microstructural features. The typical dislocation structure observed consists in equiaxed cells. The dislocation walls consist mainly in dislocations tangles, not very well defined. However, detailed inspection of several TEM specimens showed that there also exist some locations in the investigated TEM samples where the dislocation density is approximately homogeneously distributed (Figure 4. 12 lower left). This type of regions was not observed at lower deformation levels (the case previously discussed). Thus, we conclude that the main microstructural changes associated with the second region in the θ_p vs σ plot are a) an overall increase in the dislocation density, together with b) the development of some regions featuring mostly equiaxed dislocation cells.

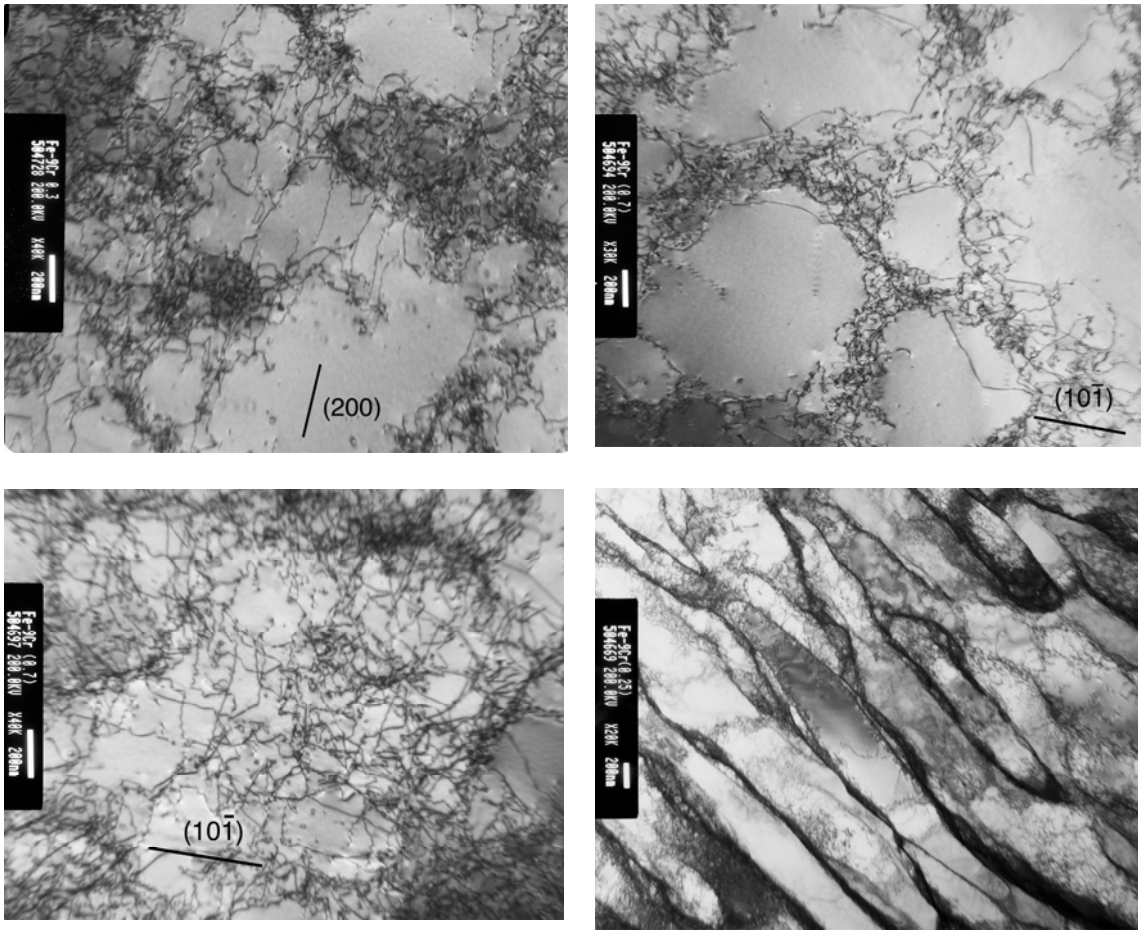

Figure 4. 12: *Deformed microstructure at 293K for the case of the Fe-9wt%Cr model alloy. Upper left:* ε *=0.03; upper right and lower left:* ε *=0.07; lower right* ε *= 0.25*

Finally, we have studied the microstructures corresponding to the last region in the θ_p vs σ plot. It is important to stress that this region actually dominates the tensile response of the model alloy when plotted as stress-strain curves ($\varepsilon > 0.07$ up to $\varepsilon \approx 0.25$). At these relatively large deformation levels, the dislocation structure is characterized by the formation of elongated cells with very clear and compact dislocation walls (Figure 4. 12, lower right). These cells, having typical thicknesses between 200 nm and 400 nm, are essentially different from those reported previously. This type of structure can be correlated with the low θ_p values observed at this stage of the deformation process. It is certainly reasonable to associate the particular features of the elongated dislocation cells (i.e. crystallographic direction of the long axis) to the particular loading path followed during the development of the structure, in our case, uniaxial deformation. In this sense, a sudden change in the deformation conditions (i.e. the direction of the strain) may lead to some complex mechanical response, until eventually the new cellular structure corresponding to the new deformation path is established.

In summary, it has been possible to correlate the post yield behavior represented by θ_p vs σ plot at 293 K with the main microstructural features of the deformed material. The total dislocation density as well as the collective dislocation behavior (cell formation) mediate the

mechanical response of the model alloy studied here. The evolution of the collective behavior seems to depend on temperature. Indeed, since the third region in the θ_p vs σ plots are related to the formation of well defined elongated cells, and considering that the beginning of this third stage occurs at lower strain levels with increasing T, we conclude that there exists a dependence of the rate of the evolution of the collective structures with T, at least in the temperature domain where the effects of the lattice friction are not important.

We have presented the tensile properties of the ferritic model alloy. In this case, it was possible to correlate the evolution of the strain-hardening with the evolution of the microstructure with strain as observed by TEM. On the contrary, in technical alloys as Eurofer97, the evolution of the hardening with plastic deformation is due to a multiplicity of factors. Therefore, it remains an open issue to determine the relevant parameters controlling the observed strain-hardening. In any case, in Figure 4. 13, we compare the θ_p vs σ plots for the Eurofer97 steel and the ferritic model alloy. It can be observed that in the initial stages of plastic deformation ($\varepsilon \approx 0.03$), θ_p of the Eurofer97 is much larger than in that of the ferritic model alloy. However, further increase of the strain level produces a fast and strong reduction on θ_p in the Eurofer97, while the effect on the ferritic model alloy data is quite moderate. Indeed, for $\varepsilon > 0.035$, θ_p is smaller in the Eurofer97 than in the model alloy. Owing to the complexity of the martensitic microstructure, it is difficult to rationalize such differences within the framework of the models that will be presented in the Section 4.3.

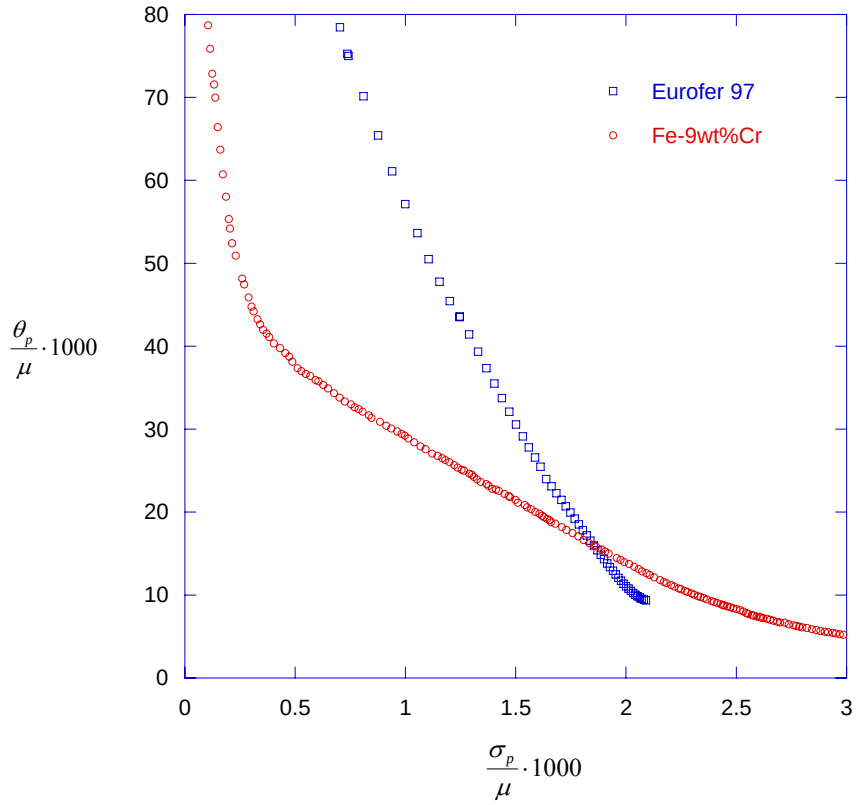

Figure 4. 13: *comparison between Eurofer 97 and the Fe-9wt%Cr model alloy at room temperature (strain rate* $= 9.25\cdot 10^{-5} s^{-1}$*).*

4. 3. Modeling of the constitutive behavior

4. 3. 1. General considerations.

The response of a thermodynamic system to a departure from its equilibrium condition is described by a *constitutive law*, which is a set of equations relating the parameters characterizing the state of the system.
The plastic deformation of metallic materials is quite complex due to the large number of parameters needed for the proper characterization of the "system". In this case, a constitutive law must relate the strain rate $\dot{\varepsilon}_{ij}$ to the stress level σ_{ij}, the temperature T, the rate of change of the stress $\dot{\sigma}_{ij}$ and the metallurgical state of the material, which is mediated mainly by its prior thermo-mechanical history. This is accounted for by several "internal" microstructural parameters ($S_1, S_2, \ldots$). Following Kocks et al. [4.2], the constitutive law may be written as a set of coupled differential equations:

$$
\begin{aligned}
&\dot{\varepsilon}_{ij} = f(\sigma_{ij}, \dot{\sigma}_{ij}, T, S_1, S_2, S_3, ...) \\
&dS_1 = f_1(\sigma_{ij}, \dot{\sigma}_{ij}, T, S_1, S_2, S_3, ...)dt \\
&dS_2 = f_2(\sigma_{ij}, \dot{\sigma}_{ij}, T, S_1, S_2, S_3, ...)dt \\
&dS_3 = f_3(\sigma_{ij}, \dot{\sigma}_{ij}, T, S_1, S_2, S_3, ...)dt \\
&.....
\end{aligned}
\qquad \text{Eqs. 4. 6}
$$

The first equation in Eqs. 4. 6 is a rate equation *at constant structure*, which is generally known as the "kinetic" equation. This expression describes mechanical response of the material in a determined metallurgical state (structure). The other equations describe the evolution of the microstructure along a certain deformation path. Note that the actual value of the internal parameters ($S_1, S_2, \ldots$) defines the metallurgical state of the material. Since the equations describing the evolution of the internal parameters are incremental, at any time in deformation history the effects of prior deformation are fully accounted for.
This type of formulation for the constitutive law emphasizes the fact that the flow stress measured under a certain loading condition depends on the prior deformation history of the material. As discussed by Hart [4.3][4.4], it is in principle possible to summarize the prior deformation history in terms of some measurable properties, in such a way that the mechanical response to a certain loading condition can be predicted without a detailed knowledge of the prior deformation history. Clearly, the "memory" of the material resides in its actual structure, which can be, at least in principle, described by a certain (very large) number of microstructural parameters. One of the main assumptions underlying the development of constitutive laws for metallic materials is that only the evolution of few parameters (typically one or two) are relevant to a certain macroscopic property being studied. In the case of the "one parameter" approach, the internal parameter is associated to the total dislocation density [4.1][4.7][4.8][4.9]. Models based on a "two parameters" approach, obviously

involve the description of a second parameter, which is in general associated with the *mobile* dislocation density [4.10].
It is important to emphasize that the accumulated strain, cannot be used alone as the only parameter governing the evolution of the microstructure during deformation. Indeed, the mechanical state of a material is not uniquely characterized by the accumulated strain (as measured from a certain arbitrary reference state), but depends on the deformation path as well. However, the most popular approaches to the constitutive description of a material are still formulated in terms of an invariant of the strain tensor (the equivalent plastic strain).

4. 3. 2. One parameter model. Modeling of the strain hardening behavior of BCC materials at high temperature.

The most successful one parameter model is based on a simplified phenomenological description of strain-hardening initially proposed by Kocks [4.1], and subsequently developed by Kocks and Mecking [4.7] and later extended by Estrin and Mecking [4.8]. A summary of the model is presented in [4.9]. An extensive review by Kocks and Mecking can be found in [4.11]. As mentioned, the structural parameter of the model is the total dislocation density, ρ, irrespective of the dislocation arrangement. In this case, the constitutive law is written as:

Eqs. 4. 7

$$\dot{\varepsilon}_{ij} = f(\sigma_{ij}, T, \hat{\sigma}),$$
$$d\hat{\sigma} = f_1(\dot{\varepsilon}_p, T, \hat{\sigma}) d\varepsilon_p,$$

where $\hat{\sigma}$ is known as the "mechanical threshold", defined as the flow stress at a certain given reference state, in this case, 0 K (absence of thermal activation). The kinetic equation depends on the type and distribution of obstacles to dislocation glide. Several expressions have been proposed, some of them based on physical arguments. For instance, assuming that there exists only one type of obstacles to dislocation glide, and assuming that the obstacles can be surmounted with the aid of thermal activation, the following expression has been proposed by Kocks, and used in several subsequent works by many others [4.2][4.5][4.6]:

Eq. 4. 8

$$\dot{\varepsilon}_p = \dot{\varepsilon}_0 \exp\left[-\frac{\Delta G_0}{kT} \left(1 - \left(\frac{\sigma}{\hat{\sigma}} \right)^p \right)^q \right]$$

where ΔG_0 is the total energy to overcome the obstacle, σ is the flow stress, p and q values depending of the particular type of obstacle to dislocation glide. $\hat{\sigma}$ is called the "mechanical threshold", and it is interpreted as the flow stress at 0 K (in absence of thermal activation). In the present approach, the mechanical state of the material would be assessed by extracting a sample of the material considered and measuring the flow stress at 0 K. In this way, $\hat{\sigma}$ would be experimentally determined [4.13]. In

several cases pure empirical laws are also postulated for the kinetic equation (see [4.9]).

Eq. 4. 9
$$\dot{\varepsilon}_p = \dot{\varepsilon}_0 \left(\frac{\sigma}{\hat{\sigma}} \right)^m$$

Note that in general, power laws are valid only in a certain interval of stresses, i.e. are not general. It is important to stress that the kinetic equation refers to a fixed obstacle structure, i.e. a constant value for the internal parameter $\hat{\sigma}$.
The next step consists in describing the evolution of the microstructure with plastic deformation:

Eq. 4. 10
$$\frac{d\hat{\sigma}}{d\varepsilon_p} = f_1(\hat{\sigma}, \sigma, T)$$

In the one parameter model, $f_1(\hat{\sigma}, \sigma, T)$ is composed by two terms representing competitive processes of storage and annihilation of dislocations segments via dynamical recovery. In the Kocks model, the mechanical threshold $\hat{\sigma}$ (the flow stress at 0 K) is related to the total dislocation density via the following expression [4.7][4.11]:

Eq. 4. 11
$$\hat{\sigma} = M\alpha\mu b\sqrt{\rho}$$

where M is the Taylor factor, M is a dimensionless constant, μ is the shear modulus and b the magnitude of the Burgers vector. This equation implies that the strength of the material is controlled only by the interaction among dislocations, as for instance, in the case of high purity single crystals. However, in "real" materials, there are other sources to dislocation glide resistance (i.e. grain boundaries). In such a case, we may assume that:

Eq. 4. 12
$$\hat{\sigma} = M\alpha\mu b\sqrt{\rho} + \tilde{\sigma}$$

where $\tilde{\sigma}$ is a certain "internal stress", rate and temperature independent. Note that the original formulation of the one parameter model was developed for FCC materials. In this case, the thermally activated mechanism controlling the kinetics of dislocation glide remains the same for all the temperatures, namely dislocation-dislocation interactions. However, based on the results presented previously, it is clear that in the case of the BCC materials, there exist at least two different temperature domains, where the kinetics of dislocation glide is controlled by different thermally-activated mechanisms in each case. In consequence, two different kinetic laws are expected to describe the mechanical behavior depending on testing temperature. If so, we expect two different expressions for the "mechanical threshold" $\hat{\sigma}$. At "high temperatures" ($T > 220$ K) the present description is appropriate since in this case, the BCC

materials behave the same way as the FCC ones and $\hat{\sigma}$ can be obtained by extrapolation of the "high temperature" $\sigma_{0.2}$ trend back to 0 K. However, the approach will fail at low temperatures due to the fact that Eq. 4. 11 and Eq. 4. 12 are not valid anymore.

Considering that the dislocation density is the microstructural parameter of the model, it is convenient to decompose the flow stress into two components, as indicated in Figure 4. 14. One component is the yield stress $\sigma_{0.2}$ and the second one, σ^{*}_{d-d}, is the contribution arising from the increase in the dislocation density $\Delta\rho(\varepsilon_p)$ due to the plastic strain increment. From the analysis of Figure 4. 14, it follows that the total contribution to the flow stress coming for the dislocation-dislocation interaction, σ_{d-d} is given by:

Eq. 4. 13 $$\sigma_{d-d}(\rho, \dot{\varepsilon}_p) = \sigma^{0}_{d-d}(\rho_0, \dot{\varepsilon}_p) + \sigma^{*}_{d-d}(\Delta\rho(\varepsilon_p), \dot{\varepsilon}_p)$$

where ρ_0 is the initial dislocation density contributing to $\sigma_{0.2}$ and $\Delta\rho(\varepsilon_p)$ is the net increase in ρ at ε_p. The yield stress itself can be further decomposed into several components. In addition to σ^{0}_{d-d}, other components are added, representing for instance the effect of the grain boundaries, carbides and precipitates, solid solution etc. on $\sigma_{0.2}$. All these contributions are considered as *athermal*, and the sum of them is referred to as $\tilde{\sigma}$:

Eq. 4. 14 $$\sigma_{0.2} = \tilde{\sigma} + \sigma^{0}_{d-d}$$

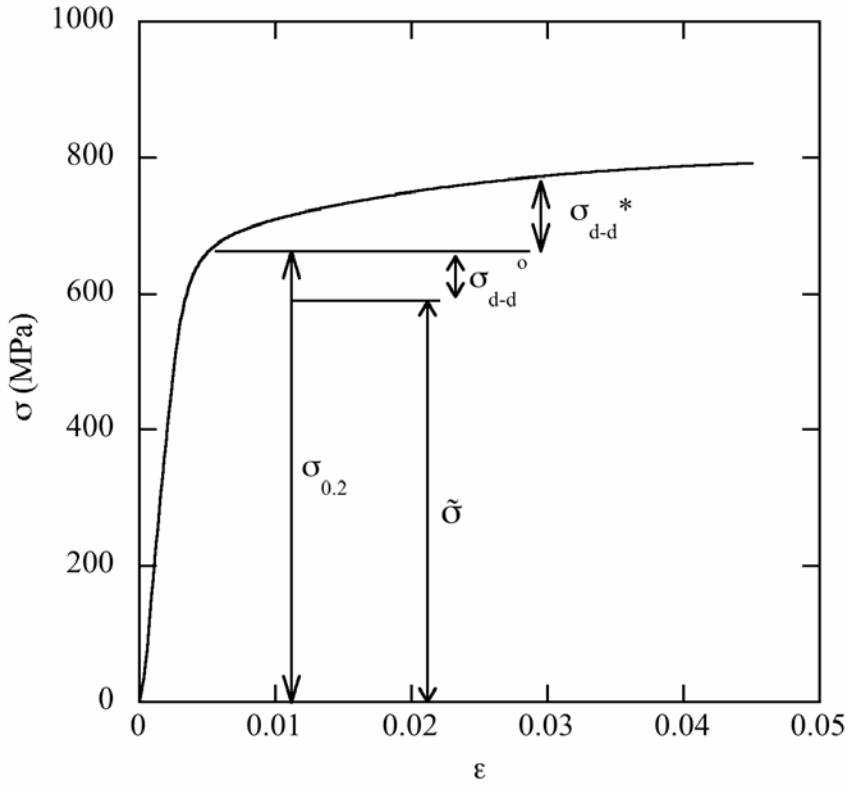

Figure 4. 14: *Schematic decomposition of the flow stress.*

These relationships can be used together with the corresponding kinetic equation, where the flow stress σ is replaced by $\sigma_{d-d} + \tilde{\sigma}$.
Considering Eq. 4. 10, there exist several formulations proposed depending on the main metallurgical features of the material. If the total dislocation density ρ is the microstructural parameter of the model, it follows that the strain-hardening is controlled by the evolution of ρ with the plastic strain, i.e. $\partial\rho/\partial\varepsilon_p$. The evolution of ρ can be modeled by considering two competitive processes [4.1]. The first one is related to storage of dislocations on the lattice (or multiplication) due to the immobilization of dislocations at obstacles. Detailed discussion about the modeling of the storage mechanisms can be found in [4.1][4.9]. Here it is just sufficient to say that the increment in shear strain associated to an increase in dislocation density $d\rho^+$ due to the storage of dislocations that have traveled a characteristic mean distance L (mean free path) is written as follows:

Eq. 4. 15
$$Md\varepsilon_p = bLd\rho^+$$

where M is the Taylor factor. The second mechanism takes into account all the different annihilation processes that may take place during straining (dynamical recovery). In terms of the derivative with respect to the strain ($d\rho^-/d\varepsilon_p$), the annihilation term is assumed to be linear in ρ. Finally, the evolution of the dislocation density with the strain is written as:

Eq. 4. 16
$$\frac{d\rho}{d\varepsilon_p} = \frac{d\rho^+ + d\rho^-}{d\varepsilon_p} = M\left(\frac{1}{bL} - k_2\rho\right)$$

where b is the Burgers vector and k_2, the recovery coefficient, depending on the strain rate and the temperature. This coefficient is modeled using a power law. A detailed discussion of this coefficient can be found in the previously mentioned references:

Eq. 4. 17
$$k_2 = k_0\left(\frac{\dot{\varepsilon}_p}{\dot{\varepsilon}_0^*}\right)^{-1/n}$$

In the case of a coarse-grained single phase material, the mean free path L is assumed to be proportional to $1/\sqrt{\rho}$, this distance being much smaller than the grain size. Eq. 4. 16 is now written as:

Eq. 4. 18
$$\frac{d\rho}{d\varepsilon_p} = M\left(k_1\sqrt{\rho} - k_2\rho\right)$$

Combining Eq. 4. 12 and Eq. 4. 18, we obtain:

Eq. 4. 19
$$\left.\frac{d\hat{\sigma}}{d\varepsilon_p}\right|_{\dot{\varepsilon}_p,T} = \frac{M^2\alpha\mu b}{2}k_1 - \frac{Mk_2}{2}(\sigma - \tilde{\sigma})$$

At a given structure, the relation between $\hat{\sigma}$ and σ is given by the kinetic equation. Considering then Eq. 4. 9, Eq. 4. 13 and in virtue of Eq. 4. 19, we can write:

Eq. 4. 20
$$\theta_p = \left.\frac{d\sigma^*_{d-d}}{d\varepsilon_p}\right|_{\dot{\varepsilon}_p,T} = \left(\frac{\dot{\varepsilon}_p}{\dot{\varepsilon}_0}\right)^{1/m}\frac{M^2\alpha\mu b}{2}k_1 - \frac{Mk_2}{2}\left[(\tilde{\sigma} + \sigma^0_{d-d} + \sigma^*_{d-d}) - \left(\frac{\dot{\varepsilon}_p}{\dot{\varepsilon}_0}\right)^{1/m}\tilde{\sigma}\right]$$

For materials having low strain rate sensitivity ($m >> 1$) the equation above can be simplified as follows:

Eq. 4. 21
$$\theta_p = \left.\frac{d\sigma^*_{d-d}}{d\varepsilon_p}\right|_{\dot{\varepsilon}_p,T} = P - P_2(\sigma^*_{d-d} + \sigma^0_{d-d})$$

where:

Eq.4 .2b
$$P = \frac{M^2\alpha\mu b}{2}k_1$$

and

Eq.4.21c
$$P_2 = \frac{Mk_2}{2}$$

As observed, in the case that the mean free path L is mediated by the dislocation density, the model predicts a linear relationship between θ_p and σ^*_{d-d}. This linear relationship between θ_p and σ^*_{d-d} has been confirmed experimentally for a great numbers of FCC single phase materials and alloys (pure Al, Cu, austenitic stainless steels, etc [4.1][4.7]-[4.9][4.11]). However, as it has been previously discussed in Section 4.2.3, for moderate strain levels, the $\theta_p - \sigma_p$ plots of the Fe-9wt%Cr model alloy show a linear relationship between these two quantities, in agreement with the predictions of the model. As discussed previously, the linear regime disappears because of the formation of elongated cells into the grains. At this stage, the hypotheses on which the model is based upon are not valid any more.
Eq. 4. 21 can be integrated assuming constant strain rate to obtain the stress-strain relationship:

Eq. 4. 22
$$\sigma^*_{d-d} = \frac{\left(P + P_2\sigma^0_{d-d}\right) - \left(P - P_2(\sigma^0_{d-d} - \sigma^*_{d-d(i)}\right)\exp\left[-P_2(\varepsilon_p - \varepsilon_{p(i)})\right]}{P_2}$$

Eq. 4. 22 is known as the Voce equation, which is commonly used to describe the stress-strain behavior of metallic materials.

In the case of a tempered martensitic steel, the initial assumption of a mean free path mediated by the dislocation density does not hold any more. Recalling Chapter 3, the martensitic microstructure is highly complex, characterized by the existence of several types of internal boundaries. Indeed, a prior austenitic grain contains high-angle boundaries (i.e. packet boundaries) as well as low-angle internal interfaces (lath and sub-block boundaries). In the following, we assume that the effective mean displacement distance L of a dislocation, (the effective averaged distance that the dislocation travels before it gets definitely stored into the microstructure) is mainly mediated by high-angle boundaries. The low-angle boundaries between laths of a same variant (<2°) and boundaries between sub-blocks are not necessarily considered as impenetrable obstacles. Therefore, a moving dislocation will be confined inside a sub-block or even a block. Further we assume that, over the limited deformation range investigated (< 5%), the effective mean displacement distance L of a dislocation is constant with deformation. The dislocation density evolution equation can be written now as follows:

Eq. 4. 23
$$\frac{\partial \rho}{\partial \varepsilon_p} = M\left(\frac{1}{b\Lambda} - k_2\rho\right)$$

Combining Eq. 4. 12 and Eq. 4. 23, we obtain:

Eq. 4. 24
$$\left.\frac{d\hat{\sigma}}{d\varepsilon_p}\right|_{\dot{\varepsilon}_p,T} = \frac{M^3(\alpha\mu b)^2}{2(\hat{\sigma}-\tilde{\sigma})}\frac{1}{b\Lambda} - \frac{M}{2}k_2(\hat{\sigma}-\tilde{\sigma})$$

Therefore, with Eq. 4. 9 and Eq. 4. 24 we have:

Eq.4.25
$$\theta_p = \left.\frac{d\sigma^*_{d-d}}{d\varepsilon_p}\right|_{\dot{\varepsilon}_p,T} = \frac{M^3(\alpha\mu b)^2}{2\left[(\sigma^*_{d-d}+\sigma^0_{d-d}+\tilde{\sigma})\left(\frac{\dot{\varepsilon}_p}{\dot{\varepsilon}_0}\right)^{-1/m}-\tilde{\sigma}\right]}\frac{1}{b\Lambda}\left(\frac{\dot{\varepsilon}_p}{\dot{\varepsilon}_0}\right)^{1/m} - \frac{Mk_2}{2}\left[(\sigma^*_{d-d}+\sigma^0_{d-d}+\tilde{\sigma})-\left(\frac{\dot{\varepsilon}_p}{\dot{\varepsilon}_0}\right)^{1/m}\tilde{\sigma}\right]$$

For a weak strain rate dependence ($m >> 1$); the factor $(\dot{\varepsilon}_p/\dot{\varepsilon}_0)^{1/m}$ can be disregarded. In this case, Eq.4.25 can be written in a simplified way as follows:

Eq. 4. 26 $$\theta_p(\sigma_{d-d}) = \frac{P_1}{\sigma^o_{d-d} + \sigma^*_{d-d}} - P_2(\sigma^o_{d-d} + \sigma^*_{d-d})$$

where:

Eq. 4. 27 $$P_1 = \frac{M^3(\alpha\mu b)^2}{2}\frac{1}{b\Lambda}$$

and

Eq. 4. 28 $$P_2 = \frac{M}{2}k_2$$

For uniaxial loading, constant strain rate and constant temperature, the differential equation Eq.4.25 can be easily integrated yielding the following expression for the stress as a function of the plastic strain:

Eq. 4. 29 $$\sigma^*_{d-d} = \sqrt{\frac{P_1 - \left(P_1 - P_2(\sigma^*_{d-d(i)} + \sigma^0_{d-d})^2\right)\exp(-2P_2(\varepsilon_p - \varepsilon_{p(i)}))}{P_2}} - (\sigma^0_{d-d})$$

A very important characteristics of this model is that it predicts a saturation stress given by:

Eq. 4. 30 $$\sigma_{sat} = (P_1 / P_2)^{0.5} - \sigma^0_{d-d}$$

4. 3. 3. Modeling of the strain hardening at low temperatures of BCC materials.

For the BCC materials at T < 0.2 T_m, the usual relationship between the flow stress and the square root of the dislocation density (Eq. 4. 11) has been shown to be no longer valid [4.15]. Actually, the origin of this change has to be searched in the micro-mechanisms controlling the motion of dislocations. It is well established that, in BCC metals, the mobility of the dislocation screw segments is strongly reduced at low temperatures, owing to the non-planar character of the dislocation core resulting in a strong lattice friction. Consequently, screw dislocations tend to arrange themselves in straight screw segments aligned along the <111> directions under the presence of a stress field. The movement of these segments occurs by a thermally-activated mechanism of kink-pair formation followed by a fast movement of the kinks along the dislocation line.

For BCC materials at low temperatures, Rauch [4.16] has presented a simple model, based upon energy balance considerations, attempting to evaluate the forest contribution to the flow stress. In this model, the motion of the moving screw segments is analyzed in terms of a concomitant lattice friction and interaction with the

forest dislocations. In the presence of obstacles to the moving screw dislocation (forest dislocation), the dislocation line adopts the configuration depicted in Figure 4.15. Such obstacles stop the kink motion. In consequence, kinks coming from both sides of the pinning point pile up against the obstacles. Finally, this description of the motion of the screw segments is well supported by the in-situ TEM observation of Louchet and Kubin [4.17].

The curvature of the dislocation line near the obstacles generates an "internal" stress that must be subtracted from the applied stress in order to determine the effective stress operative during the (thermally-activated) double kink formation event. When the cusp angle at the obstacle given by the dislocation bow-out has reached the critical value correspondent to the obstacle strength, the obstacle is surmounted and the large number of kinks of opposite sign annihilates each other. In the present work, we have used Rauch's formulation and applied it to the case of polycrystalline materials. First, we express the applied shear stress of Rauch's model, τ_a, as a function of the measured applied stress σ_a by using a Taylor factor M equal to 3 ($\sigma_a = M \cdot \tau_a$). Second, we considered the additional component for the flow stress, $\tilde{\sigma}$, which certainly cannot be neglected in case of a tempered martensitic alloy and which accounts at least for the high density of boundaries decorated by carbides. This component was not considered in the work of Rauch. In this context, the modified Rauch's relationship between the applied stress and the plastic strain can be written as follows:

Eq. 4. 31
$$\sigma = \frac{\sigma^* + 2\tilde{\sigma}}{2} + \frac{1}{2}\sqrt{(\sigma^*)^2 + 4(M\alpha\mu b)^2 \rho}$$

where σ^* is the effective stress required for double-kink nucleation *at the imposed strain rate and temperature*. For a given σ^* level, the probability of double kink nucleation strongly depends on T, in agreement with the thermally activated character of this event. However, in the framework of the model, we accept that, at a given temperature, this probability is independent of the actual state of the structure (dislocation density), i.e., $\sigma^* = \sigma^*(T)$. In other words, we assume that the obstacles to dislocation movement are far enough not to interfere with the double kink nucleation mechanism.

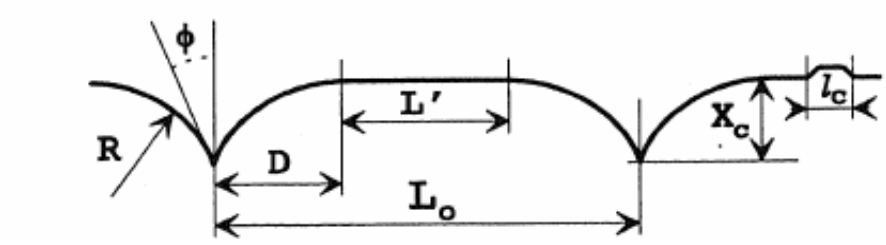

Figure 4. 15*: Configuration of a screw dislocation moving at low temperature.*

In order to write a plastic strain-hardening expression, we use the same strain dependence of the dislocation density as that in the case of high temperature, i.e., we use the Eq. 4. 23. Eq. 4. 31 can be differentiated with respect to the plastic strain (ε_p) to obtain an expression for the plastic strain hardening:

Eq. 4. 32
$$\frac{d\sigma}{d\varepsilon_p} = \frac{(M\alpha\mu b)^2}{\left[(\sigma^*)^2 + 4(M\alpha\mu b)^2\rho\right]^{1/2}} \frac{d\rho}{d\varepsilon_p}$$

Combining Eq. 4. 23 and Eq. 4. 32, we obtain:

Eq. 4. 33
$$\theta_p = \frac{M}{bL} \frac{(M\alpha\mu b)^2}{2\left(\sigma - \left(\frac{\sigma^* + 2\tilde{\sigma}}{2}\right)\right)} + \frac{Ma(\sigma^*)^2}{8\left(\sigma - \left(\frac{\sigma^* + 2\tilde{\sigma}}{2}\right)\right)} - \frac{Mk_2}{4}\left[2\left(\sigma - \left(\frac{\sigma^* + 2\tilde{\sigma}}{2}\right)\right)\right]$$

Eq. 4. 33 describes the plastic strain hardening evolution at constant plastic strain rate and temperature in the Peierls regime. Let us compare Eq.4.25 at high temperature with Eq. 4. 33 at low temperature. In the first case there are three constants to fit, namely the mean free path Λ, the annihilation coefficient k_2 and σ_{d-d}^0. Eq. 4. 30 has one additional parameter σ^*. However, $\tilde{\sigma}$ can be obtained from the high temperature fits since this component is considered athermal. Therefore, σ^* at every temperature can be estimated directly from the flow stress level and $\tilde{\sigma}$.

4. 4. Application of the model to Eurofer97 steel.

4. 4. 1. Strain hardening behavior at high temperatures.

Considering the result presented in Section 4. 2. 2, Eq. 4. 26 is expected to predicts the strain-hardening law for the Eurofer97 steel at T >220 K. To check the prediction of the model, we have calculated the strain-hardening from the experimental data and plotted it against the plastic stress, equivalent to σ^{*}_{d-d}. As an example, θ_p versus σ^{*}_{d-d} at T=293 K is presented in Figure 4. 16. Note the curvature of the θ_p - σ^{*}_{d-d} plot, which is consistent with the stress dependence of the strain-hardening as predicted by Eq.4.25. This fact is a direct consequence of the assumption of a constant mean free path with strain in the tempered martensitic microstructure. In many materials, a linear dependence of the strain-hardening with the stress is found reflecting the fact that the dislocation mean free path is not mediated by geometrical obstacle (laths or lath blocks) but by the dislocation spacing.

Keeping in mind that three-parameter fits are used to reconstruct the deformation curves over a limited strain range, special attention has to be paid to the self-consistency of the analysis. We have to emphasize here that fitting the limited strain range of the experimental data with a three parameters equations is almost certain to reproduce properly the experimental data. Therefore, we constrained the fit by imposing a value to the mean free path of the dislocations. Considering that the laths are of the order of 0.2-0.5 μm wide and few micrometers long, we selected 1 μm as the effective mean free path. In our analysis, the mean free path being related to the geometrical barriers that are the boundaries of the martensite, it is clear that the mean free path must remain essentially athermal and must have the same value over the temperature range over which the model holds. By doing so, only two parameters are left for fitting in Eq. 4. 13, which are P_2 and σ^{0}_{d-d}. In Table 4.1, we indicate the values of the coefficients that we use and that intervene in P_1, P_2 and σ^{0}_{d-d}.

M	α	G	B	L
3	0.2	80000 MPa	0.268 nm	1 μm

Table 4.1*: For these values, P_1 equals 0.93x10^6 MPa^2.*

In Figure 4. 17 four experimental tensile curves are presented with the fit done according to Eq. 4. 29. As it can be observed, the prediction of the model fits perfectly the experimental data. The temperature dependence of the two fitted parameters, σ^{0}_{d-d} and P_2, is given in Figure 4. 18 and Figure 4. 19 respectively. Interestingly, the last two plots reveal a significant temperature dependence of P_2, being an increasing function with T, while a very moderate T-dependence is found for σ^{0}_{d-d}. Such a behavior was actually expected since σ^{0}_{d-d} reflects approximately the initial total dislocation density. This value should be mainly temperature independent even though small variations associated to that of the shear modulus with temperature and to the amount of micro-plasticity taking place before macro-yielding may be expected.

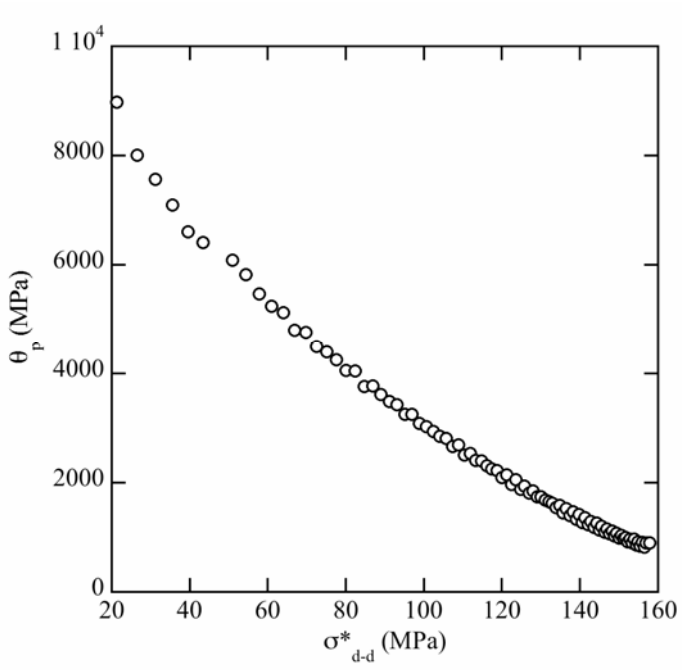

Figure 4. 16: θ_p *versus* σ^*_{d-d} *at 293 K, Eurofer97.*

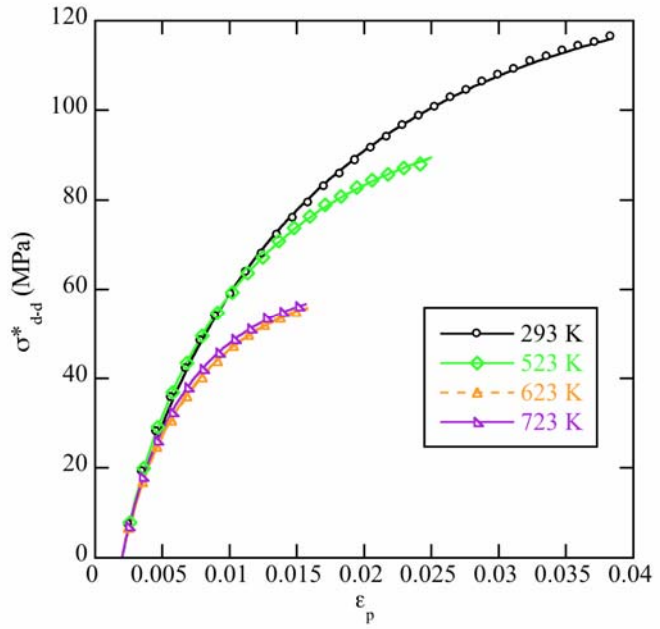

Figure 4. 17: σ^*_{d-d} *versus plastic strain at various temperatures with fit according to Eq. 4. 13, Eurofer97 steel. The dislocation mean free path L= 1* μm *is fixed,* P_2 *and* σ^0_{d-d} *are adjusted*

On the contrary, P_2, which characterizes all the dislocations annihilation processes, among which many are thermally activated, is expected to increase with temperature, as it is actually observed. The value of σ^0_{d-d} is of the order of 55 MPa, which yields, with the use of the Eq. 4. 13 an initial dislocation density of about $1.8 \cdot 10^{13} m^2$. This value is consistent with the values reported in Chapter 2.

By using Eq. 4. 14, $\tilde{\sigma}$ is found to be equal to about 475 MPa. Finally, we note that the only parameter, which remains ill-defined, is the coefficient α of the Taylor's equation. From literature, it is known that α is of the order 0.1 - 0.5. We arbitrarily picked a value of 0.2. However, fits of the quality of that shown in Eq. 4.21 can be obtained with a value of a between 0.1 and 0.5. Of course, this in turn changes the mean free path within the respective range 0.25 – 6 μm. This looks quite reasonable considering the level of simplification of such a model applied to the highly complicated microstructure of a tempered martensite. Such models, like the one we used, are aimed at rationalizing the tensile curves rather than deriving parameters, like the dislocation mean free path, from a theoretical description of the curve.

4. 4. 2. Strain-hardening behavior below room temperature

The post-yield behaviors at low temperatures are presented in Figure 4. 4. An important reduction of the curvature is identified between all the curves below 200 K and that at 223 K. As observed in Figure 4. 4, the last temperature corresponds to the limit between the Peierls dominating rate controlling process and the high temperature one. Thus, the observable decrease of the curvature of the tensile tests constitutes a clear indication of a change in the strain-hardening law. In Figure 4. 20, the plastic strain-hardening is shown against the flow stress. From 173 K down to 77 K, two strain-hardening domains are identified. The first one, following the yield point, is characterized by a drastic decrease of θ_p with increasing the flow stress. A sharp transition follows this decrease with a continuous reduction of strain-hardening with stress. The curves at 113 K and 77 K are interesting in the sense that θ_p passes by a minimum. This point has been previously discussed in Section 4.2.2.

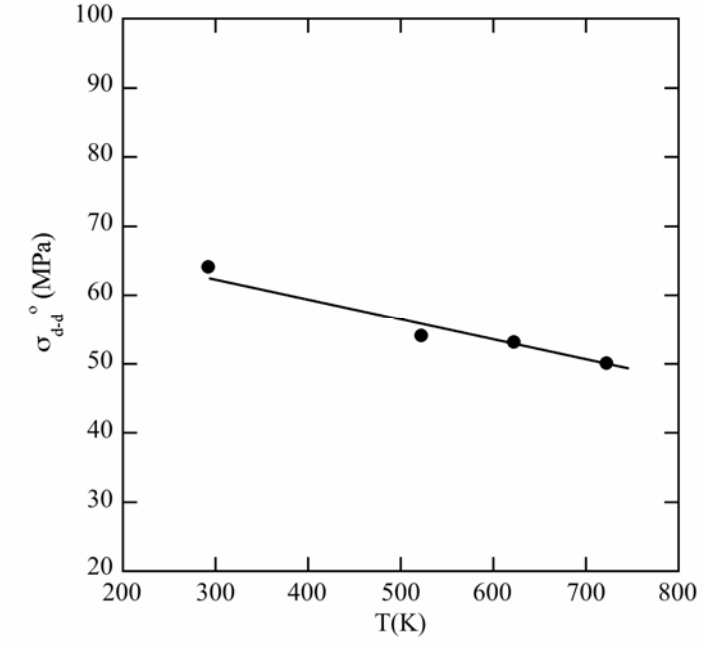

Figure 4. 18: *Fitted value of σ^*_{d-d} versus temperature, Eurofer97.*

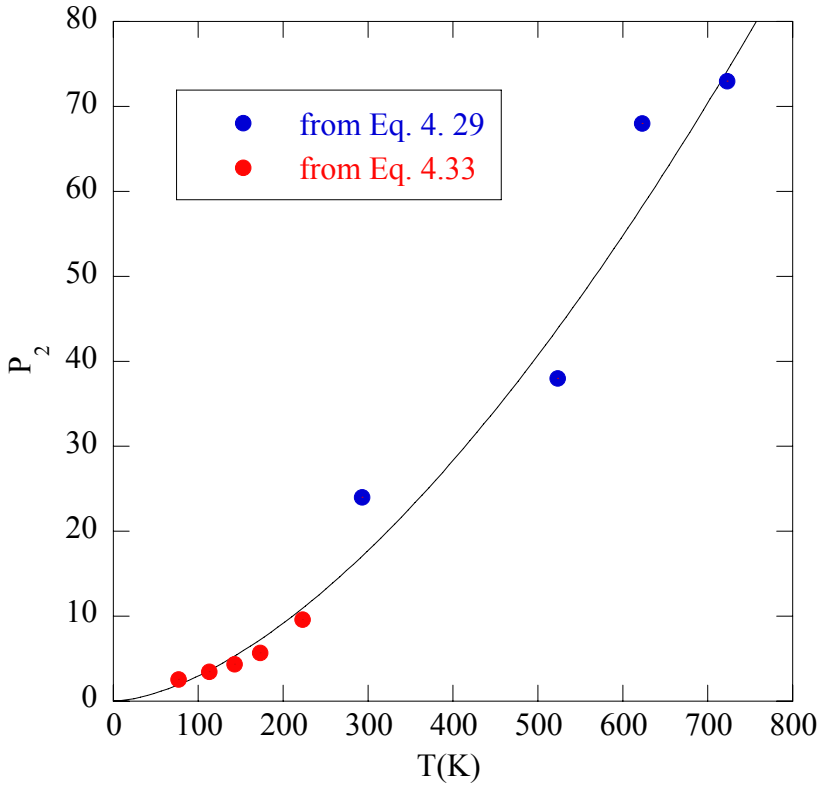

Figure 4. 19: *Fitted value of P_2 versus temperature, Eurofer97.*

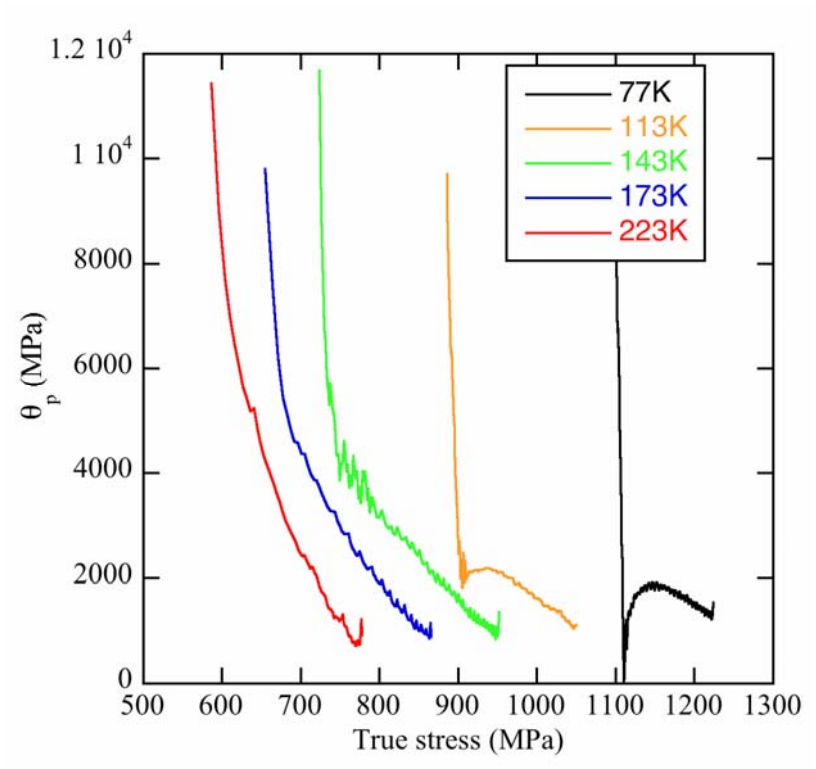

Figure 4. 20: θ_p *versus the flow stress at various low temperatures, Eurofer97.*

As expressed previously. The relationship proposed for the low temperature hardening behavior has one additional parameter, σ^*. However, $\tilde{\sigma}$ can be obtained from the high temperature fits. Indeed, since σ_{d-d}^0 has been estimated to 55 MPa, a value of 475 MPa for $\tilde{\sigma}$ can be deduced by considering Figure 4. 2.

Thus, we use this last value in Eq. 4. 33 to fit the lower temperature $\theta_p(\sigma)$ curves, together with $\Lambda = 1\ \mu m$ (dislocation mean free path) as it was done for the high temperature case. Only the values of σ^* and k_2 .are fitted.

It was found that the temperature dependence of σ^* reproduced fairly well that of the $\sigma_{0.2}$ and that the annihilation coefficient temperature dependence is consistent with that determined at high temperatures. This can be observed in Figure 4. 19 where we plot P_2 versus temperature. Finally, an example of the fitting of experimental data using Eq. 4. 33 is given in Figure 4. 21 for the Eurofer 97 at 143 K.

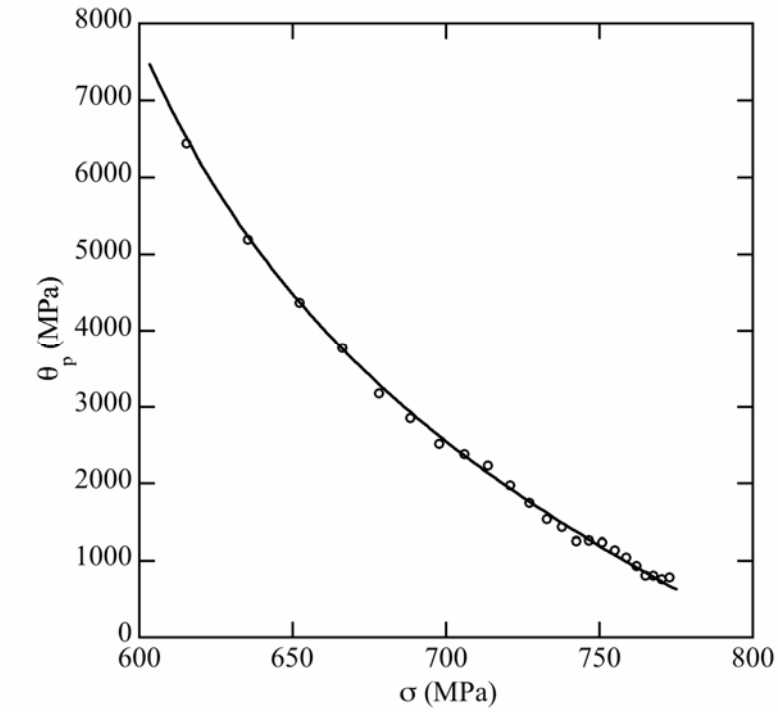

Figure 4. 21*: Plastic strain-hardening versus flow stress at 143 K, Eurofer 97*

.

References

[4.1] U. F. Kocks, "Laws for Work-Hardening and Low-Temperature Creep", J. Eng. Mater. Tech. (Trans. Of the ASME), January 1976, pp.76-85.

[4.2] U.F. Kocks, A.S. Argon, M.F. Ashby, "Thermodynamics and Kinetics of Slip" , in the series "Progress in Material Science", Vol. 19, Ed. by Chalmers, Christian and Massalski, Pergamon, 1975.

[4.3] E.W. Hart, "A phenomenological Theory for Plastic Deformation of Polycrystalline Metals", Acta Metallurgica, Vol.18, No.6, June 1970, pp.599-610.

[4.4] E.W. Hart, "Constitutive Relations for the Nonelastic Deformation of Metals", Journal of Engineering Materials and Technology, (Trans.of the ASME), July 1976, pp.193-202.

[4.5] D.Caillard, J.L. Martin, "Thermally Activated Mechanisms in Crystal Plasticity", Pergamon, 2003.

[4.6] E. Nadgornyi, "Dislocation Dynamics and Mechanical Properties of Crystals", in Progress in Material Science, Vol.31, Ed. by Chalmers, Christian and Massalski, Pergamon, 1988.

[4.7] H. Mecking, U. F. Kocks, "Kinetics of Flow and Strain-Hardening", Acta Metall. 29 (1981), pp. 1865-75.

[4.8] Y. Estrin, H. Mecking, "A Unified Phenomenological Description of Work hardening and Creep based on One Parameter Models", Acta Metall. 32 (1984) , 57-70.

[4.9] Y.Estrin, "Dislocation Density Related Constitutive Modeling", in Unified Constitutive Laws of Plastic Deformation, Ed. by A. Krausz and K. Krausz, Academic Press, 1996, pp.69-106.

[4.10] Y. Estrin, L.P. Kubin, "Local Strain Hardening and Nonuniformity of Plastic Deformation", Acta Metallurgica Vol.34, No.12, pp.2455-64.

[4.11] U.F.Kocks, H.Mecking, "Physics and Phenomenology of Strain Hardening: the FCC case", Progress in Material Science, 48, 2003, pp. 171-273.

[4.12] G. E. Dieter, Mechanical Metallurgy, McGraw-Hill Book Co, London, UK, 1988, p. 232.

[4.13] Follansbee P. S., Kocks U. F., "A Constitutive Description of the deformation of Copper Based on The use of Mechanical Threeshold Stress as an Internal State Variable", Acta Metallurgica 36, (1), 1988, pp.81-93.

[4.14] X. F. Fang, W. Dahl, Mater. Sci. Eng A203 (1995) 14.

[4.15] A.S. Keh, S. Weissmann, "Deformation Substructure in Body-Centered Cubic Metals", in *Electron Microscopy and Strength of Crystals*, eds. G. Thomas and J. Washburn, Interscience Publishers, NY, 1963, pp.231-300.

[4.16] E. F. Rauch,"The Relation Between Forest Dislocations and Stress in BCC Metals", Key Engng, Mater. Vol. 97-98 (1994), pp. 371-376.

[4.17] F. Louchet L. P. Kubin, Phil. Mag. A 39 No.4 (1979) 443-454.

[4.18] G. Gosh, G. B. Orson, Acta Materialia 50, 2002, pp.2655-2675.

[4.19] R. Bonadé, P. Spätig, "On the Strain-Hardening of Tempered Martensitic Alloys", *Materials Science and Engineering A,* 400-401, (2005), pp. 234-240.

[4.20] A.Ramar, R.Bonadé, R.Schaeublin, *to be published.*

[4.21] H.Mughrabi, "Dislocation Wall and Cell Structures and Long-Range Internal Stresses in Deformed Metal Crystals", Acta Metallurgica, Vol.31, No.9, 1983, pp.1367-79.

Chapter 5

Assessment of the fracture properties of Eurofer97 steel. Experiments and Modeling

5. 1. Introduction.

The increase of the ductile-to-brittle temperature due to irradiation in BCC alloys is a well-known phenomenon. This problem has been introduced in Chapter 2, where we have presented the main engineering tools used nowadays to assess the detrimental effects of irradiation on the fracture toughness of a given material.

Reduced-activation tempered martensitic steels are among the reference materials considered for the first wall and some structural parts of the first generation fusion reactor (DEMO). A description of typical microstructures and the mechanical properties for selected tempered martensitic steels have been presented in Chapter 3 and Chapter 4. Since these materials have a BCC structure, they are expected to display a ductile to brittle transition.

The successful design and subsequent operation of fusion reactors present important challenges to the material science community. Among others, the shift of the ductile to brittle transition temperature towards higher temperatures due to the effect of neutron irradiation is a factor that constraints the safety operational margins of the fusion reactor. In order to develop a strategy to tackle this problem, the understanding of the physical principles underlying brittle fracture phenomena in tempered martensitic steels is mandatory. This need has motivated the work presented in this Chapter, which is organized as follows.

In section 5.2 we present a brief summary of the main fracture mechanics concepts that will be frequently used along the Chapter. The main concepts related to Linear Elastic Fracture Mechanics are reviewed, together with the more recent extensions developed to deal with crack tip plasticity.

Next, in section 5.3, we present a new experimental fracture toughness database obtained for the Eurofer97 steel in the "as received" condition. Two different specimen sizes have been tested, 0.4 T C(T) and 0.2 T C(T), the last one being typically used in testing of irradiated materials. The results are discussed in detail. Special emphasis is given to the problem of size effect on fracture toughness. The datasets generated are analyzed by means of the master curve concept, following the standard ASTM E-1921. The applicability of this approach to the case of the tempered martensitic steels is studied.

In section 5.4, the phenomenon of cleavage fracture in steels is reviewed. The main microstructural features affecting fracture toughness are identified based on an extensive literature survey for the case of the RPV's and tempered martensitic steels.

In section 5.5 we introduce the local approach to cleavage fracture. We describe the main features of two different local approaches: the Weibull stress concept and the scaling model for cleavage fracture.

Finally we present in section 5.6. a model based on the concept of the “local approach” to fracture. A local criterion for cleavage fracture has been used based on the critical stress – critical area model (σ^*-A^*). We demonstrate that based on this local approach concept, it is possible to predict correctly the dependence with temperature of the lower bound for fracture toughness for the case of Eurofer97 and other tempered martensitic steels as the F82H steels.

5. 2. Fracture mechanics: Basics.

5. 2. 1. Stress fields around a crack.

For isotropic linear elastic materials, analytical expressions of the stresses generated by a crack have been derived, see for example Williams [5.1], and are expressed as:

Eq. 5. 1 $$\sigma_{ij} = \frac{K}{\sqrt{2\pi r}} f_{ij}(\theta) + T\delta_{1i}\delta_{1j} + C_{ij2}(\theta) r^{1/2} + ... + C_{ijn}(\theta) r^{\frac{n-1}{2}} + ...$$

where K is the stress intensity factor, and $f_{ij}(\theta)$ is a dimensionless angular function. The definition of the coordinate axis system ahead of the crack tip is indicated in Figure 5. 1. The second term, T, is a constant stress in the x-direction called the "transverse stress". The $f_{ij}(\theta)$ functions are normalized in such a way that $f_{yy}(\theta = 0) = 1$ for Mode I. The stress intensity factor K is a scale factor that defines the magnitude of the stress field and depends on the configuration of the cracked component (the flaw shape and size and the geometry of the part) and on the loading configuration. The expressions of K for different configurations are catalogued in tables. Considering the first two terms of the asymptotic solutions in Cartesian coordinates for Mode I of loading yields [5.6][5.5]:

Eq. 5. 2
$$\sigma_{xx} = \frac{K_I}{\sqrt{2\pi r}} \cos\frac{\theta}{2}\left(1 - \sin\frac{\theta}{2}\sin\frac{3\theta}{2}\right) + T$$
$$\sigma_{yy} = \frac{K_I}{\sqrt{2\pi r}} \cos\frac{\theta}{2}\left(1 + \sin\frac{\theta}{2}\sin\frac{3\theta}{2}\right) + 0$$
$$\sigma_{xy} = \frac{K_I}{\sqrt{2\pi r}} \cos\frac{\theta}{2}\sin\frac{\theta}{2}\cos\frac{3\theta}{2} + 0$$
$$\sigma_{zz} = \nu\left(\sigma_{xx} + \sigma_{yy}\right) \text{ for plain strain } (u_z = 0)$$

$$\sigma_{zz} = 0 \text{ for plain stress } (\sigma_{zz} = 0)$$

The displacements in Cartesian coordinates are given by:

Eq. 5. 3
$$u_x = \frac{K_I}{4\mu}\sqrt{\frac{r}{2\pi}}\left[(2\kappa - 1)\cos\left(\frac{\theta}{2}\right) - \cos\left(\frac{3\theta}{2}\right)\right] + \frac{(1-\nu)}{2\mu} Tr\cos\theta + ...$$

$$u_y = \frac{K_I}{4\mu}\sqrt{\frac{r}{2\pi}}\left[(2\kappa + 1)\sin\left(\frac{\theta}{2}\right) - \sin\left(\frac{3\theta}{2}\right)\right] - \frac{\nu}{2\mu} Tr\sin\theta + ...$$

$$\kappa = 3 - 4\nu \text{ for plain strain}$$

$$\kappa = \frac{3-\nu}{1+\nu} \text{ for plain stress}$$

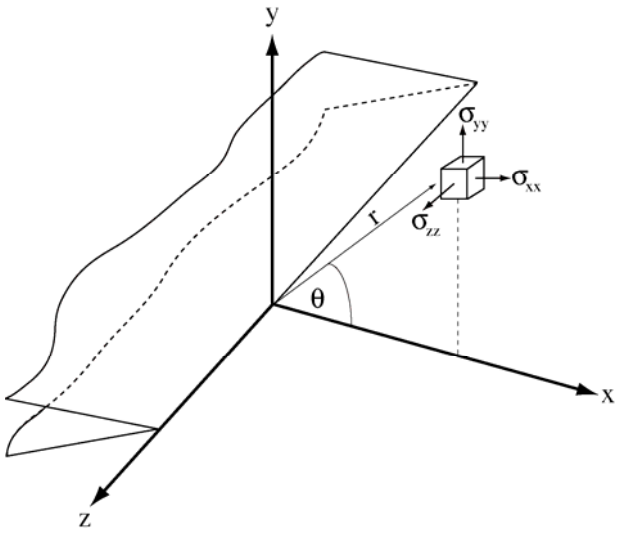

Figure 5. 1: *Definition of the coordinate axis system ahead of a crack tip*

In the following, we will study the effect of the T-stress on the size of the plastic zone at the crack tip. In order to do so, we will need the values of the principal stresses, obtained from the equations Eq. 5. 2. The calculations of the principal stresses yield:

Eq. 5. 4

$$\sigma_1 = \frac{1}{4}\left\{2T + \frac{4K}{\sqrt{2\pi r}}\cos\left(\frac{\theta}{2}\right) + \sqrt{2\left[\left(\frac{K}{\sqrt{2\pi r}}\right)^2\left(1-\cos(2\theta)\right) + 2T^2 + 2T\frac{K}{\sqrt{2\pi r}}\left(\cos\left(\frac{5\theta}{2}\right) - \cos\left(\frac{\theta}{2}\right)\right)\right]}\right\}$$

$$\sigma_2 = \frac{1}{4}\left\{2T + \frac{4K}{\sqrt{2\pi r}}\cos\left(\frac{\theta}{2}\right) - \sqrt{2\left[\left(\frac{K}{\sqrt{2\pi r}}\right)^2\left(1-\cos(2\theta)\right) + 2T^2 + 2T\frac{K}{\sqrt{2\pi r}}\left(\cos\left(\frac{5\theta}{2}\right) - \cos\left(\frac{\theta}{2}\right)\right)\right]}\right\}$$

$$\sigma_3 = \nu\left[T + 2\frac{K}{\sqrt{2\pi r}}\cos\left(\frac{\theta}{2}\right)\right]$$

Note that in Eq. 5. 2, setting $\theta = 0$ gives $\sigma_{xy} = 0$. Therefore, at $\theta = 0$ the x-axis and the y-axis are principal directions. Since we have assumed plane strain conditions, one of the principal directions will be coincident with the z-axis ($\varepsilon_{zz} = 0$) and therefore, only a rotation on the x-y plane is needed to diagonalize the stress tensor.

5. 2. 2. Plane strain fracture toughness K_{Ic}.

A precise definition of the concept of fracture toughness involves the concept of loading modes. The three loading modes usually considered in fracture mechanics are presented in Figure 5. 2. Plane strain fracture toughness, K_{Ic}, is related to specimens loaded under quasi-

static Mode I, for which plane strain and small–scale yielding conditions prevail along the crack front length. The experimental procedure described in the ASTM E-399 standard is widely used as the experimental determination of K_{Ic}. It is accepted that the plane strain conditions ensure that we will obtain a lower bound in the fracture toughness values, which can be consequently regarded as conservative. The ASTM E-399 allows the use of different types of pre-cracked specimens, typically, various geometries of bend bars and compact tension specimens. The appropriate expressions for the stress intensity factors K_I corresponding to the different specimens are also provided in the standard. Assuming that the cracks are sharp and that the material behaves elastically, the stress fields ahead of the crack tip can be estimated from Eq. 5. 2. Note that in the framework of the one-parameter linear elastic fracture mechanics, only the first order of the series expansion presented in Eq. 5. 2 is considered (i.e. $T = 0$). The fracture toughness of the material is determined from the value of the stress intensity factor K_I of the specimen being tested at the onset of fracture ($K_{(If)}$). However, $K_{(If)}$ will be only validated as the fracture toughness of the material provided that the stringent requirements on the dimensions of the specimen are met. This ensures that the fields ahead of the crack tip scales with K_I as described by Eq. 5. 2.

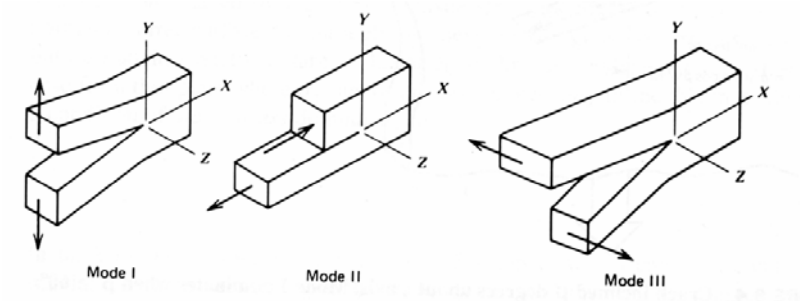

Figure 5. 2: *The three fracture modes. From reference [5.1].*

5. 2. 3. Effect of the plasticity at the crack tip.

The Eq. 5. 1 is strictly valid for the case of isotropic and elastic materials. In this framework of linear elastic fracture mechanics (LEFM) analysis, the stress level is proportional to $1/\sqrt{r}$, therefore, the stress increases up to infinite when we approach the crack tip, *regardless the load level*. However, in real materials, the elastic singularity predicted by the LEFM does not constitute a real physical solution. At the same time, the LEFM approach does not take into account any potential non-linear behavior of the material. In the case of metals, plastic deformation occurs in a small region around the crack tip. The plastic deformation will further relax the stress into the plastic area around the crack tip. In order to account for plasticity at the crack tip, several corrections to the elastic solution have been proposed to extend the validity of the elastic solutions. Such corrections are based on the existence of a very small level of plasticity at the crack tip (see Ref. [5.1] to [5.6]). In the

case of the Irwin approach, an "effective" crack of length $a + r_0$ should be considered, where a is the actual crack length and r_0 is the radius of the small plastic zone that can be estimated from Eq. 5. 2 considering plane stress conditions and a perfectly plastic material. As a result, $K_{eff} > K_{applied}$ due to the plastic correction. Then the stress fields evaluated outside the small plastic region is thus given by the stress intensity factor calculated from the "effective" crack length, K_{eff}. Plasticity corrections can extend somehow the normal validity limit of the LEFM. However, as discussed in [5.5], the corrections are based on very simple constitutive behaviors and are not reliable when plastic effects are important.

5. 2. 4. The J- Integral.

The stress intensity factor K is a pure linear-elastic parameter, valid in the context of the LEFM theory. When non-linear behaviour of the material becomes significant in terms of the strain and stress fields acting in the region around the crack tip, LEFM approach is no longer valid. However, the stress/strain fields can be calculated by using other parameters that are able to take into account the non-linear effects. The J-integral proposed by Rice [5.10] can be used to extend the fracture mechanics theory beyond the limits of the LEFM. If we consider a counter-clockwise contour around the tip of a crack, the J-integral is given by:

Eq. 5. 5
$$J = \int_{\Gamma} (w \cdot dy - T_i \frac{\partial u_i}{\partial x} ds)$$

where u_i are the component of the displacement vector and ds is a length increment along the contour Γ, T_i are the components of the traction vector, a stress vector normal to the contour Γ, whose components are given by $T_i = \sigma_{ij} n_j$ and w is the strain energy density, defined as:

Eq. 5. 6
$$w = \int_0^{\varepsilon_{ij}} \sigma_{ij} d\varepsilon_{ij}$$

Rice demonstrated that the J-integral is independent of the path of integration around the crack tip for the case of a non-linear elastic material. It is well known that for the particular case of proportional loading[1], the total deformation theory gives the same results than the incremental plasticity theory of Pranldt-Reuss. Therefore, for proportional loading case, the J-integral is also path-independent even in the case of considering an incremental flow rule, provided that the load increases monotonically.

[1] Proportional loading is defined as follows: , where is a certain point in the body and is a certain function of the time, and is a tensor independent of . During proportional loading, the directions of the principal stresses are constant and their magnitude is proportional to the time.

The J-integral can be interpreted in two different ways. The first interpretation associates the potential energy release rate in a *non-linear elastic body* that contains a crack with the actual value of the J-integral [5.5]:

Eq. 5. 7
$$J = -\frac{d\Pi}{dA}$$

where Π is the potential energy and A is the crack area. This interpretation of J is quite useful when the actual value of the J integral is measured experimentally. The interpretation in terms of the energy release rate gives rises to a relation between the stress intensity factor K and J for the special case of linear elastic materials:

Eq. 5. 8
$$J = \frac{K_I^2}{E'}$$

The second interpretation of J was suggested by Hutchinson [5.11] and Rice and Rosengren [5.12], who demonstrated that the J-integral can be used as a parameter to characterize the crack tip conditions when plasticity (non-linear) effects are important. They derived a set of equations that describe the stress and strain fields ahead of the crack tip for the case of a power-law material (a Ramberg-Osgood material), which are known as the HRR singularity since the fields diverge for $r \to 0$. The value of the J-integral defines the amplitude of the HRR field in the same way as K defines the amplitude on the fields in the LEFM approach. Therefore, J can be regarded as a stress intensity parameter. Note that the HRR analysis is done in the framework of small strains and does not describe the field at the very tip of a blunting crack. Within the framework of small strains and for a Ramberg-Osgood material, two different zones beyond a crack loaded in SSY conditions can be used to describe the stress field: one in the elastic region, where the stress fields scales with $K$and varies with $1/\sqrt{\mathrm{r}}$; and a second one inside the plastic zone, characterized by J.
Anderson [5.5] has demonstrated by means of dimensional analysis that in the case of J-dominance the stress field can be written as follows:

Eq. 5. 9
$$\frac{\sigma_{ij}}{\sigma_0} = F_{ij}\left[\frac{E'J}{\sigma_0^2, r}, \theta\right]$$

The HRR singularity obeys Eq. 5. 9 since the stress field in the J-dominated region can be written as a function of $E'J/\sigma_0^2 r$.
The concept of the J-integral can be extended to a three-dimensional problem. In this case, a local coordinate system is defined at every point in the crack front. Then the J-integral is computed for every plane having the crack front as a normal direction.

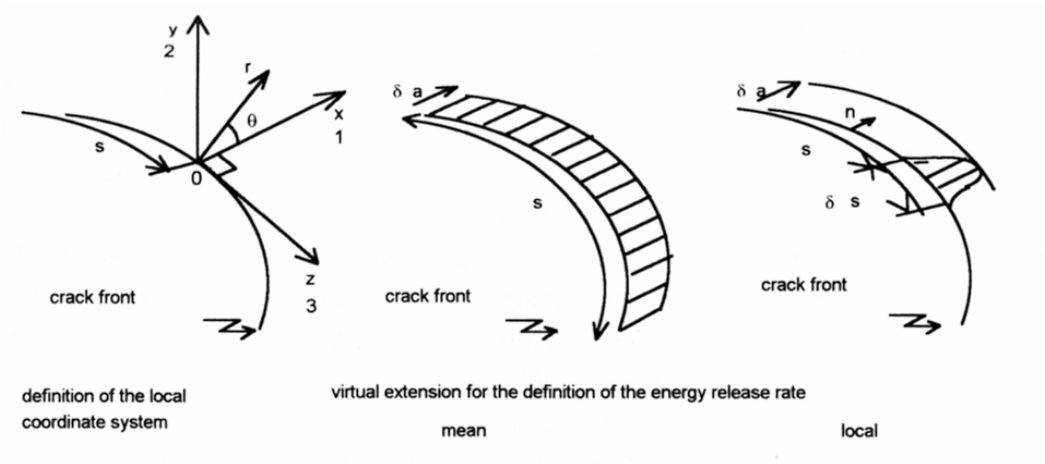

Figure 5. 3: *Definition of the 3D local coordinates system to compute J_{local} along the crack front. From [5.6].*

In the three-dimensional case, Eq. 5. 8 can be generalized as follows (Figure 5. 3) [5.6]:

Eq. 5. 10 $$\oint J(s)d\mathbf{a}(s)\mathbf{n}(s)ds = -d\Pi$$

Where $d\Pi$ is the variation of the potential energy of the cracked body for a virtual infinitesimal crack extension of the crack $d\mathbf{a}(s)\mathbf{n}(s)$ in its own plane, at the point of the curvilinear coordinate s normal to the crack front. In this way, the line integral becomes a surface integral, giving a "J-average".

5. 2. 5. Two parameters fracture mechanics characterization.

Eq. 5. 1 describes the stress fields ahead of the crack tip for the case of a linear elastic material. Therefore, it is possible to assess directly the effect of the T-stress on the fields ahead of the crack tip. We first study the T-stress effect on the hydrostatic stress and on the von Mises stress also called the equivalent stress σ_{eq} . σ_{eq} is commonly written in terms of the principal stresses as follows:

Eq. 5. 11 $$\sigma_{eq} = \sqrt{\frac{1}{2}\left[(\sigma_1 - \sigma_3)^2 + (\sigma_2 - \sigma_1)^2 + (\sigma_3 - \sigma_2)^2\right]}$$

Considering now the principal stresses of the stress fields predicted for an elastic material (Eq. 5. 5), we can derive the expression for the equivalent stress and evaluate the effect of the T stress on σ_{eq}:

Eq. 5. 12

$$\sigma_{eq} = 0.353553 \cdot \sqrt{\left(\frac{K}{\sqrt{2\pi r}}\right)^2 \left[7 - 16\nu + 16\nu^2 + 4(1-2\nu)^2 \cos(\theta) - 3\cos(2\theta)\right] + T^2\left[8 - 8\nu + 8\nu^2\right] + 2T\frac{K}{\sqrt{2\pi r}}\left[(1 - 16\nu + 16\nu^2)\cos\left(\frac{\theta}{2}\right) + 3\cos\left(\frac{5\theta}{2}\right)\right]}$$

Eq. 5. 12 shows that for a given K value, the σ_{eq} stress at a point of the body increases when compared to the case of $T = 0$. Note that the quantities, $[8 - 8\nu + 8\nu^2]$ and $[1 - 16\nu + 16\nu^2]$ are respectively positive and negative for typical values of ν. As a consequence, there is always an increase of σ_{eq} but it will be larger for negative T values than for positive ones when compared to the $T = 0$ case. If we now consider an elastic-plastic material, the previous observations can help us to gain insight into the effect of the T stress on the plastic region around the crack tip. Considering the von Mises yield condition and the associated flow rule, the dependence of the σ_{eq} with T implies that the plastic areas will increase for $T \neq 0$ when compared to the $T = 0$ case. However the case of $T < 0$ has a stronger influence on the size of the plastic region.
The effect of the T stress on the hydrostatic stress $\sigma_m = \sigma_{kk}/3$ is given by the following expression:

Eq. 5. 13

$$\sigma_m = \frac{1}{3}(1+\nu)\left[T + 2\frac{K}{\sqrt{2\pi r}}\cos\left(\frac{\theta}{2}\right)\right]$$

The Eq. 5. 13 shows that a negative T stress values decreases the hydrostatic stress level and positive T-stress values increases the hydrostatic stress level in a certain point of the continuum.

For a given specimen, the level of stress triaxiality ahead of the crack tip is referred as *constraint*. The level of constraint is usually assessed by comparing the stress fields computed by finite element methods with those obtained from a ”reference” solution for the higher triaxiality prevailing in small scale yielding conditions. The SSY fields are constructed from the boundary layer formulation [5.7]. The boundary layer model consists in a two-dimensional plane strain circular model (a mesh in finite element model) where the crack tip is located in the center of the circle, The size of the plastic zone is smaller that than R/20 (R is the radius of the model). If we consider an elastic-plastic material, a small plastic zone will exist around the crack tip. The interpretation of the boundary layer problem can be stated as follows. Let’s consider a general elastic-plastic body with a sharp crack and loaded in Mode I and in plane strain state. Let’s also assume that the loading conditions are such that the plastic zone is small enough so that the elastic stress field well outside this zone is describe by William’s expression Eq. 5. 1. Under these conditions, the numerical solutions for the stress fields are generated by imposing the node displacements of the circular mesh according to Eq. 5. 3. There exist two different boundary layer problems. The first one is called the “pure boundary layer problem” (PBL) where the T stress is zero. The second one,

when the T stress is different from zero, is called "Modified Boundary Layer problem"(MBL).
We have previously shown that in the case of T=0, the size of the plastic region is minimum given a K level. The MBL model can be used to assess the effect of the T stress on the shape and on the extension of the plastic region for a certain load level. To illustrate the effect of the T stress on the size and shape of the plastic zone, we ran a series of simulations of the MBL model with different T. The details of the finite element procedure are presented in the Section 5. 6. 2. The results are presented in

Figure 5. 4 to Figure 5. 6. They corroborate the conclusions obtained from Eq. 5. 12, namely, the plastic zone strongly increases for negative T stresses and increases moderately for positive T stresses of the same magnitude. It is concluded that the region where the stresses are dictated by the elastic singularity solutions will prevail in regions that are closer to the crack tip for specimens having T=0 or alternatively slightly positive values of T stress for increasing load levels. Note also that the T stress depends on the load level and on the geometry of the cracked body. The value of the T stress correspondent to a certain geometry can be estimated from comparing the stress field ahead of the crack tip for the case of the cracked body with the stress fields generated in the PBL model under the same load in terms of K. Again, this can only be done provided that *in the case of the cracked body*, the plastic zone is well contained into the region controlled by the elastic singularity.

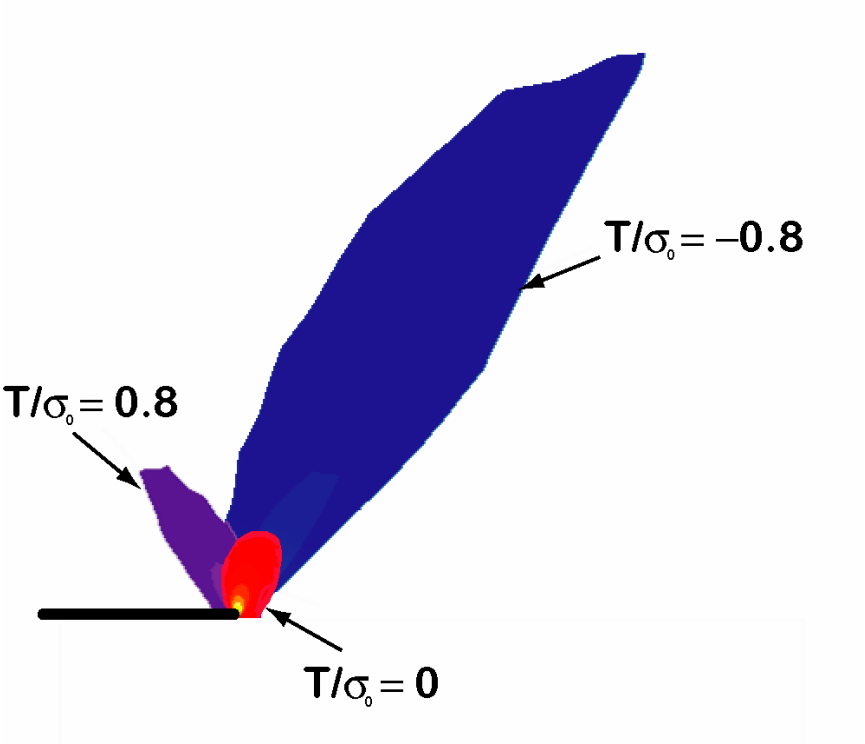

Figure 5. 4: *Effect of the T stress on the plastic zone (von Mises) ahead of the crack tip. Note the important influence of negative T stress on the size of the plastic area (Eurofer 97 at -100°C).*

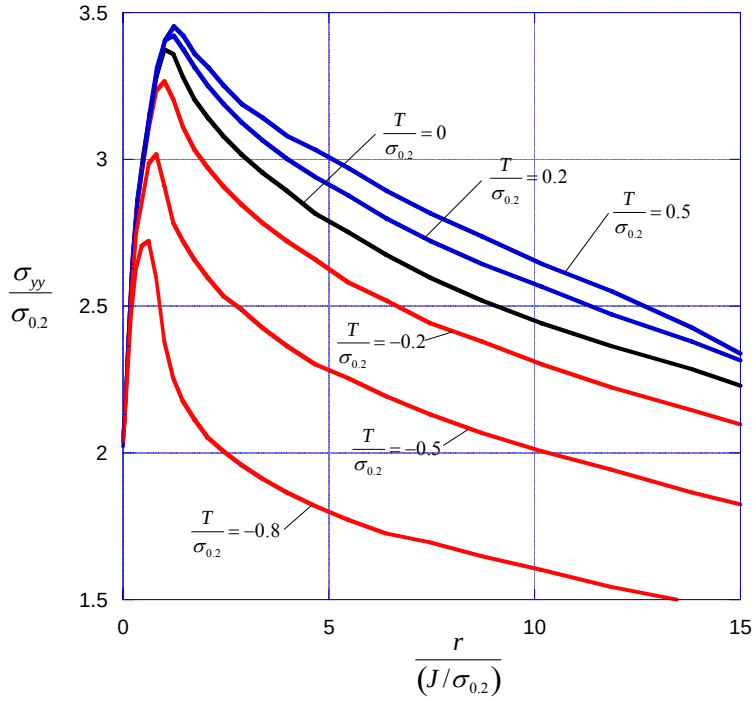

Figure 5. 5: *Effect of the elastic T stress on σ_{yy} near the crack tip for $\theta=0$. The fields are affected due to the effect of the T stress on the extension of the plastic zone (Eurofer 97 at -100°C).*

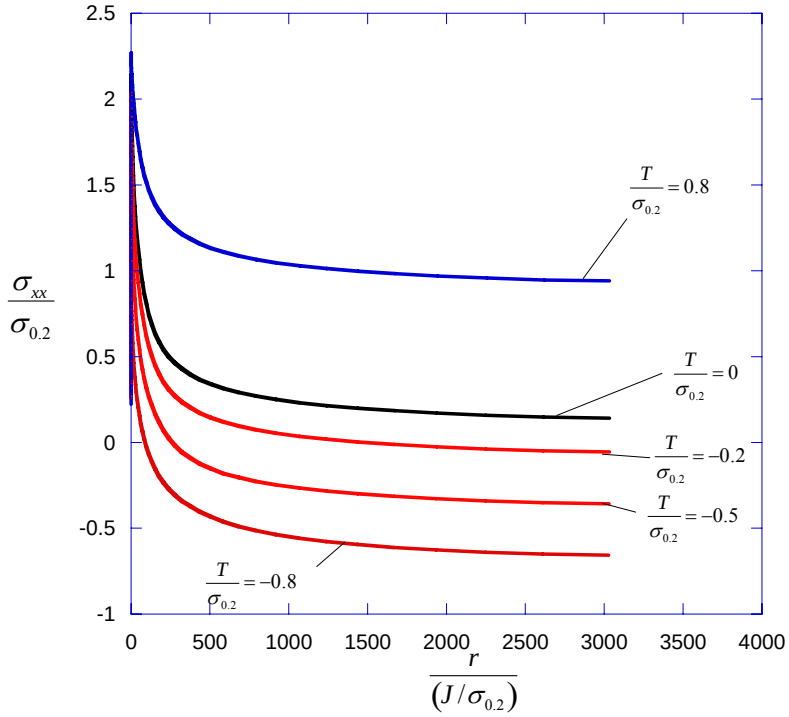

Figure 5. 6: *Effect of the T stress on σ_{xx} for $\theta=0$.*

The comparison of σ_{xx} in the region where the fields vary as $1/\sqrt{r}$ allows us to obtain the correspondent T stress. The stress intensity factor K and the T stress are related through the stress biaxiality ratio β [5.5]:

Eq. 5. 14
$$\beta = \sqrt{\pi a}\,\frac{T}{K_I}$$

The T stress approach is based on the asymptotic elastic solution. In case of large plasticity levels, plastic flow happens in large regions beyond the crack tip and therefore the elastic solution will be no longer valid. O'Down and Shih have presented the $J-Q$ theory as an appropriate tool to deal with these cases ([5.13][5.14][5.16]). They show that within a radial annulus around the crack tip the stress field has the form:

Eq. 5. 15
$$\sigma_{ij} = \sigma_{ij}\big|_{SSY,T=0} + Q\sigma_o\delta_{ij} \qquad \text{with} \qquad |\theta| < \frac{\pi}{2}, \quad \frac{J}{\sigma_o} < r < \frac{5J}{\sigma_o}$$

Actually, Q is defined for $\theta = 0$ at $r = 2J/\sigma_o$. Thus, within the spatial limit defined in Eq. 5. 15 Q corresponds to a uniform hydrostatic stress.

5. 2. 6. Experimental determination of the fracture toughness, K_{IC} and K_{Jc}.

The fracture toughness is usually determined by using standard testing conditions and specimens [5.8]. In this study, the fracture tests have been carried out on the so-called "compact tension specimens" usually identified as C(T). The typical geometry of the C(T) specimens is presented in Figure 5. 7. The stress intensity factor corresponding to this geometry is given by the following expression as a function of the load P_i [5.8]:

Eq. 5. 16
$$K_{(i)} = \frac{P_i}{BW^{1/2}}\,f(a_i/W)$$

where B and W are the thickness (breadth) and the width of the specimen respectively (Figure 5. 7), a_i is the initial crack length and $f(a_i/W)$ is a geometrical factor given by the following expression:

Eq. 5. 17
$$f(a_i/W) = \frac{\left[(2+a_i/W)\left(0.886+4.64(a_i/W)-13.32(a_i/W)^2+14.72(a_i/W)^3-5.6(a_i/W)^4\right)\right]}{(1-a_i/W)^{3/2}}$$

At the onset of fracture, $P_i = P_f$ and $K_{(i)} = K_{(f)} = K_Q$. In order to validate K_Q as K_{IC}, several constraints imposed by the ASTM E 399 standard should be fulfilled. In particular, the

specimen's dimensions should be such that the fracture process occurs mostly in plane strain conditions and in a brittle manner. These conditions are fulfilled provided that:

Eq. 5. 18 $$B,\ a > 2.5\left(K_Q / \sigma_{0.2}\right)^2$$

where a is the ligament size and $\sigma_{0.2}$ is the yield stress in tension. The constraints introduced by Eq. 5. 18 ensure that the plastic zone is very small when compared to the relevant specimen's dimensions and in particular the plastic zone is very small when compared to the zone dominated by the elastic singularity (i.e. where the stress field varies as $1/\sqrt{r}$).

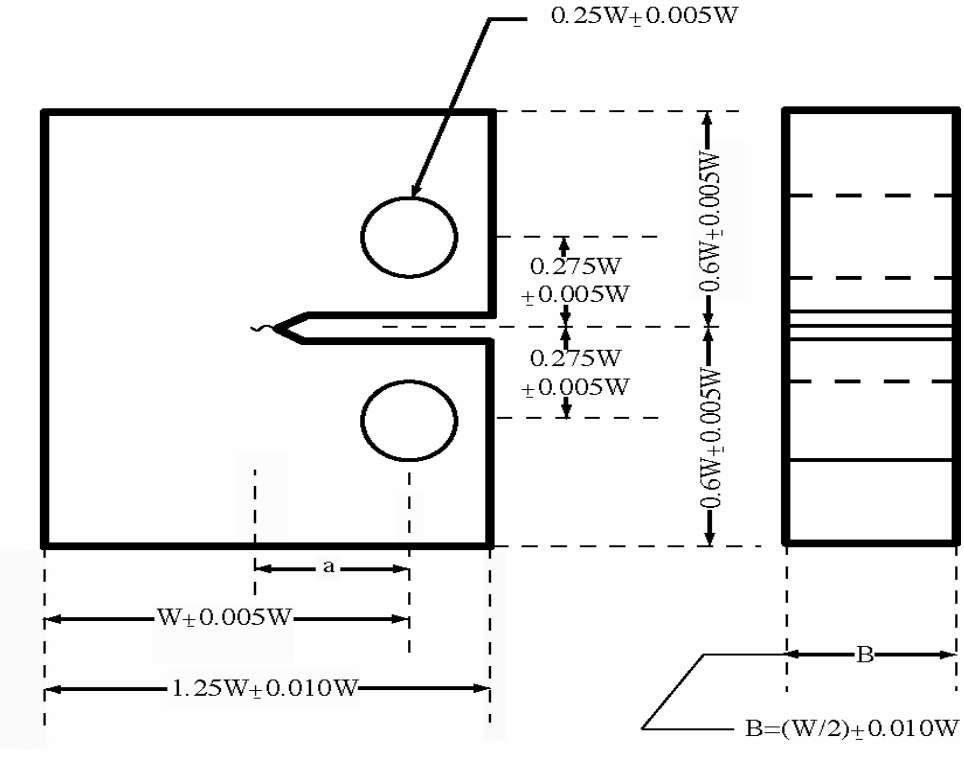

Figure 5. 7: *The C(T) specimen.*

The specimen size constraints imposed for a valid determination of K_{IC} can be relaxed if the toughness of the material is measured in terms of the critical values of the J-integral in plane strain J_{IC} (see next section). The compact specimens are one of the geometries accepted by the ASTM standard E-1820, which describes the procedure for the determination of J_{IC}. The J integral concept is also used to determine the fracture toughness of steels in the ductile-to-brittle transition region. In both cases, the experimental determination of J is based on the energy release rate definition of J. Typically, J is divided into two components:

Eq. 5. 19 $$J = J_{el} + J_{pl}$$

The elastic component J_{el} is calculated directly from the linear elastic stress intensity factor K_I, obtained from Eq. 5. 16 assuming $a = a_0$ (the initial crack length) through the following equation:

Eq. 5. 20
$$J_{el} = \frac{K^2\left(1-\nu^2\right)}{E}$$

In general, J_{pl} is calculated as follows:

Eq. 5. 21
$$J_{pl} = \frac{\eta A_{pl}}{B_N b_0}$$

where A_{pl} is the area representing the plastic work estimated from the load vs. load line displacement curve, B_N is the net specimen thickness ($B_N = B$ if no side grooves are present), b_0 is the uncracked ligament $(W - a_0)$ and for the case of the compact specimen, $\eta = 2 + 0.522 b_0 / W$. Note that the η factor is only dependent of the geometry of the specimen but it is independent on the properties of the material considered. Several η factors have been derived theoretically for certain selected configurations (see [5.5][5.17]). They have been deduced from dimensional analysis and/or plane strain FE simulations for Ramberg-Osgood materials having different hardening exponents.

It is common to convert J into an equivalent K with the equation

Eq. 5. 22
$$K_{Jc} = \sqrt{\frac{J_c E}{(1-\nu^2)}} = \sqrt{J_c E'}$$

where J_c is the elastic-plastic cleavage initiation toughness and E' is the plane strain Young's modudus. Finally, we mention that the critical crack tip opening δ_c at fracture is another toughness parameter that relates to J_c with a relation of the type:

Eq. 5. 23
$$J_c = m \sigma_y \delta_c$$

where m depends only on the constitutive behavior and on the specimen geometry. Typically values of m are about 2 [5.5].

5. 2. 7. Loss of constraint, and size limit for K_{Jc}.

Fracture toughness of steels in the ductile to brittle transition region is typically characterized by the J integral and/or K_{Jc}. In order to obtain a value K_{Jc} value that is specimen size independent, the stress fields generated by the crack should not be strongly affected by the specimen's free surfaces, but only mediated by the crack itself. The maximum load level that can be reached using a given specimen size, maintaining the previously described conditions,

will be a function of the material properties and specimen's geometry. This maximum load level is known as the specimen measuring capacity. From the point of view of the J integral concept, the measuring capacity of a fracture mechanics specimen is characterized by the dimensionless deformation level, D, which by can be expressed as:

Eq. 5. 24
$$D = \frac{K_{Jc}^2}{E' b_0 \sigma_{0.2}} = \frac{J_c}{b_0 \sigma_{0.2}} = \frac{m\delta_c}{b_o}$$

D must remain smaller than a given value mediated ultimately by the maximum crack tip opening displacement allowable. However, the constraint limit is more commonly expressed by the inverse of D with the so-called M value.

Eq. 5. 25
$$M = \frac{b_0 \sigma_{0.2} E}{K_{Jc}^2 (1 - \nu^2)} = \frac{b_0 \sigma_{0.2}}{J_c}$$

The M value has to be larger enough to avoid constraint loss effect. When the deformation level exceeds a certain limit, the stress and strain fields generated ahead of the crack are affected by the interaction with the free surfaces. As a consequence, the dominance of the singularity on the stress and strain fields is lost. The expression "loss of in-plane constraint" is used to identify the interaction of the stress fields with the free surface perpendicular to the direction of the crack propagation (back surface). Note that a loss of in-plane constraint does not directly affect a possible dominance of plane strain conditions along the crack front. Eq. 5. 25 also carries intrinsically limits in the specimen's thickness B. Indeed, in ideal conditions (a very thick specimen), the effect of the free surfaces normal to the crack front in the stress and strain fields is only restricted to a small fraction of the total crack front extension. However, when the thickness of the specimen is reduced, depending on the load level, the effect of the free surfaces on the overall behavior of the stress fields can be very important. This situation is known in fracture mechanics as a "loss of out-of-plane constraint". Plane strain conditions will prevail along the crack front of a specimen having a high degree of out-of-plane constraint. When constraint loss comes into play, from a M value too small, then fracture toughness is artificially raised.

The ASTM standard E-1921-03 (Master Curve Standard) recommends a value of M equal to 30. With such a value, Eq. 5. 25 is clearly less stringent than Eq. 5. 18 since the first one was developed to ensure the applicability of the LEFM, and the second one it is related to the use of the J integral, which allows a relatively large level of plasticity around the crack tip. However, It has been recently shown, on the basis of an extensive database obtained for the reactor pressure vessel steel A533B [5.64] that constraint loss effects occur for quite large values of M. In fact, for bend bar specimens fabricated from the reactor pressure vessel steel A533B, it was found that an M value > 100 is required to ensure fully constrained conditions. Joyce and Tregoning [5.61] confirm that a value of M > 150 is necessary to avoid sizes effect with bend bars specimens while a M value of 30 is adequate for the compact tension specimens [5.61].

5. 2. 8. Statistical effects to cleavage fracture in steels.

As mentioned in the Literature Survey (Chapter 2), cleavage fracture in steels is intrinsically statistical in nature. This is reflected by a large scatter in the transition region. In the case of highly constrained specimen or, in other words, for small scale yielding conditions, the probability of failure of a given specimen increases with the loading level, represented by K_j, according to the following three-parameter Weibull equation[5.5][5.6][5.49]:

Eq. 5. 26
$$P_f(K_J) = 1 - \exp\left[-\left(\frac{K_J - K_{\min}}{K_0 - K_{\min}}\right)^4\right]$$

The derivation of this widely used equation is shown in the Appendix 1. We just mention here that the Weibull slope 4 arises from the observation that the stress volume $V(\sigma^*)$, the volume encompassing a critical stress σ^* scales with K_j^4. In addition, the existence of a threshold in toughness, K_{min}, is the consequence of a mathematical derivation that involves the sequence of two successful mechanisms, namely crack initiation and crack propagation.

Most of the time we have to deal with specimens loaded up to levels that are not representative of small scale yielding conditions. This is especially true in the nuclear material community, which has been forced to us small specimen test techniques. Local approaches for ductile and brittle fracture have been developed over the years to take into account the specimen volume under a critical stress and the loss of constraint.

5. 3. Experimental results and analysis of the Eurofer97 fracture database.

5. 3. 1. Fracture toughness measurement with 0.4T C(T) and 0.2T C(T) in the lower transition.

We have generated an extensive database characterizing the fracture behavior of the Eurofer97 steel in the ductile to brittle transition region. 0.4T C(T) and 0.2T C(T) specimens have been used in the study.

The tests with the 0.4T C(T) specimens have been performed at five different temperatures: -100°C (32 specimens), -120°C (27 specimens), -130°C (15 specimens), -140°C (12 specimens) and -150°C (5 specimens). Specimens with both the L-T and T-L orientation were prepared. They were tested at a constant machine cross-head velocity of 0.1 mm/min.

The tests with the 0.2T C(T) specimens have been performed at only two temperatures, namely -120°C (13 specimens) and -100°C (39 specimens). The orientation of all the 0.2T C(T) specimens was the L-T one and they were tested at a constant machine cross-head velocity of 0.05 mm/min. The velocity was selected to produce approximately the same strain rate in the material ahead of the crack as in the case of the 0.4T C(T) specimens.

The results of the fracture toughness tests have been evaluated in terms of the elastic-plastic stress intensity factor K_{Jc}, derived from the value of the J integral at the onset of cleavage fracture, J_C. In the Appendix 2, all the results are summarized in Tables.

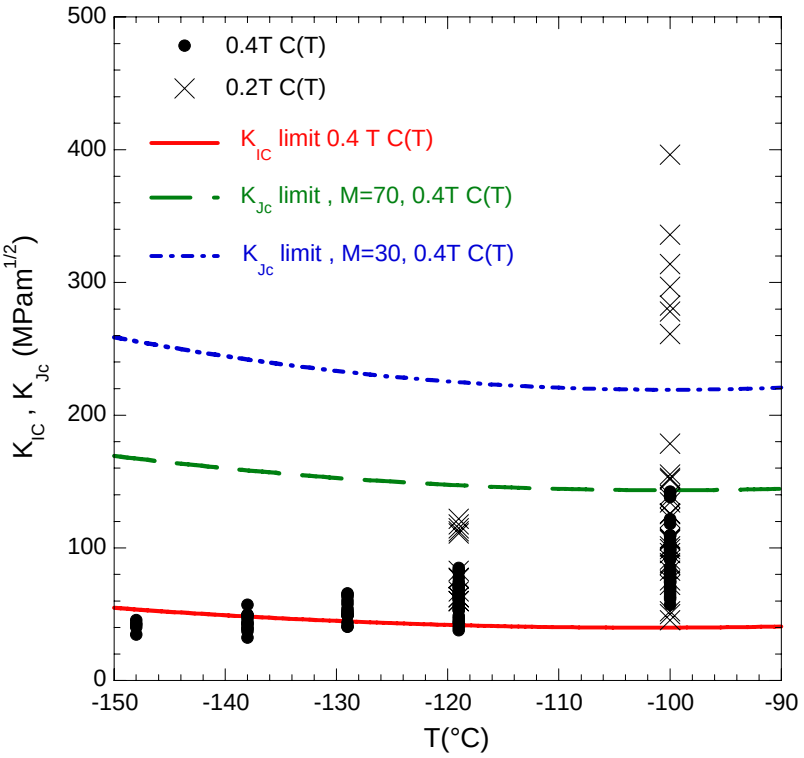

Figure 5. 8: *Raw fracture toughness data, K_{jc}. 0.4T C(T) and 0.2T C(T) specimens.*

All the results of the fracture tests are shown in Figure 5. 8, where the K_{Jc} data are plotted as a function of temperature. As can be seen, the tests were performed in the lower shelf and transition region, where the typical and inherently large scatter was observed. All specimens failed by quasi-cleavage, in some cases after some plastic deformation and crack blunting, resulting in loss of constraint. A clear difference between the 0.2T and 0.4T C(T) specimens can be seen at T = -100°C where much larger values have been measured for the smallest (0.2T C(T)) specimens. This is an unambiguous indication of constraint loss that has occurred on these specimens. In Figure 5. 8, we have also indicated, for the 0.4T C(T) specimens, three K limits. The first one in red is the K_{Ic} limit, given by Eq. 5. 18. This shows that valid K_{Ic} data can be obtained only in the lower shelf. The second one in blue corresponds to a M value of 30 (see Eq. 5. 25). This value is that recommended in the ASTM E1921-03 standard to determine T_o in ferritic steels (see next Section). All our 0.4T C(T) data actually meet the size requirement of the ASTM E1921-03. Finally the third limit is associated to a M value equal to 70, the value below which all our data point lie.

5. 3. 2. Analysis of the experimental 0.4T C(T) data using the ASTM E-1921-03 standard.

At each temperature in the ductile to brittle transition region, where the fracture toughness data are highly scattered, it is possible to determine a mean toughness value, $K_{Jc(med)}(T)$. In this way, the locus of $K_{Jc(med)}$ vs. T can be compared between different materials. It is accepted that several families of steels share the same master curve (same $K_{Jc(med)}(T)$ shape) in the transition region provided that the datasets have been corrected to account for the deviations arising from the use of different specimen's geometries (the so-called size effect). Steels having bainitic, tempered bainitic, tempered martensitic and ferritic microstructures (called hereafter, "ferritic" steels) are believed to obey the "master curve" concept. The actual shape of the master curve has been derived from testing a very extensive set of large specimens made of reactor pressure vessel (RPV) steels. The master curve equation is given by:

Eq. 5. 27
$$K_{Jc(med)}\left[MPa\cdot m^{1/2}\right] = 30 + 70\exp\left[0.019\left(T - T_0\right)\right]$$

where T is the test temperature in °C, T_0 is the reference temperature. The validity of the master curve in the case of other types of steels has been justified based on several experimental works (see for instance [5.54] to [5.59]).

The master curve approach is used in combination with the reference temperature (T_0) concept, defined as the temperature where $K_{Jc(med)}$ is equal to 100 $MPa\cdot m^{1/2}$ for the case of 1T size specimens. The ASTM E-1921-03 standard describes the determination of T_0 in the ductile-to-brittle transition (DBT) region for the general case of "ferritic" steels.

All the master curve concepts presented above have not been extensively validated for the particular case of tempered martensitic stainless steels. There is a lack of systematic studies oriented towards the validation of the master curve concept on these types of steels. The

database generated in the present work offers an excellent possibility to check the master curve concept.

5. 3. 2. 1. Brief description of the ASTM E-1921.

The determination of T_0 is based on the hypothesis that cleavage fracture in these types of steels can be well described by a weakest-link type process. A three-parameter Weibull distribution is assumed to describe the scatter in the fracture toughness values at a given temperature:

Eq. 5. 28
$$P_f(K_{Jc}) = 1 - \exp\left[-\left(\frac{K_{Jc} - K_{\min}}{K_0 - K_{\min}}\right)^m\right]$$

Two parameters of the Weibull distribution, the Weibull slope m and the assumed minimum threshold toughness value ($K_{\min}$) are considered to be independent of the temperature and equal to 4 and 20 $MPa \cdot m^{1/2}$ respectively. The scale parameter K_0 is determined at each temperature by the maximum likelihood method, and it represents the toughness value at this temperature that yields P_f =0.632.
The size effect (statistical effect associated with the crack front length) previously discussed is considered in the ASTM E-1921-03 standard based in the weakest link results as follows:

Eq. 5. 29
$$K_{Jc(x)} = K_{\min} + \left[K_{Jc(o)} - K_{\min}\right] \cdot \left(\frac{B_o}{B_x}\right)^{1/4}$$

where $K_{Jc(x)}$ is the fracture toughness of an specimen of thickness B_x. Eq. 5. 29 allows scaling of the results obtained from a given specimen size to another one. The ASTM E-1921-03 requires that the analysis must be performed in terms of a 1T size specimen (25.4 mm thick). Therefore, datasets obtained from specimens having sizes different than 1T must be corrected with the Eq. 5. 29.
In principle, the determination of T_0 must be independent from the type of specimen used and independent from the dimensions of the specific specimens used.
A censoring criterion is introduced in the ASTM E1921-03 to account for the potential loss of constraint in specimens displaying high fracture toughness values. A data point is in general considered as "valid" (i.e. size & geometry independent) if the measured K_{Jc} is smaller than $K_{Jc(limit)}$ that given by:

Eq. 5. 30
$$K_{Jc(\lim)} = \sqrt{\frac{E \cdot b_0 \cdot \sigma_{0.2}}{M \cdot (1 - \nu^2)}}$$

where M = 30. If this condition is fulfilled, the determination of T_0 is, in principle, not affected by the constraint loss effect. The M value has been proposed based on numerical studies on 3D models (see for instance [5.18]). Today, it is accepted that a value of M=30 is certainly too low for the case of SEN(B) specimens. Indeed, for this type of specimens, a limiting value of M=200 has been proposed for the determination of T_0 [5.61]. On the contrary, M=30 is accepted as a proper limit for the case of C(T) specimens.

The ASTM E1921-03 requires at least six valid tests in the temperature interval $-50 \le T - T_0 \le 50$, where T is the test temperature. The standard procedure recommends that the K_{Jc} dataset must be determined at a single temperature, as near as possible to the (estimated) T_0 temperature. In the case of small specimens, testing must be carried out at temperatures well below T_0 in order to obtain several valid fracture toughness measurements, fulfilling the size limit of Eq. 5. 30. It is also possible to perform a multi temperature analysis. However, the recommended procedure consists in generating a dataset at the same temperature as near T_0 as possible.

Once the fracture dataset has been generated and assuming that all the data points are valid data, the scale parameter K_0 is determined by means of the maximum likelihood method (see [5.8] for a description of the procedure when the dataset has censored data):

Eq. 5. 31
$$K_0 = \left[\sum_{i=1}^{N} \frac{\left(K_{Jc(i)} - K_{\min}\right)^4}{N} \right]^{1/4}$$

Having determined K_0, the mean fracture toughness value $K_{Jc(med)}$ can be easily obtained from Eq. 5. 28 as follows:

Eq. 5. 32
$$K_{Jc(med)} = K_{\min} + \left(K_0 - K_{\min}\right) \cdot \left[\ln(2)\right]^{1/4}$$

The ASTM E 1921-03 standard assumes that the temperature dependence of $K_{Jc(med)}$ is described by the master curve expression. On this basis, T_0 is given by:

Eq. 5. 33
$$T_0 = T - \left(\frac{1}{0.019}\right) \cdot \ln\left[\frac{K_{Jc(med)} - 30}{70}\right]$$

5. 3. 2. 2. Application of the ASTM E1921-03 standard to the Eurofer97 steel.

The 0.4T C(T) Eurofer97 dataset has been analyzed following the ASTM E1921-03 procedure. Since a large number of data points are available at each temperature, the single temperature approach has been chosen for the analysis of the fracture data. The standard suggests that the dataset used must be generated as close as the reference temperature as possible. Following this criterion, only two datasets have been considered for T_0 determination: -100°C and -120°C. If we only consider the dataset corresponding to -100°C,

a T_0= -89°C is obtained. Note that in this case $T-T_0$= -11°C. Alternatively, we may consider the both datasets at -100°C and -120°C. In this case, by means of the multi-temperature analysis we obtain T_0= -76°C, close to the value determined previously. The $K_{Jc(med)}$ vs. T prediction of the master curve (Eq. 5. 27) for the case of T_0=-89°C is plotted together with the complete fracture dataset (Figure 5.9). It is evident from the analysis of the figure that the experimental trend of the $K_{Jc(med)}$ values versus temperature is not well described by the master.

The results presented here raise some reasonable doubts concerning the validity of the ASTM E-1921-3 master curve approach as a proper description of the $K_{Jc(med)}$ vs. T for the particular case of tempered martensitic steels. Indeed, the results suggest that in order to properly describe the observed trend of the experimental data, another expression for the shape of the $K_{Jc(med)}$ vs. T curve shape is necessary. To further explore this possibility, the following equation has been used to fit the experimental data set:

Eq. 5. 34 $$K_{Jc} = 30 + 70\exp\left[m_1 \cdot (T - m_2)\right]$$

In Figure 5. 10, we plot the 1T corrected data, fitted with Eq. 5. 34. The figure clearly shows that the fitted curve offers a much better description of the evolution of $K_{Jc(med)}$ with the temperature than the prediction of the ASTM E1921-03 master curve. Note that the error bars in Figure 5. 10 correspond to the 90% confidence interval for the estimated $K_{Jc(med)}$, assuming a Weibull distribution having a shape parameter m=4 (the details of the procedure involved in the determination of the confidence bounds of the parameters of the Weibull distribution are presented in the Appendix 3).

Based on the fitting of the experimental data, the following expression is proposed for the evolution of $K_{Jc(med)}$ vs. T for the case of Eurofer97 (1T corrected data):

Eq. 5. 35 $$K_{Jc(med)} = 30 + 70\exp(0.04(T - T_0))$$

Consistently with Eq. 5. 35, for the case of a single temperature analysis, the reference temperature T_0 will be given by:

Eq. 5. 36 $$T_0 = T - \left(\frac{1}{0.04}\right) \cdot \ln\left[\frac{K_{Jc(med)} - 30}{70}\right]$$

Finally, the upper and lower bounds can be estimated from the following expression:

Eq. 5. 37 $$K_{Jc(0.xx)} = 20 + \left[\ln\left(\frac{1}{1-0.xx}\right)\right]^{1/4} \left\{11 + 77\exp\left[0.04\left(T - T_0\right)\right]\right\}$$

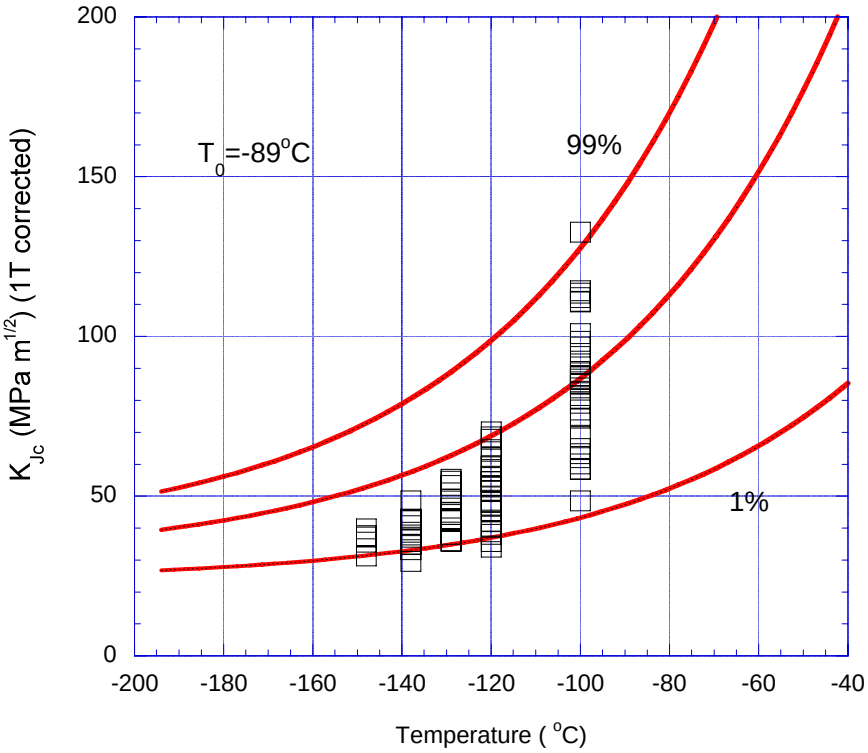

Figure 5. 9: *Experimental dataset obtained for the Eurofer97 steel. All the data corresponds to 0.4T C(T) specimens. Considering only the data at -100°C, the ASTM E1921-03 procedure yields* T_0 *=-89°C.*

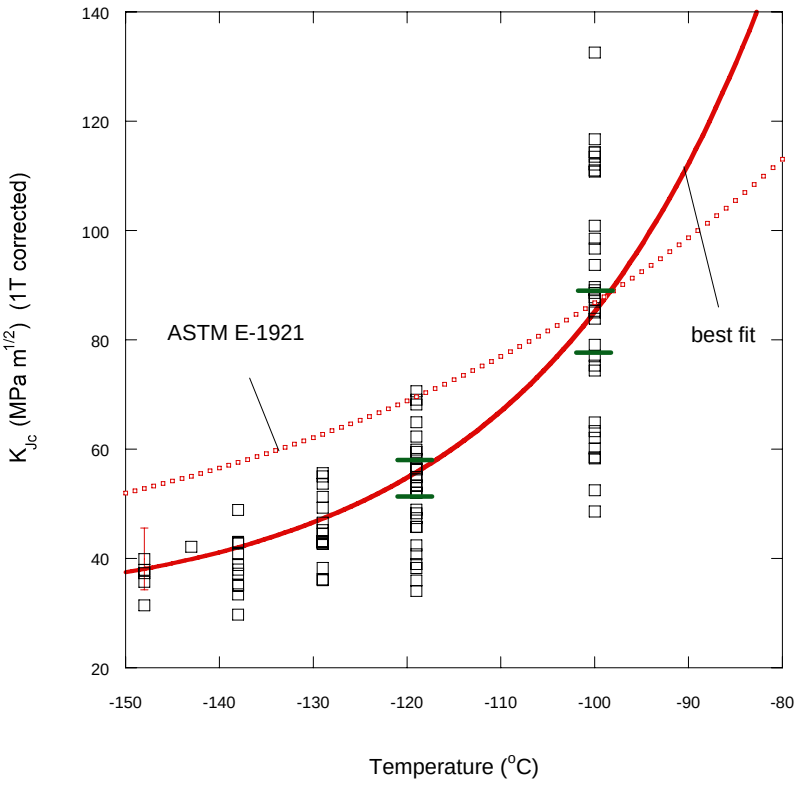

Figure 5. 10: *Fitting of the experimental data with Eq. 5. 34. The 90% confidence bound for* $K_{Jc(med)}$ *at -100°C and -120°C as determined from the experimental data is also shown.*

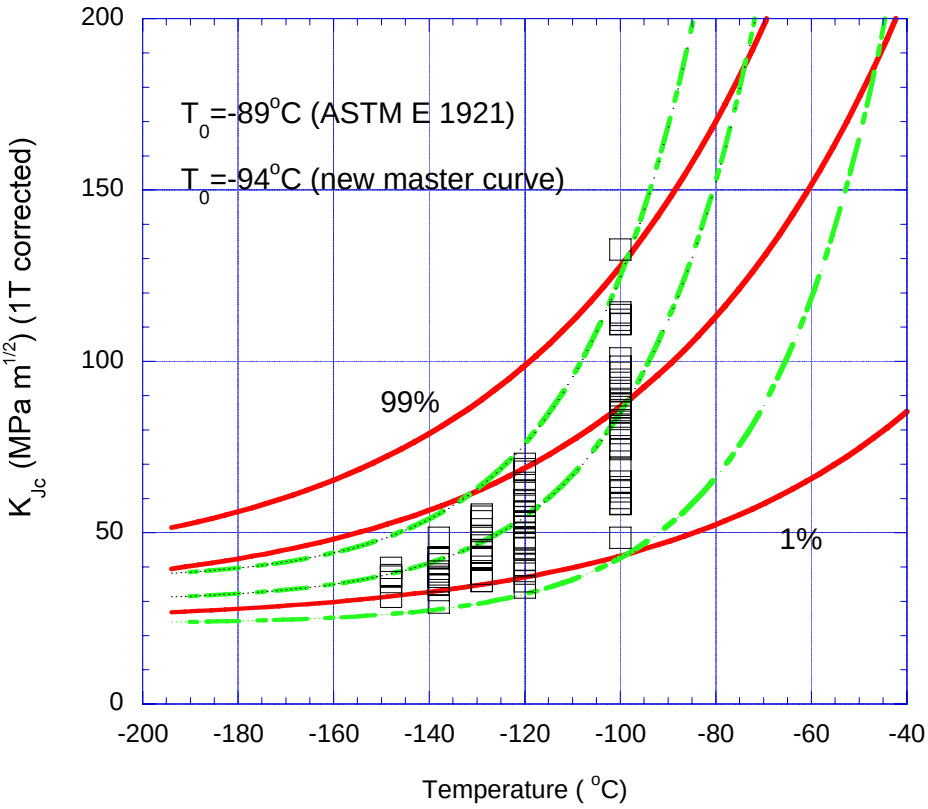

Figure 5. 11: *New master curve as given by Eq. 5. 35.The 1% and 99% confidence bounds are also shown. A T_0 =-94°C is obtained. The ASTM master curve is also shown.*

The modified master curve as given by Eq. 5. 35 and the 99% upper and 1% lower bounds as given by Eq. 5. 37 are plotted together with the experimental dataset in Figure 5. 11.
A T_0 =-94°C has been determined from the analysis of the 0.4T C(T) dataset at -100°C. The agreement between the experimental dataset and the modified expression for the master curve is excellent. The modified master curve fully accounts for the experimental trend of the $K_{Jc(med)}$ with the temperature.

The predictions of the upper and lower bounds seem also to be fully consistent with the experimental data.
J.W. Rensman [5.73] has presented a database obtained from C(T) specimens in the L-T orientation of the 25 mm thick plate and of the 14 mm and 8mm thick plates of Eurofer97 (different casts). His dataset for the 25mm plate is shown in Figure 5. 12 together with our own dataset. Considering the 25 mm plate results, the data is completely consistent with our results, giving further support to the use of Eq. 5. 35. However, the data obtained from the 14 mm and 8mm plates show a clear difference from the trend observed for the 25 mm plate. Even though in this case the number of experimental results is quite limited, the data suggest that the thinner plates may be slightly tougher than the 25mm plate.
We have accounted for these differences by means of Eq. 5. 35, implemented as described above. In this way, we obtain a T_0 = -112°C for the case of the 8mm/14 mm plates data set. Consequently, a difference of approximately 18°C seems to exist among the respective T_0 (-

112°C against -94°C for the 8mm/14mm plates and 25mm plate respectively). The results of the analysis are presented in Figure 5. 13, where Eq. 5. 35 is plotted for T_0 = -112°C together with the 1% and 99% confidence bounds as estimated from Eq. 5. 37. As observed in the figure, the agreement of the predictions of Eq. 5. 35 with the available experimental data is very good.

The complete C(T) dataset for Eurofer97 is plotted in Figure 5. 14. The predictions of the ASTM E-1921 master curve and Eq. 5. 35 are also shown. The overall description of the experimental data as given by Eq. 5. 35 is excellent. Note that for this case, the curve representing the 1% cumulative probability to fracture bounds perfectly the dataset, offering a conservative description for the risk of catastrophic failure. From an integrity assessment point of view, the validation of Eq. 5. 35 as a proper description for the evolution of $K_{Jc(med)}$ with T is a critical issue. When the lower bound (1% failure probability for instance) associated to Eq. 5. 35 is considered, the secure operational region (defined as $K_J < K_{Jc(0.01)}$ at a given temperature) for a flawed structure is much larger than that determined following the ASTM E1921 approach (see Figure 5. 14).

Concerning the shift measured in T_0 between the plates, the available Charpy data for these plates is fully consistent with the results previously presented (Figure 5. 15). Indeed, the DBT occurs clearly at higher temperatures in the case of the 25mm plate, being the shift approximately 20°C, in fully agreement with the value determined from fracture mechanical testing. The fact that the measured ΔT is the same regardless the method used for the determination of the shift is certainly remarkable and it is somehow in opposition to what it has been reported previously for the case of irradiated Eurofer97.

From the point of view of a basic fracture mechanic study, it is important to identify the metallurgical features that may lead to the observed differences in fracture toughness between the 8mm/14 mm and the 25 mm plates. However, it is in principle quite difficult to clearly identify the origin of the observed behavior. Hereafter, potential sources for the observed differences in toughness are mentioned. Albeit incomplete, the information available suggests that from a metallurgical point of view, the two plates are very similar.
The prior austenitic grain size is exactly the same in both plates [5.62], so it can be ruled out as the source for the observed differences.
Since the thickness of the plates is not the same, some microstructural differences may have arisen from the different cooling rate during normalization and tempering. Unfortunately a detailed description of the microstructure of the 8mm and 14 mm plates based on TEM studies is not available at present. A second argument that may explain the observed differences in fracture toughness can be derived from the analysis of the chemical composition of the plates. Indeed, some differences in the Cu content (0.0019 wt% and 0.0039 wt% for the 14 mm plate and 25 mm plate respectively) and in the Mo (<0.0010 wt% and 0.0023wt%) do exist between the plates. The contents for all the other alloying elements is practically the same. Therefore, the excess of Mo and Cu in the 25 mm plate may have a detrimental influence in the fracture toughness, affecting the measured T_0 temperature.

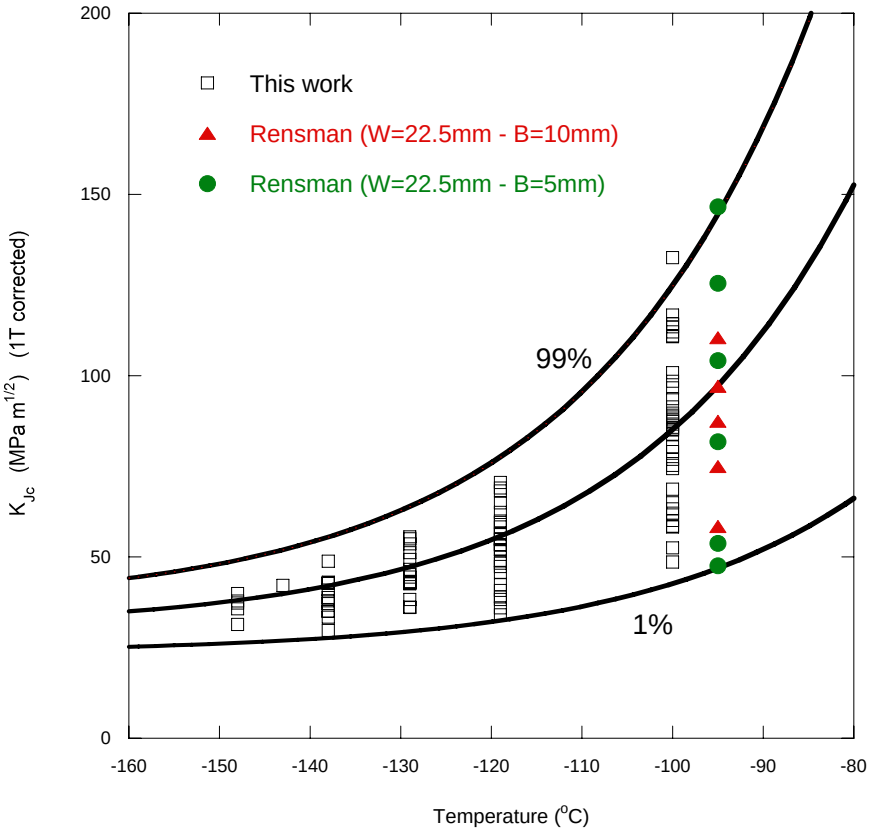

Figure 5. 12: *Compilation of the fracture data for the Eurofer97 steel (25mm plate). Note that only C(T) data was considered. Using the new master curve expression,* T_0 *=-94°C has been determined for the 25mm plate.*

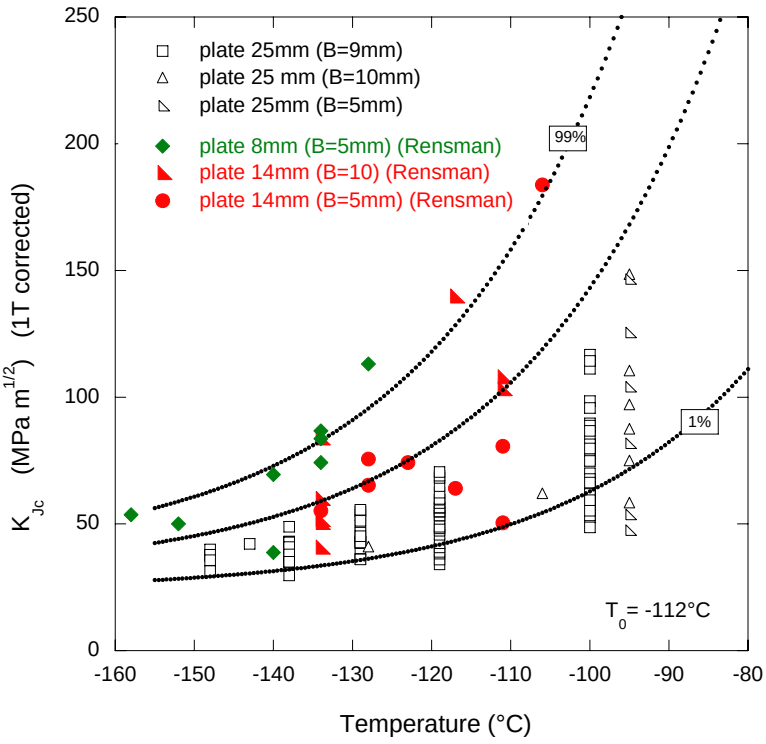

Figure 5. 13: *Master curve as given by* Eq. 5. 35 *indexed for the 14 mm plate data. A transition temperature equal to -112°C is obtained in this case.*

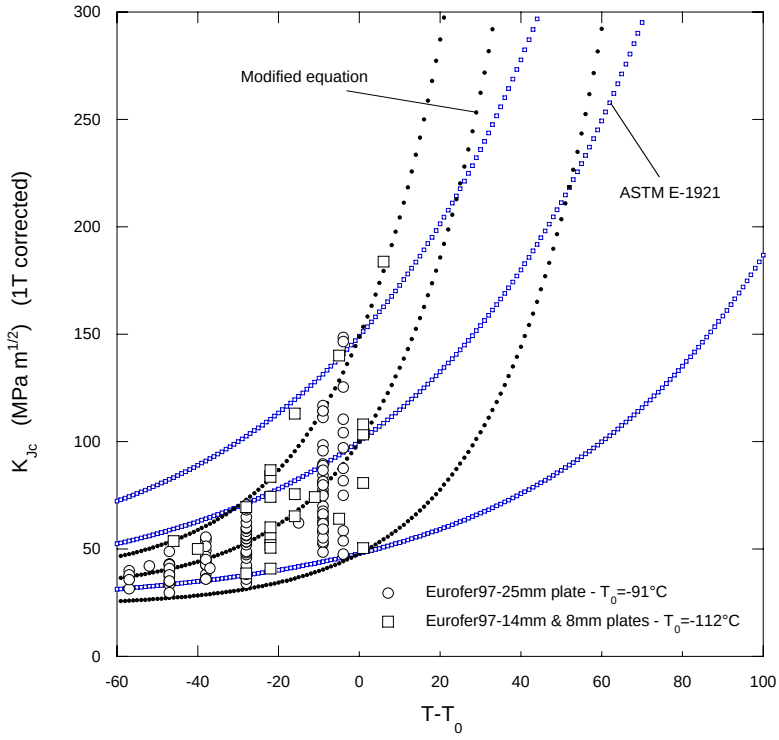

Figure 5. 14*: Compilation of the available fracture toughness data for Eurofer97 (8mm, 14mm and 25mm plates).* Eq. 5. 35 *fully accounts for the experimental results.*

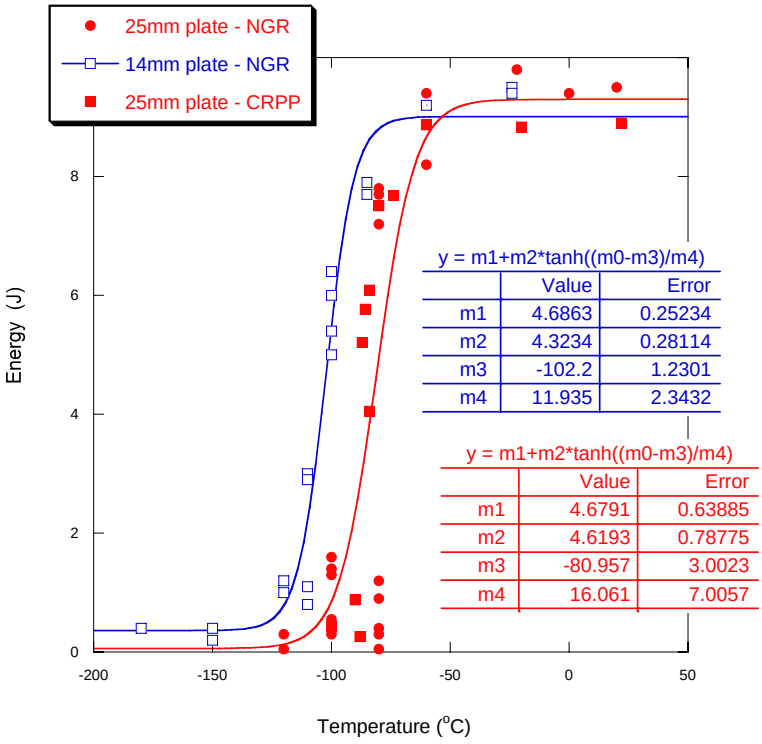

Figure 5. 15: : *Charpy data (KLST specimens) for the Eurofer97 (48 data points) and F82H mod.(29 data points) (Klueh [5.66], Dai [5.67], NRG[5.68]). The difference in the ductile to brittle transition temperature between the 14mm plate and the 252mm Eurofer97 plate is 20°C.*

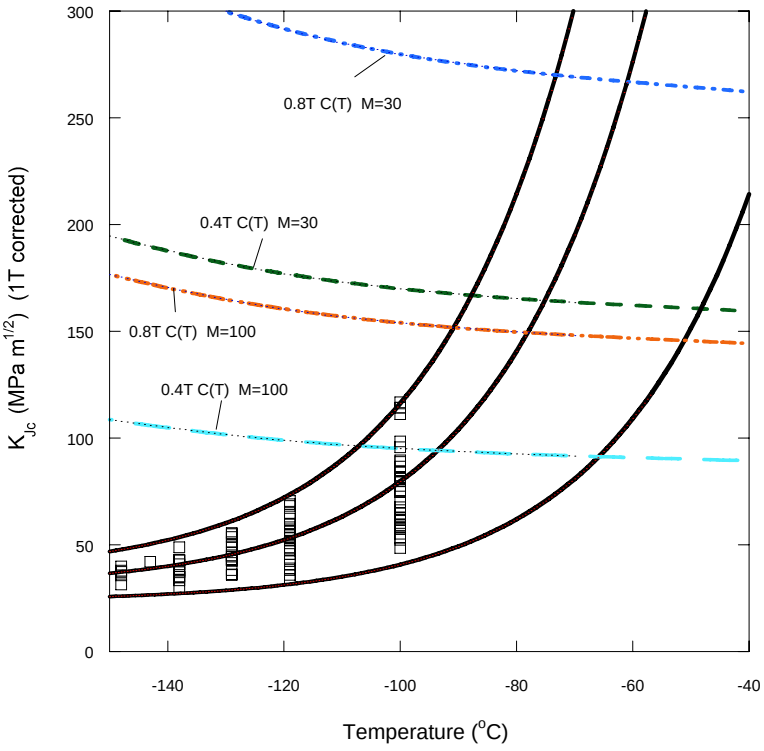

Figure 5. 16: *Deformation levels for different specimen sizes for the case of the Eurofer 97. The plot suggest that fracture toughness at higher temperatures in the transition region can be investigated by means of 0.8T C(T) specimens with very high degree of constraint.*

The conclusions presented here need to be corroborated by testing at higher temperatures in the transition region.

As shown in Figure 5. 16, 0.8T C(T) specimens are needed in order to ensure sufficient constraint at this temperature. We expect that the availability of this dataset will give strong further support to all the results previously presented.

In summary, a new master curve, valid for the Eurofer97 tempered martensitic steel has been determined in the DBT region by testing 0.4T C(T) specimens. A large number of tests have been performed at five temperatures. The scatter exhibited by the fracture toughness values in the transition region and its evolution with temperature were successfully accounted for by modifying the shape of the master curve as given in ASTM E-1921. In this sense, the 99% upper and 1% lower failure probability limits were observed to bound correctly the experimental data. All the specimens were tested at temperatures for which the M value, characterizing the constraint level was larger than 70, which is believed to be larger enough to avoid constraint loss on C(T) specimens. The experimental results indicate that the shape of the K(T) curve is steeper than that of the RPV steel as described by the ASTM E-1921 standard. Thus a modified shape has been proposed for the Eurofer97.

The analysis of our results with other published data has revealed differences in toughness between the Eurofer97, 25mm plate and the 8mm and 14mm plates. This difference is reflected in variation of about 20°C in T_0 values.

5. 3. 3. Analysis of the experimental 0.2T C(T).

In order to gain insight into the potential of the small specimen test techniques for the assessment of material toughness after irradiation, we have also tested a series of 0.2T C(T) specimens.

We have focused our efforts on only two temperatures: -120°C (13 specimens) and -100°C (39 specimens). The 0.2T C(T) database has been used to address two different problems. The first one consists in the identification of potential variations of the material toughness through the Eurofer97 plate thickness. Wallin and co-workers have presented experimental data supporting the hypothesis of the existence of such toughness variation through the thickness in the F82H steel [5.63]. Their results, obtained from SEN (B) and C(T) specimens suggest that the F82H 25 mm thick plate is more brittle in the middle section than in the regions located near the surfaces. Logically, this paper has raised some concerns in the fusion community concerning the potential existence of anisotropic properties in the thicker plates. However, to our knowledge, the results presented by Wallin et al. have not been confirmed nor refuted by posterior work. The 0.2T C(T) database generated in the framework of the present work is aimed at addressing this problem. To do so, each 0.2T C(T) specimen has been identified in such a way that it can be traced back to its original location in the 25 mm plate. In this way, the results obtained from the specimens taken from regions near the plate surfaces can be easily compared to the results obtained from specimens located in the middle section of the plate, allowing assessing the possible variation of toughness through the 25 mm thick plate of Eurofer97.

The second problem that arises naturally from the analysis of the results obtained from small specimens is related to the measurement capacity of the specimens, which is limited by the existence of the so-called loss of constraint of the specimens. A detailed discussion of these two problems is presented next.

5. 3. 3. 1. Anisotropy in the fracture toughness through the thickness.

The results for the testing at -120°C and -100°C are presented in Figure 5. 17 and Figure 5. 18. The results obtained at -120°C are especially valuable since at this temperature they do not suffer from excessive loss of constraint. The analysis of the data obtained at -120°C indicates that, in the case of the Eurofer97, the measured toughness does not indicate any thickness dependence, contrary to what has been suggested by Wallin et al in the case of the F82H.

In the case of -100°C, a more extensive testing has been carried out, since we have tested 19 specimens from regions near the plate surfaces and 20 specimens from regions in the middle section of the plate. Again, the analysis of the figure shows that the trend of the data of the two datasets is quite comparable, without indication of toughness dependence through the thickness. However, it is interesting to point out that the minimum toughness value obtained for the "surface" data is lower than the minimum toughness value obtained for the "middle section" data ($\approx 53\ MPa \cdot m^{1/2}$ to $35\ MPa \cdot m^{1/2}$ for 1T specimens). Considering that almost 20 specimens have been tested for each condition, the difference observed in the minimum

toughness value may be statistically significant. If this is the case, such difference can be rationalized based on a micromechanical model for cleavage fracture. Indeed, it is usually accepted that the fracture of brittle particles in the microstructure (carbides, inclusions, etc.) gives rise to a certain distribution of microcracks ahead of the crack tip. Under certain conditions, some of these microcracks may become critical and propagate through the material leading to a sudden failure of the specimen. The lower toughness values of the toughness distribution at a certain fixed temperature are associated to the potential existence of large particles in the stressed volume immediately ahead of the crack tip. The fracture of this large particle generates a large microcrack that, if properly oriented, propagates at lower stresses, i.e., lower K_J values. Thus, a difference in the size of the largest observed particles may be expected through the plate thickness, slightly increasing in the regions near the surface. Note that in fact, there exist slight differences in the thermo-mechanical history between the material in the middle section and near the surfaces. The material in the middle section of the plate is expected to be cooled down slower than the material near the surfaces, allowing more time for auto-tempering during the cooling of the plate. The difference in auto-tempering may generate slight differences in the amount of carbon in solid solution at the moment of tempering. Since the auto-tempering process removes some carbon from solid solution, the concentration of this element is expected to be larger in the regions near the surfaces, decreasing again perhaps in the very surface due to the expected decarburizing processes. This small difference in the carbon concentration through the thickness prior to tempering may be responsible for the difference in the largest particle sizes.

5. 3. 3. 2. Loss of constraint and constraint correction.

The ASTM E1921-03 standard introduces a correction for the fracture toughness due to a statistical size effect in fracture. This size effect follows from the interpretation of brittle fracture as a weakest link-type process, and it is expressed by Eq. 5. 29. This equation allows us to scale the toughness results obtained from a given specimen geometry to the values that we would have obtained if another geometry (size) were been used. However, the foregoing statement is only valid for the case of well constrained data, which in term of ASTM E-1921 means M >30. As discussed previously in Section 5.2.7, lost of constraint strongly affects the experimental results when the measuring capacity of the specimen specimens has been reached. Consequently, it give rises to apparent high fracture toughness values. Lost of constraint problems are in general associated to the use of small specimens, which are typically used in the assessment of the degradation of fracture toughness due to irradiation in a given material.

When testing a set of small specimens the dataset obtained will be composed of “valid” (well constrained) data points and “invalid” data points. In principle, it may be possible to determine an “experimental” lower bound for fracture toughness from testing small specimens, provided that the lower toughness data points are valid data. However, this is certainly impractical since a prohibitive large number of tests will be needed at each temperature of interest. On the contrary, one of the main advantages of the method described in ASTM E 1921 consists on the fact that only a few tests are needed to assess the integrity

of a given material. As described previously in Section 5.3.2.1, the method is based on the assumption that in the case of cleavage fracture, fracture toughness data follows a three parameter Weibull distribution, where only one parameter is unknown, K_0. In principle, only few specimens are needed to estimate K_0. However, a dataset were several data points suffer from lost of constraint is not expected to follow the Weibull distribution. To deal with this problem, the present version of ASTM E1921 assumes that the censoring procedure with censoring limit of M =30 is the only tool needed to account for the lost of constraint problem. Assuming that this hypotheses is correct and provided that the standard procedure is closely observed, the values estimated for the relevant parameters of the Weibull distribution from a 0.2 T C(T) dataset composed of valid and invalid data would be expected to be the same (in an statistical sense) than the values estimated from other specimens sizes, i.e. 0.4T C(T). Note that no constrain corrections of any kind intervenes in the process.

A direct consequence of this is that the relevant information concerning the in-service evolution of the material's fracture toughness could be assessed by using small testing specimens. ASTM E 1921 use the shift in the "reference temperature" to assess the degradation of fracture toughness due to the in service conditions. The quantification of the shift in the transition temperature is assumed to be independent of the specimen size and geometry used for testing, provided that the procedure described in the standard is closely observed.

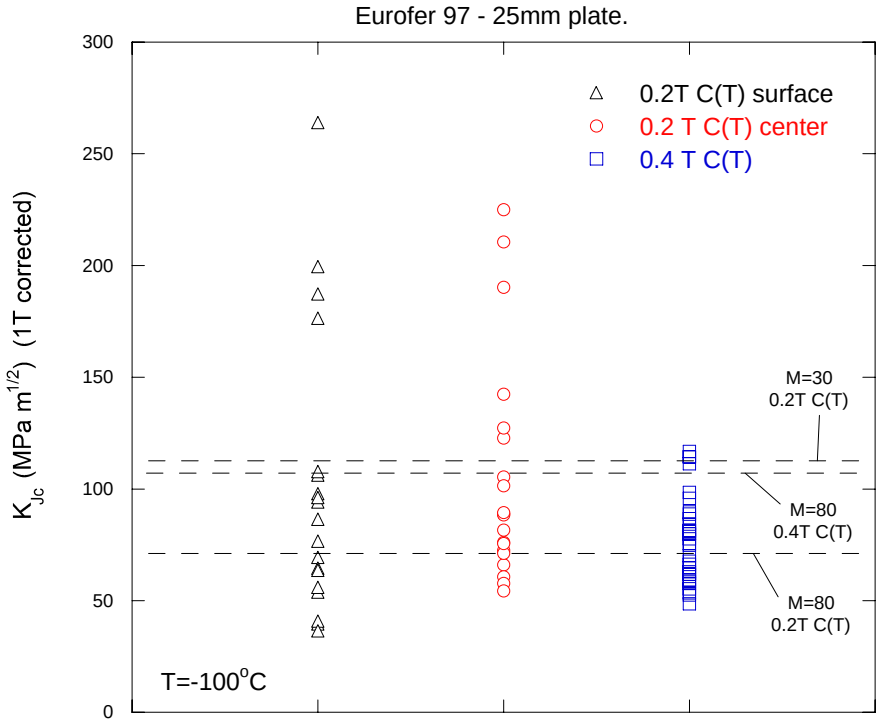

***Figure 5. 17**: K_{Jc} data for the 0.2T C(T) specimens at T = -100°C*

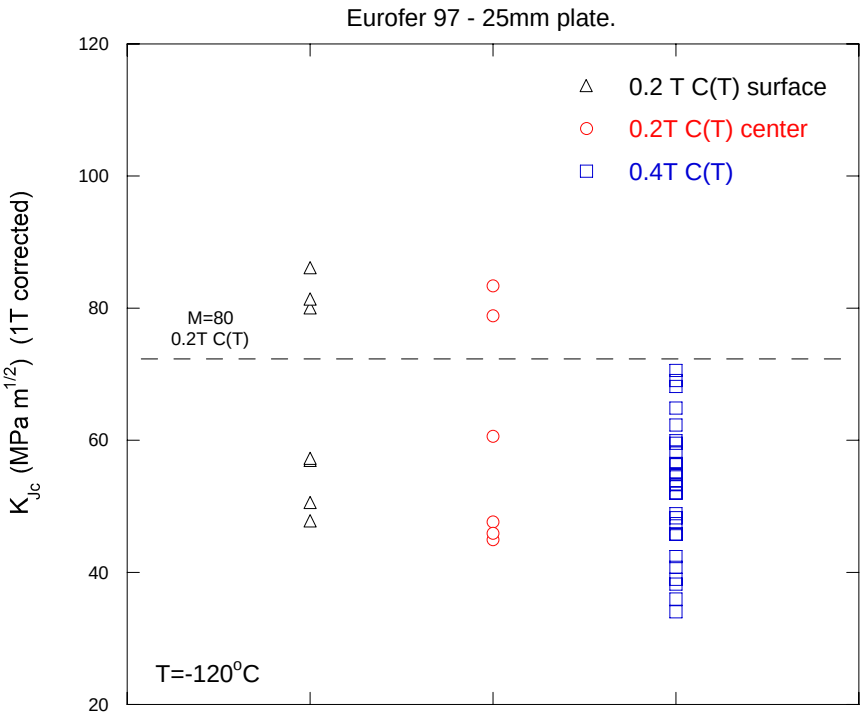

Figure 5. 18: *K_{Jc} data for the 0.2T C(T) specimens at T = -120°C*

The statistical analysis of the fracture data obtained from the 0.2T and 0.4T C(T) specimens has been performed following ASTM E1921. A Weibull slope m=4 and a minimum toughness value $K_{\min} = 20MPa \cdot m^{1/2}$ have been assumed. Consistently, only the shape parameter K_0 has been estimated by means of the maximum likelihood method. Once K_0 has been estimated, the $K_{Jc}(med)$ was derived from Eq. 5. 28 by setting $P_f = 0.5$. The 99% confidence bounds for $K_{Jc}(med)$ have been obtained following the procedure described in the Appendix 3. Finally, the cumulative 99% probability to fracture, $K_{Jc}(99\%)$, was calculated from Eq. 5. 28, by using the estimated K_0 value. Logically, the uncertainty in the real value of $K_{Jc}(med)$ will be reflected in an uncertainty in $K_{Jc}(99\%)$.
The correspondent confidence bounds for $K_{Jc}(99\%)$ has been determined by means of the following expression:

Eq. 5. 38
$$\Delta K_{Jc}(99\%) = \Delta K_0 \cdot \ln\left[\frac{1}{0.01}\right]^{1/m}$$

The meaning of ΔK_0 in the foregoing equation is made clear considering that $K_0 \pm \Delta K_0$ defines a certain confidence interval for the estimated K_0, i.e. 95% confidence interval.

Let's first focus our attention on the datasets at -120°C (Figure 5.19). In this case, both datasets (0.2T and 0.4T C(T)) are composed only of "valid" data (M>30), therefore, the

censoring procedure does not need to be applied. It can be observed that the median toughness $K_{Jc}(med)$ as determined from the 0.2T C(T) specimens is significantly higher than the correspondent value as measured from 0.4T C(T) specimens. Indeed, we have obtained $K_{Jc}(med)=66\,MPa\cdot m^{1/2}$ for the case of 0.2T C(T) specimens (considering both middle section and surface specimens together) against 52.9 $MPa\cdot m^{1/2}$ for the case of 0.4T C(T) specimens. Most important, since the 99% confidence intervals for the estimation of $K_{Jc}(med)$ do not overlap each other, both datasets can be considered to be statistically different with a 99% of confidence (Figure 5.19). We may conclude that the scaling of the 0.2T C(T) dataset by means of Eq. 5. 29 does not generate a statistically equivalent set of data when compared to the 0.4T C(T) dataset, at least for the material and the experimental conditions considered here.

It is certainly possible that some of the 0.2T specimens suffer from significant loss of constraint, even though the minimum M value obtained for the case of 0.2T dataset presented here (-120°C) is M =55, well over the accepted value of M =30. If so, the loss of constraint on the specimens displaying higher toughness values can be identified as the main reason for the failure of Eq. 5. 29. Finally, by increasing the censoring limit (i.e. M =80), it may be possible to improve the agreement in estimation of K_0 ($K_{Jc}(med)$ from both datasets.

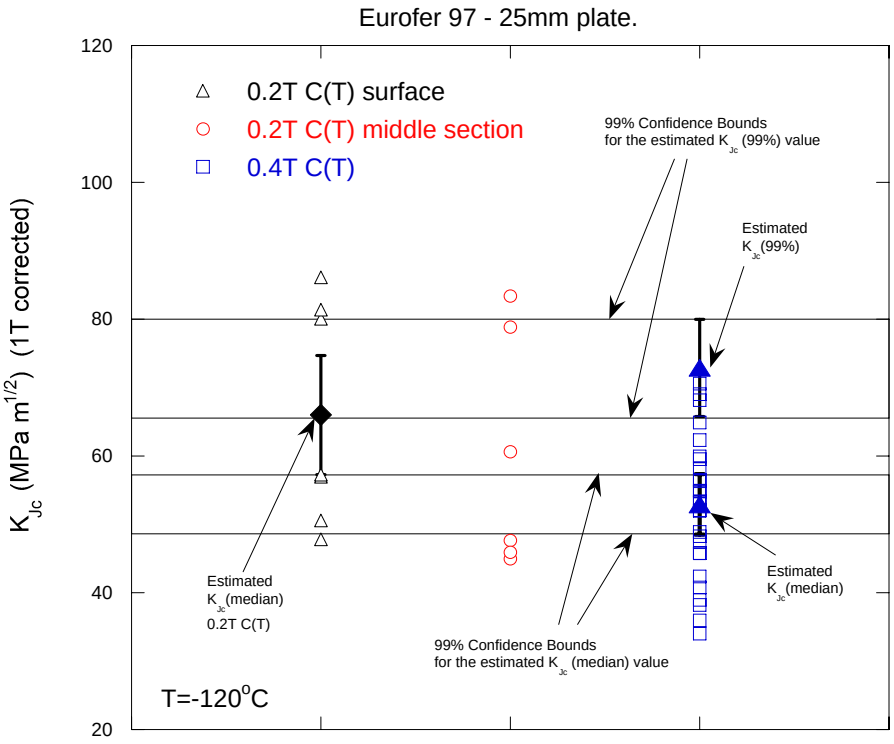

Figure 5. 19: *Statistical analysis of the median toughness value for the 0.2T C(T) and 0.4T C(T) specimens at -120°C. Note that the 99% confidence bounds for $K_{Jc}(med)$ as determined form 0.4T C(T) specimens does not overlap with the correspondent 99% confidence bounds for $K_{Jc}(med)$ as determined from 0.2T C(T) (indicated in the Figure as error bars). This means that the two datasets are statistically different with a 99% of confidence.*

The observed difference in the $K_{Jc}(med)$ values between the 0.2T and 0.4T C(T) datasets would be logically reflected in a difference in the estimated reference temperature T_0. Recalling now Eq. 5. 36, we obtain T_0=-92°C for the 0.4T C(T) dataset and T_0=-104°C for the 0.2T C(T) dataset. Note that the uncertainty in T_0 due to the uncertainty in the estimation of K_0 for the case of 0.4T C(T) specimens is approximately $\pm 5°C$. Therefore, the difference of 15°C in T_0 as determined from each dataset does not seem to be so serious.
The analysis of the datasets obtained at -100°C from both 0.2T and 0.4T C(T) specimens can help us to gain further insight into the problem of the loss of constraint. At this temperature, some 0.2T C(T) specimens suffer from severe loss of constraint, as reflected in the high toughness values obtained for some 0.2T C(T) specimens in comparison to the well constrained 0.4T C(T) dataset (Figure 5. 17).

As stated previously, we have tested 32 0.4T C(T) specimens and 39 small 0.2T C(T) specimens. The large number of specimens tested ensures a good statistical confidence of the results hereafter presented.
The first point we would like to make concerns the lower toughness values as determined from the two datasets. Even though this point has been discussed previously, it is important to remark that the lower K_{Jc} values obtained from the 0.2T and 0.4T C(T) specimens are quite comparable after scaling with Eq. 5. 29. In consequence, the lowest toughness values obtained from small specimens can be used with confidence in the estimation of a certain lower bound limit in the lower ductile to brittle transition region, i.e. near T_0.
Concerning the determination of $K_{Jc}(med)$ from small specimen data, we have again applied the censoring procedure described in ASTM E1921-03 to the 0.2T C(T) dataset, and a value of $K_{Jc}(med)$=89.5 $MPa \cdot m^{1/2}$ has been obtained. Note that this value is just outside of the 99% confidence interval for $K_{Jc}(med)$ as determined from the 0.4T C(T) data, $79.8 \pm 8.3 MPa \cdot m^{1/2}$. As in the previous case of the –120°C 0.2T C(T) dataset, this fact suggests that the limiting M value used in the censoring procedure may be to lenient concerning the avoidance of the loss of constraint on the C(T) specimens. Indeed, if the limiting value for M is increased, a much better agreement is obtained for the $K_{Jc}(med)$ values as estimated from both datasets. For instance, setting the limiting M value as M=50 we obtain $K_{Jc}(med)$=81.7 $MPa \cdot m^{1/2}$. For the case of M=80, we obtain $K_{Jc}(med)$=75.5 $MPa \cdot m^{1/2}$. Both values are well inside the 99% confidence interval for $K_{Jc}(med)$ as determined from the 0.4T C(T) data and therefore there are no arguments to favor one instead of the other.

Since a large dataset is available for the case of 0.2T C(T) specimens, it is interesting to study the effect of the M limiting value in the predicted $K_{Jc}(med)$ for the case of a smaller datasets i.e. 10 data points). This analysis strongly concerns the testing of irradiated material to determine the post irradiation fracture properties, where a small number of specimens is usually available. We study the effect of the number of tests on the estimation of the parameter distribution by randomly selecting different sets of n results from the original 0.2T C(T) dataset. The random selection has been carried out with the aid of a random number generator. We have formed new sets containing 10, 15, 20, 25, and 30 results. The process

was repeated 30 times for every case in such a way that 30 sets of 10 elements, 30 sets of 20 elements and so on have been created and analyzed using the censoring procedure at a single temperature described in ASTM E1921. Consistently, we have considered only datasets having at least 6 valid results. The analysis has been carried out for two different M limiting values: M=30 and M=80. The results are presented in Figure 5. 20, where the empty symbols stand for the results obtained from considering M=80 for the censoring limit and the full symbols stand for M=30. As expected, the selected M limiting value has the strongest effect on the estimation of $K_{Jc}(med)$. It is clear from Figure 5. 20 that the $K_{Jc}(med)$ values generated from M=30 predicts in general values well outside the 99% confidence interval for $K_{Jc}(med)$ as determined from the 0.4T C(T) dataset. The number of specimens tested does not seem to have a very strong influence on the scatter of the $K_{Jc}(med)$ values. However, when M=80 is used for the censoring limit, the $K_{Jc}(med)$ values scatters in the region of the 99% confidence interval for $K_{Jc}(med)$, improving in this way the prediction of this value when compared to the 0.4T C(T) dataset. These results together with the previously analysis at T = -120°C allow concluding that a limiting value of M=80 leads to a much accurate $K_{Jc}(med)$ determination in comparison to the less conservative value of M=30. Based on the present results it is certainly advisable to consider revision of the current ASTM E1921-03 standard, increasing the limiting value of M=30 to a new value of M=80.

For C(T) specimens, the censoring procedure with M=80 seems to account for all the problems related to the loss of constraint phenomenon. In this sense, no further corrections whatsoever seem to be needed to account for the constraint loss in the specimens, provided that the proper M limiting value has been used in the censoring procedure.

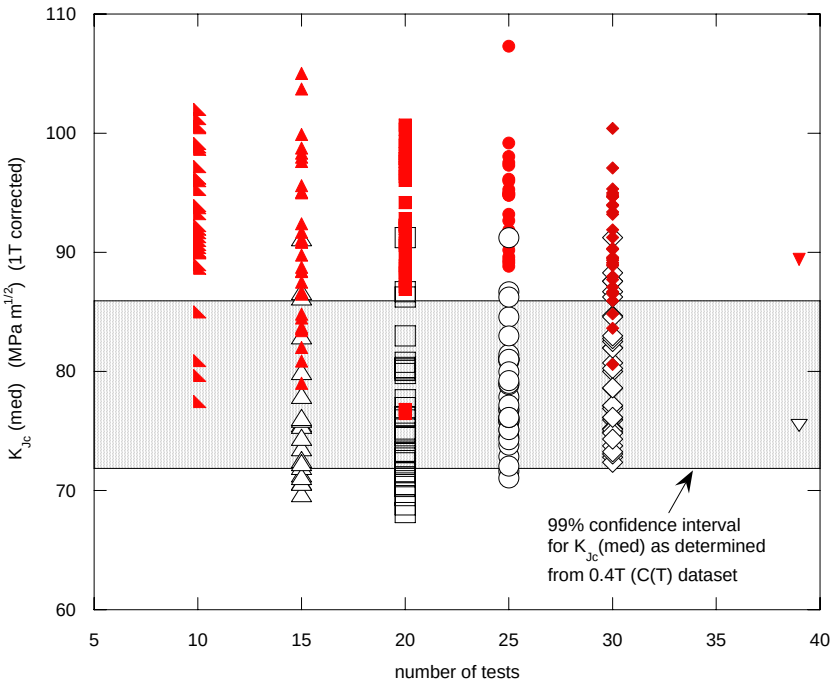

Figure 5. 20: *Effect of the censoring limit on the* $K_{Jc}(med)$ *value determined from the 0.2T C(T) specimens. Full symbols: censoring limit given by M=30. Empty symbols, censoring limit given by M=80. See text for discussion.*

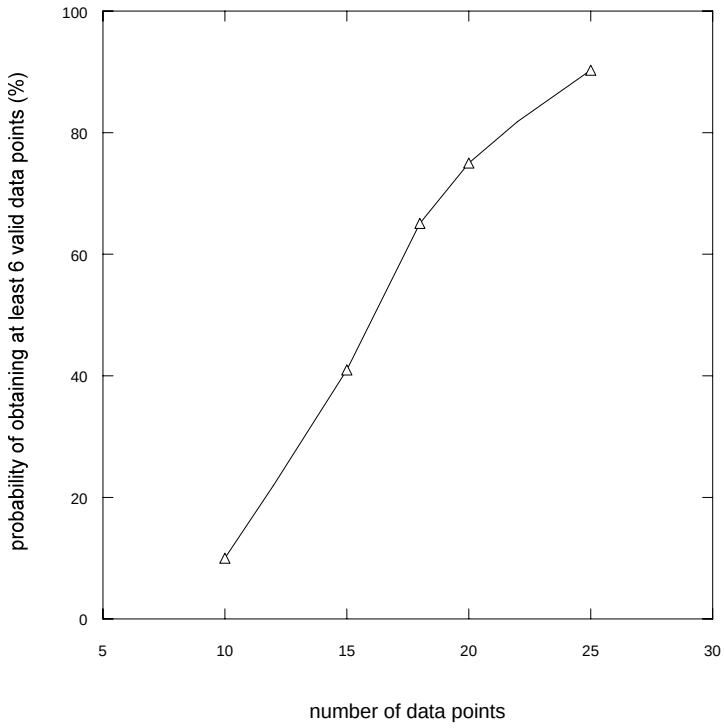

Figure 5. 21: *Probability of having 6 valid data point from a random selection process versus the number of data point considered, 0.2T C(T) specimens at -100°C.*

The logical drawbacks associated with the implementation of a critical value of M=80 are related to the difficulty of generating datasets containing at least six valid data points when testing is carried out temperatures near T_0. As described previously, ASTM E1921 requires at least six valid data points. In order to gain further insight into this point, let's consider again the 0.2 T C(T) dataset at -100°C. By means of a random selection process, it is possible to form several small datasets containing 10 data points each.
Assuming now a limiting value of M=80, the analysis of 1000 of such small datasets shows that only 10% of the datasets will include at least 6 valid data points. If instead, we now consider datasets composed by 12 data points, it is observed that approximately 22% of the datasets will be expected to include at least 6 valid data points. Figure 5. 21 shows the results obtained from the analysis of datasets having up to 25 data points. Of course if the tests were carried out at even higher temperatures than -100°C, i.e. T_0 or even higher temperatures, the situation would have been even worse. Again, the implications of the foregoing discussion are especially important in the case of testing irradiated material.

5. 3. 3. 3. Further evidence supporting M=80.

The potential effect of the loss of constraint can be assessed by estimating T_0 for different increasing M values using the variable censoring procedure. The technique simply consists in increasing the value of M in Eq. 5. 30 and calculating the corresponding T_0 value. By

increasing M, the number of censored data in the dataset will also increase, and consequently, a reduction in the number of the "valid" data points will be observed. This technique has been previously used by Joyce and Tregoning [5.61] to assess the effects of the limiting M values on T_0, determined by means of the multi-temperature analysis for the case of an extensive database of RPV steels.

In this study, the variable censoring procedure has been applied to the case of a single temperature database, 0.4T C(T) dataset at -100°C. In contrast to the work of Joyce and Tregoning, all the variables involved in the analysis where precisely known (b_0, $\sigma_{0.2}$, etc.). The value of M has been increased up to 250, where only 9 data points among the original 32 were still valid. The results obtained are presented in Figure 5. 22. The error bars represent the 85% and 15% confidence upper and lower bounds for T_0. The average value for T_0 estimated from the variable censoring procedure following ASTM E192-03 is T_0=-79.1°C. As it can be seen in Figure 5. 22, this value agrees quite well with the estimated confidence interval for T_0 for different M values. However the trend of the data indicates a slight increase of T_0 for increasing M values, with an overall variation of about 8°C.

In order to check the consistency of the analysis, we have performed a multi-temperature analysis based on the datasets at -100°C and -119°C. The reference temperature so obtained was T_0= -76°C, thirteen degrees higher than the value determined from the -100°C dataset, assuming M=30. This difference can be considered as "large" based on the number of results considered (59 data points). The $K_{Jc(med)}$ vs. T prediction of the master curve (Eq. 5. 27) with T_0=-89°C is plotted together with the complete fracture dataset (Figure 5.9).

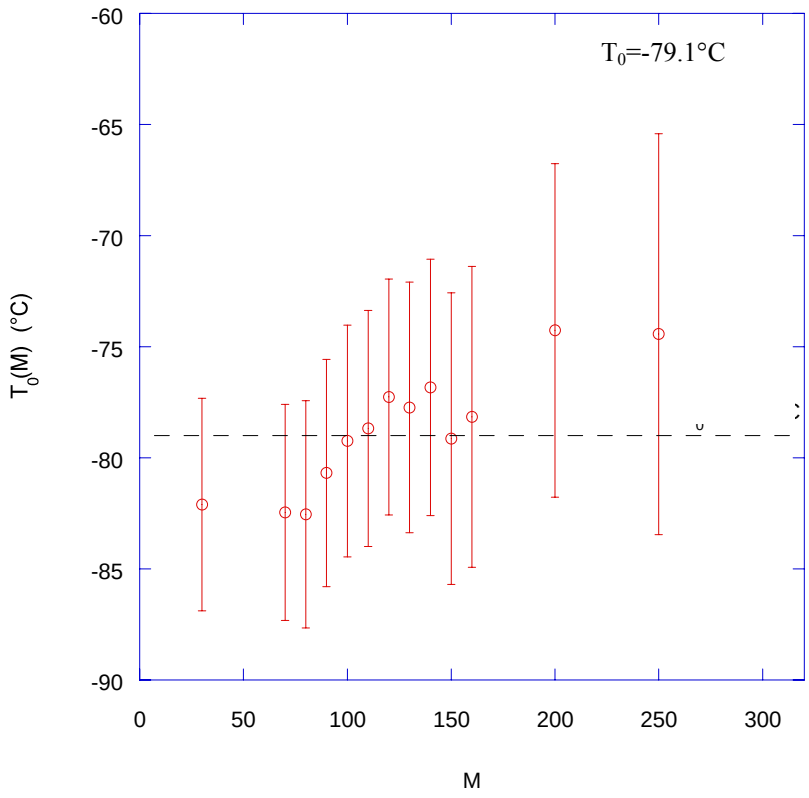

Figure 5. 22: *Estimation of T_o using different M values for the censoring procedure.*

It is clear that the experimental trend of the $K_{Jc(med)}$ values with T is not well described by the ASTM E-1920 master curve for the case of T_0=-89°C. In fact, assuming T_0=-76°C does not bring any improvement in this sense.
This observation is especially relevant to the case of the upper bound as predicted by the ASTM E 1920 standard. The lower bound prediction seems to work better. Again the results presented raise some reasonable doubts concerning the validity of the ASTM E1920-03 master curve as a proper description of the $K_{Jc(med)}$ vs. T in the particular case of the Eurofer 97.

5. 3. 4. Comparison between Eurofer97 and F82H mod.

In the present section, we analyze the results obtained from different C(T) specimens for the case of the F82H steel, a tempered martensitic steel similar in composition and thermal treatment to the Eurofer97. The database for the F82H has been taken from the literature [5.55][5.58][5.60][5.74] and is presented in Figure 5. 23, including a description of the specimen sizes and origin of the material used. The data has been analyzed following the ASTM E1921 procedure. A multi-temperature analysis is clearly the appropriate approach to deal with this database. Note we have only included C(T) data in the analysis. The SEN(B) data and the DC(T) data are only included for comparison. Among the C(T) data, four data points have been censored because of violation of the condition given by Eq. 5. 30. The reference temperature so obtained is T_0=-106°C. The mean K_{Jc} value as given by the master curve expression, Eq. 5. 27, is plotted in Figure 5. 23 together with the 1% and 99% bounds for the cumulative probability to fracture. As can be observed, this procedure accounts satisfactorily for the C(T) experimental fracture database for the F82H, a conclusion in sharp contrast with the results for the 25mm plate of Eurofer97. Only one C(T) point is located below the 1% confidence bound. Based on the available data at the present, we can conclude that the master curve expression given by Eq. 5. 27 seems to offers a very good description of $K_{Jc(med)}$ versus temperature for the F82H steel.
A large dataset obtained from SEN(B) specimens is also available for the F82H. When typical SEN(B) results are compared with the C(T) results, it is well known that the SEN(B) data indicates a higher toughness level for the material under analysis than the C(T) data. This is the reason why we have not included any SEN(B) dataset in the analysis so far, in an attempt to reduce the number of variables involved in the analysis. To illustrate this point, it is interesting to consider Figure 5. 24, where typical SEN(B) results are presented [5.63]. Comparing these results with those plotted in Figure 5. 23, we conclude that indeed, the SEN(B) data indicate higher toughness levels than the dataset obtained from C(T). However, a very interesting fact must be highlighted. As shown in Figure 5. 23, the lowest toughness values as obtained from SEN(B) specimens are fully consistent with those determined with C(T) specimens. Therefore, it seems quite reasonable to conclude that the experimental "lower bound" may be independent from the specimen type used. However, by increasing the load level, the SEN(B) specimens tends to loose constraint much faster than the C(T) ones, displaying higher toughness values than in this last case. Based on this results, it seems

advisable to review the censoring limit (given by M=30) for the case of the SEN(B) specimens. Finally, The Eurofer97 database and the F82H database are plotted together in Figure 5. 25, where the temperature axis has been normalized with the reference temperature T_0. When plotted in this way, the two datasets does not look so different from each other. However, the lack of experimental data for the Eurofer97 at higher temperatures impedes the derivation of further conclusions.

In fact, different M values may be needed to describe the proper censoring limit in the case of the C(T) and SEN(B) specimens.

It is also worth to briefly discuss the main features of the DC(T) dataset presented by Sokolov [5.74]. This dataset does not follow the overall trend of the data presented in Figure 5. 23. Note that only three points are over the mean fracture toughness level, suggesting a higher transition temperature than the one determined from the analysis of the C(T) data. The low fracture toughness values obtained at relatively high temperatures (up to -30°C) are certainly unexpected considering the size of the specimens tested (B=4.5mm), Small specimens tend to lost constraint rapidly at temperatures higher than -100°C.

To conclude, we will highlight the most relevant differences in the fracture toughness behavior between the Eurofer 97and the F82H steels. Figure 5. 25 shows the F82H database previously used for the determination of the reference temperature analysis, together with our Eurofer97 database. We have also included the database presented by Rensman, which was obtained from the 14 mm plate and 25 mm Eurofer97 plate.

Finally, it is also interesting to analyze the Charpy data available for different plates of these two steels. The observed behavior can be correlated to the fracture toughness data presented in Figure 5. 23. The Charpy data for the 14mm and 25 mm plate of Eurofer97 are presented in Figure 5. 26 (left).

The Charpy curve for the Eurofer97 features a well-defined ductile-to-brittle transition, for both, the 14mm and 25 mm plates. Some differences in fracture toughness of these two plates are highlighted in the Charpy data. Indeed, the transition temperature of the 14 mm as determined from Charpy is lower than the correspondent to the 25mm plate, being the difference approximately 20°C in very good agreement to the difference determined from C(T) specimens (T_0 =-92°C for the 25mm plate against T_0 =-112°C for the 14 mm plate). Note that the transition temperature determined from Charpy test is approximately 10°C higher than the one determined from well constrained C(T) specimens.

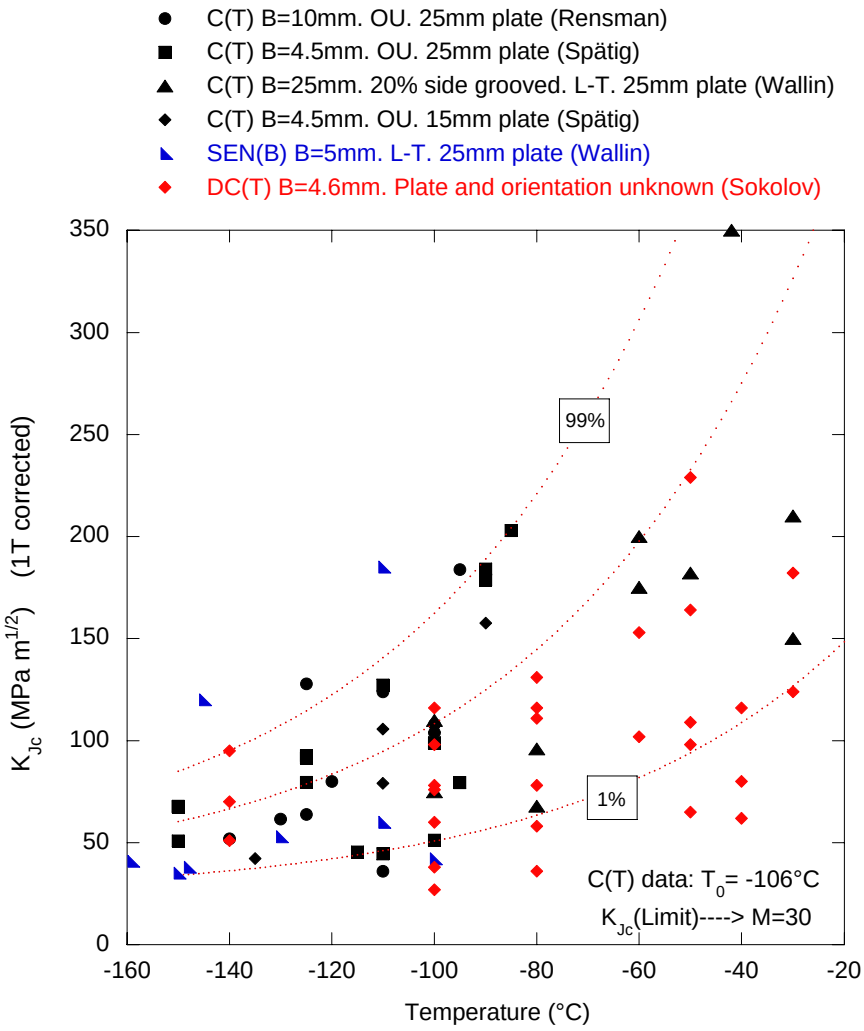

Figure 5. 23: *F82H mod. dataset obtained from 25mm plate (see text for references). The reference temperature was determined from a multi-temperature analysis with M=30. Note that the DC(T) and SEN(B) datasets were not included in the analysis.*

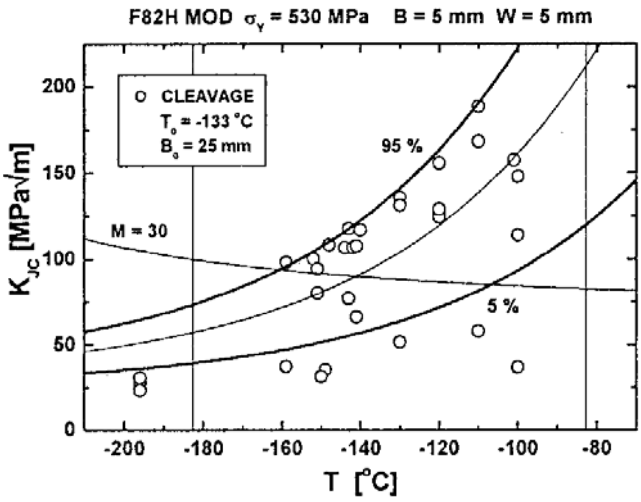

Figure 5. 24: *SEN(B) dataset for the F82H mod., obtained form the 25mm plate [5.63].*

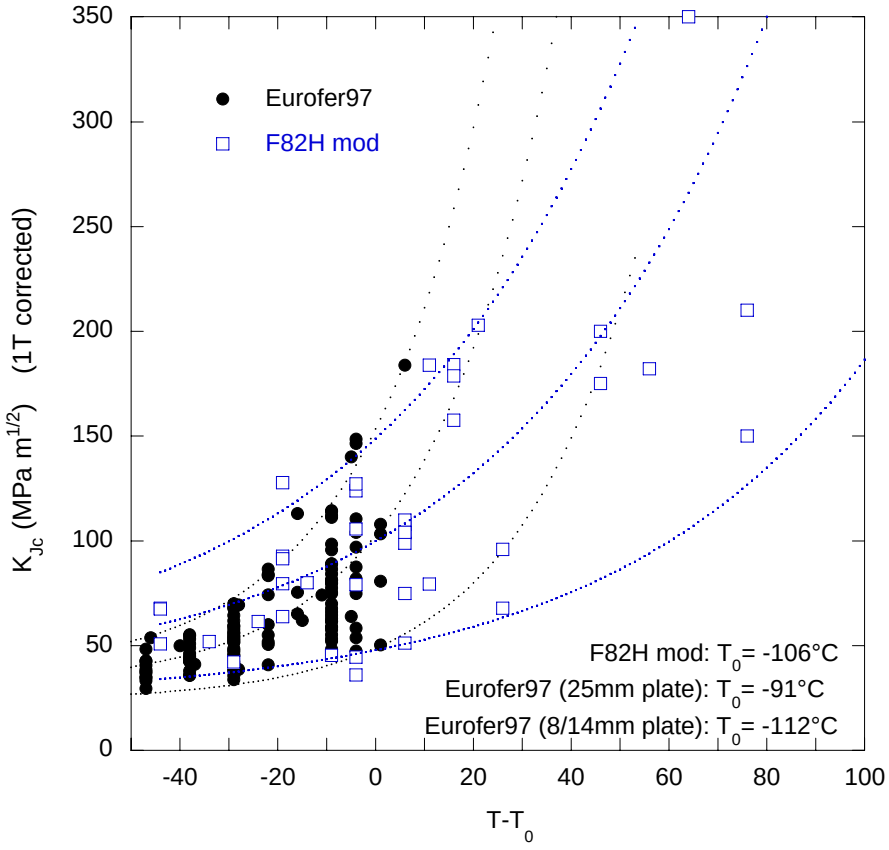

Figure 5. 25: *F82H mod and Eurofer97 datasets.*

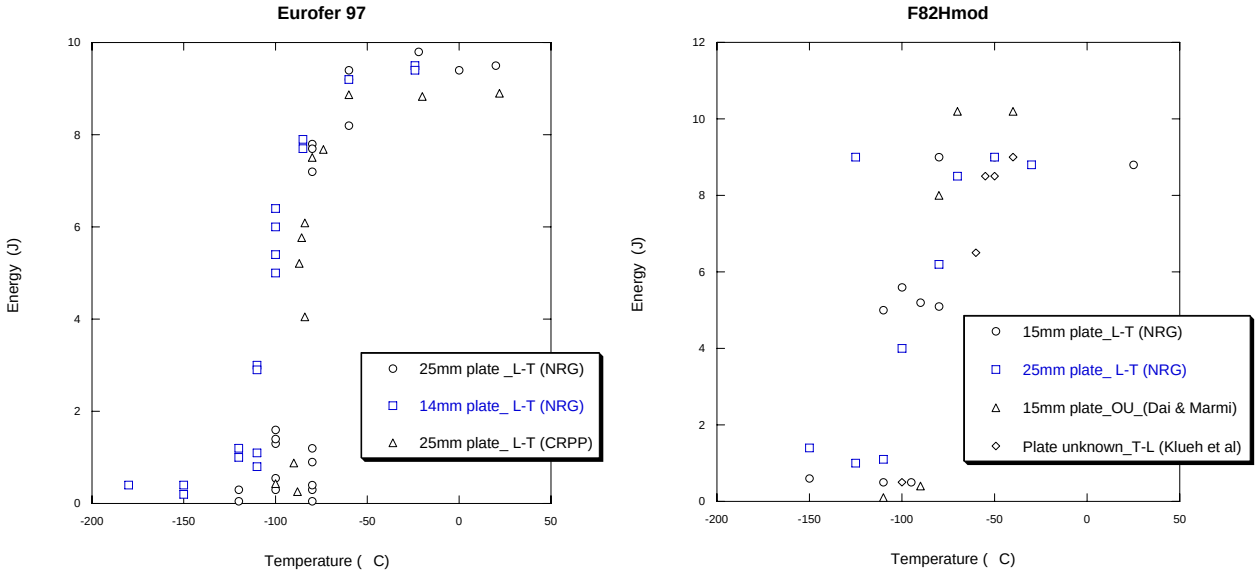

Figure 5. 26: *Charpy data (KLST specimens) for the Eurofer97 (48 data points) and F82H mod.(29 data points) (Klueh [5.66], Dai [5.67], NRG[5.68])*

The upper shelf energy seems to be the same for both plates. However, there are no enough data points for the 14 mm plate at this region to fully conclude about this fact.
The Charpy results for the F82H mod. are presented in Figure 5. 26 (right). In this case, no differences in the Charpy behavior are detected among the plates investigated. In comparison to the Eurofer97, the transition in the F82H occurs in a broader temperature range. This fact can be somehow correlated with the larger scatter observed in the fracture toughness data at a given temperature, when compared to the Eurofer 97 dataset. Also, larger scatter seems to exist in the upper shelf region of the Charpy curve. However, the average upper shelf energy level is very similar to the one obtained for the Eurofer97.

5. 4. Cleavage fracture stress in ferritic, bainitic and martensitic steels.

The objective of this section is to review the fundamental results related to the study of cleavage fracture mechanisms. Such discussion will be relevant in the context of the modeling of the experimental data presented in Section 5.3.
The section is organized as follows: firstly, the results obtained from *notched* specimens are discussed for the case of mild and spheroidized steels. Next, the main results obtained on martensitic and bainitic steels are reviewed and discussed. Finally, the extension of the concepts to the case of pre-cracked specimens is briefly discussed.

5. 4. 1. Cleavage in mild and spheroidized steels.

There exists broad agreement in the fracture community about the fact that slip-initiated cleavage fracture in spheroidized and mild steels is controlled by the attainment of a critical *tensile* stress σ^*. The brittle fracture process involves the separation of atomic planes in the material. For BCC metals and alloys, the cleavage planes are usually the $\{100\}$ since these planes have the lowest atomic density, and consequently, the number of atomic bond to break is reduced when compared with other families. To break the atomic bonds, it is necessary to reach the theoretical cohesive strength of the material, which is usually estimated from the quantity E/π. This is a very large stress and can only be reached because of the existence of local stress concentrators in the material.
The stress concentrators are micro-cracks, which for technical alloys are typically formed by fracture of small second phase particles. The stress increases locally due to the effect of the cracked particle until eventually fracture occurs. The *remote stress* that needs to be applied in order to reach the theoretical cohesive strength of the material in the region dominate by the stress concentrators is named σ^*. Several experiments support the fact that σ^* is a quantity independent of temperature and strain rate. The main results supporting this statement are critically reviewed next.

In 1966, Knott [5.20] presented a work where he studied in details the effect of hydrostatic stress on the fracture behavior of mild steels using notched specimens. Knott tested two low-carbon mild steels, from which bend bars specimens with V- notches where machined. The angles of the notches were varied from 45° to 105°. The notched bars were deformed in four-point bending at various temperatures. He used the *slip-line field theory*, which assumes plain strain conditions and rigid-perfectly plastic materials, to analyze the stress state in the specimens. The maximum tensile stress acting ahead of the notch is estimated from the notch geometry (angle and root-radius) and the yield stress in shear at the temperature considered. It is important to mention that in this approach, the value of the maximum stress acting ahead of the notch tip is determined by the size of the plastic zone, the notch angle and the yield stress, it reaches a maximum value in the moment of general yielding (i.e. when the plastic zone ahead of the notch tip has spread through the specimen cross-section and in consequence, a departure of the linear behavior is observed in the load –displacement curve).

The maximum tensile stress in the plane of fracture is reached at a certain distance ahead of the notch tip and then it remains approximately constant up to the elastic-plastic interface. This stress level can be estimated from the following expression [5.21][5.22]:

Eq. 5. 39 $$\sigma_{\max} = 2\tau_y\left(1+\frac{\pi}{2}+\frac{\theta}{2}\right) \qquad 6.4°< \theta <114.6°$$

where τ_y is the yield stress in shear and θ the notch angle. Knott calculated the maximum stress acting on the specimens when the fracture load was coincident with the general yielding load at temperatures between –102°C and –144°C. He observed that the maximum stress ahead of the crack tip at the onset of fracture (the critical fracture stress σ^*) was constant for the materials and temperatures analyzed, being in the order of 950MPa. It is important to stress that in the context of the slip line field theory, the existence of a temperature-independent fracture stress also implies the independence of σ_f from the hydrostatic component of the stress field. Knott interpreted the critical tensile stress in terms of the tensile stress necessary to propagate a slip-initiated micro-crack. Following Cottrell's approach to fracture in smooth specimens, the propagation condition can be written as [5.23]:

Eq. 5. 40 $$\sigma_f = \frac{2\mu\gamma}{k_y^s d^{1/2}}$$

where μ is the shear modulus, γ represents the true surface energy of the ferritic lattice plus some amount of energy expended in plastic work, d is the grain diameter and k_y^s is the slope of the Hall-Petch plot of shear yield stress against $d^{-1/2}$ The value of γ estimated was 10 J/m^2. By using this approach, he was able to link the local stress acting in a certain region of the material with the grain size. This concept establishes a local criterion for cleavage fracture. In other words, failure of the specimen can be predicted if we know the stress distribution in the material (the "local" stresses) and the material microstructural features.

Oates [5.24] and Wilshaw, Rau and Tetelman [5.25], drew similar conclusions, i.e., fracture in mild steels can be explained by means of a critical tensile stress mechanism. In an attempt to improve the accuracy of the stress values calculated by slip line field theory, Griffith and Owen [5.26] studied the magnitude and distribution of stresses and strains generated in a 4-point bending specimen using finite elements simulations, assuming plane strain and a linear strain hardening law. They reanalyzed previous data of Griffiths and Oates [5.27] on notched 4-point bend specimens of Fe-3%Si alloy. Based on the FE simulations, they conclude that in the case of this last material, the maximum local stress at the moment of fracture is a quantity almost independent of temperature.

In the case of mild steels, there exists a clear dependence of σ^* with the grain size. Curry and Knott [5.28][5.29] made an important contribution to the understanding of this phenomenon, explaining why the observed strong dependence of σ^* on the ferritic grain size was not

predicted by the theoretical models available for cleavage fracture. Typically, in normalized mild steels, the carbides are located mainly in grain boundaries. Curry and Knott used the Smith cleavage fracture criterion [5.30] to explain the creation of a micro-crack from the fracture of a grain boundary carbide due to a dislocation pile-up of length equal to half the grain diameter. After reanalyzing the data published, they showed that there is a general relationship between the largest observed grain boundary carbide thickness C_0 and the ferritic grain size d. By using the empirical relationship observed between C_0 and d in combination with the Smith model, they were able to fit the experimental data using a value of the effective surface energy γ_p equal to 14 J/m^{-2}. Following Curry and Knott, it is not possible to apply the Smith criterion to the case of spheroidized steels for two main reasons: a) the stress intensity associated with the shape in the crack nucleus is reduced and b) dislocation pile-ups across a grain diameter are not present. Indeed, they proposed that in the case of spheroidized steels, it is reasonable to ignore any dislocation contribution and treat the problem as a Griffith-crack propagation of a penny-shaped crack nucleus, with radius equal to the carbide particle radius r. The Griffith-Orowan criterion is based on an energy balance between the energy needed to create the new surfaces and the energy released during the crack propagation. Therefore, the critical condition for the *propagation* of microcracks is given by [5.31]:

Eq. 5. 41 $$\sigma^* = \left(\frac{\pi \cdot E \cdot \gamma_p}{2(1-\nu^2) \cdot r} \right)^{1/2}$$ penny-shaped microcracks.

Eq. 5. 42 $$\sigma^* = \left(\frac{2 \cdot E \cdot \gamma_p}{\pi(1-\nu^2) \cdot r} \right)^{1/2}$$ through thickness microcracks.

$\gamma_p = \gamma_s + W_p$, where γ_s is the true surface energy of the ferritic matrix and W_p is the plastic work term, associated with the energy dissipated by the propagating crack [5.36].

From the point of view of the micro-cracks, σ^* is considered as the "remote" stress acting in the area where the stress concentrators are located. If the stress concentration in the micro-crack is high enough to propagate it into the ferritic matrix, the micro-crack grows and may lead to macroscopic failure. In the case of ferrite, the true surface energy γ_s is of the order of 2 J/m^2. The value for the effective plastic energy γ_p derived by Curry and Knott for the case of the spheroidized plain carbon steels was about 14 J/m^2.

It is worth mentioning that Eq. 5. 42 can be derived from the original Smith's model after neglecting the effect of the dislocation pile-ups. In both cases, the microstructural parameter affecting σ^* is the carbide radius. Fracture will occur when the largest favorably-oriented cracked particle is subjected to a local tensile stress high enough to satisfy the crack propagation energy balance, in the sense of the Griffith criterion. The largest crack nucleus present in the material can be estimated by the 95th percentile carbide radii.

In summary, for the case of normalized mild steels and spheroidized steels, the results outlined above gave strong support to the hypothesis that the critical event in cleavage

fracture consisted in the propagation of micro-cracks, which were generated after carbide fracture. Note that if the propagation of microcracks were the controlling step in the fracture process, it would mean that the creation of microcracks occurs prior to the fulfillment of the propagation conditions. However, at the present, the typical scatter observed in fracture toughness the ductile-to-brittle transition region is associated to an initiation-controlled process. This point is discussed in section 5.6.

5. 4. 2. Cleavage in bainitic and martensitic steels.

For bainitic and martensitic microstructures, it is also accepted that cleavage fracture can be rationalized in terms of a critical stress criterion. However, since the microstructures involved are more complex than the ones characteristic of mild steels, to obtain a relationship between the fracture properties and certain microstructural features is a much more difficult task.

Brozzo et al. [5.32] determined the relationship between microstructure and cleavage resistance in low carbon 3Cr-2Mn bainitic steels with different carbon and sulphur contents (for carbon, 0,025wt%C and 0.050wt%C). The fracture stress σ^* was determined from three-point bending tests on Charpy V-notch specimens by means of the slip-line field theory. σ^* values were calculated only for one temperature in each case (at the general yielding temperature) and it was not possible to check the temperature independence of σ^* for each material tested. The values for σ^* estimated were much higher than the ones obtained in mild steels, ranging from 1600 MPa to 2800 MPa. In this case, the σ^* values appeared to be very sensitive to the bainitic packet size. Indeed, σ^* was found to be consistently higher for materials with smaller bainitic packet size (smaller prior austenitic grain size) than those with bigger bainitic packet size. Specifically, the difference in σ^* in the same material due to variations in the bainitic packet size ranges from 400 MPa to 800 MPa (the calculated rate of change was $\Delta\sigma_f/\Delta d_B^{-1/2} \approx$ 190 MPa mm$^{1/2}$). These facts give support to the hypothesis that bainitic packet would be the microstructural unit controlling cleavage. Brozzo et al. suggested that the critical stage for cleavage in the case of bainitic steels would be the propagation of a Griffith crack from one bainitic packet to an adjacent one. Based on the Griffith-Orowan model, they were able to fit the experimental results assuming a value for the effective surface energy γ_p of 120 J/m^2, certainly much higher than the 14 J/m^2 estimated by Curry and Knott in spheroidized steels.

Curry [5.33] performed a series of experiments in a A508 Class II steel, commonly used in reactor pressure vessels. Two different thermal treatments were applied to obtain a fully tempered granular bainitic microstructure and an upper bainitic microstructure. The specimens used were single edge notched bend bars with different notch angles, which were tested in the four-point bending configuration. Again, the stress field was derived from the slip-line field theory. He observed a large scatter in the fracture loads in the two material conditions, for a given notch angle and temperature. Curry claimed that cleavage fracture was predominantly tensile stress controlled. The fracture stress σ^* was found to be approximately 2500 MPa $\pm$ 400MPa for the upper bainite microstructure and 1600 MPa

±100MPa in the case of the tempered bainite. He also determined that the critical fracture stress increases slightly in specimens having smaller notch angles.

Curry also used the finite elements results published by Griffith and Owens [5.26] to recalculate the σ^* from the fracture loads. The results look in good agreement with the data generated by slip line field theory, varying from approximately 2900 MPa to 2200 MPa in the case of the upper bainitic structure and from 2000 MPa to 1600 MPa for the tempered microstructure. Combining these experimental values with the Griffith-Orowan formulation (assuming an effective surface energy γ_p of 14 J/m^2), it is possible to estimate the radius of the brittle particles that could generate the initial Griffith-micro-cracks in the microstructure. The values for the maximum and minimum radius of the particles obtained were 1.8 μm and 0.9 μm respectively. However, particles of these sizes were not present in the microstructures analyzed. Therefore, he concluded that fracture was not nucleated by cracked carbides particles in the steels analyzed.

Curry observed that the cleavage facets in the fracture surfaces were of the same size as the bainitic packets. Following the work of Brozzo et al. [5.32], he calculated σ^* from the bainitic packet size assuming an effective surface energy γ_p of 120 J/m^2. The values obtained for σ^* were in good agreement with the experimentally determined σ^* values, giving further support to the hypothesis that the bainitic packet size is the microstructural parameter controlling cleavage fracture. In other words, the unstable propagation of Griffith micro-cracks (having the same size as the bainitic packet size) into the ferritic matrix would be the critical step that leads to macroscopic cleavage. Nevertheless, the fact that the value used for γ_p is one order of magnitude higher than in the case of mild steels raises several concerns regarding this hypothesis.

Beremin et al. [5.34] performed a series of experiments on three different heats of a tempered- bainitic A508 Class 3 steel, called heats A, B and C respectively. The tests were carried out with specimens having different geometries, including four-point bend specimens and axisymmetric notched tensile bars with different notch radii. Finite elements simulations were used to calculate the maximum tensile stress at the onset of fracture. They presented several results obtained from the axisymmetric specimens at constant temperature of 77 K. The fracture stress values were calculated from FE simulations (it is worth saying that the simulations were carried out with the constitutive behavior corresponding to 373 K, and the stress values were corrected afterwards using a correction factor, reducing the accuracy of the calculation). If cleavage fracture were controlled by a critical tensile stress mechanism, we would expect roughly the same value for the critical fracture stress on specimens having different notch geometries and/or loading modes (uniaxial loading/bending). However, a clear increase in the calculated fracture stress was observed for specimens with smaller notch radius. Indeed, specimens with notch radius larger than 2 mm showed consistently lower values for σ^* when compared with the specimens with notch radius of 0.2 mm. Regarding the microstructural feature that actually controls cleavage fracture, a correlation between the lath packet length and the cleavage facet was observed in heat C. The same correlation was observed in the heats A and B between the ferritic grain size and the cleavage facets.

In order to gain insight into the nature of the scatter observed in the results, the Beremin group tested several specimens (heat A) at the same temperature. The tests were carried out

at 77 K on specimens with 0.2 mm of notch radius and different flank angles, 90° and 45°. Twelve specimens were tested in each case. For the 90° flank angle specimen, the loads to fracture P_f vary from 37 kN to 64 kN while for the 45° flank angle specimen, P_f varies from 28 kN to 52 kN. The average P_f for the 45° specimens is lower than for the 90° specimens, as expected since the stress concentration is higher for the first case. Consistent with the previous report of Curry, a large scatter was observed in the results. The calculated values for the critical fracture stress were consistently lower in the case of specimens having large notch radius when compared with the values of σ^* derived for smaller notch radius (again, the same trend is observed in the data presented by Curry [5.33]). This observation, together with the typical scatter of the data is very important since it revealed the intrinsic statistical nature of cleavage.

The dependence of σ^* with the notch radius was also discussed by Tetelman et al. [5.39]. They found that in the case of high nitrogen steels, σ^* is also observed to decrease when the notch radius is increased.

In opposition to the conclusions presented previously, Saario et al. [5.37] claimed that cleavage fracture in bainitic steels is probably induced by the fracture of carbides. The results were developed based in previous works of Kotilainen [5.38] and Wallin [5.36]. They based their arguments on the fact that the measured critical fracture stress is considerably smaller when measured from smooth tensile specimens when compared to the values generally obtained from notched specimens. As previously discussed, such observation is in agreement with the experimental data of Tetelman et al. [5.39] Curry [5.33] and Beremin [5.34].
Kotilainen [5.38] was able to determine σ^* in notched bend specimens (2055 MPa at 100 K) and also in smooth tensile specimens (1230 MPa at 77 K). This difference was explained on the basis that in the case of smooth specimens, the principal stress field is relatively uniform trough the thickness. Therefore it is expected that cleavage will be always initiated by the *largest* existing defect. Assuming that the Griffith-Orowan mechanism is operative, this is directly reflected in lower σ^* values. On the contrary, the stress fields ahead of the notch strongly depend on the distance to the notch tip. In a *local* sense, the fracture criterion expressed by the Griffith-Orowan equation can be now fulfilled by smaller particles than in the case of the homogeneous stress field. In fact, the region of material in the plane of the notch subjected to the highest values of tensile stresses is certainly small for a notched specimen (and even much smaller for a pre-crack specimen). Therefore, the size of the defect that ultimately leads the specimen to fracture is determined by statistical competition within the defect population. Consequently, σ^* values can be higher in notched specimens when compared to smooth specimens.
Regarding the microstructural parameter controlling fracture in bainitic steels, Wallin [5.36] has suggested that the carbides could play a central role in cleavage fracture; again in clear disagreement with the arguments presented by Curry and Brozzo et al. Following this idea, and considering the carbide distribution observed in a CrMoV- bainitic steel; Saario showed that the Griffith-Orowan model can fit the experimental data satisfactorily when considering an effective surface energy γ_p of 8.8 J/m^2 instead of the 14 J/m^2 suggested by Curry and the

120 J/m^2 proposed by Brozzo et al. Indeed, a reduction in the value for the effective surface energy considered in the Griffith-Orowan equation is reflected by a reduction in the dimension of the critical defect. This fact may explain the lack of correlation observed by Curry [5.33] between the size for the critical particles predicted by the Griffith-Orowan equation (assuming γ_p=14 J/m^2) and the microstructures analyzed. Furthermore, Wallin [5.36] presented solid arguments (not discussed here) supporting the hypothesis that the plastic work term W_p in the Griffith-Orowan equation should be smaller in bainitic steels than in ferritic and spheroidized steels. Clearly, these arguments give support to the results presented by Saario et al.

Bowen et al. [5.40] developed a wide range of microstructures in A533B pressure-vessel steel, trying to clarify the relationship between microstructural parameters and toughness in this steels, including auto-tempered martensite and tempered martensite. Bainitic microstructures where also produced. They used two types of specimens in their research: a) single edge notched bend specimens pre-fatigued in accordance with BS5447 were used to determine K_{IC} in the temperature interval –20°C to –196°C and b) notched bend specimens with θ=45° and root radius of 0.25 mm. Bowen et al. observed that the σ^* values calculated from the experimental data obtained from notched bend specimens are approximately independent of temperature for all the microstructures analyzed. In fact, the data for the as-quenched (auto-tempered) martensites was scattered, with σ^* varying between 3600 MPa and 3800 MPa in the temperature range between –160°C to –100°C. For the tempered martensite (8hs@ 615°C) the σ^* values varies between 3150 MPa and 3250 MPa in the temperature range–170°C to –130°C. These stresses are much higher than those observed in the case of the bainitic microstructures, 1800 MPa to 2000 MPa. The effect of prior austenitic grain size and packet size on the fracture toughness and on the σ^* was also analyzed. No influence whatsoever of these microstructural features on σ^* was observed. The carbide size distributions of several of the microstructures analyzed were obtained, to assess any effect of this microstructural parameter over σ^*. Bowen et al. concluded that the toughness in the martensitic microstructures analyzed (as-quenched and tempered martensites) was mediated primarily by the size distribution of the carbides. They showed that σ^* consistently decreases for with increasing carbide size. Nevertheless, the trend was not the expected for the case of the as quenched martensite having very small carbide sizes (average size on the order of 15 nm). By using the Griffith-Orowan equation, a very high value of σ^* can be expected, not consistent with the experimental value of σ^*. Bowen suggested that there exists a lower limit for the carbide size below which σ^* is not increasing with further carbide refinement. Finally, the effective surface energy γ_p was estimated to range between 7 J/m^2 and 9 J/m^2 in good agreement with the data of Saario et al.[5.37].

In summary, the results reviewed above indicates that brittle fracture in bainitic and tempered martensitic steels is mainly controlled by the carbide size distribution.

5. 4. 3. Critical stress concept for pre-cracked specimens.

Ritchie, Knott and Rice [5.41], hereafter RKR, proposed that in pre-cracked specimens, the fracture criterion should include not only the attainment of a critical stress ahead of the crack

tip but also a certain critical distance over which the stress is higher than the critical stress. In other words, the principal stress ahead of the crack tip should equal or exceed the critical stress over a "characteristic" distance that is related somehow to the microstructural features. The basic idea behind the RKR model is that the local stress acting over a certain micro-crack should be high enough ($\sigma_{22}^{max} \geq \sigma_f$) to initiates the micro-crack propagation, but at the same time the stress field should be able to propagate the crack through the material.

For notched specimens, this is certainly not a concern since the stress acting in the neighboring area around a certain micro-crack can be considered "uniform" due to the small stress gradients when compared to characteristic micro-structural distances like the grain size (remember that the Smith model discussed previously and the Griffith-Orowan model, both assumes uniform "remote" stress). On the contrary, in pre-cracked specimens the stress gradients are much higher than in notched specimens. Propagating microcracks could be then arrested into the ferritic matrix due to the sudden decrease in the driving force for propagation.

5. 5. The local approaches to cleavage.

The so-called local approaches to cleavage fracture are based on the concept that cleavage fracture arises when a certain "critical" stress state is reached in the material. The stress state of the material ahead of the crack tip is defined by a function depending on the particular local approach model. This function is usually evaluated in terms of a component or several components of the stress tensor in a defined region of material ahead of the crack tip. When the function reaches a critical value, fracture occurs. The local approach has several advantages when compared to the classic fracture mechanics represented by the stress intensity factors and the J integral values. In particular, since the approach is "local", it is in principle independent of the constraint level and specimen size limits. However, the successful application of the local approach required a very detailed numerical model of the cracked component under analysis. It must be emphasized that the calibration procedures of such models are not always universal and remain an open issue to address.
There exist basically two different local approaches. The first one is a statistical approach based upon the so-called Weibull stress concept, originally proposed by Beremin [5.34] and further developed by several researchers. The second version of the local approach derives from the early work of Ritchie, Knott and Rice [5.41] on the critical stress acting over a certain critical distance (or critical area or critical volume). Both models enable the transfer of critical value of K_j values from one specimen size/geometry to another by taking into account the respective constraint level and volume sampling. These concepts are presented hereafter.

5. 5. 1. The Weibull stress.

Beremin [5.50] proposed a new approach that was widely spread through the fracture community. This approach considers different micro mechanisms that eventually lead the specimen or structural component to fracture in a local scale. As a consequence, the model can be derived from basic considerations of fracture micromechanics. The intrinsic randomness associated with cleavage fracture in the transition regime is taken into account through Weibull statistics and the weakest link concept.

5. 5. 1. 1. Material volume under homogeneous stress.

The material volume V_p is divided into several small volumes V_0. We can assign a certain cumulative probability of failure to these small volumes as a function of the maximum principal stress σ_I, $p(\sigma_I)$. Assuming a statistical independence between the volumes and owing to the fact that the stress is the same in all the small volumes, we can write the cumulative probability of non-failure for the material volume as:

Eq. 5. 43
$$1 - P_{V_p}(\sigma_I \le \sigma_I^*) = \prod_i^n p_i(\sigma_I \le \sigma_I^*) = \left[p_i(\sigma_I \le \sigma_I^*)\right]^n$$

where $n = V_p / V_o$. The product is extended to all the small volumes V_0 included in the process volume V_P characterized by the plastic zone.
In the weakest link approach, the cumulative probability of failure of the volume V_p can be expressed as:

Eq. 5. 44 $$P_{V_p}(\sigma_I \le \sigma_I^*) = 1 - \exp\left[-\frac{V_P}{V_0} p_i(\sigma_I \le \sigma_I^*)\right]$$

Beremin calculated the probability of failure of the V_0 volumes using the assumption of a certain local criterion controlling fracture based upon the fact that cleavage is a stress-controlled process. As such, macroscopic cleavage will occurs when the stress acting over a microcrack is large enough to allow the unstable propagation of the crack. Microcracks are usually assumed to be initiated by fracture of brittle particles, mainly carbides, which are embedded in the matrix. Therefore, the distribution of microcrack lengths is associated to the number and distributions of carbides sizes. Beremin proposed that the probability of finding a microcrack of length between l and $l + dl$ can be estimated from the following expression:

Eq. 5. 45 $$p(l)dl = \frac{\alpha}{l^\beta} dl$$

where α and β are material constants. Then, invoking the Griffith-Orowan equation, we can relate the critical length of the micro-crack with the corresponding principal stress acting in the volume:

Eq. 5. 46 $$p(\sigma_I \le \sigma_I^*) = p(l \ge l_c) = \int_{l_c}^{\infty} \frac{\alpha}{l^\beta} dl$$

where :

Eq. 5. 47 $$l_c(\sigma_I) = \frac{2E\gamma}{\pi(1-\nu^2)\sigma_I^2}$$

Finally, an expression for the cumulative probability of failure of the small volumes $p_i(\sigma_I \le \sigma_I^*)$ is obtained:

Eq. 5. 48 $$p_i(\sigma_I \le \sigma_I^*) = \left(\frac{\sigma_I^*}{\sigma_u}\right)^m$$

where, σ_I^* should be understood as the principal stress acting on the material volume under consideration. The parameter σ_u and m are given by:

Eq. 5. 49 $$\sigma_u = \alpha\left(\frac{2E\gamma}{\pi(1-\nu^2)}\right)^{1-\beta}(2\beta-1)$$

and

Eq. 5. 50 $$m = 2\beta - 2$$

This is a two-parameters Weibull distribution. The interesting point is the fact that this distribution function has been derived from basic physics assumptions about the micromechanics of fracture in the material. Consistently, Mudry [5.52] has indicated that the same distribution function can be obtained if we consider other carbide distribution functions. Finally, replacing Eq. 5. 48 in Eq. 5. 44, we obtain:

Eq. 5. 51 $$P_{V_p}(\sigma_I \le \sigma_I^*) = 1 - \exp\left[-\frac{V}{V_0}\left(\frac{\sigma_I^*}{\sigma_u}\right)^m\right]$$

The two constants that should be determined experimentally are m and $V_0\sigma_u{}^m$. The value of V_0 can be arbitrarily chosen since the stress acting on the material is homogeneous.
Eq. 5. 51 predicts a size effect in P_f. If two different volumes of material have the same probability of fracture, then:

Eq. 5. 52 $$\frac{V_1}{V_2} = \left(\frac{\sigma_{I,spec2}}{\sigma_{I,spec1}}\right)^m$$

5. 5. 1. 2. Plastic volume under non-homogeneous stress. Weak stress gradients.

The notched specimens are a good example of this case. The approach is also representative of pre-cracked specimens loaded to high J values. The analysis is carried out in the same way as in the previous section. The total volume under consideration is subdivided in smaller volumes V_0. The assumption of statistical independence between the V_0 volumes and the description of the defect distribution inside V_0 are still valid. However, the stress state in each small volume depends on its position with respect to the stress concentrator. Nevertheless, inside every small volume V_0, the maximum principal stress is considered constant. With these assumptions, it can be demonstrated that:

Eq. 5. 53 $$P(\sigma_I \le \sigma_I^*) = 1 - \exp\left[\sum_i -\frac{V_0}{V_{ref}} p_i(\sigma_I \le \sigma_I^*)\right] = 1 - \exp\left(-\frac{1}{V_{ref}}\sum_{i=1} V_0\left(\frac{\sigma_{I,i}}{\sigma_u}\right)^m\right)$$

The reference volume introduced in Eq. 5. 53 is arbitrary. The inclusion of this reference volume makes the formulation well suited for FEM calculation. In this case, V_0 may be associated to the volume of every element. However, the element volumes are usually not constant since the elements are refined in the crack tip region. By weighting the probabilities of failure of the small volumes with V_{ref}, we take into account this size effect in V_0. Beremin defined a quantity called Weibull stress as follows:

Eq. 5. 54
$$\sigma_W = \sqrt[m]{\sum_i \frac{V_{0,i}}{V_{ref}} (\sigma_{I,i})^m}$$

The summation should be carried out over the process volume (plastic zone). Thus, the probability of fracture can be written as:

Eq. 5. 55

$$P(\sigma_I \le \sigma_I^*) = 1 - \exp\left(-\frac{1}{V_{ref}} \sum_{i=1} V_{0,i} \left(\frac{\sigma_i}{\sigma_u} \right)^m \right) = 1 - \exp\left(-\frac{1}{V_{ref} \sigma_u^m} \left((V_1 \sigma_{I,1})^m + (V_2 \sigma_{I,2})^m + ... \right) \right)$$

$$= 1 - \exp\left[-\left(\frac{\sigma_W}{\sigma_u} \right)^m \right]$$

or, by using an integral expression:

Eq. 5. 56
$$P(\sigma_I \le \sigma_I^*) = 1 - \exp\left[-\frac{1}{V_{ref}} \int_{V_p} \left(\frac{\sigma}{\sigma_u} \right)^m dV \right] = 1 - \exp\left[-\left(\frac{\sigma_W}{\sigma_u} \right)^m \right]$$

The probability of failure of the volume is now described by a two-parameter Weibull distribution. The shape parameter m and the scaling parameter σ_u are material properties. The introduction of the so-called Weibull stress is fundamental. The basic concept underlying the Weibull stress is the fact that the same value of the Weibull stress in different configurations will result in the same probability to fracture. Note that the exponent m in this case is not the same that the one used to describe the scatter of the K_j results in Section 5.3 (m=4).

5. 5. 1. 3. Sharp gradients. The crack tip problem.

From dimensional analysis, it was demonstrated that in SSY conditions, the stress field ahead of the crack tip can be expressed as ([5.5][5.6]):

Eq. 5. 57
$$\frac{\sigma_{ij}}{\sigma_y} = f_{ij}\left(\frac{r}{(K/\sigma_y)^2}, \theta\right)$$

The assumption that the stress is constant over a certain small volume V_0 may still be valid in the case of weak stress gradients. This situation is likely to happen when the plastic volume is large (large K_I/σ_y values). In this case, V_0 is still considered the minimum volume that can be chosen without violating the statistical independence assumption and that of constant stress acting on the volume.
Now, combining Eq. 5. 54 and Eq. 5. 57, the Weibull stress is expressed as:

Eq. 5. 58
$$\sigma_W = \sqrt[m]{\sum_j \sum_i \frac{V_{0,ij}}{V_{ref}} \left[\sigma_y f\left(\frac{r_i}{(K_I/\sigma_y)^2}, \theta_j\right)\right]^m}$$

The summation is carried out over all the elements inside the plastic region. The expression above is well suited for numerical analysis. Eq. 5. 58 can also be converted into an equivalent 3-D integral form:

Eq. 5. 59
$$\sigma_W^m = \frac{1}{V_{ref}} \int_{V_P} \left[\sigma_y f\left(\frac{r}{(K_I/\sigma_y)^2}, \theta\right)\right]^m r dr d\theta dz$$

Assuming a constant K_I value and plane strain conditions, and carrying out the same change of variables as that done in the Appendix 1 (Eq.A1.16), expression of the Weibull stress in this case becomes:

Eq. 5. 60
$$\sigma_W^m = \frac{\sigma_y^{m-4} K_I B}{V_{ref}} \int_{V_P} f(u,\theta) u du d\theta = \frac{\sigma_y^{m-4} K_I B}{V_{ref}} \Omega^*$$

Finally, the probability of failure can be estimated using Eq. 5. 60:

Eq. 5. 61
$$P(K_I < K_{JC}) = 1 - exp\left(-\frac{\sigma_y^{m-4} K_I^4 B \Omega^*}{V_{ref} \sigma_u^m}\right)$$

The previous derivation is only valid for the case of SSY where J or K describe the stress field completely.

5. 5. 2. Scaling model for cleavage fracture. Critical stress – critical area model (σ*-A*).

The stress and strain fields around a loaded crack can be easily obtained from FE simulations. The use of a local model for cleavage fracture allows relating the stress/strain fields ahead of the crack tip to fracture toughness. The different micromechanical models used nowadays are derived from the early work of Ritchie, Knott and Rice (RKR) [5.41], who proposed that cleavage fracture occurs if the stress level acting on a critical distance ahead of the crack tip (λ^*) exceeds a critical threshold value σ^*. λ^* and σ^* actually describe the conditions under which the material undergoes brittle fracture. Based on this approach, Anderson, Dodds and co-workers ([5.44] to [5.47]) presented a model to correct constraint effects on the fracture toughness values based on a local criterion for the occurrence of cleavage fracture.

We have previously shown that the single-parameter fracture mechanic approach breaks down when excessive plasticity develops in the crack tip zone (large scale yielding, LSY). However, assuming that a certain that a local criterion needs to be fulfilled in order for cleavage fracture to happens, it is then possible to predict the occurrence of cleavage from such a local approach, even for the case of LSY. The local conditions are typically stated in terms of the stress and the strain fields, which eventually are mediated by the crack and the geometrical features of the specimen/component.

The model presented by Dodds and Anderson is based upon the assumption that the probability of brittle fracture of a specimen or component depends on the volume of material over which the principal stress exceeds a certain value:

Eq. 5. 62
$$P_f = P\left[V(\sigma_I)\right]$$

where $V(\sigma_I)$ is the cumulative volume sampled in which the principal stress is $\geq \sigma_I$. Based on this simple micromechanical model, they propose to scale the fracture toughness results obtained from specimens having low constraint level to a higher constrained specimen. The scaling procedure is performed by comparing the critical experimental J value (hereafter J_{exp}) to the critical J value correspondent to the SSY case (J_o). The parameter J_o corresponds to the load level that generates the same $V(\sigma_I)$ in the pure boundary layer model as that existing in the crack tip region of a real specimen at the onset of fracture. These two J values define a scaling factor which can be used to correlate the experimental toughness values with that obtained in a highly constrained case, represented in the model by the pure boundary layer model. The constant scaling factor is defined as J_{exp} / J_o. Dodds and Anderson identified J_{exp} as the apparent driving force for fracture while J_o is defined as the effective driving force.

The J_o parameter is calculated as follows. From dimensional analysis it is possible to demonstrate that in the case of SSY, the fields ahead of the crack tip are described by the following expression, equivalent to Eq. 5. 57:

Eq. 5. 63 $$\frac{\sigma_1}{\sigma_0} = f_I\left(\frac{J}{\sigma_0 r}, \theta\right)$$

where r is the radial distance for the crack tip and θ is the angle formed with the crack plane and J accounts for the load level. Inverting Eq. 5. 65, we obtain the following expression:

Eq. 5. 64 $$r(\sigma_I/\sigma_0, \theta) = \frac{J}{\sigma_0} g(\sigma_I/\sigma_0, \theta)$$

Finally, Eq. 5. 64 allows us determining the area inside the maximum principal stress contour:

Eq. 5. 65 $$A(\sigma_I/\sigma_0) = \frac{J^2}{\sigma_0^2} h(\sigma_I/\sigma_0)$$

where:

Eq. 5. 66 $$h(\sigma_I/\sigma_0) = \frac{1}{2}\int_{-\pi}^{\pi} g^2(\sigma_I/\sigma_0, \theta) d\theta$$

The previous equations present a very useful result that will be used subsequently: under SSY conditions ($T = 0$), the area enclosed by a certain stress level $A(\sigma_I/\sigma_0)$ scales with J^2. However, if the specimen or the component undergoes constraint loss at a given load level or J, the area determined by the principal stress level (σ_I) will be less than that predicted for SSY conditions:

Eq. 5. 67 $$A(\sigma_I/\sigma_0) = \phi \frac{J^2}{\sigma_0^2} h(\sigma_I/\sigma_0)$$

where $\phi \leq 1$.

An "effective" J is defined in such a way that when this J level is applied to the SSY model, the area enclosing a certain selected principal stress (σ_I) is the same as the area enclosed by the same σ_I in the LSY case:

Eq. 5. 68 $$A(\sigma_I/\sigma_0) = \frac{{J_0}^2}{\sigma_0^2} h(\sigma_I/\sigma_0)$$

Finally, we obtain:

Eq. 5. 69
$$\frac{J}{J_0} = \sqrt{\frac{1}{\phi}}$$

Anderson and Dodds developed the original model and its subsequent variations from plane strain FE models. Their main goal was to deal with the problem of the in-plane constraint loss, characteristic in the case of shallow cracks. Unfortunately, since they used 2D simulations for their studies, the effects of the out of plane constraint where not considered. However, this limitation is overcome by introducing the concept of effective thickness B_{eff} :

Eq. 5. 70
$$V = 2\int_0^{B/2} A(\sigma_I, z)dz = B_{eff}\, A_c(\sigma_I)$$

where $A_c(\sigma_I)$ is the area inside the σ_I contour at the middle plane of the three-dimensional specimen. Dodds et al. demonstrated in [5.47] that the results presented are independent of the actual σ_I value selected. In other words, the ratio J/J_o is insensitive to σ/σ_o.
The approach presented previously has been extended beyond its original scope of scaling low constraint toughness data at a constant temperature [5.69], giving rise to the so-called "critical stress-critical volume model", which has been applied to model the median fracture toughness versus temperature in the transition.

5. 5. 3. Critical stress – critical volume model (σ*- V*).

In the framework of the σ^*-V^* model, it is assumed that brittle fracture occurs when the volume of material encompassed by a certain critical stress level σ^* reaches a critical value V^*. Once the critical conditions have been met, the probability to fracture (P_f) takes a certain value. In general, we can write:

Eq. 5. 71
$$P_f = P\left[V^*, \sigma^*\right] = \alpha \le 1$$

For instance, it may be possible to identify the critical values of σ^*-V^* that leads to a fracture probability of 50% at a given temperature ($K_{Jc(med)}(T)$), or for any other fracture probability, like for instance the lower or upper bound limit $K_{Jc(0.xx)}(T)$ where 0.xx = 0.01 or 0.99. It is clear that modeling the σ^*-V^* model is quite similar to the one proposed by Dodds and Anderson (scale toughness model). However, it is possible to identify significant differences between these two approaches. The scale toughness model was basically proposed to account for the geometrical effects on fracture. The model was not intended to predict the variation of fracture toughness with the temperature. A central point of the Dodds and Anderson's model is that the scaling results are independent of the critical stress contour

considered for the calculation of the areas (or the volumes) for the SSY case and real specimens. Therefore, the stress level selected and the resultant area (volume) enclosed have no special physical meaning.

In contrast, the critical stress-critical volume model was originally proposed to account for the evolution of the fracture toughness with the temperature. Note that the underlying hypothesis is exactly the same in both models, namely, Eq. 5. 71. If the evolution of the critical parameters with the temperature is known, then it is possible to estimate any probability to fracture at any temperature:

Eq. 5. 72 $$P_f = P\left[V^*(T), \sigma^*(T)\right] = \alpha \leq 1$$

The original version of the critical stress-critical volume model assumes that the critical values σ^*-V^* are independent of the temperature. This hypothesis is mainly justified based on the experimental results reviewed in the section 5.4. In consequence, the dependence of fracture toughness with temperature will be only mediated by the dependence of the material constitutive behavior with the temperature. Indeed, a change in the material constitutive behavior will be reflected in the fact that, in order to verify the assumed critical σ^*-V^* conditions, different load levels will be needed at different temperatures. The central point of the critical stress-critical volume model is related to the fact that the predicted toughness evolution with the temperature will be now very sensitive to the selected critical σ^*-V^* conditions. In consequence, the values for the critical parameters needs to be carefully calibrated by following a well established calibration procedure.

5. 6. Finite element simulations, reconstruction of the K(T) curve.

In this Section, we describe the main elements of the critical stress-critical area/volume model. The modeling process is aimed at understanding the main factors controlling the experimental behavior of brittle fracture in the continuum level. Therefore, we have attempted to support the following developments by physically-based arguments.

As discussed in Section 5.5, there exists at the present two models based on the local approach concept. These models are in principle able to predict both, the size effect on fracture and the effect of the temperature on fracture toughness. However, the main advantage of the local approach to fracture is that it would allow us to solve the problem of "transferability", i.e. to estimate the fracture probability for a given flawed component and/or structural element *in any constraint condition* from the fracture properties of the correspondent material as measured from a standard procedure using fracture specimens. At the same time, the approach can be used to study the effect of neutron irradiation on fracture toughness.

The first model, known as the "Weibull stress model" derives from the early work of Beremin [5.34] and it has been discussed in detail by Gao et al [5.71]. The model, which is very popular among researcher in the fracture mechanics community, has been extensively used in RPV steels [5.72]. However, in our opinion, the Weibull stress approach has several drawbacks, which are mainly associated with the difficulty in the calibration of the different parameters involved since at least one of them is temperature-dependent [5.76]. Indeed, the determination of a proper calibration procedure is still an open subject. All the procedures that have been proposed require complex manipulation of numerical results obtained from detailed finite element calculations of the crack configuration under analysis. This fact certainly prevents the Weibull stress approach from gaining popularity in the engineering community, who are supposed to use this tool for practical purposes.

On the contrary, the second model, which is based on the concept of the critical stress-critical area/volume is relatively straightforward to implement. The main hypotheses and elements of the critical stress-critical area/volume were described previously in Section 5.5.2 and Section 5.5.3. Based on these arguments, we have chosen this second approach to model the $K_{Jc}(T)$ in the case of the Eurofer 97.

We will show that the *critical stress-critical volume* ($\sigma^* - V^*$)model can be in principle used to describe the main features of brittle fracture in the DBT region, where the fracture process is controlled by the creation of microcracks due to the fracture of second phase particles. We will show that the approach is consistent with the weakest link interpretation of brittle fracture.

We will demonstrate that the *critical stress-critical area* model ($\sigma^* - A^*$) can be used to model the main features of brittle fracture when it is controlled by the "propagation" of pre-existing microcracks. This is the case of the fracture phenomenon in the lower shelf, where no size effect and scatter in K_{Jc} is observed. Finally, we will shown that the $\sigma^* - A^*$ model is well suited to model an engineering lower bound for the fracture toughness data oriented to technical applications.

5. 6. 1. Finite element calculations

The finite element calculations have been performed using ABAQUS/Standard (6.5) which uses the Newton's method to solve the nonlinear equilibrium equations. Since large deformation levels are expected in the region near the crack tip, geometrical nonlinearity is expected. A finite strain ("large displacements") approach has been implemented to account for this problem.
Plane strain linear elements with reduced integration have been used in all the models. This type of elements is typically used in fracture mechanics problems due to its inherent advantages to model cases involving high levels of plastic strain, as it is the case in the crack tip region. Fully integrated elements may suffer from "locking" behavior, i.e. shear and volumetric locking. However, since linear reduced integration elements have only one integration point, the elements may suffer from hourglassing, i.e. they get distorted in such a way that the strains calculated at the integration point are all zero, which may leads to uncontrolled distortion of the mesh. This problem commonly arises in the crack tip region and can be eliminated by refining the mesh locally.

5.6.1.2. Compact tension specimen C(T)

A representative mesh of the C(T) specimen used in the present work is presented in Figure 5. 27. Due to symmetry considerations, only half of the specimen was modeled. Symmetry boundary conditions are applied on the crack plane.
The loading of the model is carried out through the displacement of a rigid body in contact (frictionless) with the specimen. In this way, the total load applied at any instant of the simulation can be easily obtained from the reaction force acting on the rigid body.
As it can be observed, the crack tip in the non-deformed configuration is represented as a small notch having a finite root radius. Following McMeeking [5.65], a solution independent of the initial notch geometry is eventually attained provided that the opening of the notch exceeds five times the initial notch dimensions. As a consequence, the results presented here are accepted to represent the blunting of an initially sharp crack.

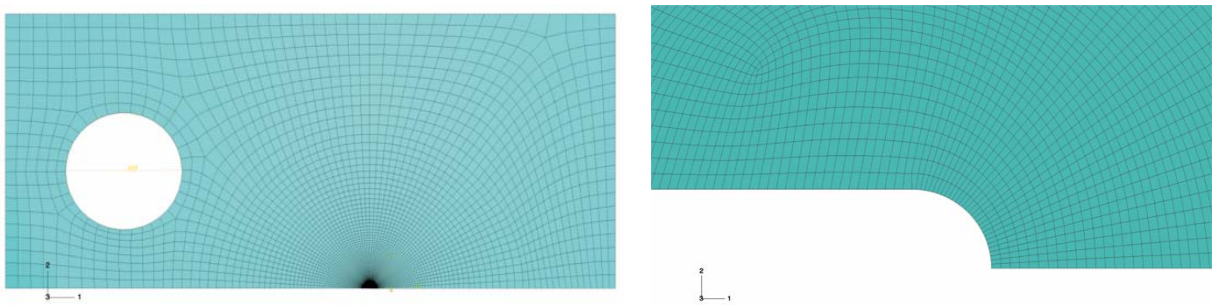

Figure 5. 27: *Right: finite element mesh used in the present work. Right: Detail of the crack tip in the initial configuration.*

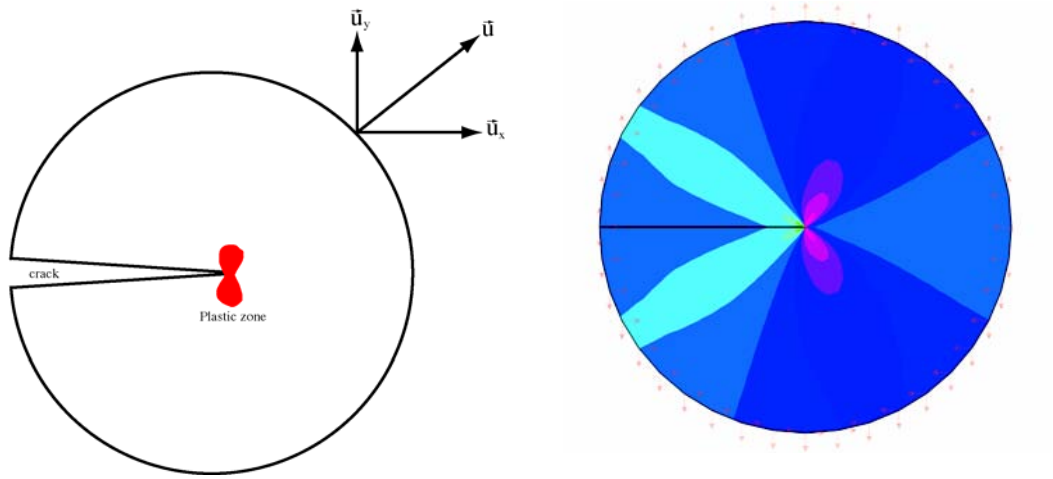

Figure 5. 28: *Left: diagram showing the boundary layer problem. Right: FE results for a plane strain calculation. The principal stress level relates to the different color contours in the plot (higher stress level corresponds to reddish hues)*

Three different FE models have been considered to generate the numerical results, the only difference among them being the initial crack tip radius: r_0 (model c_1), $2\,r_0$ (model c_2) and $3\,r_0$ (model c_3) respectively. This difference in the initial crack tip radius allows us to investigate different load levels without deforming excessively the elements in the region of the crack tip.

The evolution of the areas with the principal stress level $A(\sigma_I)$ has been determined from the previously described three models at four different temperatures:-120°C, -100°C, -90°C and -80°C.

Finally, the loading level was determined by means of the J-integral, calculated for different closed line contours in the models. The expected path independence of J arises for contours far enough from the crack tip.

5. 6. 1. 3. Small scale yielding model.

We have built a fully circular model, based upon the pure boundary layer model (T-stress=0), which contains a small notch radius ρ_o representing the crack tip.

The opening of the crack was performed in Mode I by imposing the displacements Δx and Δy as given by the elastic solution for the crack tip strain field. These displacements were applied to the nodes on the outer circular boundary. Assuming a T-stress equal to zero, Δx and Δy are written as:

Eq. 5. 73

$$\Delta x = K\frac{1+\upsilon}{E}\sqrt{R/2\pi}\cos\left(\frac{\theta}{2}\right)\left(3-4\upsilon-\cos\theta\right)$$

Eq. 5. 74 $$\Delta y = K\frac{1+\upsilon}{E}\sqrt{R/2\pi}\,\sin\left(\frac{\theta}{2}\right)\left(3-4\upsilon-\cos\theta\right)$$

where r is the radial distance from the crack tip and θ is the angle between the crack plane and the direction to the node, ν is the Poisson's ratio and E the Young's modulus. Note that the imposed displacements scale with the applied stress intensity factor K. 2D linear reduced integration elements were used.
In order to make sure that the initial tip radius does not affect the stress fields generated by the crack, we ran simulations such that the crack tip opening displacement δ assures that the ratio δ/ρ_o is larger than 4. A schematic draw of the boundary layer problem, together with the FE model are presented in Figure 5. 28.

5. 6. 2. Calculation of the area enclosed by a certain stress level in the case of SSY conditions.

One of the main difficulties concerning the implementation of the model is related to the determination of the area or volume of material enclosed by a certain stress level as a function of the loading level, expressed by the appropriate stress intensity factor (in our case, K_J).
In the particular case of plane strain SSY conditions, the area encompassed by a stress level (as given by a certain component of the stress tensor, σ_{ij}) scales with the $K_J(T)^4$:

Eq. 5. 75 $$A(\sigma_{ij}) = c\left[\sigma_{ij},\sigma(\theta_1,\theta_2,...,T)\right]\cdot\left[K_J(T)\right]^4$$

where $c\left[\sigma_{ij},\sigma(\theta_1,\theta_2,...,T)\right]$ is a constant that depends on the magnitude of the particular component of the stress tensor and on the constitutive behavior of the material under analysis, represented here by the function $\sigma(\theta_1,\theta_2,...,T)$.
The values for the constant $c\left[\sigma_{ij},\sigma(\theta_1,\theta_2,...,T)\right]$ can be determined from the analysis of the FE solutions for the pure boundary layer model (Figure 5. 28). Eq. 5. 75 is plotted schematically in Figure 5. 29 for different stress levels. Note that the first principal stress σ_I was selected as the appropriate stress magnitude to consider, consistently with the procedure described in the early development of the scale toughness model [5.46][5.47].
In the case of real specimens, Eq. 5. 75 needs to be modified to account for the sensitivity of the stress fields to the specific specimen geometry when compared to those predicted by the pure boundary layer model (SSY). In this sense, it is important to stress the fact that the result expressed in Eq. 5. 75 is only valid for the case of SSY, i.e. T-stress equal to zero.
For the real case of SEN(B) or C(T) specimens where $T \neq 0$, the fields in the crack tip region are not self-similar in the $r\sigma_0 / J$-space.

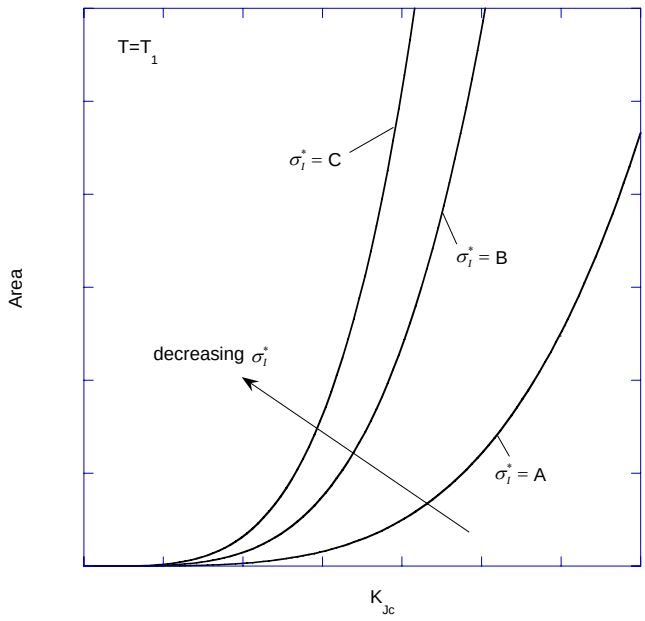

Figure 5. 29: *Variation of the area enclosed by a certain principal stress level as a function of* K_J.

As discussed previously in section 5. 2. 5, a two -parameter approach is typically used to describe the fields in this region ($J-Q$ model). In this framework, we recall that the fields in the vicinity of the crack can be written as follows:

Eq. 5. 76 $$\frac{\sigma_{ij}}{\sigma_0} = \tilde{f}_{ij}(\frac{J}{\sigma_0 r},\theta;Q) = f_{ij}(\frac{J}{\sigma_0 r},\theta) + Q\delta_{ij}$$

In the particular case of the principal stress σ_I, we can write [5.47]:

Eq. 5. 77 $$\frac{\sigma_I}{\sigma_0} = \tilde{f}_I(\frac{J}{\sigma_0 r},\theta;Q) = f_I(\frac{J}{\sigma_0 r},\theta) + Q \qquad \text{valid for } \frac{J}{\sigma_0} \le r \le 5\frac{J}{\sigma_0}$$

In analogy with Eq. 5. 75, the area enclosed by a certain principal stress contour will be given now by the following equation:

Eq. 5. 78 $$A(\frac{\sigma_I}{\sigma_0} - Q) = \frac{J^2}{\sigma_0^2} h(\frac{\sigma_I}{\sigma_0} - Q)$$

Note that the area enclosed by $(\sigma_1/\sigma_0 - Q)$ will be now self-similar in the $x/(J/\sigma_0) - y/(J/\sigma_0)$ space. As stated by Eq. 5. 78, $A(\sigma_1/\sigma_0 - Q)$ scales now with J^2 (not $A(\sigma_I/\sigma_0)$).

Therefore the SSY relationship between $A(\sigma_I/\sigma_0)$ and J^2 cannot be used in cases where the T-stress (and in consequence the Q fields) is different of zero. However, as we will see in next sections, the relationship between the areas enclosed by a certain critical stress level and

the loading level (expressed by J or K_J) can still be expressed as a power law having exponent $\neq 4$.

An example of the effect of the geometry on the stress fields in the crack tip region is presented in Figure 5.30. The figure shows the results for the evolution of $\sigma_{22}/\sigma_{0.2}$ in the self similar space ($J/\sigma_0/r$) as obtained from 2D plane strain C(T) model for Eurofer97 steel at -80°C. The effect of the (positive) T-stress in the stress fields near the crack tip is evident when the C(T) curves are compared to the SSY curves as given by the pure boundary layer model.

Increasing the load level (indicated here by the parameter $b\sigma_{0.2}/J$), increases the T stress level (which is proportional to K_J) and consequently, increases the Q level in the crack tip region. Note that the $J-Q$ annulus seems to be smaller than in the case of the modified boundary layer results, being the approach approximately valid for $2.5J/\sigma_0 \le r \le 5J/\sigma_0$.

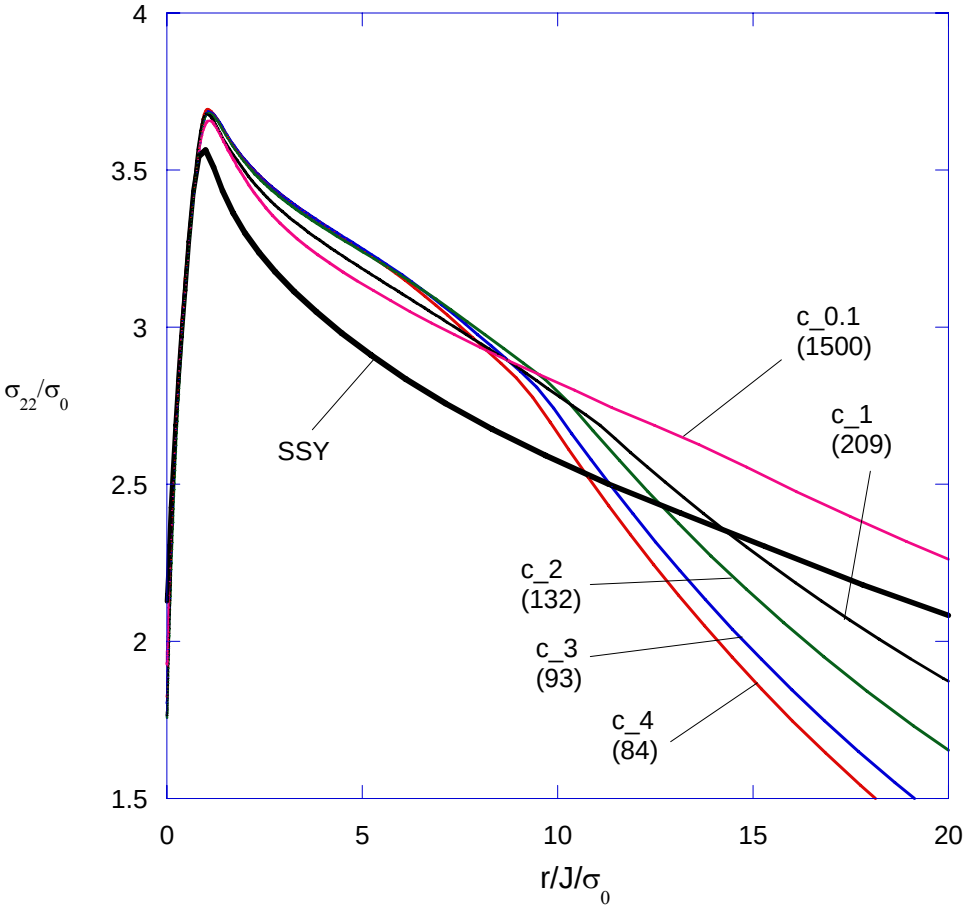

Figure 5. 30: *Comparison between the SSY calculation and C(T) specimens calculations. The effect of the geometry of the specimen on the stress fields is highlighted. In brackets, the parameter* $b\sigma_{0.2}/J$ *indicating the load level.*

5. 6. 3. The critical stress-critical volume model.

Let's assume we have generated a dataset from specimens having a given thickness B by testing several specimens at different temperatures in the ductile-to-brittle transition region. We will assume that the area and volumes enclosed by a certain stress level are related to K_J through a power law, similar to Eq. 5. 75 but having $m \neq 4$. In the case of the volume V, we can write:

Eq. 5. 79
$$V = c_V \left[B, \sigma_I^*, \sigma\left(\theta_1, \theta_2, ..., T\right) \right] \cdot \left[K_J \right]^m$$

where c_V is the proportionality constant between V and $\left(K_J\right)^m$, and depends on the critical stress level, the constitutive behavior of the material and the specimen thickness. The exponent m may depend on temperature. The local criterion for fracture (Section 5.5.3) allows us to write the following expression:

Eq. 5. 80
$$V_{(0.xx)}^* = c_V \left[B, \sigma_I^*, \sigma\left(\theta_1, \theta_2, ..., T_1\right) \right] \cdot \left[K_{Jc(0.xx)}(T_1) \right]^m = c_V \left[B, \sigma_I^*, \sigma\left(\theta_1, \theta_2, ..., T_2\right) \right] \cdot \left[K_{Jc(0.xx)}(T_2) \right]^m$$

where $K_{Jc(0.xx)}(T_i)$ accounts for the fracture toughness corresponding to a probability to fracture $P_f = 0.xx$ at the temperature T_i, and $V_{(0.xx)}^*$ represents the corresponding critical volume. Finally, the relationship between the K_{Jc} values at two different temperatures will be given by:

Eq. 5. 81
$$\frac{K_{Jc(0.xx)}(T_1)}{K_{Jc(0.xx)}(T_2)} = \left\{ \frac{c_V \left[B, \sigma_I^*, \sigma\left(\theta_1, \theta_2, ..., T_2\right) \right]}{c_V \left[B, \sigma_I^*, \sigma\left(\theta_1, \theta_2, ..., T_1\right) \right]} \right\}^{1/m}$$

The meaning of Eq. 5. 80 can be better understood with the help of Figure 5. 31, where the volume enclosed by a given stress level is plotted as a function of the stress (using $K_{Jc(0.xx)}$ as a parameter) for three different temperatures.
Figure 5. 31 shows several curves that are associated to different $K_{Jc(0.xx)}(T)$ values. Each curve is representative of a particular loading level, therefore, there exist an infinite number of them. For the particular cases presented in Figure 5.31, the curves intercept each other in two points, labeled "a" and "b". The $K_{Jc}(T)$ values corresponding to the curves intersected in the point "i" are labeled as $K_{Jc}^{(i)}(T)$. The crossover points define different sets of potential critical parameters $\sigma_I^{*(i)}$ and $V^{*(i)}$. Note that there is an infinite number of such $\sigma_I^{*(i)}$-$V^{*(i)}$ pairs.

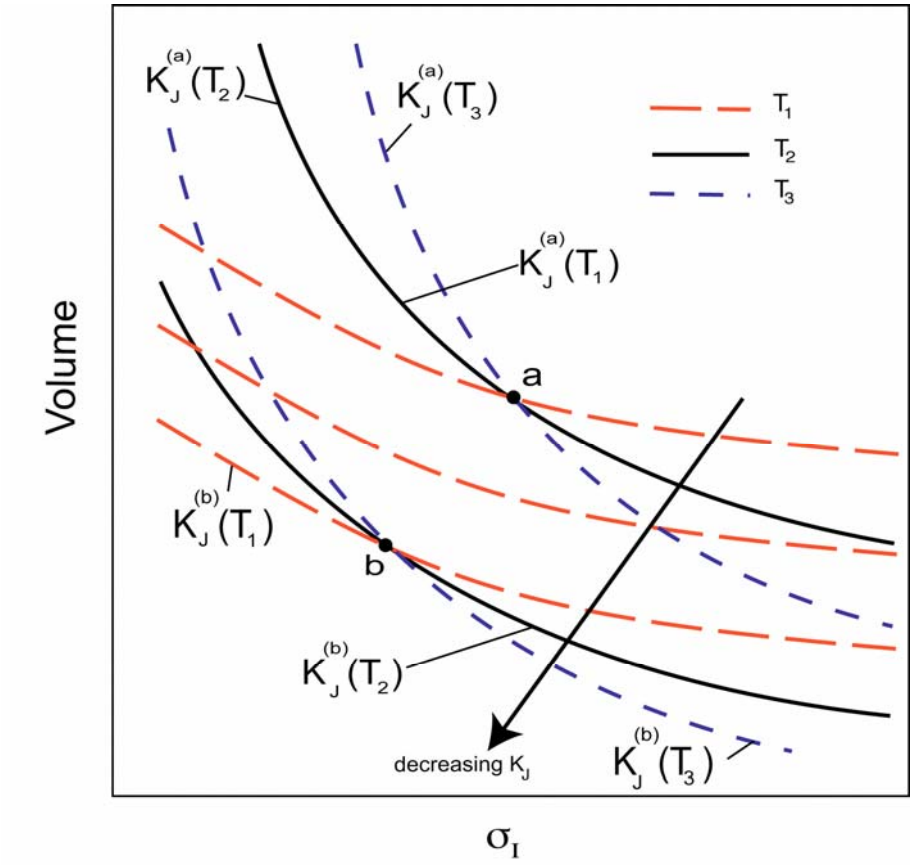

Figure 5. 31: *Schematic plot of the volume enclosed versus the stress for different K_j values at different temperatures.*

All the $K_{Jc}^{(i)}(T)$ values related to a certain critical set $\sigma_I^{*(i)}$-$V^{*(i)}$ satisfy Eq. 5. 80, i.e. for a given probability to fracture, we can write:

Eq. 5. 82

$$V_{(0.xx)}^{*(i)} = c_V\left[B,\sigma_I^{*(i)},\sigma\left(\theta_1,\theta_2,...,T_1\right)\right]\cdot\left[K_{Jc(0.xx)}^{(i)}(T_1)\right]^m = c_V\left[B,\sigma_I^{*(i)},\sigma\left(\theta_1,\theta_2,...,T_2\right)\right]\cdot\left[K_{Jc(0.xx)}^{(i)}(T_2)\right]^m$$
$$= c_V\left[B,\sigma_I^{*(i)},\sigma\left(\theta_1,\theta_2,...,T_3\right)\right]\cdot\left[K_{Jc(0.xx)}^{(i)}(T_3)\right]^m$$

where $i = a,b,.....$

In the example shown in Figure 5. 31, the points "a" and "b" define two different set of temperature-independent critical values, $V^{*(a)} - \sigma_I^{*(a)}$and $V^{*(b)} - \sigma_I^{*(b)}$. Since there exist an infinite number of such pairs, the model is not purely predictive, i.e., the evolution of the probability to fracture for a given material, represented here by $K_{Jc(0.xx)}$, cannot be assessed just from the knowledge of the constitutive behavior. A calibration procedure is then needed. This fact is reflected in Eq. 5. 81, which shows that the critical stress-critical volume model only allows us to determine the $K_{Jc}(T)$ ratios between fracture toughness values at different

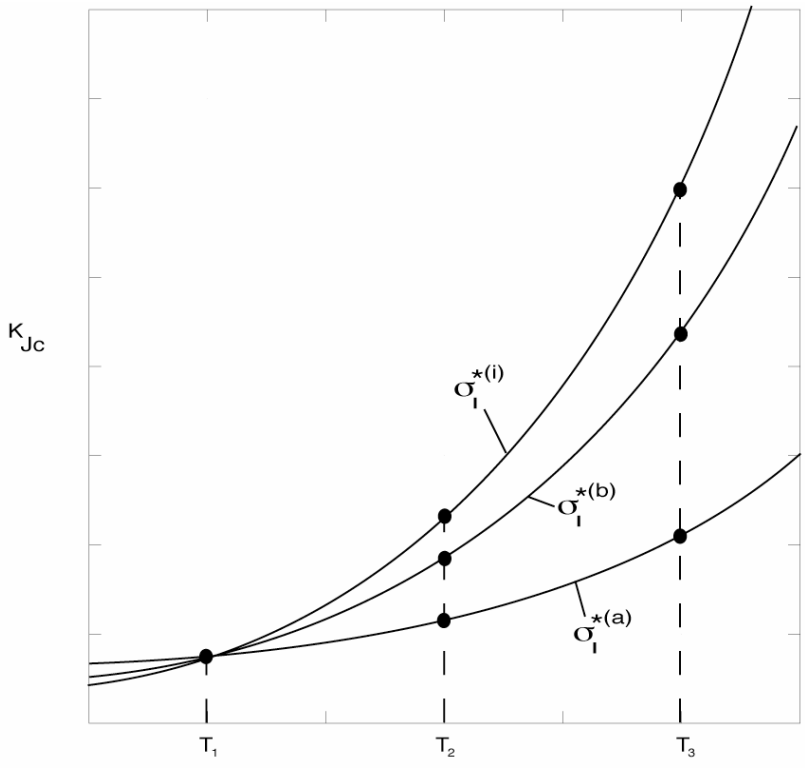

Figure 5. 32: *Schematic reconstruction of the* $K_{Jc(0.xx)}(T)$ *curve based upon the critical stress – critical volume model, assuming that the fracture toughness level is known for a certain cumulative probability for fracture at the temperature* T_1.

temperatures. Concerning this last point, it is important to re-emphasize that there exists in principle an infinite number of solutions for Eq. 5. 80. This is schematically represented in Figure 5. 32, where the evolution of $K_{Jc}(T)$ is plotted for three different values of the critical parameters. The simplest way to estimate the critical parameters consists on comparing the predicted $K_{Jc}(T)$ curve for a given cumulative probability to fracture with the corresponding experimental curve. For instance, assuming that the experimental locus for the $K_{Jc(med)}(T)$ is known, the σ_I^*, V^* values whose associated $K_{Jc}(T)$ curve better match the experimental $K_{Jc(med)}(T)$ curve, will be accepted as the critical parameters for the 50% cumulative probability to fracture. The same procedure can be implemented for other cumulative probability to fracture levels.
The foregoing conclusions also allies to the $\sigma^* - A^*$ model.

5. 6. 4. Micromechanics of fracture in the DBT region and the lower shelf.

Early studies of brittle fracture in steels where based on the study of notched bend bar specimens and spheroidized steels. The critical event leading to fracture was found to be the propagation of microcracks formed by fracture of carbides into the matrix, and therefore, the fracture process was understood as “propagation controlled”. In other words, the fracture of the relatively large carbides present in this type of steels (the “initiation” step) was envisaged as a process occurring early in the loading history (before the attainment of the propagation

conditions). In this interpretation, macroscopic brittle fracture occurs as soon as the local stress level is high enough to propagate the pre-existing microcracks. The "critical stress" leading to fracture was assumed to be the maximum tensile stress level ahead of the crack tip at the moment of fracture. This "local" stress level (which was typically estimated from very simplified methods) was found to be relatively constant and independent of temperature, supporting the interpretation that fracture was controlled by the attainment of a given local tensile stress level. As discussed in Section 5.5, this stress level was linked to the conditions needed for the propagation of microcracks by means of the Griffith-Orowan equation. The observed scatter in the measured load to fracture was thus associated to the natural distribution of microcrack sizes, which is in turn associated to the carbide size distribution.

In the case of steels with much smaller second phase particles (i.e. as quenched martensite, tempered martensite, tempered bainite), it was impossible to explain satisfactorily the fracture process in terms of the Griffith-Orowan equation and therefore, it was accepted that the critical event leading to fracture in these materials was not the propagation of microcracks. In contrast, in an initiation-controlled process, brittle fracture was expected to be independent from the local tensile stress level. Instead, a critical shear strain is postulated to control the formation of microcracks due to the actions of dislocation pile ups.

Nowadays it is broadly accepted that depending on the temperature at which the fracture process takes place and the overall stress levels and stress gradients present in the material, brittle fracture can be characterized as *initiation-controlled* or a *propagation-controlled* process [5.70]. However, the meaning of this statement is slightly different than the one discussed previously.

The initiation stage involves the creation of microcracks in the crack tip region. The details concerning the microcrack creation will depend upon the particularities of the microstructure under study. The second stage is obviously associated to the propagation of these microcracks into the ferritic matrix.

Fracture of pre-cracked specimens in the DBT region is accepted to be "initiation controlled". This actually implies that the conditions for the propagation of microcracks are fulfilled before its formation. Note that the first microcracks to be formed are the most critical ones (i.e. originated by the biggest particles located in the most critical positions in the crack front) and therefore, the generation of only few microcracks can give rise to macroscopic fracture. Typically, the microcracks acting as the initial nucleus for the fracture process are formed due to the fracture of second phase particles and therefore, its features (size, distribution, etc.) are linked to those of the particles. However, it is evident that other mechanisms for the microcrack formation should be operative in the case of very clean materials having no second phase particles in its microstructure (i.e. as quenched martensite).

The main experimental support to the identification of fracture in the DBT region as an initiation-controlled process comes from the analysis of fracture surfaces by means of Scanning Electron Microscope (SEM). Several researchers have shown that in the case of specimens tested at temperatures in the DBT region, it is possible to identify clear initiation sites [5.70][5.76] that are frequently associated to second phase particles.

Assuming that the key microstructural features associated to microcrack formation are homogeneously distributed in the material, the probability of finding a critical suitable

initiation site (i.e. a site that once activated, the so formed microcrack will be able to propagate itself through the ferritic matrix) will certainly depend on the volume of material undergoing a given stress level. The typical statistical size effect observed in the fracture toughness values in the DBT region can be explained on this basis, giving further support to the fact that the main features of brittle fracture in the DBT region are consistent with an "initiation controlled" fracture process. It is worth mentioning that even valid K_{IC} values (the "plane strain" fracture toughness measured following ASTM E399), also shown a statistical size effect in the DBT region [5.77].

The σ^*-V^* model is totally consistent with a weakest link interpretation of the fracture process and in consequence, also consistent with an initiation controlled mechanism, predicting the following size effect for typical fracture specimens:

Eq. 5. 83
$$\frac{K_{Jc(2)}}{K_{Jc(1)}} = \left[\frac{B_{(1)}}{B_{(2)}}\right]^{1/4}$$

where B accounts for the crack front length. It is well known that the same result is obtained from weakest-link considerations accepting that the distribution of fracture toughness values at a given temperature in the DBT region follows a two-parameter Weibull distribution. A clear drawback of Eq. 5. 83 arises for large crack fronts (large volumes of stressed material). In this case, the fracture toughness values predicted will steadily decreases until eventually very low values will be attained. Since this situation is clearly unsounded from a physical point of view, the classical description of brittle fracture in the DBT region includes a threshold (a third parameter in the Weibull distribution) that represents a minimum stress intensity needed to trigger fracture, $K_{\min}$. We have already seen that the ASTM E1921 standard assumes $K_{\min}$=20 $MPa \cdot m^{1/2}$. However, this value is only a mathematical parameter and it has no particular physical meaning.

The case of a propagation-controlled fracture is described next. The process of brittle fracture in the lower shelf is considered to be propagation-controlled. Consistently, no initiation sites can be found in fracture surfaces of specimens tested at very low temperatures. The microcracks seem to be formed before the conditions for propagation are fulfilled. In the moment of fracture, a large number of microcracks located along the crack front start to propagate and that is the reason why no "initiation sites" are identified in the fracture surfaces of specimens tested at temperatures typical of the lower shelf.

Accepting that fracture in the lower shelf is propagation-controlled, and assuming that the microstructural features associated to initiation sites remain the same than in the DBT region, the propagation conditions seems to be independent of the size distribution of microcracks, at least for the case of pre-cracked specimens. This statement is also consistent with the fact that steels having quite different microstructures display very similar fracture toughness levels in the lower shelf (approximately 40 $MPa \cdot m^{1/2}$), which also suggest that the fracture event is somehow dominated by the phenomena in the mesoscale (nm).

Propagation-controlled fracture is associated to the lack of statistical size effect, and consequently, the fracture data does not suffer from the scatter observed in the DBT region.

From a continuum point of view, it is likely that the propagation conditions are not only mediated by the stress level in a given region of the material but also by the stress gradients. Very high stress gradients, typical for pre-cracked specimens at lower shelf temperatures, can lead to the arrest of an otherwise critical microcrack. Unfortunately, our knowledge on the overall phenomena controlling the initiation and posterior propagation of the microcracks is quite limited. Ultimately, the problem cannot be fully discussed under the continuum approximation since brittle fracture is a truly multiscale problem.

The $\sigma^* - A^*$ model is inspired on the ideas discussed previously. Since the maximum stress level ahead of the crack tip does not depends on the loading level, the size of the critical area is associated to the magnitude of the stress gradients, and therefore, it contains the key points to correctly model the main features of a propagation-controlled fracture process. In consequence, we propose that the critical conditions for propagation can be expressed by the critical parameters of the $\sigma^* - A^*$ model.

Finally, the link between the $\sigma^* - V^*$ and the $\sigma^* - A^*$ models can be explained in the following terms. As indicated previously, the fracture process can be initiation-controlled only if the conditions for propagation are fulfilled before the formation of microcracks. This is the reason why Eq. 5. 83 fails for large stressed volumes, i.e., the conditions for propagation were never considered. In other words, $\sigma^* - V^*$ model applies provided that the conditions for propagation stated by the $\sigma^* - A^*$ are previously fulfilled.

The main aspects of the discussion up to here are summarized next:

a) *Brittle fracture in steels can be rationalized as an "initiation-controlled" process or a "propagation-controlled" process.*

b) *We postulate that the $\sigma^* - V^*$ model is well suited to model the main features of "initiation-controlled" fracture. Size effects predicted by the $\sigma^* - V^*$ model agrees with the prediction of the weakest-link approach.*

c) *We postulate that the $\sigma^* - A^*$ model is well suited to model the main features of "propagation-controlled" fracture. At the continuum level, the microcrack propagation phenomenon is governed by the stress gradients ahead of the crack tip.*

Having summarized the discussion, we would like now to include a new element into consideration. As it was pointed out previously, the statistical size effect is one of the main features of fracture toughness values in the DBT region. However, there is enough experimental evidence indicating that it may be possible to determine an engineering lower bound for brittle fracture that actually does not depend on the specimen size (see for instance Figure 5.35).

To further stress this point, note that in the classic interpretation of the statistical size effect, the fracture toughness size dependence arises because of the different probabilities of finding a suitable triggering point in specimens having different sizes. If an "absolute" lower bound for fracture exists, the statistical size effect cannot take place there simply because all the specimens displaying the lowest fracture toughness values *will already contain the most*

suitable initiation site in the most sensible place in the crack front by definition. Once the stress level is high enough to activate this critical initiation site, macroscopic fracture will proceed provided that the conditions for propagation are fulfilled. However, for low K_J values, as it is the case in the lower bound, the propagation conditions may not be fulfilled due to the existence of very high stress gradients in the crack tip region, and in consequence, the formed microcracks could be arrested, probably in the particle/matrix interface itself. The overall fracture process for the specimens having the lowest fracture toughness levels may then become propagation-controlled, in a similar way than in the case of the lower shelf. If this were the case, the absolute lower bound could also be modeled by the $\sigma^* - A^*$ approach. Note that the interpretation of the fracture process for the lower bound in the DBT region as a propagation-controlled process is consistent with the size independence of the lower bound.

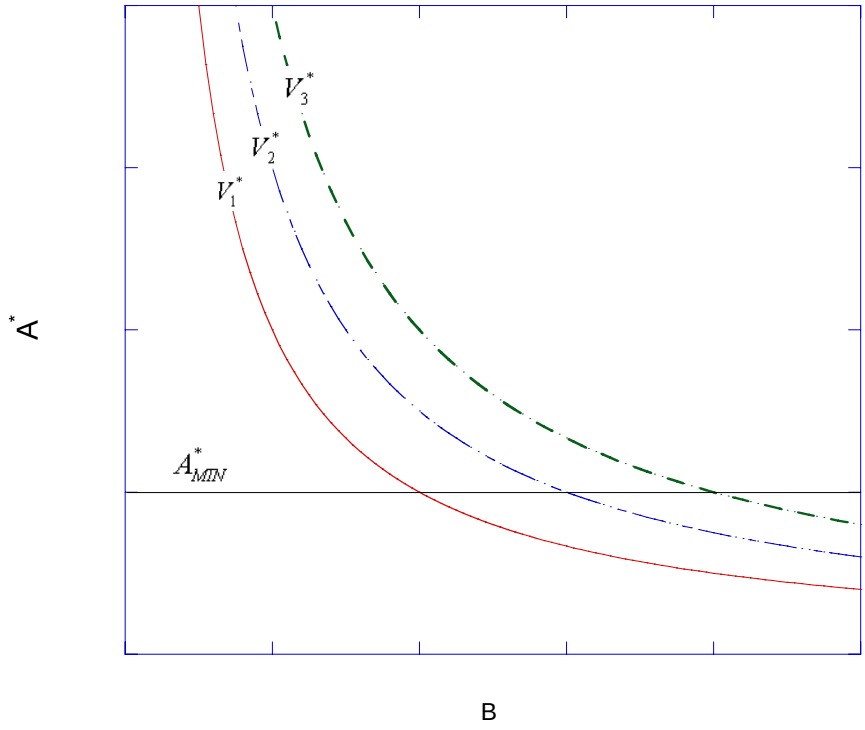

***Figure 5. 33**: Schematic B-dependence of the critical area A* at given critical V*. The minimum level of A_{min} is also indicated.*

5. 6. 5. Application of the $\sigma^* - A^*$ model.

In order to check the validity of the model for the case of the Eurofer97, we have undertaken a systematic analysis of 2D plane strain finite element simulations from -196°C to -50°C. Hereafter we briefly describe the main variables that have been considered.

5. 6. 5. 1. Constitutive description of Eurofer97.

The constitutive behavior of the Eurofer97 has been obtained from tensile tests at the temperature of interest. As we showed it in Chapter 3, the level of uniform plastic deformation that can be reached is in the order of 10% for these types of steels. As expected, FE simulations of blunting cracks indicates that large deformations are obtained near the crack tip. Since such large deformations cannot be obtained experimentally (at least in a simple and relatively straightforward way) we have used two limiting relationships for the plastic behavior at large deformations. The first one consists of a saturated law (Eq. 4. 22 in Chapter 4) and the second one displays a Stage IV (constant strain hardening) at large plastic deformations (linear extension of the true-stress true-strain from the onset of necking). We have not found any significant difference in the results derived from these two constitutive descriptions. Therefore, the non-saturated constitutive description has been systematically implemented in the calculations. No strain rate dependence has been considered so far. In consequence, the constant c in Eq. 5. 74 can be now re-written as follows:

Eq. 5. 84 $$c\left[\sigma_I^*, \sigma(\theta_1, \theta_2, ..., T_1)\right] = c\left[\sigma_I^*, \sigma(\bar{\varepsilon}_p, T_1)\right]$$

where $\bar{\varepsilon}_P$ stands for the equivalent plastic strain.

5. 6. 5. 2. Determination of the areas.

The areas encompassed by a certain stress level have been determined from a program used for the post processing of the numerical data. The program, which is written in FORTRAN, is able to read the ABAQUS output file. The coordinates and the principal stress level of each node are obtained for each time increment. During this stage, the nodes are also associated to a particular element. The critical area is then calculated as follows. The area of each element is first calculated. Next, this area is multiplied by the number of nodes fulfilling the stress condition, namely, $\sigma_I \geq \sigma_c$. The result so obtained is subsequently divided by the number of nodes defining the elements (in our case, four nodes (2D linear quadrilateral elements)). The process is extended to all the nodes in the FE mesh.
Provided that the mesh is refined enough, this procedure ensure a good averaging for the elements defining the boundary of the area. In consequence, the bias in the estimated value of the true area is quite small.

5. 6. 5. 3. Finite element simulation results.

We have previously shown that in the special case of SSY (pure boundary layer model), the area enclosed by a certain stress level will be proportional to the fourth power of K_J. This fact is a consequence of the self-similarity of the stress fields in the $r/K_J^2/\sigma_0^2$ non-dimensional space. In the real case of fracture specimens, the stress fields ahead of the crack

Temp.	Critical Stress (MPa)										
	2200	2150	2100	2070	2050	2030	2000	1970	1950	1930	1900
-50°C				2.61E-07	7.35E-07	1.39E-06	2.88E-06	5.13E-06	7.38E-06	1.01E-05	1.58E-05
-80°C			2.76E-07	1.48E-06	2.77E-06	4.60E-06	8.09E-06	1.40E-05	2.04E-05	2.65E-05	4.33E-05
-90°C			1.55E-06	3.45E-06	5.15E-06	7.29E-06	1.18E-05	2.00E-05	3.11E-05	3.95E-05	6.71E-05
-100°C	2.31E-06	5.27E-06	1.11E-05	1.66E-05	2.06E-05	2.64E-05	3.52E-05	4.53E-05	5.38E-05	6.40E-05	7.61E-05
-120°C	1.06E-05	2.00E-05	3.39E-05	4.44E-05	5.25E-05	6.20E-05	7.58E-05	9.26E-05	1.05E-04	1.18E-04	1.40E-04
-145°C	8.10E-05	1.84E-04	3.36E-04	4.67E-04	5.68E-04	6.88E-04	8.93E-04	1.10E-03	1.34E-03	1.57E-03	1.95E-03
-160°C	6.45E-04	8.75E-04	1.27E-03	1.58E-03	1.82E-03	2.08E-03	2.53E-03	3.03E+03	3.40E-03	3.80E-03	4.44E-03
-196°C	4.69E-03	5.51E-03	6.79E-03	6.65E-03	7.44E-03	8.52E-03	9.05E-03	9.60E-03	1.04E-02	1.02E-02	1.50E-02

Table 5. 1: c *coefficients obtained for 0.4T C(T) specimen.*

Temp.	Critical Stress (MPa)										
	2200	2150	2100	2070	2050	2030	2000	1970	1950	1930	1900
-50°C				4.5	4.5	4.5	4.5	4.5	4.5	4.5	4.5
-80°C			4.97	4.78	4.74	4.71	4.71	4.69	4.67	4.67	4.65
-90°C			4.79	4.75	4.74	4.75	4.75	4.70	4.68	4.68	4.63
-100°C	4.61	4.61	4.61	4.61	4.61	4.61	4.61	4.61	4.61	4.61	4.61
-120°C	4.61	4.61	4.61	4.61	4.61	4.61	4.61	4.61	4.61	4.61	4.61
-145°C	4.59	4.46	4.41	4.36	4.34	4.32	4.29	4.27	4.25	4.23	4.21
-160°C	4.30	4.26	4.23	4.21	4.19	4.18	4.15	4.13	4.12	4.10	4.08
-196°C	3.96	3.95	3.93	3.95	3.93	3.91	3.91	3.91	3.90	3.92	3.84

Table 5. 2: *exponent m obtained for 0.4T C(T) specimen.*

tip departs from the one-parameter description due to the increasing effect of the higher order terms in Eq. 5. 1. The particular case of the C(T) specimens is shown in
Figure 5. 30, where the stress fields for different loading levels are plotted together with the correspondent SSY case. Two conclusions can be derived from the inspection
Figure 5. 30: a) the stress fields in the real case are not self similar in the $r/K_J^2/\sigma_0^2$ space, and b) the area enclosed by a certain stress level in the case of a real specimen (i.e. C(T) or SEN (B)) cannot be derived accurately from SSY calculations. Even though the area encompassing a given stress level will not be proportional to the fourth power of K_J any longer, it is still possible to relate the area and K_J through a power law with exponent $m \neq 4$. The data obtained from the numerical simulations has been fitted with the following general expression:

Eq. 5. 85 $$A = c_A (K_J)^m$$

where c_A and m are constants.
Note that since , the numerical results (which have arbitrary length units) needs now to be scaled to represent a particular specimen size, i.e. 0.4T C(T). In consequence, the constant in Eq. 5. 85 will now depend on the size of the specimen. However, it is relatively straightforward to scale the constant as obtained for a given specimen size to another

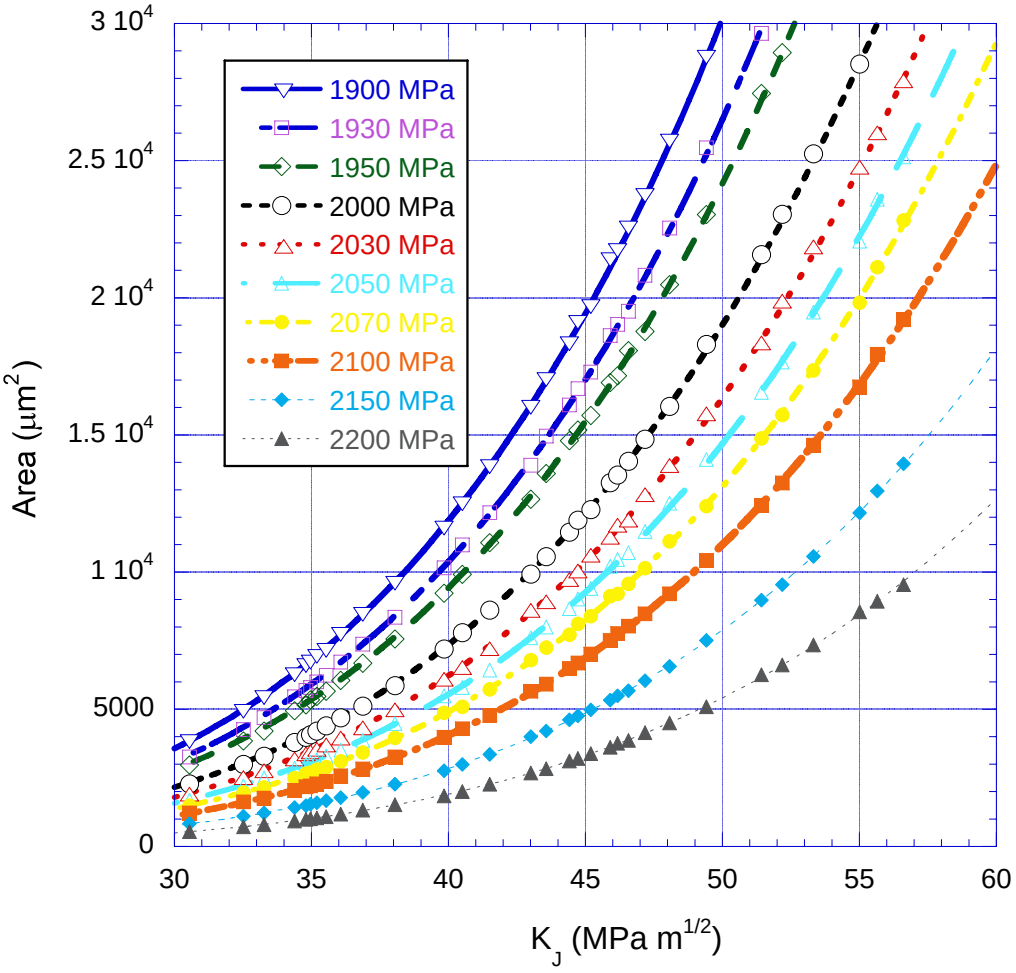

Figure 5. 34: *Plot of the area enclosed by different principal stress levels as a function of for the case of a 0.4T C(T) specimen. Temperature=-80°C.*

specimen size. For instance, if is known for a sT C(T) specimen, the corresponding value for a nT C(T) specimen will be:

Eq. 5. 86

$$c_{nT} = c_{sT}\left(\frac{n}{s}\right)^{(2-m/2)}$$

The results presented in this section corresponds to a 0.4T C(T) specimen.

Figure 5. 34 presents the typical evolution of A as a function of the loading level, expressed by K_J, for the case of the Eurofer97 at T= -100°C. Eq. 5. 85 was observed to adjust perfectly the numerical data. The exponent in Eq. 5. 85 takes values ranging between 3 and 5 for all the temperatures considered here (-50°C down to -196°C). The coefficients in Eq. 5. 85 obtained from the fitting process are presented in Table 5. 1 and Table 5.2.

5. 6. 5. 4. Comparison of the plane strain results with experimental data. Analysis of an engineering lower bound curve.

The experimental fracture toughness data of the Eurofer97 has been used to estimate an empirical lower bound for the fracture toughness. In order to do so, the approach followed here was similar to the one used in the development of the ASME lower bound curve for fracture toughness of RPV steels, i.e. to find a curve that is actually observed to perfectly bind the experimental data. Since the database used contains more than hundred results, we do believe that the description of the lower bound for Eurofer97 we offer in the present paper is quite conservative for the temperatures tested. However, the lack of experimental data at temperatures higher than -100°C introduces a degree of uncertainty for temperatures near the upper DBT region.

In Section 5.3, we have shown that that evolution of the median fracture toughness values with temperature ($K_{Jc(med)}(T)$) for the Eurofer97 is not well described by the master curve expression given in ASTM E1921. This conclusion arose from the comparison of the predicted evolution of $K_{Jc(med)}(T)$ as given by the master curve and the experimentally determined $K_{Jc(med)}$ values at -100°C and -120°C. Note that these two temperatures are in the DBT region, and therefore, the master curve concept should work, as it is observed in RPV steels.

There are two possible explanations to the discrepancy between the master curve and the Eurofer97 dataset. The first explanation is based on the assumption that the -120°C dataset is too close to the lower shelf and in consequence, the master curve concept and the weakest link concepts do not apply for this type of steels. However, for $T \geq$-100°C, the approach may works correctly. If this were the case, the general criterion for the applicability of the master curve ($|T - T_0| \leq 50°C$) should be revised for the case of tempered-martensitic steels.

The second explanation has been already discussed in Section 5.3.2.2 and assumes that fracture properties of the Eurofer97 do not obey the master curve concept. In consequence, the master curve expression cannot account for the fast increase of $K_{Jc(med)}(T)$ with increasing temperature, as suggested from the analysis of the Eurofer97 dataset.

In order to calibrate the model, we need to determine a lower bound for the experimental data. In order to do so, we will identify a given cumulative probability to fracture $K_{Jc(0.xx)}(T)$ with an engineering lower bound for fracture toughness. To determine the appropriate value for $0.xx$, we have analyzed the Euro dataset [5.75]. This dataset has been obtained from testing DIN 22NiMoCr37, a steel similar to the A508 C1.3 The T_0 estimated is in the range of -87°C to -97°C, depending on the particular dataset considered and the method used for the T_0 estimation [5.70]. A T_0 = -91°C is obtained for the dataset generated at -91°C from 0.5T C(T) specimens, almost the same than the T_0 estimation for Eurofer97, using similar specimens (0.4T C(T) @ -100°C). The Euro dataset is presented in Figure 5.35. The mean, 99% and 1% upper and lower bounds are also plotted assuming T_0 =-91°C. Note that rough data is presented in the plot. As it can be observed, the 1% limit actually bounds perfectly the whole dataset. Therefore, $K_{Jc(0.01)}(T)$ can actually be considered as an

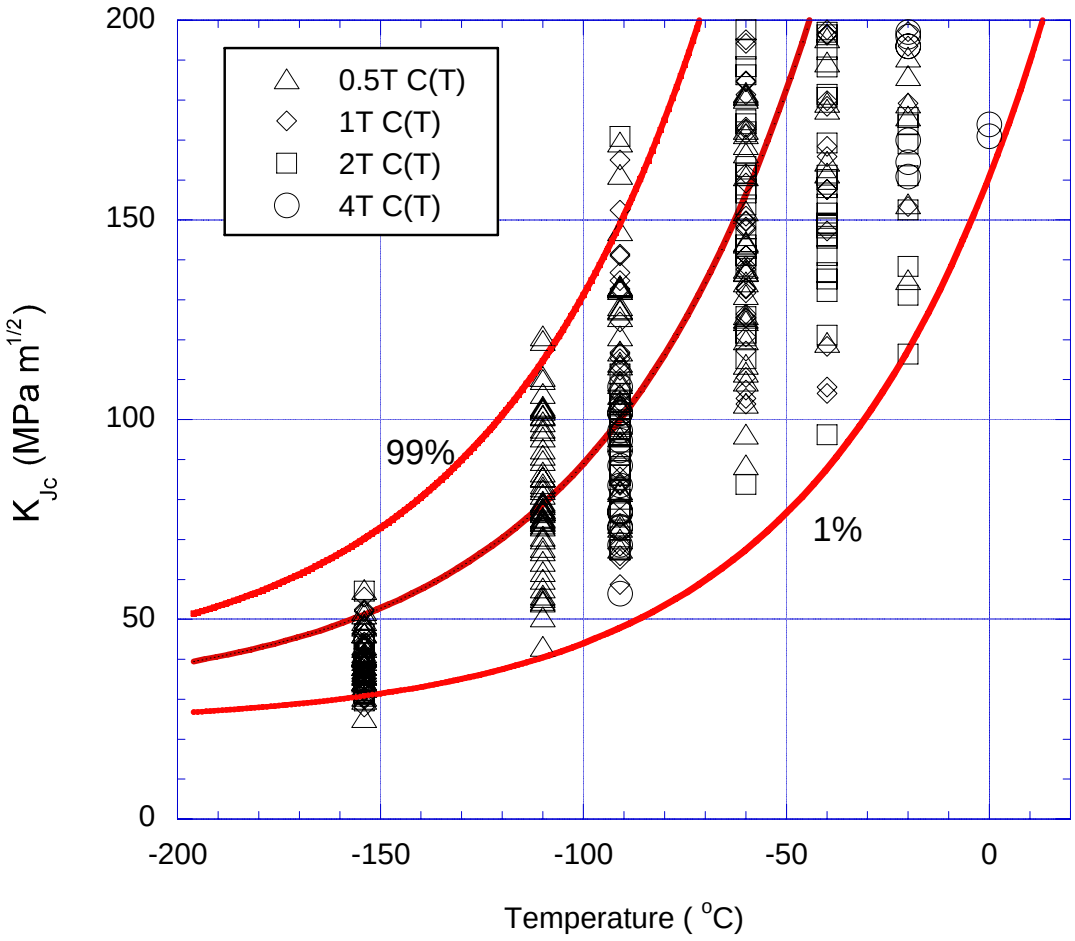

Figure 5.35: The Euro dataset. The data suggest that the 1% confidence bound can be considered as an engineering lower bound for fracture.

engineering lower bound for fracture in the DBT region. Consistently, the same criterion will be used for Eurofer97.

Based on this assumed lower bound curve, the calibration of the parameters of the $\sigma^* - A^*$ model is performed as follows. In virtue of Eq. 5.86 and recalling the results presented in Table 5.1 and Table 5.2, it is now possible to plot the areas A as a function of the principal stress level that defines its boundary, for different loading conditions represented by K_J. The same process is performed for all the temperatures simulated. With this information available, we focus our attention in only two temperatures (i.e. -120°C and -80°C). These two curves will intercept each in a certain point P whose coordinates (area, stress) will depend upon the values selected for K_J at each temperature. Finally, it is possible to select the proper K_J values for all the others temperatures in such a way that all the curves will intercept each other in the point P. The coordinates of this point may represent a set of critical parameters $A^* - \sigma^*$. The K_J values are then considered to be the critical ones, K_{Jc}. Plotting the corresponding K_{Jc} values as a function of the temperature allows us to visualize the predicted temperature dependence of the fracture toughness for the chosen critical conditions, which are represented by the crossover point P.

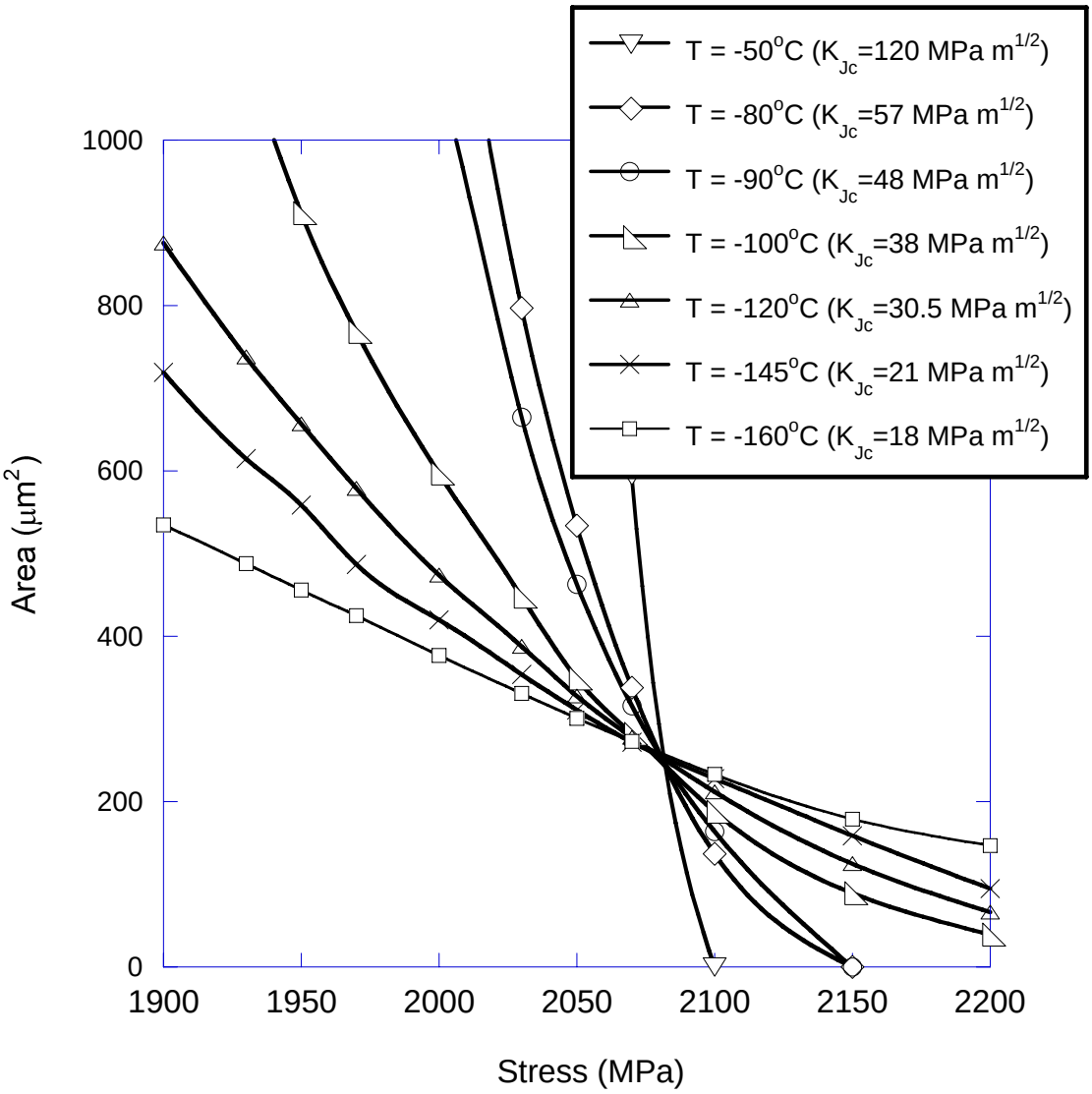

Figure 5.36: An example of the calibration procedure. In this case, the lower bound as determined from Eq. 5.37 (1%) has been considered.

The calibration process consists in finding by iteration, the proper crossover point in such a way that the predicted dependence with temperature for K_{Jc} agrees with the experimental lower bound. This procedure can be easily implemented in a spreadsheet and the proper values for σ^* and A^* can be found after a small number of iterations. The overall calibration procedure is presented in Figure 5.36 for the lower bound as determined from the new master curve for Eurofer97.

The numerical results analyzed here include three temperatures in the lower shelf (-196°C, -160°C and -145°C) and five temperatures in the DBT region (-120°C, -100°C, -90°C, -80°C, and -50°C). The prediction of the σ^* - A^* model for the evolution of the lower bound for fracture toughness with temperature is plotted in Figure 5.37 for the two cases considered: mean fracture toughness given by the master curve expression (ASTM E1921) and Eq. 5.35 respectively. As it can be observed in the plot, the agreement between the experimental lower bound and the prediction of the model is excellent in both cases. The critical values obtained

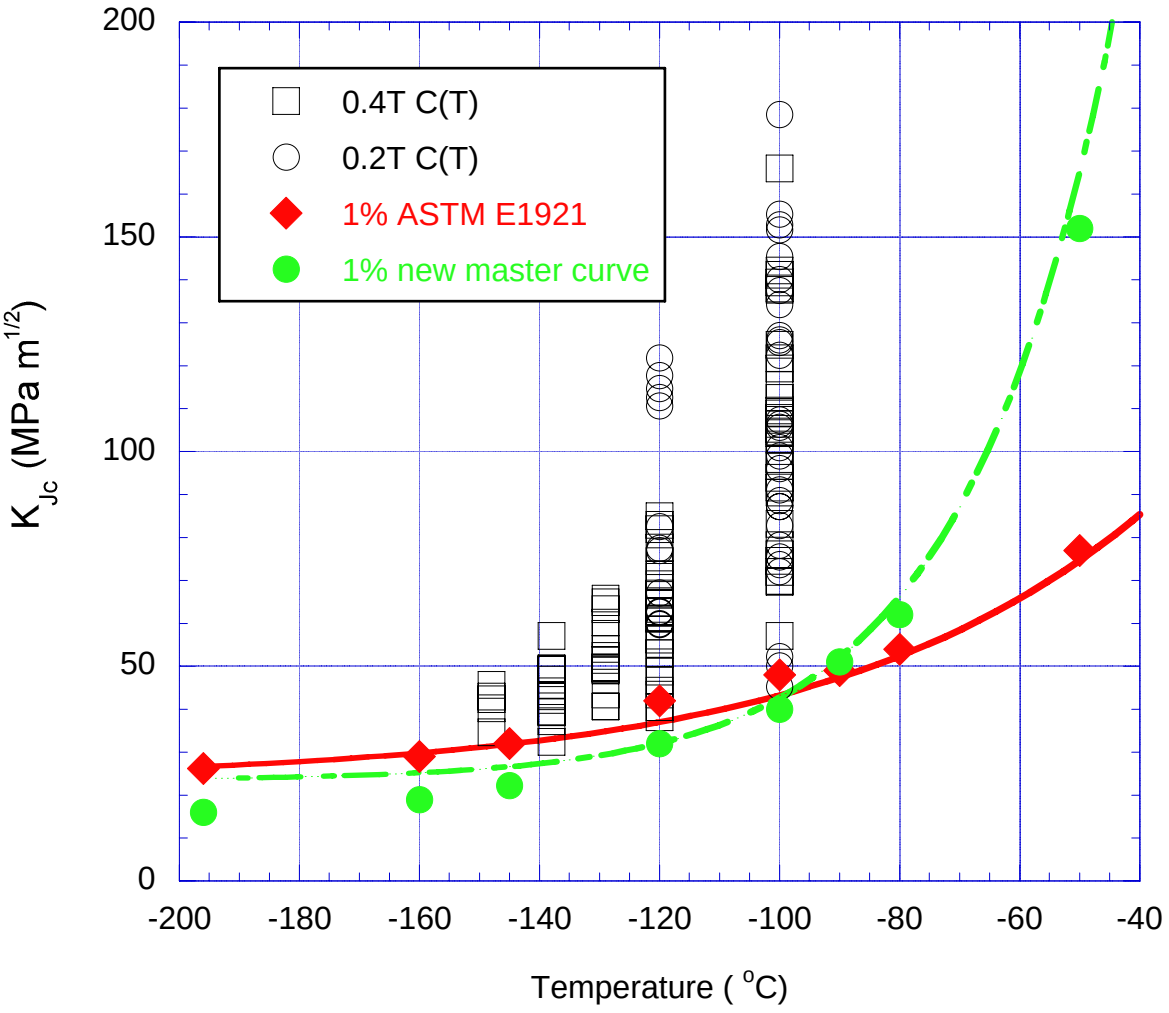

Figure 5.37: Predictions of the model for the two cases considered. Note that the data is not size corrected since the engineering lower bound is size-independent.

are $A^* \approx 3800\ \mu m^2$ and $\sigma_I^* \approx 1920\ MPa$ for the 1% confidence bound as estimated from the ASTM E1921 master curve and $A^* \approx 280\ \mu m^2$ and $\sigma_I^* \approx 2080$ MPa for the 1% confidence bound estimated from Eq. 5. 37.

Clearly, an increase of σ_I^* and a decrease of A^* give rises to a steeper lower bound curve in the DBT region. It is important to note that the predicted fracture toughness for the lower shelf depends on the critical values assumed. However, this dependence is mild. In our opinion, the strength of the model resides in the fact that even though the mechanical behavior of the Eurofer97 is strongly temperature dependent in the lower shelf region, the model predicts fairly constant fracture toughness values. In virtue of these observations, we may conclude that the $\sigma^* - A^*$ model is able to catch reasonably well one of the main features of brittle fracture in the lower shelf, i.e. a very weak temperature dependence of the fracture toughness.

In summary, we believe that these results gives good support to the fact that the evolution of a given lower bound can be modeled at the continuum level, by using the local approach

described here. In this sense, the temperature dependence of the lower bound seems to be only mediated by the constitutive behavior of the material under analysis, which in the case of Eurofer97 and in general, BCC metals and alloys, is dominated by the strong effect of the temperature on the flow properties.
The validity of the approach can be challenged by applying the model to others specimen geometries, i.e. SEN(B) specimens. It is well known that the reference temperature T_0 depends on the geometry of the specimen used for the determination. For instance, the reference temperature T_0 determined following the ASTM E-1921 is lower than the one determined from C(T) specimens. The σ^* - A^* model should be able to predict this result.

5. 6. 5. 5. Limitations of the approach

The critical stress-critical volume model is based on the calculation of the stress-strain fields from FE numerical simulations. In other words, the model is based on the continuum approach where, continuum mechanics theory laws are applied. However, cleavage fracture is a highly complex phenomenon, which involves several simultaneous mechanisms acting at very different scales on the material, ranging from the atomic level up to the geometrical scale of the component/specimen. Unfortunately, at present, the tools and techniques that may be needed to model all these coupled phenomena simply do not exist or in the best case, they are in the very early stages of their development. Finite element simulations have been the main modeling tool in the fracture community for the last decades. Although not always recognized, there exists a clear limit for the application of continuum mechanics to the problem of cleavage fracture. This limit is associated with the existence of inherent length scales involved in the cleavage phenomena. Indeed, let us consider the implementation of the critical stress-critical volume model. As mentioned previously, the model is based on the accurate description of the local stress fields generated by the crack tip, at the continuum level. Typically, the region of interest around the crack tip will be characterized by lengths in the order of 100 microns (see Figure 5.38). Therefore, we describe, based on the hypothesis of the continuum, the stress-strain fields associated to the crack for distances equivalent in microstructural terms to only a few grains. In such a case, the true stress fields in the surroundings of the crack tip region might be better described by crystal plasticity (in opposition to continuum plasticity) or by a strain-gradient plasticity theory.

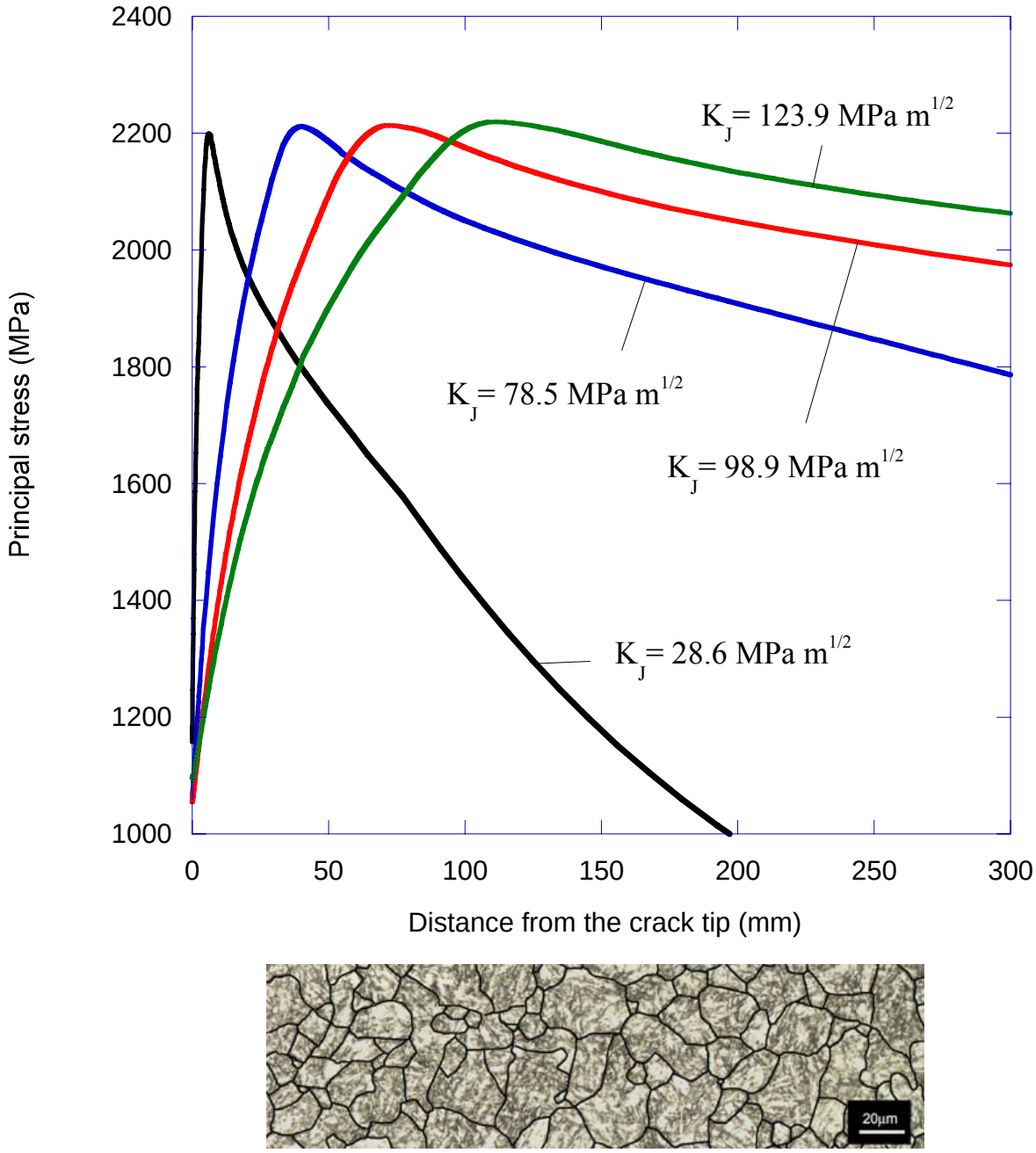

Figure 5. 38: Principal stresses for different loading level as estimated from FE simulations and metallographical observation of Eurofer97. The length scales are the same in both plots. In microstructural terms, the predicted stress gradients are quite high.

References

[5.1]. Griffith A.A., "The Phenomena of Rupture and Flow in Solids", *Philosophical Transactions*, Series A, Vol. 221, 1921, pp.163-98.

[5.2]. Williams M.L., "On the Stress Distribution at the Base of a Stationary Crack", *Journal of Applied Mechanics*, Vol. 24, March, 1957, pp.109-14.

[5.3]. Inglis, C.E., "Stresses in a Plate Due to the Presence of Cracks and Sharp Corners", *Transactions of the Institute of Naval Architects*, Vol. 55, 1913, pp.219-41.

[5.4]. Hertzberg R.W., "Deformation and Fracture Mechanics of Engineering Materials", 4th Edition, Wiley & Sons, Inc., 1996.

[5.5]. Anderson T.L., "Fracture Mechanics, Fundamentals and Applications", 2nd Edition, CRC Press Inc., 1995.

[5.6]. Miannay D. P., "Fracture Mechanics", Springer-Verlag Inc., 1998.

[5.7]. S. G. Larson, A. J. Carson, "Influence of Non-Singular Stress Terms and Specimen Geometry on Small Scale Yielding at Crack Tip in Elastic-Plastic Materials, *J. Mech. Phys. Sol.* 21 (1973) 263

[5.8]. Annual Book of ASTM Standards 2004", Volume 03.01, ASTM International, 2004.

[5.9]. Orowan; *Trans.Inst.Engrs.and Shipbuilders in Scotland*, 1945-6, 89, pp.165-215.

[5.10]. Rice J.R., "A Path Independent Integral and the Approximate Analysis of Strain Concentration by Notches and Cracks", *J. of Applied Mechanics*, Vol. 35, 1968, pp.379-86.

[5.11]. Hutchinson J.W., "Singular Behaviour at the End of a Tensile Crack in a Hardening Material", *J. of Mechanics and Physics of Solids*, Vol.16, 1968, pp.13-31.

[5.12]. Rice J. R., Rosegreen G. F., "Plane Strain Deformation Near a Crack Tip in a Power-Law Hardening Material", J. *of Mechanics and Physics of Solids*, Vol.16, 1968, pp.1-12.

[5.13]. O'Down N. P., Shih C.F., "Family of Crack tip Fields Characterized by a Triaxiality Parameter-I, Structure of Fields", *Journal of Mechanics and Physics of Solids*, Vol.39, 1991, pp.989-1015.

[5.14]. O'Down N. P., Shih C.F., "Family of Crack tip Fields Characterized by a Triaxiality Parameter-I, Fracture Applications", *Journal of Mechanics and Physics of Solids*, Vol.40, 1992, pp.939-963.

[5.15]. C. Fong Shih, N. P. O'Dowd, M. T. Kirk, "A Frame Work for Quantifying Crack Tip Constraint" in *Constrain Effect in Fracture*, Hackett, Schwalbe, Dodds Eds., ASTM STP 1171, Philadelphia, 1993, pp.2-20.

[5.16]. N.P.O'Dowd, "Applications of two Parameter Approaches in Elastic-Plastic Fracture Mechanics", *Engineering Fracture Mechanics*, Vol.52, No.3, 1995, pp.445-465.

[5.17]. Rice, J. R., Paris P.C., Merkle J.G., "Some Further Results of J-Integral Analysis and Estimates", *ASTM STP 536*, American Society of testing and Materials, Philadelphia, 1973, pp.231-245.

[5.18]. Nevalainen M., Dodds R.H., "Numerical Investigation of 3-D Constraint Effects on Brittle Fracture In SE(B) and C(T) Specimens", *International Journal of Fracture* 74, 1995, pp.131-61.

[5.19]. D.Hull; *Acta Metal*., Vol.9, 1961, pp.191-204.

[5.20]. J.F.Knott; *Journal of the Iron and Steel Institute*, 204, 1966, pp.104-111.

[5.21]. R.Hill; "Mathematical Theory of Plasticity", Clarendon Press, 1950.

[5.22]. A.P.Green and B.B.Hundy; *J. Mech. Phys. Solids*, 1956, vol.4, pp.128-144.

[5.23]. A.H.Cottrell; *Transactions of the AIME*, 212, 1958, pp.192-203.
[5.24]. G.Oates; *J.Iron Steel Inst*., Vol.206, 1966, pp.930.
[5.25]. Wilshaw, Rau and Tetelman; *Engineering Fract. Mechanics*, Vol. 1, 1968, pp.191-211.
[5.26]. J.R.Griffiths and D.R.J.Owen; *J.Mech Phys. Solids*, 1971, Vol.19, pp.419-31
[5.27]. Griffith and Oates;
[5.28]. D.A.Curry, J.F.Knott; *Metal Science*, Jan.1976, pp.1-6.
[5.29]. D.A.Curry, J.F.Knott; *Metal Science*, Nov.1978, pp.511-14.
[5.30]. E.Smith; " Physical basis of Yield and Fracture", *Conf. Proc. Inst. Phys., Phy. Soc*., Oxford, 1966, pp. 36.
[5.31]. G.E.Dieter; "Mechanical Metallurgy", Mc Graw Hill, 1988.
[5.32]. P.Brozzo, G.Buzzichelli, A.Mascanzoni, M.Mirabile; *Metal Science*, April 1977, pp.123-129.
[5.33]. D.A.Curry; *Metal Science*, Vol.16, Septembre 1982, pp.435-440.
[5.34]. F.M.Beremin, "A Local Criterion for Cleavage Fracture of a Nuclear Pressure Vessel Steel", *Metallurgical Transactions A*, Vol.14A, Nov. 1983, pp. 2277-87.
[5.35]. A.Pineau; "Advances in Fracture Research", *Proceedings of the 5th International Conference on fracture (ICF5),* Vol.2, 1981, pp.553-577.
[5.36]. K.Wallin; T.Saario, K.Törrönen, *Metal Science*, Vol.18, Jan. 1984, pp.13-16.
[5.37]. T.Saario, K.Wallin, K.Törrönen; *J.of Engineering Mat.and Tech*., Vol.106, April 1984, pp.173-177.
[5.38]. H.Kotilainen; "Materials and Processing Technology", *Publication 23*, 1980, Espoo, Technical Research Center of Finland.
[5.39]. A.S.Tetelman; T.R.Wilshaw, C.A.Rau, *Int. Journal of Fracture Mechanics*, Vol.4, Nro.2, June 1968, pp.147-157.
[5.40]. P.Bowen, S.G.Druce, J.F.Knott; *Acta Metall*. Vol.34, No.6, 1986, pp.1121-1131.
[5.41]. R.O.Ritchie, J.F.Knott and J.R.Rice; "On the Relationship Between Critical Tensile Stress and Fracture Toughness in Mild Steels", *J. of Mech. Phys. Solids*, 1973, Vol.21, pp.395-410.
[5.42]. Anderson, T.L., "Fracture Mechanics, Fundamentals and Applications", CRC Press, 1995.
[5.43]. Anderson, T.L, Stienstra, D.I.A, and Dodds, R.H. Jr., "A Theoretical Framework for Adressing Fracture in the Ductile-Brittle Transition Region." *Fracture Mechanics: 24th Volume, ASTM STP 1207,* American Society for Testing and Materials, Philadelphia, 1995.
[5.44]. Anderson T. L., Dodds R.H., "Simple Constraint Corrections for Subsize Fracture Toughness Specimens", *Small Specimens Test Techniques Applied to Nuclear Reactor Pressure Vessel, Thermal Annealing and Plant Life Extension, ASTM STP 1204*; W. R. Corwin, F.M. Haggag and W.L.Server Eds., American Society for Testing and Materials, Philadelphia, 1993, pp.93-105.
[5.45]. Anderson T. L., Dodds R.H., "Specimen Size Requirement for Fracture Toughness Testing in the transition region", *Journal of Testing and Evaluation*, Vol.19, No.2, 1991; 123-134.
[5.46]. Dodds R.H., Anderson T.L., Kirk M., "A Framework to Correlate a/W ratio Effects on Elastic-Plastic Fracture Toughness (Jc)", *International Journal of Fracture* 48, 1991, pp. 1-22.
[5.47]. Dodds R.H., Fong Shih C., Anderson T.L., "Continuum and Micromechanics Treatment of Constraint in Fracture", *International Journal of Fracture* 64, 1993, pp.101-133.

[5.48]. Wallin K., ”Statistical Aspects of Constrain Effects With Emphasis on Testing and Analysis of Laboratory Specimens in the Transition Region”, *Constrain Effects in Fracture ASTM STP 1171,* E.M. Hackett, K.H.Schwalbe and R.H.Dodds, Eds., American Society for Testing and Materials, Philadelphia, 1993, pp.264-288.

[5.49]. Wallin K., “The Scatter in K_{IC} Results”, *Eng. Fracture Mech.* Vol.19, No.6, 1984, pp.1085-1093.

[5.50]. Beremin F.M., “A Local Criterion for Cleavage Fracture of a Nuclear Pressure Vessel Steel”, *Metall. Transactions A, Vol.14A, 1983, pp.2277-2287.*

[5.51]. Pineau A., “Review of Fracture Micromechanisms and a Local Approach to Predicting Crack Resistance in Low Strength Steels”, in *Advances in Fracture Research (Fracture 81), Proceedings of the 5th International Conference on Fracture (ICF5),* Ed. by D.Francois, 1981, pp. 553-577.

[5.52]. Mudry F., “A Local Approach to Cleavage Fracture”, *Nuclear Eng. Design 105, 1987, pp.65-76.*

[5.53]. Minami F., Brückner-Foit A., Munz D., Trolldenier B., *International J. of Fracture 54, 1992, pp.197-210.*

[5.54]. Wallin K., “Microscopic nature of Brittle Fracture”, Journal the Physique IV, Colloque C7, supplement au Journal de Physique III, Vol. 3, Nov.1993, pp.575-584.

[5.55]. Rensman J., van Hoepen J., Bakker J., den Boef R., van der Broek F., van Essen E., «Tensile Properties and Transition Behaviour of RAFM Steel Plate and Welds Irradiated Up to 10 dpa at 300°C », *Journal of Nuclear Materials* 307-311, 2002, pp.245-49.

[5.56]. Rensman J, Hofmans H., Schuring E., van Hoepen J., Bakker J., den Boef R., van der Broek F., van Essen E., « Characteristics of Unirradiated and 60°C 2.7dpa irradiated Eurofer 97 », *Journal of Nuclear Materials* 307-311, 2002, pp.250-55.

[5.57]. Odette G.R., Yamamoto T., Kishimoto H., Sokolov M., Spätig P., Yang W., Rensman J., Lucas G., “A Master Curve Analysis of F82H Using Statistical and Constraint Loss Size Adjustments of Small Specimens Data”, *Journal of Nuclear Materials*, 329-333, 2004, pp.1243-1247.

[5.58]. Wallin K., Laukkanen A., Tähtinen S., “Examination on Fracture Resistance of F82H Steel and performance of Small Speciems inTransition and Ductile Regimes”, in *Small Specimens Test Techniques: Fourth Volume ASTM STP 1418*, Sokolov M.A., J.D. Landes, G.E. Lucas Eds. American Society of Testing and Materials, PA. 2002, pp.33-

[5.59]. Sokolov M. Klueh R., Odette G.R. Shiba K. Tanaigawa H. in *Effects of Irradiation on Materials, 21st International Symposium, ASTM STP 1447*, American Society For Testing and Materials, 2004.

[5.60]. Spätig P., E. Donahue, G. R. Odette, G. E. Lucas, M. Victoria, “Transition Regime Fracture Toughness-Temperature Properties of Two Advanced Ferritic/Martensitic Steels”. *Material Research Soc. Symp. Proc.- Multiscale Modeling of Materials*, Editors: L.P. Kubin, J.L. Bassani, K. Cho, H. Gao, R.L.B. Selinger, 2001 p. Z7.8.1-Z.7.8.6.

[5.61]. Joyce J.A., Tregoning R.L., “Determination of Constraint Limits for Cleavage Initiated Toughness Data”, *Engineering Fracture Mechanics* 72, 2005, pp.1559-79.

[5.62]. E.W.Schuring, H.E. Hofmans, “Metallographic Characterisation of Eurofer 97 Plate and Bar Materials” ECN-C—00-108, NGR, October 2000.

[5.63]. Wallin K., Laukkanen A., Tahtinen S., “Examination on Fracture Resistance of F82H Steel and Performance of Small Specimens in Transition and Ductile Regimes”, *Small Specimens Test Techniques: Fourth Volume, ASTM STP 1418*,

M.A: Sokolov, J.D. Landes, G.E. Lucas, EDs., American Society for Testing and Materials, PA, 2002.

[5.64]. Rathbun H.J., Odette G.R., Yamamoto T., Lucas G.L., "Influence of Statistical Constraint Loss Size Effects on Cleavage fracture Toughness in the Transition.-A Single Variable Experiment and Database", *Engineering Fracture Mechanics*, Vol. 73, January 2006, pp.134-158.

[5.65]. McMeeking R.M., "Finite Deformation Analysis of Crack-Tip Opening In Elastic-Platic Materials And Implications for Fracture", *J. Mechanics and Physics of Solids*, Vol. 25, 1977, pp.357-381.

[5.66]. Klueh R.L, Gelles D.S., Jitsukawa S., "Ferritic/Martensitic Steels-Overview of Recent Results", *Journal of Nuclear Materials* Vol.307-311, 2002, pp. 455-65.

[5.67]. Dai Y., Marmy P., "Charpy Impact Test on Martensitic/Ferritic Steel After irradiation in SINQ Target 3", *J. of Nuclear Materials*, Vol.343, August 2005, pp.247-252.

[5.68]. H.E. Hoffmans, "Tensile and Impact Properties of Eurofer97 Plate and Bar", 20023/00.38153/P, NGR, 2000.

[5.69]. Odette G.R., He M.Y., "A Cleavage Toughness Master Curve Model", *J. of Nuclear Materials*, Vol. 283-287, 2000, pp.120.127.

[5.70]. Wallin K., "Master Curve Analysis of the "Euro" Fracture Toughness Dataset" *Engineering Fracture Mechanics* 69, 2002, pp. 451-481.

[5.71]. Gao X., Ruggieri C. and Dodds J.R., "Calibration of Weibull Stress Parameters Using Fracture Toughness Data", International Journal of Fracture 92, 1998, pp.175-200.

[5.72]. Euromech –Mecamat 96, First European Mechanics of Materials Conference on Local Approach to Fracture '86-'96, in *Journal the Physique IV*, Colloque C6, Supplément au journal de Physique III, No.10, A. Pineau, G.Rousselier Eds., 1996.

[5.73]. J.W. Rensman, NRG Irradiation Testing: Report on 300°C and 60°C Irradiated RAFM Steels, NRG report 20023/05.68497/P (2005).

[5.74]. Sokolov M.A., Klueh R.L., Odette G.R., Shiba K. and Tanigawa H., "Fracture Toughness Characterization of Irradiated F82H in the Transition Region", on Effects of Radiation on Materials: 21st International Symposium, ASTM International, 2004.

[5.75]. J. Heerens, D. Hellmann, Eng. Fract. Mechanics 69 (2002), 421-449.

[5.76]. Tanguy B., Besson R., Piques R., Pineau A., Eng. Fract. Mech. 72,.2005,pp.49-72.

[5.77]. Wallin K., "Comparison of the Scientific Basis of Russian and European Approaches for Evaluating Irradiation effects in Reactor Pressure Vessels", European Network on Ageing Materials Evaluation and Studies, VTT Technology, 1994.

Chapter 6

Conclusions and future work

A detailed microstructural analysis of the tempered martensitic Eurofer97 steel has been undertaken. The main microstructural features of this steel were identified and discussed, including prior austenitic grain size, internal structure of the prior austenitic grains, analysis of second phase particles and description of the dislocation structure in the as-received condition. A high purity Fe-9wt%Cr ferritic model alloy has been developed and its microstructure has also been analyzed in detail.

The plasticity of the Eurofer97 steel and of the ferritic model alloy was studied by means of tensile tests, which were carried out over a broad range of temperatures (77 K-473 K) and strain rates. The plastic flow of these alloys has been modelled using the one-microstructural parameter model (dislocation density). As expected for the body-centered cubic metals and alloys, two different temperature regions were identified; these regions are characterized by different temperature dependences of the yield stress and of the plastic strain-hardening. The, first region, at $T > 200K$ was modelled based on the Kocks model originally developed for single phase face-centered metals and alloys. This model provided a successful description of the hardening behavior for the Eurofer97 steel. For the ferritic alloy, the one-parameter model was applied successfully only in a small range of plastic deformation. The formation of elongated dislocation cells has been identified as the microstructural feature responsible for the departure of the model predictions. In the low temperature regime $T < 200K$, the lattice friction on the screw segments strongly influences dislocation dynamics. We have modified a model originally proposed by Rauch to account for the effect of the lattice friction. A general constitutive law has been developed for the Eurofer97 at low temperatures. The modified model described properly the experimental data with parameters consistent with the characteristics of the microstructure. Finally, the analysis of the effect of temperature on the parameters of the two models was consistent with the expected trends of the physical phenomena associated to it.

It has been clearly demonstrated that the toughness master curve of the rector pressure vessel (RPV) steels, does not describe properly the temperature dependence of the fracture toughness in the case of the tempered martensitic steel Eurofer97. Based on our extensive experimental data obtained with well constrained C(T) specimens of the 25 mm thick plate, a new master curve has been proposed:

$$K_{Jc(med)} = 30 + 70\exp\left[0.04(T - T_0)\right]$$

A possible variation in fracture toughness through the thickness of the 25 mm plate has been investigated using small 0.2 T C(T) specimens. No variation in fracture toughness has been observed.

Size effects in fracture toughness has been studied by comparing 0.2 T C(T) and 0.4 T C(T). We have demonstrated that the censoring limits determined from the ASTM E1921 procedure (M=30) is too lenient. Based on detailed statistical analysis of the fracture data, a new M value of 80 is proposed for the C(T) specimens.

A comparison between our data and data from other authors revealed an important difference in fracture toughness between the 14 mm and the 25 mm plates of Eurofer97. This difference has been assessed by determining the transition temperature T_0 using the procedure described in the ASTM E-1921 standard combined to the new expression for the master curve.

We have compiled a fracture toughness C(T) database for the F82H mod. The results have been compared to the Eurofer97 database. We have demonstrated that both datasets share a common lower bound curve for fracture toughness. However, the upper bounds defined by the extension of the scatter at different temperatures are very different. Indeed the F82H mod. steel features a larger scatter band for all the temperatures analyzed. The differences in fracture toughness were correlated to those observed on Charpy tests with KLST specimens.

A local model for cleavage fracture has been used to predict correctly the lower bound fracture toughness curve for Eurofer97. The model assumes that cleavage fracture occurs when a critical condition is attained. This critical condition is defined by a critical stress σ^* acting on a critical area A^*. Detailed 2D finite element modelling of C(T) specimens has been undertaken to determine the dependence of the area encompassed by a certain stress level on the load level represented by K_J. In this sense, we have demonstrated that the relation between these two quantities strongly depends on the particular specimen geometry used. Consequently, the use of general Area-K_{Jc} correlations as obtained from small scale yielding conditions cannot be used in the context of the σ^* - A^* model.
The calibration of the parameters of the model (the critical stress and the critical area) has been accomplished by considering the available experimental fracture toughness data. The 1% cumulative probability to fracture has been selected as a convenient lower bound for fracture in the range of temperatures of interest. The critical parameters have been chosen in such a way that the predicted lower bound dependence with temperature better match the experimental lower bound.

Future work

From the point of view of the author of the present work, the following points need further development:

a) Concerning the determination of the fracture toughness curve for eurofer97, it is fundamental to test the material at temperatures higher than -100°C. 0.8 T C(T) specimens can be cut from the 25mm plate. Testing of these specimens can be carried out at temperatures up to -80°C, keeping a high level of constraint. These experiments will give further support to the new master curve expression proposed for the case of Eurofer97.

b) It is fundamental to generate more fracture toughness data for the Eurofer97 14mm plate, to confirm the applicability of the new master curve in this case.

c) A detailed microstructural comparison between the 14mm plate and the 25mm plate need to be undertaken. This type of comparative studies may allow a proper determination of the microstructural factors influencing the fracture toughness behavior for martensitic stainless steels. This knowledge is fundamental for the future design and development of materials.

d) From the point of view of the finite element simulations, 3D simulations need to be run to assess on the validity of the critical stress-critical volume model.

Appendix 1

Weibull statistics

Let's consider a statistical variable x. The distribution function $F(x)$ of the statistical variable x is usually defined as the probability that x being equal or smaller than a certain value x_0:

Eq. A1. 1 $$P(x \le x_0) = F(x_0)$$

The function $F(x)$ is also known as the cumulative probability function of the statistical variable x.Weibull proposed the following distribution function $F(x)$:

Eq. A1. 2 $$F(x) = 1 - \exp(-\varphi(x))$$

From the point of view of the weakest link concept, this approach can be used to describe the cumulative probability of failure of every single link that composes the complex system under analysis. In this way, the probability of non-failure of every single link can be written:

Eq. A1. 3 $$\overline{p}(x \le x_0) = \exp(-\varphi(x_0))$$

The cumulative probability of non-failure of the complex system $\overline{P}(x \le x_0)$ can be derived from the probability of failure of the single links. Let's assume that we are applying the weakest link concept to a chain formed by n links. In this case, the statistical variable under consideration is the load applied to the chain, L. The cumulative probability of non-failure of any link in the chain is described by Eq. A1. 2, where $x_0 = L_0$, is the load. This load is of course the same for all the links considered since they are in serie. Assuming statistical independence between the links it is possible to write the probability of non-failure of the chain (system) as:

Eq. A1. 4 $$\overline{P}_n(x \le L_0) = \left[\overline{p}(L_0)\right]^n = \exp\left[-n\varphi(L_0)\right]$$

Thus, the cumulative probability to failure is:

Eq. A1. 5 $$P_n(x \le L) = 1 - \exp\left[-n\varphi(L)\right]$$

Weibull postulated that the function $\varphi(x)$ may be written like:

Eq. A1. 6 $$\left[\frac{x-\mu}{\eta}\right]^m$$

Combining Eq. A1. **4**5 and Eq. A1. **5**6 we immediately obtain the well-known 3-parameters Weibull distribution, which has been observed to describe properly the statistical behavior of complex system that follows a weakest-link type failure process. The parameter m in Eq. A1. 6 is known as the Weibull slope, η is the scale parameter and μ is the location parameter.

Application to fracture in the lower transition region.

Let's consider a volume of material. This volume V may be considered as composed by several small volumes V_0. In the weakest link approach, these small volumes will play the same role than the links in the example of the chain. Under the weakest link assumption, we will accept that the failure of one of these small volumes will trigger macroscopic cleavage fracture on the specimen under study.

It is well accepted that cleavage in steels is a stress-controlled process. Therefore, it is assumed that the principal stress acting on every volume controls the probability to failure of the volume, i.e. the statistical variable under consideration will be the principal stress $\sigma_I(\mathbf{x})$ that is acting on the volume V_0. The position of the volume V_0 is refered by the vector ($\mathbf{x}$).

It is fundamental to outline that the distribution of stresses in the material has a very strong influence in the further development of the weakest link formulation. Clearly, it is not the same to consider the stress distribution produced by a sharp crack present in a loaded specimen compared with the homogeneous stress distribution observed in the calibrated section of a tensile specimen that undergoes uniaxial loading.

For the sake of clarity, it is worth considering three different cases. The first once consists in a certain volume of material under the action of a homogeneous stress field. The second case consists in a certain volume of material where weak stress gradients are present. Finally, we consider the case of very sharp stress gradients acting on the material.

Homogeneous stress.

Let's consider a material volume at a temperature T. We assume that the material fails by cleavage with almost no plastic deformation. In order to fix the ideas, we can visualize a uniaxial tensile test where the specimen breaks immediately after yielding. In this example, we take into account the potential influence of plastic deformation over cleavage fracture in the material under analysis. We do not considering the effects of the strain rate over cleavage fracture either.

As it was described previously, the material is divided into several small volumes. In this case, the stress state acting on every one of these volumes *is the same*:

Eq. A1. 7 $$\sigma_I(\mathbf{x}) = \sigma_I = cte$$

In analogy to Eq. A1. 4, if it is assumed that cleavage fracture follows a weakest-link behavior, the cumulative probability of failure of a certain volume of material V that under a homogeneous and uniaxial stress level σ_I is described by:

Eq. A1. 8 $$P_V(\sigma \le \sigma_I) = 1 - \exp\left[-\frac{V}{V_0}\varphi(\sigma_I)\right]$$

From the equation above, it is possible to derive a size effect predicted by the weakest link theory. Taking logarithms in Eq. A1. 8

Eq. A1. 9 $$\ln\left[1 - P_V(\sigma_I)\right] = -\frac{V}{V_0}\varphi(\sigma_I)$$

If we now assume that the probability to fracture in the specimens is the same, we can write:

Eq. A1. 10 $$V_1\varphi(\sigma_{I,V_1}) = V_2\varphi(\sigma_{I,V_2}) = cte$$

Finally:

Eq. A1. 11 $$\frac{V_1}{V_2} = \frac{\varphi(\sigma_{I,V_2})}{\varphi(\sigma_{I,V_1})}$$

Weak stress gradients.

In this case, the stresses acting on the different volumes are not identical due to the existence of stress gradients in the material. This is the case of notched specimens or specimens where the blunting of the crack tip prevents the development of very steep stress gradients. The fundamental assumption that underlies the development presented above, is the fact that the small volumes V_0 can be taken small enough as to consider the stress state approximately constant inside each single volume. At the same time, the small volumes are large enough to accept that the statistical independence assumption of the volumes is still valid. In practical terms, this means that every small volume encompasses several grains in the microstructure.

We consider only the material inside a certain process volume, i.e. the plastic volume V_P. The probability of failure of any volume of material outside this region is considered null.
Assuming statistical independence between the small volumes V_0, the cumulative probability of non-fracture of the specimen under a remote stress σ_{rem}, $\overline{P}_{V_p}(\sigma \le \sigma_{rem})$, can be expressed as:

Eq. A1. 12 $$\overline{P}_{V_p}(\sigma \le \sigma_{rem}) = \prod_i \exp\left[-\varphi(\sigma_I(\mathbf{x}_i))\right] = \exp\left[-\sum_i \varphi(\sigma_I(\mathbf{x}_i))\right]$$

The quantity $\sigma_I(\mathbf{x}_i)$ refers to the local maximum principal stresses generated by the remote stress in the position $\mathbf{x}_i$. The sum should be extended to all the small volumes inside the plastic volume V_P. It is very important to recognize here that Eq. A1. 12 links a macroscopic quantity (σ_{rem}) with a local quantity ($\sigma_I(\mathbf{x}_i)$).
This equation may be tested experimentally by means of notched specimens tested at the temperature T where fracture occurs by pure cleavage.

Steep stress gradients

In principle, for large K_I/σ_y values, the stress gradients ahead of the crack tip are still small enough to make the assumption of constant stress inside the small values V0 still valid. For small values of K_I/σ_y, this hypothesis does not hold any more since the stress vary by several hundreds of MPa over distances of the order of a micron. This kind of problems have also been treated with the same approach used for the case of weak stress gradients assuming a sort of average stress into the small volume V_0.
In the case of mode I of loading, small scale yielding (SSY), assuming that the T-stress is zero, the components of the stress tensor that defines the stress field ahead of the crack tip can be written as:

Eq. A1. 13 $$\sigma_{ij}(r,\theta) = \sigma_y f_{ij}\left(r/(K_I/\sigma_y)^2, \theta\right)$$

where r and θ are the polar coordinates that defines the position vector $\mathbf{x}$. Considering only the principal stress and in virtue of Eq. A1. 13, we can write:

Eq. A1. 14 $$\varphi(\sigma_I(r_i,\theta_i)) = \varphi\left[\sigma_y f\left(r_i/(K_I/\sigma_y)^2, \theta_i\right)\right]$$

Replacing Eq. A1. 14 in Eq. A1. 12, we obtain:

Eq. A1. 15 $$P_{V_p}(\sigma \le \sigma_{rem}) = 1 - \exp\left[-\sum_i \varphi\left[\sigma_y f\left(r_i/(K_I/\sigma_y)^2, \theta_i\right)\right]\right]$$

Let's assume that the K_I value and the process volume shape are constant along the crack front. We can rewrite Eq. A1. 15 in an integral form:

Eq. A1. 16 $$P_{V_P}(\sigma \le \sigma_{rem}) = 1 - \exp\left[-\int_{V_P} \varphi\left[\sigma_y f\left(r/(K_I/\sigma_y)^2, \theta\right)\right] B r dr d\theta\right]$$

Changing variables, $u = r/(K_I/\sigma_y)^2$ in Eq. A1. 16:

Eq. A1. 17 $$P_{V_P}(\sigma \le \sigma_{rem}) = 1 - \exp\left[-B\left(\frac{K_I}{\sigma_y}\right)^4 \int_{V_P} \varphi\left[\sigma_y f(u,\theta)\right] u du d\theta\right]$$

We postulate that:

Eq. A1. 18 $$\varphi\left[\sigma_y f(u,\theta)\right] = \varphi_1(\sigma_y)\varphi_2(f(u,\theta))$$

Then, because of the fact that the fields are self-similar in u, we can write

Eq. A1. 19 $$\int_{V_P} \varphi_2\left[f(u,\theta)\right] u du d\theta = \Omega = cte$$

The integral in Eq. A1. 19 is also convergent since the blunting of the crack tip prevents the stresses to increase without limit. It is important to stress the fact that we will obtain a different value of Ω for configurations where the T-stress is no the same.
Finally, if we describe the load level using K_I instead of σ_{rem}, Eq. A1. 17 can be written as:

Eq. A1. 20 $$P_{V_P}(K_I \le K_{J_C}) = 1 - \exp\left[-B\left(\frac{K_I}{\sigma_y}\right)^4 \varphi_1(\sigma_y)\cdot\Omega\right] = 1 - \exp\left[-\left(\frac{K_I}{\beta_K}\right)^4\right]$$

where :

Eq. A1. 21 $$\beta_K^4 = \frac{\sigma_y^4}{B\Omega\varphi_1(\sigma_y)}$$

and K_{Jc} is the critical K value derived from J_C value. This is usually the case in the transition region where K_{Ic} values are usually not obtained since the specimen size requirement is not easily fulfilled. Anyway, the validity of K_{Jc} is very well accepted.

β is a material property and is clearly temperature dependent on the yield stress. It also depends on the geometry of the specimen not only because of B but also because different T-stresses generated in different configurations result in different values for Ω. The numerical value of β coincides with the K_I value that generates 63% of probability to failure. Eq. A1. 20 is a description of the scatter of the K_{J_C} results when SSY conditions (i.e. a single parameter describe properly the stress field ahead of the crack tip) and the weakest link mechanism is a correct working hypothesis. It is important to stress that we did not need to formulate an explicit assumption about the function $\varphi(\sigma(r_i,\theta_i))$ in the development presented above. The formulation has also been derived without imposing any assumption about the local conditions that may lead to fracture. Eq. A1. 20 is sometimes written in terms of J_C as:

Eq. A1. 22
$$P_V(J_C) = 1 - \exp\left[-\left(\frac{J_C}{\beta_J}\right)^2\right]$$

In practice, Eq. A1. 20 and Eq. A1. 22 have two main drawbacks: they predict zero as a minimum toughness and it overestimates the observed experimental scatter of J_C.

The prediction of zero minimum toughness is not plausible from a physical point of view. Clearly, a crack will need a certain driving force to propagate in the material. If the driving force is not high enough the crack is arrested. This argument supports the inclusion of a threshold value K_{TH} below which the propagation of the crack is impossible.

The overestimation of the scatter has been usually addressed by considering a conditional probability of propagation. This basically means that we include the possibility of a propagating crack to be arrested. Wallin has discussed this problem in detail. His argumentation is based on the idea that weakest link is a necessary condition for cleavage but is not sufficient condition for macroscopic cleavage. Following this approach, the initiation of cleavage cracks is still governed by a weakest-link type mechanism. Once cleavage initiates, the crack can propagate in an unstable fashion through the material generating macroscopic cleavage or it can be arrested. In this case, the overall probability of fracture will be equal to the probability of initiation times the probability of propagation of the crack.

Anderson et al. has analysed the problem of the propagation of the crack. They concluded that the probability of propagation of the crack depends in part in the relative misorientation of the grain where the crack has been initiated with the neighboring grains. The probability of arresting the crack in a grain boundary will be higher in the case of highly misoriented grains. In this way, the conditional probability of propagation was evaluated over a range of K_I values. The results were fitted with the expression

Eq. A1. 23 $$P_{propag} = \alpha\left(K_I - K_0\right)^{\beta}$$

The incorporation of this equation into the probabilistic analysis leads to a very complicated distribution function that is very difficult to apply to experimental data.
Nevertheless Stienstra showed that this complicated function may be approximated by a three-parameters Weibull distribution previously proposed by Wallin:

Eq. A1. 24 $$P_{V_p}(K_I \le K_C) = 1 - \exp\left[-\left(\frac{K_I - K_{TH}}{\theta_K - K_{TH}}\right)^4\right]$$

where K_{TH} represents the threshold value for K_I.

Difficulties in the experimental validation of the weakest link approach.

As discussed previously, if cleavage fracture can be characterized as a weakest link process, the distribution of the experimental K_{Jc} values at a certain temperature is well described by the Weibull distribution. It was demonstrated that theoretical considerations suggest that a two-parameter distribution having Weibull slope m=4 should describe properly the experimental dataset. However, since a two-parameter distribution cannot predict the existence of a lower threshold value for the fracture toughness ($K_{\min}$), the two-parameter distribution has been relegated in favor of a three-parameter Weibull distribution, with m=4.
Early studies have pointed out the important effect of the number of test on the confidence interval of m. To better illustrate this point, let's consider the following example. We have generated several sets of random numbers between 0 and 1. If these numbers are considered as probabilities to fracture, it is then possible to generate different sets of K_{Jc} values based on a three-parameter Weibull distribution where the values of the parameters are known.
The different K_{Jc} datasets have been generated assuming m=4, $K_{\min}$=20 $MPa \cdot m^{1/2}$ and K_0=71 $MPa \cdot m^{1/2}$ (representative of the K_0 value of the Eurofer 97 at -100°C for 1T specimens). Once the datasets have been generated, it is possible to determine the value of m from the slope of a fitted straight line in a $\ln\left[\ln\left(1/(1-P_f)\right)\right]$ vs. $\ln(K_{Jc} - K_{\min})$ plot. The results so obtained are presented in Figure A1. The analysis of the figure indicates that when sets of 30 K_{Jc} values are considered, the values of m obtained through range between approximately m=2 to m=6, consistently with the values of the 99% confidence bounds that would have been obtained through more elaborated methods like the likelihood ratio confidence bounds. The variation of the confidence interval with the number of tests can be assessed when the data corresponding to sets of 10 K_{Jc} is considered. In this case, the value of m ranges between m=1.5 and m=8.

In this work, less that 32 experimental data points are available for every temperature test. As a consequence, the values obtained for the distribution moments from the analysis of the experimental datasets will suffer from the uncertainties described previously.

Determination of the Weibull slopes from different K_{Jc} sets of values generated from Eq. A1. 24, assuming K_0=70 $MPa \cdot m^{1/2}$ and $K_{\min}$=20 $MPa \cdot m^{1/2}$. 50 sets of 10 elements and 35 sets of 30 elements have been analyzed.

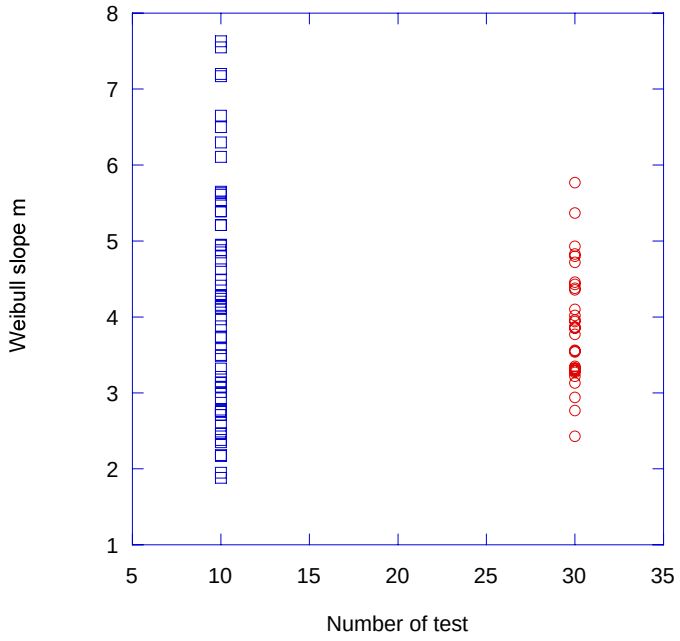

Figure A1: *Variation of the experimentally determined Weibull slope m as a function of the number of experimental data points available. m varies between 2 and 8 for the case of experimental determination from groups of ten data points. The uncertainty in m decreases slightly when m is determined from groups of 30 data points.*

Appendix 2
Fracture toughness data

Test temperature: -129°C — Specimen type: 0.4T C(T)
$\sigma_{0.2} = 727 MPa$ - $E = 216.1 GPa$ — Dimensions: B= 9mm W=18mm.

Specimen ID	a_0/W	P_f (N)	K_{Jc} ($MPa \cdot m^{1/2}$)		M	Orientation
			0.4T C(T)	Corrected to 1T		
B29	0.46	6117	43.5	38.1	907.3	L-T
B26	0.47	5685	40.8	36.0	1011.4	L-T
B25	0.47	6900	49.8	43.0	677.9	L-T
B21	0.53	6925	49.0	42.4	620.2	L-T
B19	0.48	7643	57.7	49.0	496.5	L-T
B18	0.49	6730	51.4	44.3	611.7	L-T
B17	0.48	6679	49.6	42.8	671.6	L-T
B16	0.49	7082	54.1	46.3	552.4	L-T
B15	0.47	8867	65.0	54.7	398.6	L-T
B14	0.48	6567	49.3	42.6	679.2	L-T
B13	0.48	7021	52.4	45.0	601.9	L-T
B10	0.49	5282	40.6	35.9	983.3	L-T
B9	0.48	8453	63.3	53.4	412.5	L-T
B8	0.48	8696	65.7	55.3	382.3	L-T
B7	0.49	7869	60.2	51.0	447.3	L-T

Test temperature: -138°C — Specimen type: 0.4T C(T)
$\sigma_{0.2} = 826 MPa$ - $E = 216.6 GPa$ — Dimensions: B= 9mm W=18mm.

Specimen ID	a_0/W	P_f (N)	K_{Jc} ($MPa \cdot m^{1/2}$)		M	Orientation
			0.4T C(T)	Corrected to 1T		
B30	0.49	7457	57.1	48.6	565.3	L-T
B27	0.50	5354	42.1	37.1	1019.0	L-T
B24	0.51	5452	44.2	38.6	908.5	L-T
B23	0.48	4956	37.3	33.3	1353.6	L-T
B22	0.49	6515	49.6	42.9	748.0	L-T
B20	0.47	6711	49.4	42.7	784.9	L-T
B11	0.47	6721	49.2	42.6	790.3	L-T
A27	0.50	4342	32.5	29.6	1711.8	L-T
A12	0.50	5422	39.3	34.9	1171.7	L-T
A11	0.47	6426	46.9	40.8	870.1	L-T
A10	0.50	5840	43.1	37.8	974.6	L-T
A8	0.47	5365	39.4	35.0	1232.6	L-T

Test temperature: -148°C — Specimen type: 0.4T C(T)
$\sigma_{0.2} = 885 MPa$ - $E = 217.1 GPa$ — Dimensions: B= 9mm W=18mm.

Specimen ID	a_0/W	P_f (N)	K_{Jc} ($MPa \cdot m^{1/2}$)		M	Orientation
			0.4T C(T)	Corrected to 1T		
A5	0.55	4946	45.6	39.7	841.0	L-T
A4	0.53	4880	42.3	37.2	1021.9	L-T
A3	0.54	4757	43.0	37.8	964.2	L-T
A2	0.54	3850	34.7	31.3	1482.7	L-T
A1	0.54	4517	40.2	35.6	1105.3	L-T

Test temperature: -100°C $\sigma_{0.2} = 666MPa$ - $E = 214.6GPa$			Specimen type: 0.4T C(T) Dimensions: B= 9mm W=18mm.			
Specimen ID	a_0/W	P_f (N)	K_{Jc} $(MPa\cdot m^{1/2})$		M	Orientation
			0.4T C(T)	Corrected to 1T		
A21	0.47	11625	109.51	89.1	127.6	L-T
A22	0.48	13822	139.33	112.1	77.3	L-T
A26	0.48	13930	141.18	113.5	75.3	L-T
A28	0.50	8215	69.9	58.5	295.4	L-T
B11	0.50	12587	165.9	132.6	52.4	L-T
B1.1	0.50	7138	57.10	48.6	442.7	L-T
B1.2	0.50	12080	138.0	111.0	75.8	L-T
B2.1	0.50	11964	121.7	98.5	97.5	L-T
B2.2	0.50	10614	107.34	87.4	125.3	L-T
B3.1	0.50	12220	137.71	110.8	76.1	L-T
B3.2	0.50	8601	76.16	63.3	248.9	L-T
B4.1	0.50	10813	107.89	87.8	124.0	L-T
B4.2	0.49	10817	104.6	85.3	134.6	L-T
B5.1	0.50	8558	74.56	62.1	259.7	L-T
B5.2	0.49	8312	72.00	60.1	284.0	L-T
B6.1	0.50	10530	104.26	85.0	132.8	L-T
B6.2	0.50	10582	108.9	88.6	121.7	L-T
B7.1	0.50	12395	142.27	114.3	71.3	L-T
B7.2	0.49	8182	69.70	58.3	303.1	L-T
B8.1	0.48	11841	124.87	100.9	96.3	L-T
B8.2	0.50	10129	96.62	79.1	154.6	L-T
B9.1	0.50	11504	115.47	93.7	108.3	L-T
B9.2	0.50	9460	91.71	75.3	171.6	L-T
B10.2	0.50	9280	90.52	74.4	176.2	L-T
B11.1	0.50	9685	93.91	77.0	163.7	L-T
B12.1	0.50	10602	102.76	83.9	136.7	L-T
B12.2	0.48	12277	119.36	96.7	105.4	L-T
B13.1	0.50	8788	78.26	64.9	235.7	L-T
B13.2	0.49	10579	98.25	80.4	152.5	L-T
B14.1	0.50	9227	83.17	68.7	208.7	L-T
B14.2	0.49	10932	105.33	85.8	132.7	L-T
B15.1	0.49	11453	106.50	86.7	129.8	L-T
B15.2	0.49	11117	112.49	91.4	116.4	L-T

Test temperature: -120°C $\sigma_{0.2} = 697MPa$ - $E = 215.6GPa$			Specimen type: 0.4T C(T) Dimensions: B= 9mm W=18mm.			
Specimen ID	a_0/W	P_f (N)	K_{Jc} $(MPa\cdot m^{1/2})$		M	Orientation
			0.4T C(T)	Corrected to 1T		
B6	0.47	9278	66.7	56.0	343.9	L-T
B5	0.49	8272	62.9	53.1	372.2	L-T
B4	0.50	7681	55.2	47.2	473.7	L-T
B2	0.48	7560	56.3	48.0	473.6	L-T
B1	0.48	8213	61.2	51.8	400.8	L-T
A30	0.46	6642	46.7	40.6	714.8	L-T
A29	0.47	6796	48.8	42.2	642.5	L-T
A25	0.47	9391	69.1	57.9	320.5	L-T
A24	0.47	5297	38.1	34.0	1054.1	L-T
A19	0.49	8511	64.7	54.5	351.7	L-T
A18	0.47	5628	40.5	35.8	932.9	L-T
A17	0.45	10249	70.8	59.2	316.8	L-T
A16	0.46	8884	62.7	52.9	396.6	L-T
A15	0.47	8520	61.1	51.7	409.9	L-T
A14	0.46	7568	53.1	45.5	552.9	L-T
A13	0.47	9055	64.9	54.6	363.3	L-T
B3	0.47	9252	66.9	56.2	341.9	L-T
B28	0.48	10385	77.7	64.5	248.7	L-T
A9	0.48	11356	85.0	70.1	207.8	L-T
A8-2	0.49	9219	71.3	59.6	289.6	T-L
A8-1	0.48	10982	81.9	67.8	223.8	T-L
A7-2	0.48	7032	53.1	45.5	532.4	T-L
A7-1	0.46	10548	74.4	62.0	281.6	T-L
A6-2	0.49	10895	83.0	68.6	213.7	T-L
A6-1	0.47	7891	57.2	48.7	467.7	T-L
A5-2	0.47	6058	43.5	38.1	808.6	T-L
A5-1	0.50	5641	44.4	38.8	732.2	T-L

Test temperature: -100°C $\sigma_{0.2} = 666MPa$ - $E = 214.6GPa$			Specimen type: 0.2T C(T) Dimensions: B= 4.5mm W=9mm.			
Surface						
Specimen ID	a_0/W	P_f (N)	K_{Jc} $(MPa\cdot m^{1/2})$		M	Orientation
			0.2T C(T)	Corrected to 1T		
C12.1	0.50	2625	72.1	53.8	138.8	L-T
C11.1	0.52	3393	278.0	187.4	9.0	L-T
C10.4	0.50	3130	152.8	106.2	30.9	L-T
C8.4	0.50	2841	96.1	69.3	78.2	L-T
C8.1	0.51	3577	296.7	199.5	8.0	L-T
C6.1	0.50	3140	140.1	97.9	36.8	L-T
C5.4	0.50	3354	261.2	176.5	10.6	L-T
C4.1	0.50	3120	122.5	86.5	48.1	L-T
C3.4	0.50	2200	50.1	39.5	287.6	L-T
C2.4	0.48	2916	75.5	56.0	131.5	L-T
C2.1	0.47	3150	107.4	76.7	66.3	L-T
C10.1	0.52	3120	155.3	107.8	28.7	L-T
C11.4	0.50	2908	88.6	64.5	92.0	L-T
C9.1	0.51	2839	134.3	94.2	39.2	L-T
C1.4	0.49	2357	52.3	40.9	269.5	L-T
C3.1	0.49	2031	45.3	36.4	358.4	L-T
C6.4	0.48	3293	137.5	96.3	39.7	L-T
C7.1	0.48	2915	87.2	63.6	98.7	L-T
C5.1	0.48	3244	396.2	264.1	4.8	L-T
Middle section						
C12.3	0.48	3101	126.0	88.8	47.3	L-T
C12.2	0.47	2991	91.1	66.1	92.3	L-T
C11.3	0.49	3072	125.4	88.4	46.8	L-T
C11.2	0.49	2816	101.0	72.6	72.2	L-T
C10.3	0.52	2841	99.0	71.3	70.7	L-T
C9.2	0.51	3015	336.0	225.0	6.3	L-T
C8.3	0.48	3461	178.5	122.9	23.6	L-T
C6.3	0.51	2958	106.4	76.0	62.5	L-T
C6.2	0.53	2608	82.8	60.7	99.1	L-T
C5.3	0.50	3130	282.6	190.3	9.0	L-T
C5.2	0.50	2878	105.7	75.6	64.7	L-T
C1.3	0.49	3276	151.7	105.4	32.0	L-T
C9.3	0.51	3393	313.7	210.6	7.2	L-T
C1.2	0.50	2680	73.7	54.8	132.9	L-T
C2.3	0.49	2725	78.2	57.8	120.3	L-T
C3.2	0.49	3116	145.4	101.4	34.8	L-T
C3.3	0.50	3227	208.8	142.5	16.6	L-T
C4.2	0.50	3010	127.0	89.4	44.7	L-T
C4.3	0.48	2915	87.2	63.6	98.7	L-T

Test temperature: -120°C $\sigma_{0.2} = 697 MPa$ - $E = 215.6 GPa$			Specimen type: 0.2T C(T) Dimensions: B= 4.5mm W=9mm.			
Surface						
Specimen ID	a_0/W	P_f (N)	K_{Jc} $(MPa\cdot m^{1/2})$		M	Orientation
			0.2T C(T)	Corrected to 1T		
B11-4	0.55	2330	62.9	47.8	172.8	L-T
B12-1	0.48	2815	77.0	57.0	133.1	L-T
B12-4	0.52	3380	121.9	86.1	49.0	L-T
B14-1	0.49	2890	67.1	50.6	171.8	L-T
B14-4	0.50	3453	112.6	80.1	59.9	L-T
B16-1	0.49	3151	77.5	57.3	128.9	L-T
B16-4	0.49	3296	114.7	81.4	58.9	L-T
Middle section						
B11.3	0.48	2890	110.7	78.9	64.4	L-T
B12.2	0.49	3487	117.7	83.4	55.9	L-T
B12.3	0.50	2750	62.6	47.7	193.5	L-T
B16.2	0.51	2518	59.7	45.8	208.7	L-T
B16.3	0.47	2825	60.0	46.0	223.4	L-T
B14-3	0.50	3087	82.6	60.6	111.1	L-T

Appendix 3

Maximum likelihood estimator (MLE) method. Confidence intervals.

In this appendix, we present several important statistical concepts used in this work.

The parameters of the Weibull distribution can be estimated from the experimental data by means of the maximum likelihood estimator method. The likelihood function L is defined for n data points as follows [A.3.2], [A.3.3].

Eq. A3. 1 $$L(X_1, X_2, ..., X_n; \theta_1, \theta_2, ...\theta_m) = \prod_{i=1}^{n} f(X_i; \theta_1, \theta_2, ...\theta_m)$$

where X_i are the data points, f is the probability density function (pdf) and θ_i are the m parameters to be estimated.
Taking logarithms we obtain:

Eq. A3. 2 $$\ln(L) = \sum_{i=1}^{n} \ln(f(X_i; \theta_1, \theta_2, ...\theta_m)$$

The estimate for each parameter θ_i is obtained by maximizing $\ln(L)$ with respect to all the parameters. This is done by solving simultaneously the following set of equations:

Eq. A3. 3 $$\frac{\partial \ln(L)}{\partial \theta_m} = 0$$

It is important to stress that each estimate $\hat{\theta}_i$ is a random variable, i.e., a new set of n experimental data points produces a new set of values of the estimated parameters. As an example, let's consider the three-parameters Weibull distribution, given by [[A.3.5]]:

Eq. A3. 4 $$f(t) = \frac{\alpha}{\beta}\left(\frac{t-\gamma}{\beta}\right)^{\alpha-1} \exp\left[-\left(\frac{t-\gamma}{\beta}\right)^{\alpha}\right]$$

$\alpha, \beta > 0$ and $0 \le \gamma \le t \le \infty$

Eq. A3. 5 $$F(t) = 1 - \exp\left[-\left(\frac{t-\gamma}{\beta}\right)^{\alpha}\right]$$

The median value :

Eq. A3. 6 $$\mu = \gamma + \beta \cdot \Gamma\left(1 + \alpha^{-1}\right)$$

The variance:

Eq. A3. 7 $$\sigma^2 = \beta^2 \left\{ \Gamma\left(1+2\alpha^{-1}\right) - \left[\Gamma\left(1+\alpha^{-1}\right)\right]^2 \right\}$$

where Γ is the gamma function. Assuming γ known, the three–parameter Weibull distribution, the MLE estimators will be given by the following expressions:

Eq. A3. 8 $$\frac{1}{n}\sum_{i=1}^{n}(t_i - \gamma)^{\hat{\alpha}} = \hat{\beta}^{\hat{\alpha}}$$

Eq. A3. 9 $$\frac{1}{n\hat{\beta}^{\hat{\alpha}}}\sum_{i=1}^{n}(t_i - \gamma)^{\hat{\alpha}} \cdot \ln(t_i - \gamma) - \frac{1}{n}\sum_{i=1}^{n}\ln(t_i - \gamma) = \frac{1}{\hat{\alpha}}$$

These equations must be solved simultaneously by iteration for $\hat{\alpha}$ and $\hat{\beta}$.

Confidence bounds

We have described in the previous section one of the classic methods for the parameter determination. In this way, it is possible to obtain estimated values for the unknown parameters from the experimental data. Since these values are merely estimations, the determination of the confidence intervals for the estimations is fundamental. Before describing the method used for the determination of the confidence intervals, it is worth discussing briefly the concept of confidence bounds. As described previously, the estimated parameters are random variables. Consequently, they have an associated probability distribution.

Let us consider for instance an experiment where we have a population of 30 samples. From these 30 samples, we can estimate values for the unknown parameters. If this experiment is repeated several times, we can generate a large set of estimated values, which will be characterized by a probability distribution.

For the sake of clarity, we will consider a one-parameter problem. Once the unknown parameter value has been estimated, we are interested in determining the confidence bounds for our estimation. The confidence bounds are interpreted as follows: Let's assume that we determine a certain confidence interval, let's say 90%, by means of an appropriate method. The 90% bounds of our confidence interval are given by $a(\hat{\theta})$ and $b(\hat{\theta})$. The interval so determined is such that the probability that θ (the true value of the parameter) belongs to the interval $\left[a(\theta); b(\theta)\right]$ is 90%. Note that the bounds of the confidence interval are functions of the estimated parameter $\hat{\theta}$, therefore, they are also random variables. If the previously described experiment were repeated 100 times, each replication would lead to a new $\hat{\theta}$ value. For each of these estimates, we can calculate a certain confidence interval, i.e., 90%. Then, the true value of the parameter must be contained in about 90 of these intervals.

Determination of the confidence intervals.

a) Normally distributed data.

We introduce first the case of the normally distributed data. Next, the general case of non-normal data is presented.
Let's consider a certain hypothetical population infinitely large. In general, such a population (that we will name the "parent population") will be characterized by a certain mean value μ ad a certain variance σ^2. We perform an experiment which consists in sampling n times the population. From the n-experimental data points obtained, it is then possible to *estimate* the mean of the population $\hat{\mu}$:

Eq. A3. 10 a $$\hat{\mu} = \frac{1}{n}\sum_{i=1}^{n} X_i$$

Obviously, the quality of $\hat{\mu}$ as a good estimation of μ (the real mean of the distribution) increases for larger values of n. The real variance of the distribution, σ^2, can be also estimated from the experimental data experimental data as follows:

Eq. A3. 10 b $$\hat{s}^2 = \frac{1}{n-1}\sum_{i=1}^{n}\left(X_i - \hat{\mu}\right)^2$$

Finally, the estimated standard deviation will be given by:

Eq. A3. 11 $$\hat{s} = \sqrt{\frac{1}{n-1}\sum_{i=1}^{n}\left(X_i - \hat{\mu}\right)^2}$$

Note that all the concepts are completely general, independent of the type of the distribution that characterizes the population (normal, Weibull, etc.)
Since the estimated parameters are random variables, they are described by a certain distribution of probabilities. Therefore, it is also possible to estimate the mean and the standard deviation of the distribution of the means, $\mu_{\hat{\mu}}$ and $\sigma_{\hat{\mu}}$ respectively. There exist a general relationship between the mean and the standard deviations of the parent distribution (μ and σ), and the correspondent mean and standard deviation of the distribution of the means:

Eq. A3. 12 $$\mu_{\hat{\mu}} = \mu$$

Eq. A3. 13 $$\sigma_{\hat{\mu}} = \frac{\sigma}{\sqrt{n}}$$

Again, these two equations are general in the sense that they are independent of the type of distribution that characterizes the population (the parent distribution). Since the value of μ and σ are not known, we can use the estimators given by:

Eq. A3. 14 $$\hat{\mu}_{\hat{\mu}} = \hat{\mu}$$

Eq. A3. 15 $$\hat{\sigma}_{\hat{\mu}} = \frac{\hat{s}}{\sqrt{n}}$$

Following the definitions given in the previous section, we are interested in determining a certain confidence level from our estimation. In the particular case of normally distributed data, the confidence statement can be expressed as follows [[A.3.1]]:

Eq. A3. 16
$$P\left[\frac{\left|\hat{\mu}_{\hat{\mu}}-\mu\right|}{\hat{\sigma}_{\hat{\mu}}}\le A\right]=P\left[\frac{\left|\hat{\mu}-\mu\right|}{\hat{\sigma}_{\hat{\mu}}}\le A\right]=\gamma$$

In the special case of samples for a normal distribution, the statistics

$$t=\frac{\hat{\mu}-\mu}{\hat{\sigma}}$$

is known as Student's t. Note that t has a different distribution for each value of the degree of freedom, defined in this context as $n-1$. Consequently, by mean of the t distribution we can write:

Eq. A3. 17
$$P\left[-t_\alpha\le\frac{\hat{\mu}-\mu}{\hat{\sigma}_{\hat{\mu}}}\le t_\alpha\right]=1-2\alpha$$

using Eq. A3. 15, we obtain:

Eq. A3. 18
$$P\left[\hat{\mu}-t_\alpha\frac{\hat{s}}{\sqrt{n}}\le\mu\le\hat{\mu}+t_\alpha\frac{\hat{s}}{\sqrt{n}}\right]=1-2\alpha$$

In words, the confidence statement now says that the probability that μ lies in the random interval $\hat{\mu}\pm t_\alpha\hat{\sigma}$ is $1-2\alpha$.
The following example illustrates the problem. If we want to obtain the 95% confidence interval, $\alpha=0.025$ and if ten data points have been considered, then, $t_\alpha = t_{0.025} = 2.262$ (for 9 d.o.f.). Finally: $\mu=\hat{\mu}\pm 2.262\hat{\sigma}$ with a 95% of confidence.

b) General case

There exist three general methods for the estimation of the confidence intervals in the general case (data not normally distributed, several parameter to be estimated) [[A.3.4]]. We only discuss the so-called likelihood ratio method for the determination of the confidence bounds. This method is based in the following asymptotic property of the likelihood function:

Eq. A3. 19
$$2\ln\left[\frac{L(\hat{\theta})}{L(\theta)}\right]=\chi_{\alpha,t}$$

The function in the left hand has asymptotically a chi-squared distribution. Finally, the confidence statement will be given by the following expression (see ref. [A.3.4], Chapter 9):

Eq. A3. 20
$$P\left[\chi^2_{\frac{1-\alpha}{2},t} \le 2\ln\left[\frac{L(\hat{\theta})}{L(\theta)}\right] \le \chi^2_{\frac{1+\alpha}{2},t}\right] = \alpha$$

Practical examples for the particular case of brittle fracture.

As discussed in Chapter 5, the Weibull distribution is the appropriate framework to analyze fracture data. The problem consists in finding the numerical values of the different coefficients of the distribution from a certain number of experimental data points.
For the case of brittle fracture, the Weibull cumulative probability function is usually written as follows:

Eq. A3. 21
$$P(K_{Jc}) = 1 - \exp\left[-\left(\frac{K_{Jc} - K_{\min}}{K_0 - K_{\min}}\right)^m\right]$$

Combining the expression of $P(K_{Jc})$ with a generator of random numbers, it is possible to obtain easily a set of n random K_{Jc} values. This set of random K_{Jc} values can be used to illustrate the procedures described previously. Since the real values of the parameters of the distribution are known, the results obtained from the application of the methods for parameter determination and statement of confidence intervals can be assessed.
In the present example, we have generated sets of 31 K_{Jc} values. We have generated 20000 of such sets, assuming K_0=85.24 $MPa \cdot m^{1/2}$, $K_{\min}$=20 $MPa \cdot m^{1/2}$ and m=4. It is further assumed that the only unknown parameter that needs to be estimated is K_0. From these values, we obtain $K_{Jc(med)}$=79.53 $MPa \cdot m^{1/2}$, correspondent to the 50% of cumulated probability, and $K_{Jc(mean)}$=79.13 $MPa \cdot m^{1/2}$ (via Eq. A3. 6).
The estimated values for K_0 and $K_{Jc(med)}$ ($\hat{K}_0$ and $\hat{K}_{Jc(med)}$ respectively) have been obtained for each set of 31 K_{Jc} values. K_0 has been estimated by means of the MLE method as follows (Eq. A3. 8):

Eq. A3. 22
$$\hat{K}_0 = \left[\sum_{i=1}^{n} \frac{\left(K_{Jc(i)} - K_{\min}\right)^4}{n}\right]^{1/4} + K_{\min}$$

$\hat{K}_{Jc(med)}$ and $\hat{K}_{Jc(mean)}$ have also been calculated from the set of 31 data points. A histogram for the K_0 values is shown in Figure A3.1.
As it can be seen, the distribution of the $\hat{K}_0$ value is almost normal. The mean value obtained was $\hat{K}_{0(mean)}$=85.56 $MPa \cdot m^{1/2}$ and the median is $\hat{K}_{0(med)}$=85.60 $MPa \cdot m^{1/2}$. The standard deviation $\sigma_{\hat{K}_0}$ is 2.98 $MPa \cdot m^{1/2}$. Note that $\hat{K}_{0(mean)}$ and $\hat{K}_{0(med)}$ are slightly biased with respect to the real value of K_0=85.24 $MPa \cdot m^{1/2}$. Similar results can be obtained for $\hat{K}_{Jc(med)}$.
Since $\hat{K}_{Jc(med)}$ was determined for every set of 31 K_{Jc} values, we may want to obtain a given corresponding confidence interval, say 90%. This problem is greatly simplified due to the fact that the assumed Weibull slope is $m = 4$. A Weibull three-parameters pdf is plotted in Figure A3. 2 for the particular case of $m = 4$. As it can be seen, the distribution is very

similar to the normal distribution. The high degree of "normality" of the Weibull pdf for the case of $m = 4$ suggest that we may treat the data as "normal" data for the particular case of the determination of the confidence bounds. As explained before, this fact allows us to use the Student's t distribution instead of the more complicated method of the likelihood ratio method.

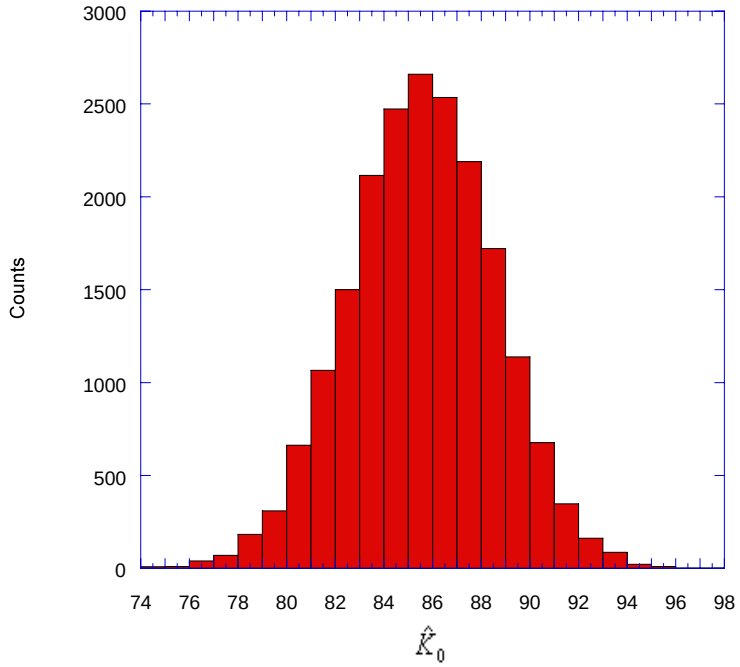

Figure A3. 1: *Histogram of the distribution of the estimated* $\hat{K}_0$ *value.*

Accepting the data as "normal" data, the confidence bounds are determined as follows. First the mean ($\hat{K}_{Jc(mean)}$), and the standard deviation ($\hat{s}_{K_{Jc}}$) are calculated from the 31 K_{Jc} values generated. Next, the standard deviation of the $\hat{K}_{Jc(mean)}$ distribution is estimated from $\hat{s}_{K_{Jc}}$ via Eq. A3. 15. Finally we calculate the confidence bounds through Eq. A3. 18 using a table for the Student's t distribution. For the case of the 90%confidence bounds, we obtain:

Eq. A3. 23
$$P\left[\hat{K}_{Jc(mean)} - 1.697\frac{\hat{s}_{K_{Jc}}}{\sqrt{n}} \le K_{Jc(med)} \le \hat{K}_{Jc(mean)} + 1.697\frac{\hat{s}_{K_{Jc}}}{\sqrt{n}}\right] = 0.9$$

where $t_{0.05} = 1.697$ for 30 d.o.f. (n-1), and

$$1.697\frac{\hat{s}_{K_{Jc}}}{\sqrt{n}} = \Delta K_{Jc(mean)}$$

Eq. A3. 23 must be interpreted as the confidence interval. If we consider a large number of sets of 31 K_{Jc} values, the corresponding $\hat{K}_{Jc(mean)}$ values and the associated 90% confidence intervals, we may expect that the true $K_{Jc(mean)}$ value is contained in approximately 90% of the confidence intervals determined from each set. Indeed, the analysis of 500 showed that 99.3% of the intervals contained the true $K_{Jc(mean)}$ value. This result is presented in Figure A3. 3, where only 50 $\hat{K}_{Jc(mean)}$ values and its 90% confidence intervals have been plotted for

the sake of clarity. It can be seen that only 4 intervals do not contain the true $K_{Jc(med)}$ value, indicated in the plot with a dotted line.

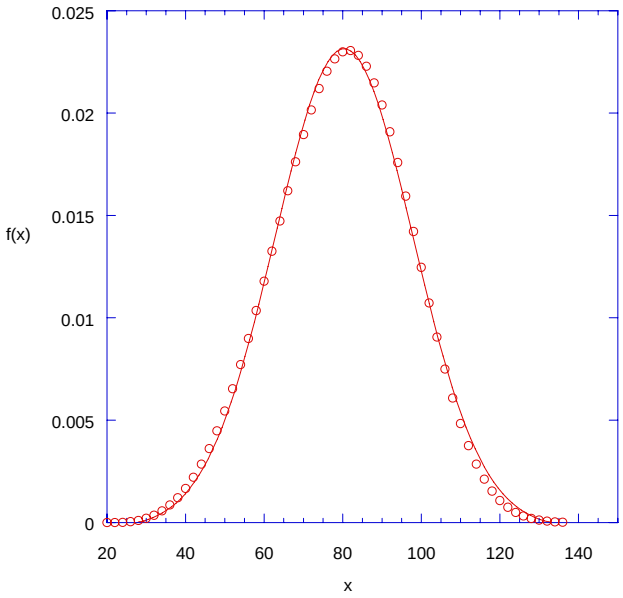

***Figure A3. 2**: Weibull pdf for m=4 fitted with a normal pdf.*

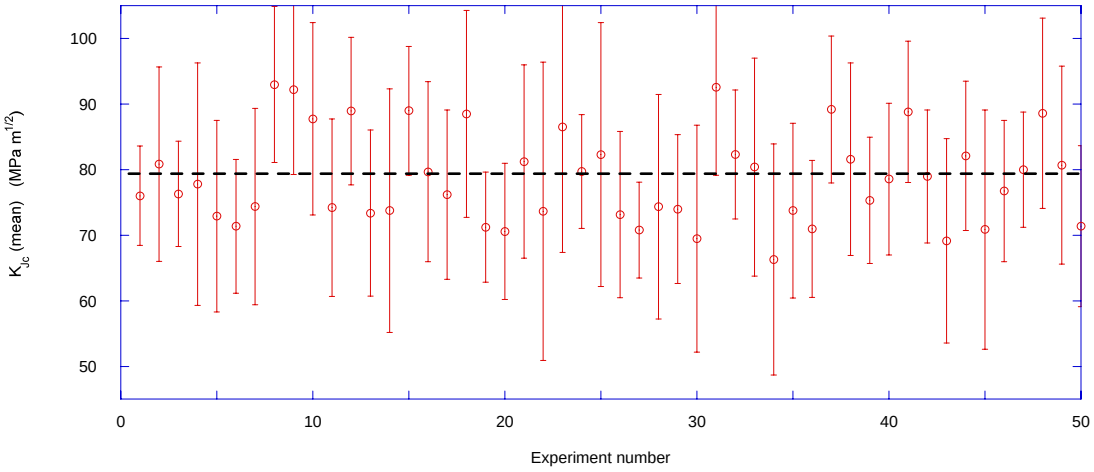

***Figure A5. 1:** K_{Jc}(mean) with the corresponding 90% confidence bounds obtained from sets of 31 data. The true K_{Jc}(mean) is out the confidence interval only in one case.*

The confidence bounds for $\hat{K}_0$ can be calculated from the extreme values of $\hat{K}_{Jc(mean)}$ via Eq. A3. 6. For instance, in the case of the 90% upper confidence bound:

Eq. A3. 24

$$\Delta\hat{K}_0 = \frac{K_{Jc(mean)} + \Delta\hat{K}_{Jc(mean)} - K_{\min}}{\Gamma(1+\alpha^{-1})} - \hat{K}_o$$

An alternative way for determining $\Delta\hat{K}_0$ is based on the fact that $K_{Jc(mean)} \approx K_{Jc(med)}$. Consistently, we may expect that $\Delta K_{Jc(mean)} \approx \Delta K_{Jc(med)}$. Since:

Eq. A3. 25 $$K_{Jc(med)} = K_{\min} + (K_0 - K_{\min}) \cdot [\ln(2)]^{1/m}$$

then, we can write the following approximate expression:

Eq. A3. 26 $$\Delta\hat{K}_0 = K_{\min} - \hat{K}_0 + (\hat{K}_{Jc(med)} + \Delta K_{Jc(mean)} - K_{\min}) \cdot [\ln(2)]^{-1/m}$$

Note that $\hat{K}_{Jc(med)}$ can be obtained in two different ways: a) by using Eq. A3. 25 and the estimated $\hat{K}_0$ using MLE method, or b) by calculating the median of the experimental data. These two values are expected to be different. The numerical experiment shows that for small datasets, $\hat{K}_{Jc(med)}$ as determined from the MLE method better estimates the real value of $K_{Jc(med)}$. Finally, the uncertainty in K_0 will be reflected by an uncertainty in the determination of the reference temperature T_0.

In summary, we have demonstrated via numerical experiments the fact that, assuming that brittle fracture is well described by a Weibull distribution having a slope m=4, the confidence intervals on the parameters of the distribution can be well estimated by the Student's t distribution. This is a consequence of the high degree of "normality " of the Weibull distribution having m=4.

References to the Appendix 3:

[A.3.1] Steel R.G.D:, Torrie J.H., Principles and Procedures of Statistics, A Biometrical Approach, 2nd Edition, Mc Graw-Hill, 1980.

[A.3.2] Beck J.V., Arnold K.J., Parameter Estimation in Engineering and Science, J.Wiley and Sons, Inc., 1977.

[A.3.3] Bard Y., Nonlinear Parameter Estimation, Academic Press, 1974.

[A.3.4] Eadie W.T., Drijard D., James F.E., Roos M., Sadoulet B., Statistical Methods in Experimental Phisics, 3rd Reprint, Elsevier, 1971.

[A.3.5] Mc Cormick N.J., Reliability and Risk Analysis, Methods and Nuclear Power Applications, Academic Press, 1981.

Acknowledgements

The “Acknowledgements” are commonly at the end of most of the PhD’s on the planet. However, in a personal level, I feel that it is the most important section in the manuscript. It has not been easy at all to reach this point in my scientific career. To finish a PhD requires a lot of work and commitment during several years. In this sense, I am convinced that I did my best. However, I am fully aware of the fact that if I was able to finish this PhD, it is, without any doubt, because of the support, encourage and love of my family along these years. In particular, I must thanks to my wife Guadalupe who was with me in very difficult moments, teaching me the real meaning of the words “strength”, “courage” and “perseverance”. Her example has been my best source of inspiration.

I have also to thanks my PhD director, Philippe Spätig. It has been a privilege to me to work with him. Working with Philippe implies being involved in a continuous brainstorming. He was always confronting me with the correct questions, being ready to discuss about “the ongoing topic” in any moment of the day. The time we have spent working together has certainly shaped me as a material scientist.

I want also to mention Emiliano Campitelli, who was “sharing the burden” of the PSI with me in the pubs in Baden along several nights (well, we can also include some afternoons here…..)

Many thanks also to my colleagues and former colleagues at CRPP/PSI: Nadine, Robin, Amuthan, Yu, Zbigniew, Raluca, Krami, Pierre, Caroline, Stefan, Jan, Apostolos, Gabriel, Nita, Yao and Tibor, who made the difference in my everyday life at PSI.

Finally, I want to thanks my friends, Jorn Verwey and Mayoo van Wissen for their support and love during my stay in Switzerland. With time, they became “my family” in the country.

Curriculum Vitae

Raul Alejandro Bonadé

Born in Mendoza, Argentina, October 13th, 1972.

2002-2005: PhD at École Polytechnique Fédérale de Laussanne (Switzerland), Centre de Recherche en Physique des Plasmas, Fusion Technology-Materials Group.

PhD Thesis: "*Constitutive Behavior and Fracture Properties of Tempered Martensitic Steels for Nuclear Applications: Experiments and Modeling*"

1997-2001: Materials Engineering – Instituto de Tecnología prof. Jorge Sábato at Comisión Nacional de Energía Atómica (National Atomic Energy Commission of Argentine), graduate as Master in Materials Engineering (August 2001).

Master´s Thesis: "*Study of Localized Corrosion Processes in Al-Cu-Li Alloy*s" at Centro Atómico Constituyentes in Argentine and at Departamento de Corrosión y Protección, Centro Nacional de Investigaciones Metalúrgicas, (Corrosion and Protection Department, National Center for Metallurgical Research), Madrid, Spain.

1992-1995: Industrial Engineering - Engineering School at Universidad Nacional de Cuyo, Argentina.